Differential absorption LiDAR for the total column measurement of atmospheric CO_2 from space

Thesis submitted for the degree of
Doctor of Philosophy
at the University of Leicester

by

James Lawrence
Department of Physics and Astronomy
University of Leicester

September 2011

Contents

Abstract

Since the beginning of the industrial revolution (1750 to 1800) the Earth's atmospheric composition has undergone significant change as a result of human activities, in particular the burning of fossil fuels. As a consequence the atmospheric concentrations of a number of gases known to be influential to the Earth's climate have increased far beyond natural levels.

Atmospheric gases such as carbon dioxide which naturally exist in the Earth system have increased in correlation with anthropogenic emissions. The effect of this perturbation on the Earth system has been predicted through computer simulations to have undesirable consequences on the Earth's future climate. The present measurement systems for atmospheric carbon dioxide have limited spatial coverage and temporal resolution which restricts their ability to accurately attribute observations of atmospheric composition to particular terrestrial sources and sinks. This inability to accurately locate and quantify the key carbon dioxide sources and sinks in the terrestrial and marine biospheres is hindering the understanding of the processes that are driving the Earth's natural uptake of approximately half of the anthropogenic carbon dioxide emissions. With such uncertainty it is currently unknown precisely how the Earth's climate will respond to global warming in the future. Through computer simulation it has been demonstrated that improving the spatial distribution of global measurements of atmospheric carbon dioxide is likely to advance the present understanding of the Earth's terrestrial sources and sinks. Regions that require particular improvement in measurement coverage are the southern oceans owing to a lack of landmass on which to site instruments, and much of the tropics because of difficulties in locating instruments in some of the worlds more politically unstable regions.

Satellite remote sensing instruments which measure atmospheric carbon dioxide from low Earth orbit provide some coverage of these sparsely sampled locations, however cloud cover often prevents measurements being made (particularly in the tropics), and limited latitudinal coverage caused by current instruments using passive remote sensing techniques prevents measurements at very high and low latitudes (including much of the southern ocean during local winter). An alternative remote sensing technique has been proposed in

the scientific literature for measuring atmospheric carbon dioxide concentrations using laser emissions from a satellite platform known as total column differential absorption LiDAR (TC-DIAL). The TC-DIAL technique has been identified as having the theoretical potential to meet the coverage and precision requirements to greatly aid in identifying and quantifying terrestrial carbon dioxide sources and sinks. The TC-DIAL technique has the potential to achieve these goals largely owing to its unique capabilities of being able to make measurements during both the day and night and at all latitudes with a footprint which may be small enough to see between patchy cloud cover in the tropics.

This thesis builds on previous studies of the TC-DIAL measurement technique from a satellite platform to assess its current and future capabilities to meet the observation requirements defined by the atmospheric carbon and modeling scientific communities. Particular investigations are carried out to assess the optimum system configuration in the context of global carbon modeling using up-to-date spectroscopy and instrument parameters for the latest technology. Optimum systems for both direct and heterodyne detection TC-DIAL instruments are defined, and it is found that direct detection provides the lowest retrieval errors under clear sky conditions. For a system based on current technology TC-DIAL retrievals are expected to have errors of approximately 0.68 ppm for direct detection and 1.01 ppm for heterodyne detection over a 50 km surface track.

Using global cloud statistics two suitable pulse repetition frequencies (PRF) for a heterodyne detection system have been identified as 5 and 15 kHz. These PRF's provide the minimum probability of an effect known as cross signal contamination occurring when measurements are made in the presence of cloud. In this thesis it is shown that the retrieval error incurred by cross signal contamination is > 16 ppm for a heterodyne detection TC-DIAL system measuring through cloud with optical depth > 2.

The most important retrieval error component in TC-DIAL retrievals has been found to be the uncertainties introduced by the use of numerical weather prediction data for the ancillary atmospheric profiles. The limited spatial resolution of current NWP models (> 20 km) implies the uncertainties associated with the ancillary data are required to be treated as systematic, and as a consequence their errors dominate over other TC-DIAL retrieval errors following multiple pulse integration.

Acknowledgements

Acknowledgements for 4 years of very personal and intensive work such as the research and writing of a PhD thesis can (in my opinion) only truly be attributed to the author and his or her immediate family. In my particular case I owe this thesis largely to my fiancée Claire, who has had to live with some of the less desirable consequences of this unusual choice of employment. For us the normal progression through life has been put on hold for a very long time in the name of career progress, and for this reason and for her patience over the last seven and a half years I dedicate this thesis (for what it's worth) to my scrumpet, Claire.

Arriving at the stage of writing the acknowledgements of my own PhD thesis and having the opportunity to publish academically inappropriate words like 'scrumpet' is only possible because of support I received from my parents during my undergraduate career. Their invaluable contribution of offering residency for my duration at university as an undergraduate student helped me avoid the devastating cost of a modern academic education which to me and my family was a very oppressive debt to incur.

I'll take this opportunity to mention those who gave me the inspiration to undertake a PhD in the first place. First (and most importantly) is Dr Roland Leigh, who as my supervisor during my fourth year undergraduate project made me realise that research was within my capability and that support was at hand when needed, and second to Dr Emmett Brown and his time travelling Delorean, who made me realise in a fundamental way that science involved exploration and adventure - I haven't yet worked out how to make a flux capacitor, but I'm working on it.

I'd also like to acknowledge Rosie Graves for buying me an ice cream when I needed to chill out after my job interview, Nishad Karim for her eternal energy and distractions from work, Limey, Tomasz , Joe, Ed, Alex and Austin for just generally being a laugh whenever I actually had time to laugh (and allowing me to shoot some of them during a paintball game), my old cat Pickles, our borrowed cat Cosmo, our current cats Marmite and Crumpet and our seven hamsters for the stress relief that having pets bring! Also Dr Hartmut Boesch for always providing his time and help when requested throughout my PhD, and finally my supervisor Professor Paul Monks for steering this thesis roughly towards its final destination.

List of Figures

List of Tables

1. The scientific context

The following chapter reviews and defines the Earth's atmosphere and its underlying dynamical processes, and investigates the importance of suitably measuring and therefore understanding atmospheric carbon dioxide.

1.1 The Earth's atmosphere

The Earth's atmosphere may be loosely defined as a thin body of gas surrounding the Earth's surface and is one of the principal components of the environment necessary for life on Earth to exist. It contains molecular oxygen which is required for plant and mammal respiration, it protects the surface from harmful radiation and meteorite impacts and provides essential thermal insulation via the greenhouse effect (Section 1.2). Its main constituents are presented in Table 1.1-1.

The Earth's atmosphere can be classified into separate vertical layers defined by inversions in its temperature profile (Figure 1.1-1). The first layer nearest the surface is known as the boundary layer which covers the first 1-2 km of the atmosphere. This is a region of considerable vertical mixing and has air movements which are strongly influenced by friction with the Earth's surface. The next layer up by height is known as the free troposphere which extends up to the tropopause where the first temperature inversion occurs. The tropopause is present at an altitude of approximately 8 km near the poles and 18 km at the equator. Above the tropopause is the stratosphere which extends up to approximately 50 km and has a strong positive temperature gradient with altitude owing to a warming effect caused by ozone absorption of high energy UV radiation. Above the stratosphere is the mesosphere which extends up to approximately 80 km altitude and is considered to be the coldest area within the Earth system as temperatures drop significantly with altitude and can get below -120 °C. Finally the thermosphere is the largest of the atmospheric layers and extends from the mesopause up to the exosphere (around 600 km). The thermosphere is aptly named as temperatures within it can rise up to 1,500 °C due to absorption of high energy solar radiation by residual oxygen (Platt and Stutz, 2008). Although the magnitude of the temperature in the thermosphere is very high, its atmospheric density is very low and there are many artificial satellites currently in orbit within the thermosphere despite the magnitude of its temperature (including the International Space Station).

Gas	Chemical Formula	% Mixing Ratio
Nitrogen	N_2	78.08
Oxygen	O_2	20.95
Argon	Ar	0.93
Carbon dioxide	CO_2	0.039
Neon	Ne	0.0018
Helium	He	0.00052
Methane	CH_4	0.00018
Krypton	Kr	0.00011
Xenon	Xe	0.00009
Hydrogen	H_2	0.00005

Table 1.1-1 Atmospheric constituents and their mixing ratios, data from (Platt and Stutz, 2008)

The Earth's atmosphere has a vertical mass distribution which follows an approximate exponential decay law, with 50% of its mass existing below 5 km, and 99% below 50 km. Large global circulatory patterns perpetually transport the atmosphere's mass around the planet, sustained by incoming solar energy differentially heating the Earth's atmosphere making it warmer at the equator. Air masses are transported from the equatorial regions to the northern and southern latitudes as a result of the Brewer-Dobson Circulation (BDC) which is a phenomenon that is driven by planetary waves forcing the movement of air masses in both hemispheres. The conservation of angular momentum as a result of the Earth being approximately spherical in shape and spinning on a fixed axis implies that horizontally moving air masses (as a result of breaking and dispersing planetary waves) experience a force which encourages the air masses to rotate owing to northern and southern latitudes being closer to the centre of the Earth's axis of rotation than the areas nearer the equator. An example of the conservation of angular momentum in the context of tropospheric air masses which also observe this effect (but on a smaller scale) is presented in Figure 1.2-1.

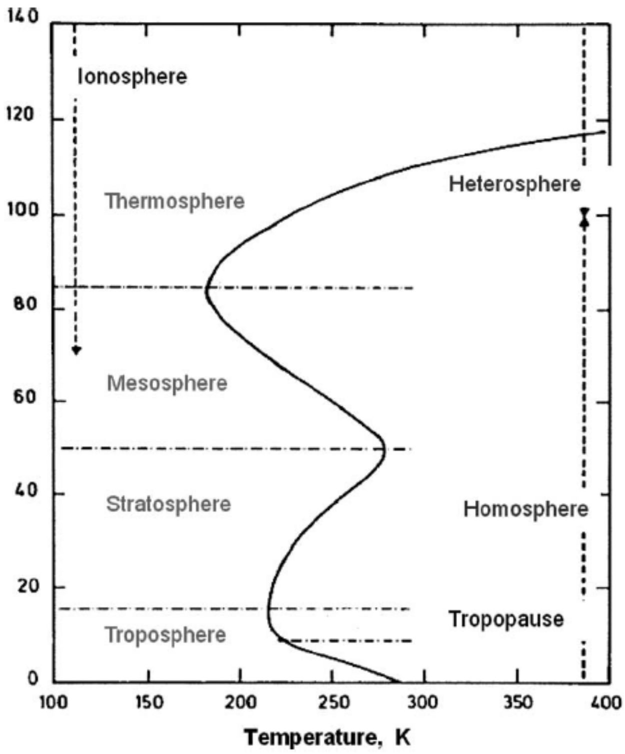

Figure 1.1-1 Layers of the Earth's atmosphere divided according to temperature inversions, image from (Platt and Stutz, 2008)

1.2 The Earth's Greenhouse Effect

The Earth's greenhouse effect is an important thermal insulation process which occurs within the Earth's atmosphere. The majority of solar radiation incident on the Earth consists of visible wavelengths which pass through the atmosphere largely unimpeded until they reach the surface where they are either reflected or absorbed. The absorbed radiation leads to a warming of the Earth's surface and causes the surface to emit infrared (IR) electromagnetic radiation in response. The emitted IR radiation is absorbed by naturally occurring atmospheric greenhouse gases, including atmospheric water vapour (H_2O), carbon dioxide (CO_2), methane (CH_4), nitrous oxide (N_2O) and ozone (O_3). The absorbed radiation is re-emitted by these gases in all directions, including out to space and back toward the surface. Some of the downward portion of the radiation reaches the ground and causes a warming of the surface and lower atmosphere, a process analogous to the effect a glass roof has on the air within a greenhouse.

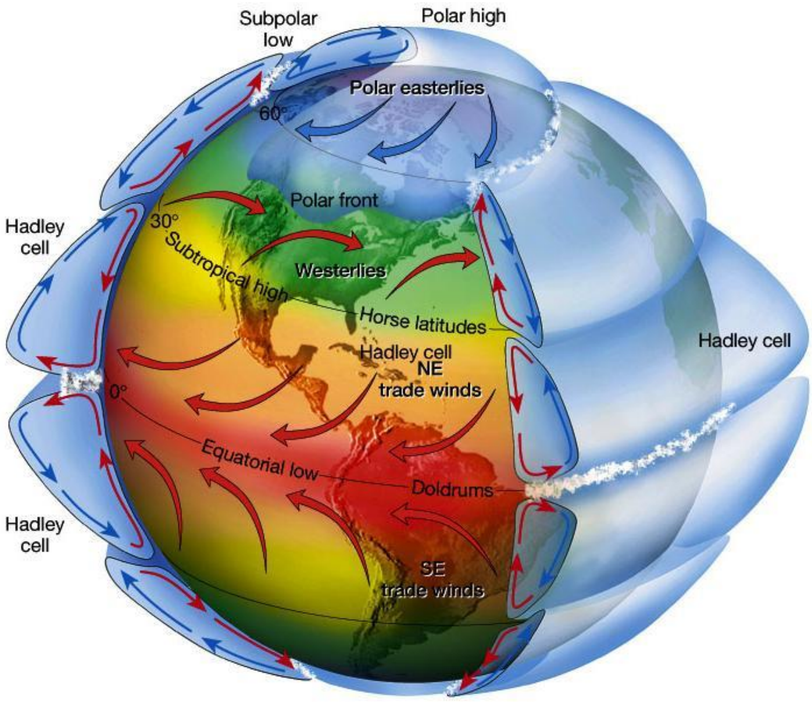

Figure 1.2-1 Idealised, three cell atmospheric convection in a rotating Earth showing tropospheric air mass movements, image from (Lutgens and Tarbuck, 2000)

The Earth's greenhouse effect can be classified into two distinct categories known as *natural* and *enhanced*. Both categories are driven by the same physical processes.

The natural greenhouse effect is vital to maintaining the Earth's climate and refers specifically to the greenhouse effect caused by naturally occurring concentrations of greenhouse gases in the Earth's atmosphere. The average surface temperature of the Earth is approximately 15 °C, however without the natural greenhouse effect it would be approximately -6 °C (Houghton, 2005).

The enhanced greenhouse effect refers to the addition of anthropogenically released greenhouse gases into the Earth's atmosphere leading to an enhanced warming of the Earth's surface. The extra warming beyond natural levels is expected to lead to changes in the Earth's climate. It has been estimated that a doubling in atmospheric carbon dioxide will result in approximately 2.5 °C increase in global surface temperatures (IPCC, 2007).

The most dominant greenhouse gas in the Earth's atmosphere is naturally occurring water vapour owing to its abundance and significant absorbing properties in the IR region of the electromagnetic spectrum. Water vapour is often considered to be a special greenhouse gas when referring to its anthropogenic effect on the Earth's climate as it is only indirectly influenced by anthropogenic emissions through feedback mechanisms. As a result it is often omitted when referring to the most important anthropogenically enhanced greenhouse gases (for example its omission in Figure 1.4-4), yet its reaction to a changing climate is highly important. The second most dominant greenhouse gas is CO_2 which is the main anthropogenic contributor to the enhanced greenhouse effect. Anthropogenic CO_2 is introduced to the atmosphere in large quantities as a by-product of combustion processes such as energy production and transportation. Observations of global temperature increases have stimulated much scientific interest in anthropogenic greenhouse gases, particularly CO_2.

1.3 Atmospheric carbon dioxide

Carbon dioxide is a chemical compound consisting of two oxygen atoms covalently bonded to a carbon atom. It is present as a well mixed trace gas in the Earth's atmosphere and is chemically unreactive. Its atmospheric concentration is currently 390 ppm and has a positive trend in concentration of approximately 2 ppm per year (IPCC, 2007). The transfer of CO_2 between the atmosphere and biosphere occurs over a range of time scales, from the very short processes of respiration and photosynthesis to the very long term sequestration processes caused by the sinking of CO_2 through ocean circulation. A molecule of CO_2 spends on average approximately 5 years in the Earth's atmosphere, however the variety of time scales over which the processes happen and their various abilities to remove carbon from the atmosphere for extended periods of time result in CO_2 having an atmospheric life time of anything up to 200 years (IPCC, 2007).

The past history of the Earth's atmospheric CO_2 has been revealed by analysis of air bubbles trapped in Antarctic ice cores (Siegenthaler et al., 2005) (Figure 1.3-1). For the last half a million years atmospheric temperature and CO_2 have undergone regular long-term cycles corresponding to interglacial periods caused by variations in the Earth's orbital motion (Hays et al., 1976). It has been shown from analysis of ice volumes within each glacial cycle that the Earth's orbit cannot be solely responsible for the amplitude of the observed temperature and CO_2 variability. For climate models to reproduce the Earth's climate cycles properly they require the inclusion of complex feedback mechanisms. An example of one such mechanism is the feedback link between atmospheric temperature and CO_2 via the greenhouse effect and their influences on biospheric processes (Houghton, 2005). The need for such processes to be present in climate models in order to reproduce past climate events indicates that feedback mechanisms have an important role to play in the Earth's future climate.

Previous atmospheric CO_2 concentrations obtained from composite ice core data sets have shown that the CO_2 concentration has remained between 180 and 290 ppm over the last 650,000 years. Prior to human intervention in recent history (last 1000 years), the atmospheric concentration had been relatively stable at the peak of the last glacial cycle at approximately 280 ppm (Barnola, 1998). Since the industrial revolution however (around 1800), the concentration has risen dramatically by approximately 30% to the current level of 390 ppm (Figure 1.3-2). The cause of the increase has been attributed to human activities for a number of compelling reasons. The most notable evidence comes from observations made of atmospheric CO_2 over the past four decades which show an approximate proportionality between rising atmospheric concentrations and industrial CO_2 emissions (Keeling, 1989). Furthermore, current atmospheric CO_2 contains the isotopic signatures of fossil fuel burning in the form of depleted carbon-13 (Prentice and Lenton, 2001; Ehleringer et al., 2005), and atmospheric CO_2 concentrations are much higher in the Northern Hemisphere (where most emissions occur) than in the Southern Hemisphere.

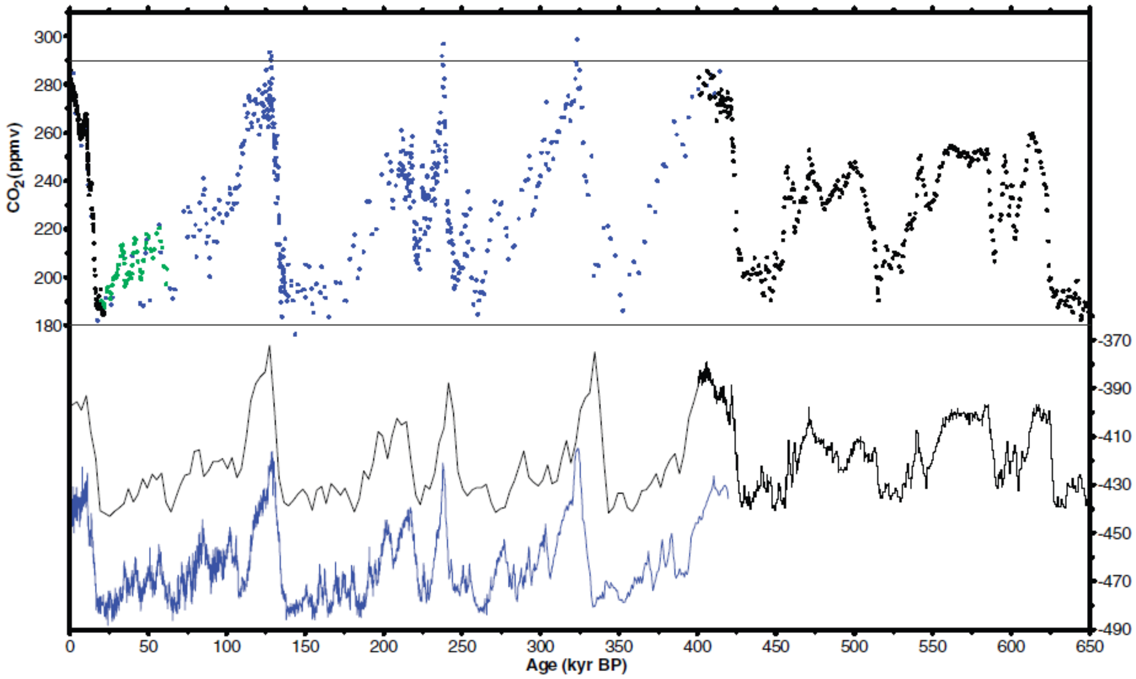

Figure 1.3-1 Composite CO_2 record over six and a half ice age cycles going back 650,000 years showing CO_2 concentrations (top panel) and Deuterium (δD) concentrations (bottom panel) which indicates the Earth's past temperature. Image from (Siegenthaler et al., 2005)

Complex climate models are used to make future projections of the Earth's climate in an attempt to understand the impact of current and future anthropogenic greenhouse gas emissions. As the magnitude of the future emissions is unknown, the climate models are run for a number of different scenarios to attain a range of possible climate futures. The most commonly used scenario is known as the 'business as usual' scenario which refers to emissions continuing to increase at their present rate. Projections using this scenario indicate that atmospheric CO_2 is likely to reach over 540 ppm by the year 2100, and temperatures are expected to rise by between 1.4 and 5.8 °C. The consequence of such a future is the likelihood of more extreme weather events including droughts, heat waves and floods. It is also likely that precipitation will increase owing to a warmer atmosphere, and the oceans are expected to rise by between 0.1 and 0.9 m as a result of thermal expansion and increased input from melting land ice (Houghton, 2005).

In-situ measurements of atmospheric CO_2 concentrations have shown there to be strong seasonal and diurnal cycles. The most famous presentation of this data which combines both the positive anthropogenic trend and the seasonality is known as the Keeling curve (Figure 1.3-3).

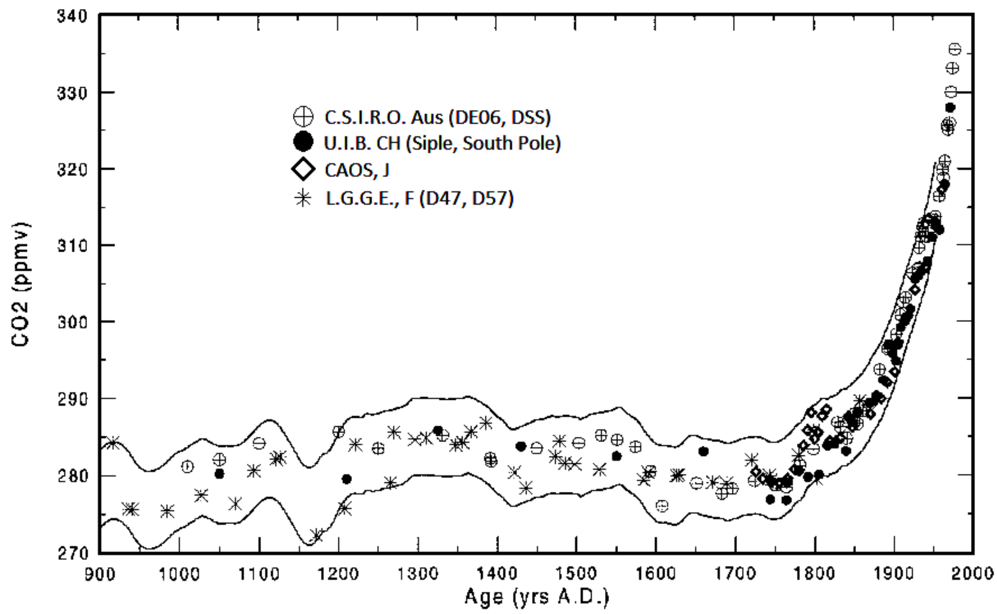

Figure 1.3-2 Atmospheric carbon dioxide measurements obtained from the analysis of ice cores for the last 1000 years, image from (Barnola, 1998)

Both the diurnal and seasonal cycles are driven by the biospheric processes of respiration and photosynthesis. During winter months (decay season) the biosphere acts as a net source of CO_2 whilst during spring and summer months (growing season) it acts as a net sink. The magnitude of the seasonal cycle in the Northern Hemisphere has been measured at approximately 12 ppm peak to trough. This is 6 times larger than the annual positive trend caused by anthropogenic emissions.

The magnitude of the diurnal cycle varies between locations and depends strongly on the proximity of the measurements to local sources and sinks. In a study obtaining CO_2 concentrations from tall towers in forested areas, the diurnal cycle was measured at approximately 40 ppm in the summer and only 5 ppm in the winter (Bakwin et al., 1998; Hurwitz and Ricciuto, 2003).

Some of the CO_2 measurement systems currently in operation do not have the facility to accurately measure the diurnal cycle owing to insufficient measurement frequency (the FLASK network) or a fundamental reliance on solar illumination (the TCCON network).

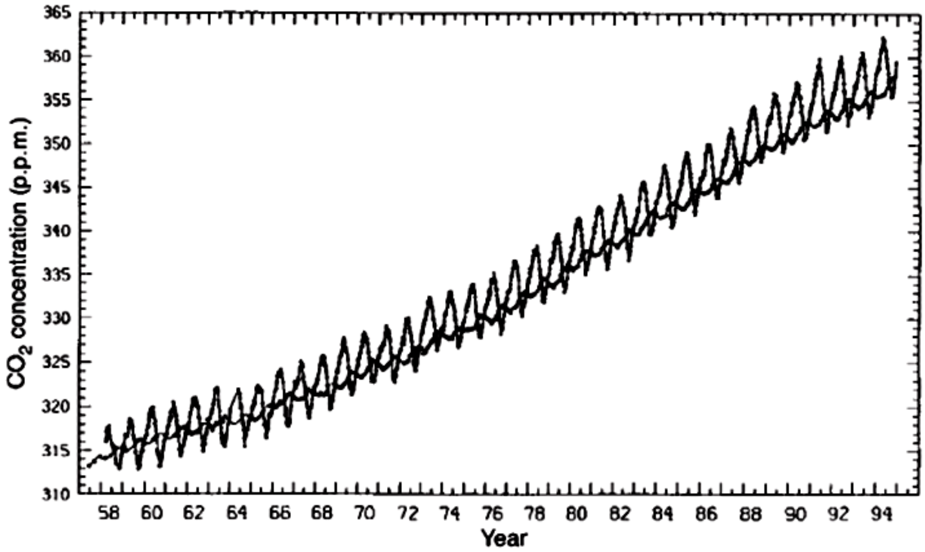

Figure 1.3-3 In-situ atmospheric CO_2 concentration measurements (monthly averaged) from Mauna Loa Observatory known as the Keeling curve, image from (Keeling et al., 1995)

Aircraft campaigns taking in-situ measurements of atmospheric CO_2 have identified a strong latitudinal dependency in both the CO_2 concentration and its seasonal cycle (Nakazawa, 1991; Anderson et al., 1996). The campaigns found the seasonal amplitude to be significantly larger in Northern Hemisphere than at the equator and in the Southern Hemisphere (Figure 1.3-4). The difference in the amplitudes has been attributed to the presence of more landmass in the north providing greater respiration, photosynthesis and anthropogenic emissions. The same measurement campaigns have also identified a temporal lag in the CO_2 seasonal cycle as a function of latitude owing to slow atmospheric transport of northern hemispheric air to the Southern Hemisphere. From the high northern latitudes to the equator the phase delay has a magnitude of approximately two months. In the Northern Hemisphere the CO_2 maxima occurs during March and April, whilst in the Southern Hemisphere where the seasons are reversed it occurs during August and September.

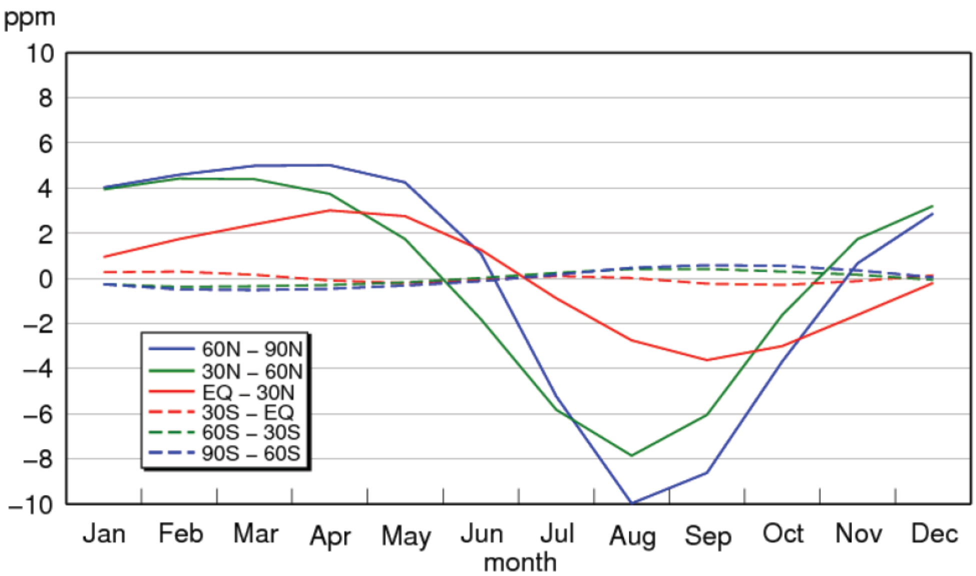

Figure 1.3-4 Average CO_2 seasonal cycles for 30° latitudinal zones (WMO, 2010)

The vertical distribution of CO_2 is relatively constant in the mid latitudes, however at high latitudes the vertical distribution is modified by global transport patterns (section 1.1). Measurements made by Anderson et al, (1996) during an aircraft campaign revealed that there are large gradients (around 10 ppm) in the vertical profile of atmospheric CO_2 at high northern latitudes in the winter months. These strong variations occur as a result of a buildup of CO_2 near the surface during the winter combined with the presence of older air masses (depleted of CO_2) arriving at higher altitudes from the tropics (Anderson et al., 1996). In the mid latitudes these gradients are less pronounced as there is greater vertical mixing and a regular influx of clean air from the tropics. In the tropical regions the vertical profile is almost constant as a result of very rapid vertical mixing.

Measurements of the global transport of CO_2 and other carbon compounds and molecules (such as CH_4) in the Earth's atmosphere provide indicators for the magnitude and locations of the sources and sinks of atmospheric carbon. Understanding the transport of carbon around the Earth is critical for understanding and predicting atmospheric concentrations of key greenhouse gases such as CO_2.

1.4 The Carbon Cycle and Global Warming

The Earth's carbon cycle is a naturally stable system in which carbon is transferred from the biosphere to the atmosphere and back again (Figure 1.4-1). The natural processes which drive the cycle such as photosynthesis and respiration are perturbed by human activities through the release of anthropogenic carbon into the atmosphere. The anthropogenic carbon is mainly released through fossil fuel combustion in the form of CH_4 and CO_2 (67%) (mainly CO_2), however a significant proportion also originates from land use change and deforestation (33%) (IPCC, 2007).

Approximately half of the anthropogenic CO_2 emissions remain in the atmosphere with the other half being sequestered by the terrestrial and marine biospheres (Figure 1.4-2). These biospheres along with the Earth's atmosphere form the three main reservoirs which store carbon in the Earth system. The ocean holds the most carbon, storing about 37,000 GtC in its deep waters. The terrestrial biosphere and atmosphere hold significantly less, about 2,500 GtC and 750 GtC respectively. The processes which transfer carbon between the reservoirs have a considerable variety of time scales. Carbon taken down to the deep ocean through ocean circulation processes is considered to have left the climate system for hundreds of years, whereas carbon sequestered by soils and vegetation on the Earth's surface may be returned on much shorter time scales (Houghton, 2005).

The Earth's oceans currently act as sinks for atmospheric CO_2 owing to their capability to dissolve CO_2 at the air-sea interface to form carbon in the water. The chemical reaction for this process is aided by CO_2 being slightly acidic and the oceans slightly alkaline. Equations 1 to 5 describe the chemical reactions leading to the sequestration of atmospheric CO_2 from the atmosphere (Feely et al., 2001).

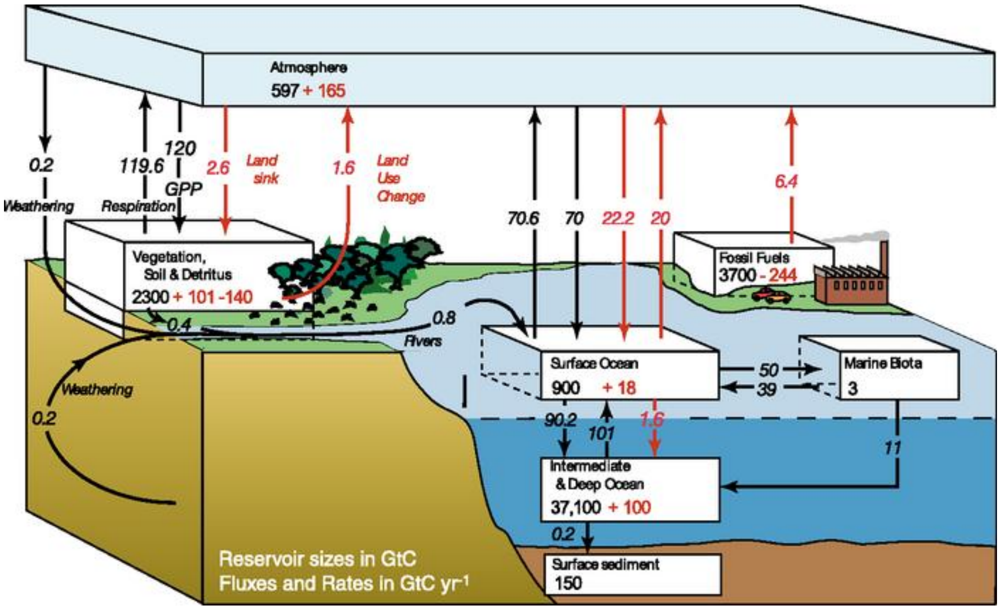

Figure 1.4-1 Depiction of the carbon cycle showing anthropogenic (red) and natural (black) terrestrial fluxes, image from (Sarmiento and Gruber, 2002)

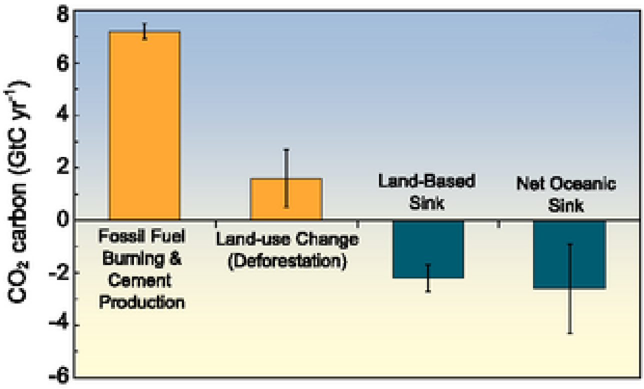

Figure 1.4-2 Carbon flux estimates with error bars for the key CO_2 sources and sinks, image from (IPCC, 2007)

$$CO_2(gas) \rightleftharpoons CO_2(aq) \quad (1)$$

$$CO_2(aq) + H_2O \rightleftharpoons H_2CO_3 \quad (2)$$

The carbonic acid (H_2CO_3) dissociates to form carbonate and bicarbonate ions,

$$H_2CO_3 \rightleftharpoons H^+ + HCO_3^- \qquad 3$$

$$HCO_3^- \rightleftharpoons H^+ + CO_3^{2-} \qquad 4$$

The net reaction is therefore,

$$CO_2(aq) + H_2O \rightleftharpoons H_2CO_3 \rightleftharpoons H^+ + HCO_3^- \rightleftharpoons H^+ + H^+ + CO_3^{2-} \qquad 5$$

The air-sea exchange establishes an equilibrium between the CO_2 dissolved in the surface waters and the CO_2 present in the air above the surface. This exchange occurs in the upper levels of the ocean allowing the absorbed carbon to remain active in the carbon cycle. The process of removing the carbon from the climate system for a long period of time is achieved by so called 'oceanic pumps' which transport the carbon down to the deep oceans where it remains for hundreds of years. The main pump mechanisms are:

- Phytoplankton photosynthesis which stores carbon within the organism itself until it dies. When it does the carbon is 'removed' from the climate system by sinking down to deeper waters. This is known as the biological pump.
- Sinking of cold water around the North Atlantic and Southern Oceans. This transfers surface carbon to deeper waters where it stays until resurfacing thousands of years later having been transported by the thermohaline circulation. This is known as the solubility pump.

Although the net air-sea carbon flux is negative (sink), the warm tropical oceans are outgassing CO_2 to the atmosphere with a mean flux of approximately 0.7 GtC yr^{-1} (Gloor et al., 2002). The southern oceans and the northern hemisphere extratropical oceans are sufficiently strong sinks to counteract this by absorbing 1.5 GtC yr^{-1} and 1.2 GtC yr^{-1} respectively (Takahashi et al., 2002) (Figure 1.4-3).

The southern ocean is a particularly poorly sampled region of the globe even though it is considered an important large-scale sink of atmospheric CO_2, and as a result the temporal and spatial variability of the southern ocean sink is currently poorly understood. Developing a ground network for consistent and continuous observations of CO_2 concentrations in the southern hemisphere is very difficult owing to a substantial fraction of the surface being ocean. Current satellite remote sensing instruments have difficulty observing oceanic targets due to low surface albedo and limited latitudinal coverage as a result of their reliance on solar radiation. The southern ocean is also often too cloud covered to be observed by the current passive remote sensing systems (IPCC, 2007).

As the ocean is the largest store of carbon and the greatest sink for anthropogenic emissions, its reaction to changes in climate is of great importance. From the combined consideration of many feedback mechanisms it is believe that ocean uptake will diminish in the future as a result of climate change and anthropogenic emissions. Two of the main reasons for this conclusion are that increased ambient temperatures are expected to slow down the ocean circulation which transports CO_2 to deeper waters, and increased ocean acidity as a result of CO_2 uptake will make it more difficult for CO_2 to dissolve in the ocean, thus creating a positive feedback on the climate system.

The terrestrial sink removes carbon from the atmosphere through the process of photosynthesis, which converts water and CO_2 into organic plant biomass $(\mathrm{CH_2O})$ and oxygen (equation 6) (Berner, 2004).

$$n\mathrm{CO_2} + n\mathrm{H_2O} + h\nu = (\mathrm{CH_2O})_n + n\mathrm{O_2} \qquad 6$$

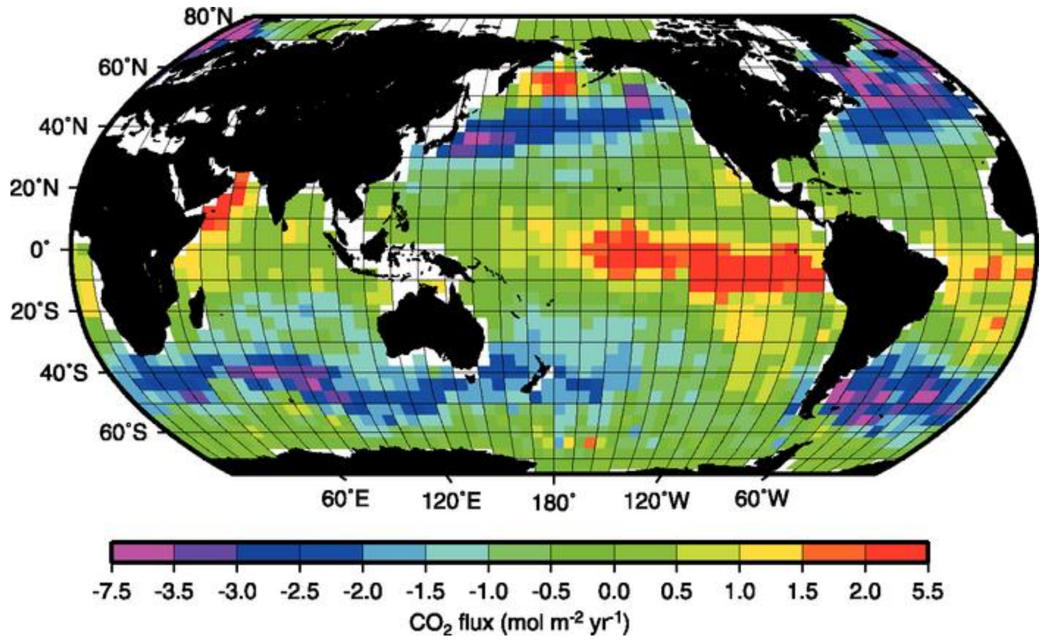

Figure 1.4-3 Sea to air flux estimates (4° x 5°) of CO_2 computed using 940,000 measurements of surface water pCO_2 collected since 1956 and averaged monthly (IPCC, 2007)

Part of the converted carbon is released back into the atmosphere through respiration during the plant's life and is released via decay following its death. The net amount of carbon removed from the atmosphere by photosynthesis alone is estimated to be 120 GtC yr^{-1} (Ciais et al., 1997). The total re-emission of that carbon by respiration and decay should approximately cancel this out in order to maintain a natural equilibrium. Despite significant deforestation in the tropical regions however in the 1990's it was estimated that the terrestrial biosphere was taking up approximately 1.4 ± 0.7 GtC yr^{-1} (IPCC, 2007). This sink was named the 'missing sink' or the 'residual sink' owing to the fact that its exact location was unknown, and because it's net magnitude was derived in part by balancing the overall carbon cycle budget. Since the IPCC 2007 report however the so called missing terrestrial sink has been better constrained and understood by studies considering the magnitude of fossil fuel emissions, the atmospheric increase in CO_2 (CO_2 atmospheric growth rate) and the ocean uptake of that CO_2. Latest estimates suggest that the vast majority of the terrestrial sink occurs in the world's forests with a net uptake from forests of 1.1 ± 0.8 GtC yr^{-1} with Africa and South America being most responsible (Pan et al., 2011; Sarmiento et al., 2010).

The main processes that contribute to the residual carbon sink are believed to be a combination of the CO_2 fertilisation effect which increases the rate at which vegetation grows as a result of increased CO_2 in the atmosphere, and the use of nitrogen fertilisers which help soils sequester carbon. Despite recent studies which have better constrained the terrestrial CO_2 sinks however there are still very large uncertainties associated with their precise location and magnitude (Houghton, 2005).

The effect of climate change on biomass processes is particularly difficult to predict owing to the limited ability of models to forecast accurately enough the future conditions which affect its productivity. For example, water availability and temperature have a significant impact on photosynthesis, respiration and decomposition rates. Greater atmospheric CO_2 stimulates biomass growth for certain plant species, yet higher temperatures slow down the rate at which plants grow. A particularly important positive feedback mechanism on the Earth's future climate which leads to significant model uncertainty is the thawing of permafrost in northern high latitudes. Approximately 20% of the Earth's landmass is covered by permafrost which contains significant quantities of previously sequestered carbon (IPCC, 2007). The release of CO_2 from thawing permafrost is likely to be coincident with the release of other trace gases such as CH_4 resulting in significant atmospheric composition change. Identifying the onset of atmospheric CO_2 release from permafrost thaw and understanding the magnitude and variability of the CO_2 release rates is critical if climate models are to accurately predict the Earth's future climate (Hanson et al., 2007). One recent example of an observed climate impact on the terrestrial carbon cycle is the consecutive droughts in the Amazon rainforest, a region shown to be susceptible to a warming climate. In-situ measurements made in the Amazon observed a significant release of carbon during and following the 2005 drought (Phillips et al., 2009). Houghton et al. (2005) propose from a summary of relevant scientific literature that most terrestrial sink mechanisms are likely to weaken in the future as a result of a warming climate.

The particular importance of anthropogenic CO_2 as a greenhouse gas can be measured by its radiative forcing capability. Radiative forcing is a measure of the net change in the Earth's radiation budget as a result of an imbalance between the total incoming and outgoing electromagnetic radiation in the Earth system. Positive radiative forcing causes a warming at the Earth's surface whereas a negative radiative forcing leads to a cooling effect. The net radiative forcing of the Earth's atmosphere is calculated relative to an unperturbed system, the IPCC use the year 1750 as their base in order to isolate the industrial era.

Figure 1.4-4 provides a summary of the most important anthropogenic radiative forcing contributions to the Earth's climate system for gas concentrations post industrial revolution. CO_2 has a considerably higher radiative forcing effect on the Earth's radiation budget than any other anthropogenic greenhouse gas in the Earth's atmosphere. Its absorbing capability is below that of CH_4 but its atmospheric concentration is over two orders of magnitude higher.

There is significant evidence to support the theory that anthropogenic emission of greenhouse gases (in particular CO_2) is leading to changes in the Earth's climate. In-situ measurements of land surface temperature and sea surface temperature (SST) have shown that over the last 150 years the Earth's mean annual surface temperature has increased by 0.6 ± 0.2 °C, with 1996 to 2006 ranking amongst the warmest years in instrumental records (since 1850). Furthermore, the observed rate of increase in the surface temperature is currently the largest ever recorded, with the temperature rise over the last 50 years being twice that of the rise over the last 100 years. Also computer simulations of the Earth's climate system are only able to reproduce the observed rate of temperature increase if they include anthropogenic emissions (Figure 1.4-5). Analysis of these results indicate there to be a 95% probability that the warming observed is attributed to the enhanced greenhouse effect (Berger, 2000).

In addition to the rise in global surface temperatures, the average water vapour content of the atmosphere has increased since the 1980s, which is broadly consistent with the extra water vapour warmer air is able to store and forms an indicator for atmospheric warming. Furthermore, snow cover has declined in both hemispheres and there has been a gradual reduction in the world's glaciers with large sections of the polar ice sheet breaking away (Scambos et al., 2000; Muller et al., 2003). The Earth's oceans are also rising at an increased rate as a result of melting land ice and thermal expansion (Figure 1.4-6). Recent tidal gauge measurements have shown a sea level rise of approximately 1.8 mm yr^{-1} over the last 70 years (Douglas, 2001; Peltier, 2001).

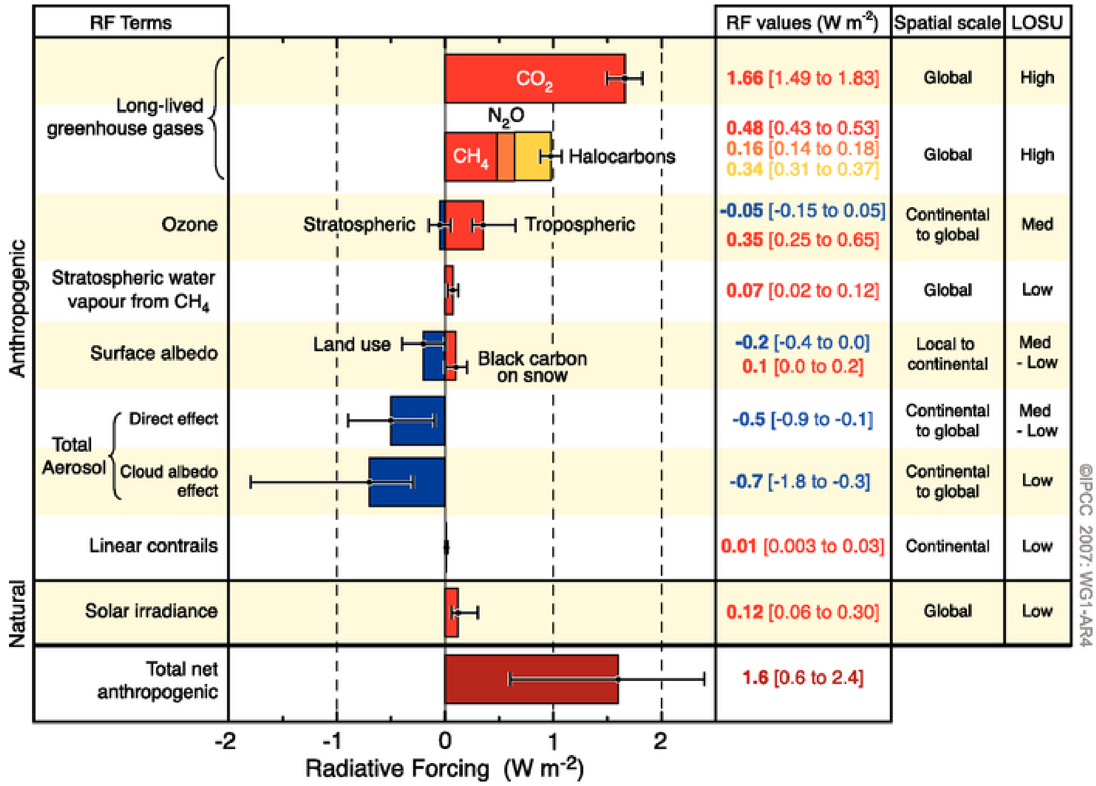

Figure 1.4-4 Radiative forcing contributions for the main agents and mechanisms which effect the Earth's radiation budget, anthropogenic CO_2 is the largest contributor. Image from (IPCC, 2007)

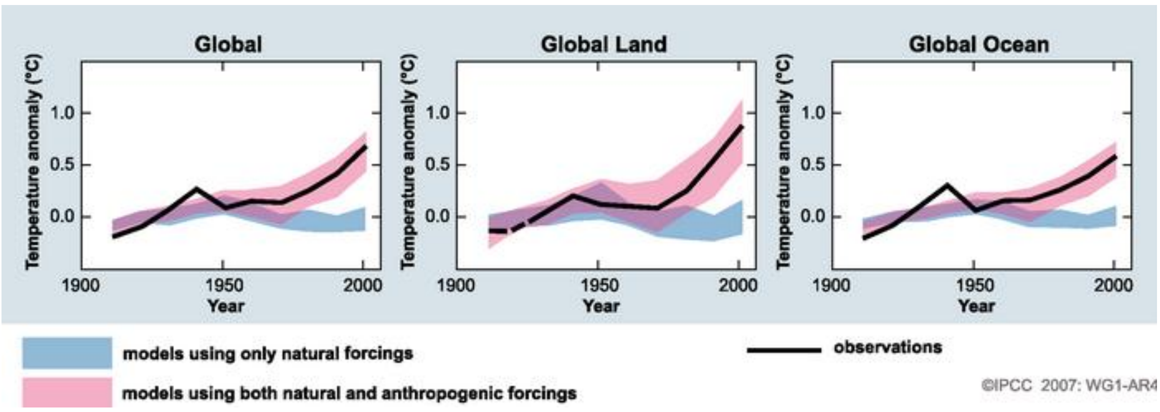

Figure 1.4-5 Global surface temperature records split into land and ocean biomes for observations and model simulations with and without anthropogenic forcings. Image from (IPCC, 2007)

The presented evidence for human induced global warming and climate change has prompted action from the international community to mitigate carbon emissions and provide mechanisms for sustainable development. An enforceable and legally binding climate change mitigation policy known as the Kyoto protocol was introduced in 2005.

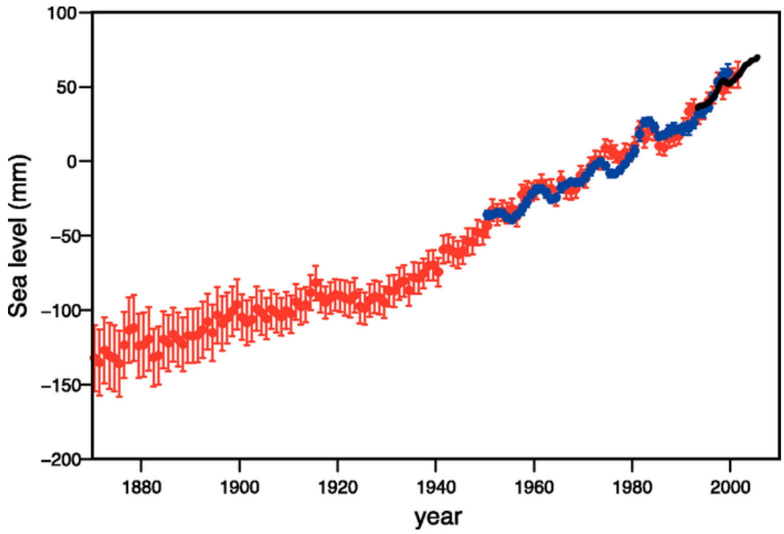

Figure 1.4-6 Annual averages of the global mean sea level based on reconstructed sea level fields since 1970 (red), tide gauge measurements since 1950 (blue) and satellite altimetry since 1992 (black), image from (IPCC, 2007)

1.5 Climate Change mitigation: The Kyoto Protocol

The Intergovernmental Panel on Climate Change (IPCC) is a scientific body formed in 1998 by the United Nations Environment program and the World Meteorological Organisation (WMO). Its objective is to provide a clear scientific view on the current state of knowledge in climate change science. Alongside the IPCC is the Framework Convention on Climate Change (FCCC) which is an organisational body conceived to implement policies to help mitigate climate change. The FCCC have concluded that the only way to slow climate change is to stabilise atmospheric greenhouse gas concentrations with focus on CO_2.

In an attempt to reduce the global emissions of the main greenhouse gases a legally binding international contract known as the Kyoto Protocol was introduced. The major feature of the Kyoto Protocol is that it sets binding targets for 37 industrialised countries for reducing greenhouse gas emissions. It amounts to an average of 5% reduction against 1990 levels for the period 2008-2012. The protocol recognised that developed countries are principally responsible for the current levels of greenhouse gases in the Earth's atmosphere as a result of over 150 years of industrial activity. As a consequence a heavier burden was placed on developed nations under the principle of 'common but differentiated responsibilities'.

Under the treaty the affected countries are required to meet their targets primarily through national measures. However, the Kyoto Protocol offers them additional means of meeting their targets through a number of extra mechanisms. One such mechanism is known as emissions trading (carbon market), in which countries failing to meet their quota can purchase carbon units from countries which have exceeded their required targets.

The protocol was adopted in Kyoto, Japan and entered into force on the 16th February 2005 (United Nations, 1998). The commitment period for the protocol ends on the 31st of December 2012. Its impending conclusion has been met with recent political impetus towards an agreement for the continuation of the Protocol beyond 2012. Rounds of negotiations are currently underway to devise a continuation methodology. The most recent talks (at time of writing) for the continuation of the Kyoto Protocol were held in Mexico in 2011 at a United Nations climate change conference. The outcome of the conference was an agreement adopted by the states' parties that called for a large Green Climate Fund proposed to be worth $100 billion a year by 2020 to assist poorer countries in financing emission reductions and adaptation.

1.6 Measuring atmospheric carbon dioxide

Much of our understanding of atmospheric CO_2 is derived from in-situ measurements made over the last 60 years. The first continuous atmospheric CO_2 data series were produced by Keeling et al, (starting in 1958) using an infrared (IR) gas analyser in Mauna Loa, Hawaii. The results from Keeling's research showed strong seasonal cycles in the atmospheric CO_2 concentrations and a positive trend driven by anthropogenic emissions (Keeling et al., 1995). Keeling's site in Hawaii was joined by a number of other in-situ measurement sites in various locations around the globe also using IR gas analysers. These sites were deliberately located in remote areas to avoid local source and sink contributions so as to provide data on the overall background increase of atmospheric CO_2.

The IR gas analysers used by Keeling and others are highly accurate and measure CO_2 with a time resolution of only a few minutes. Such a high temporal resolution is desirable for achieving accurate integrated measurements and is required for properly observing the diurnal cycle. In the 1990's it was recognised that much greater coverage of CO_2 measurements was required to provide the basis of estimating the terrestrial sources and sinks. Many of the measurement sites which subsequently appeared were part of flask sample programs, which involved capturing air in sealed containers in-situ and taking them to central well calibrated laboratories for later analysis. The flask method is significantly cheaper than the IR gas analysers but their temporal resolution is limited to the regularity in which the samples are collected. Recently more advanced instruments known as (and developed by) Picarro (also IR gas analysers) have been deployed for accurately and reliably measuring in-situ atmospheric CO_2 concentrations. These instruments are generally less expensive and do not require constant on-site maintenance as was the case for the IR gas analysers used by Keeling et al.

Measurement programs using both the flask method and the IR gas analysers are still running today and have recently been added to by the inclusion of the Total Column Carbon Observing Network (TCCON) which currently operates 10 Fourier Transform Spectrometers (FTS) measuring the direct solar spectra in the NIR spectral region. The single most extensive atmospheric CO_2 measuring network is operated by the National Oceanic and

Atmosphere Administration (NOAA), which contains 6 IR gas analyser instruments and over 50 flask sampling sites across the globe. Other international laboratories make similar observations using ground stations, flux towers, aircraft and ships as measurement platforms. The data from all these sites are collated by the World Data Centre for Greenhouse Gases (WDCGG) and the Carbon Dioxide Information Analysis Centre (CDIAC) (IPCC, 2007).

Despite the extensive global network of measurement sites (Figure 1.6-1), their uneven geographical distribution hinders the understanding of the carbon cycle, limiting some regions (those which are more poorly sampled) to continental and ocean basin scales only. Furthermore, many of the sites lack sufficient temporal resolution to observe irregular short term CO_2 events which might be of importance to better understanding the biospheric mechanisms driving CO_2 exchanges.

The coverage limitations of the surface measurement network present a strong need for an alternative and complementary measurement system to provide higher density spatial sampling.

Satellite remote sensing has been shown to provide improved spatial coverage compared to the surface network particularly in the world's tropical regions where strong terrestrial sinks are believed to be (Hungershoefer et al., 2010), however, the measurement accuracy and precision of current satellite instruments for measuring surface fluxes is significantly poorer than the equivalent measurements made on the ground and their dependence on solar illumination limits them to daytime observations only. Furthermore, satellite instruments generally obtain total column measurements as opposed to near surface measurements, and recent studies have shown this to be significantly less sensitive to the surface fluxes than measurements made on the ground. Simulations have shown that the maximum amplitude of the CO_2 seasonal cycle observed by a total column measurement is approximately 50% smaller than the amplitude observed at the surface (Olsen and Randerson, 2004). Despite these drawbacks however current satellite remote sensing data in the form of total column measurements of atmospheric CO_2 have been shown to be valuable to carbon flux models alongside in-situ sites (Houweling et al., 2004; Hungershoefer et al., 2010).

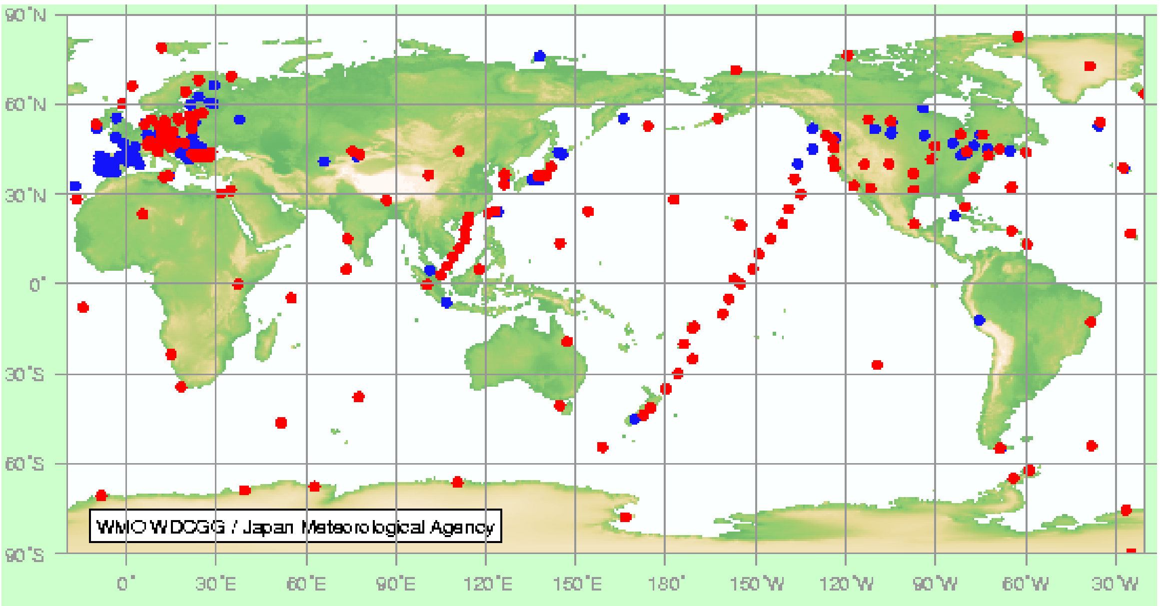

Figure 1.6-1 In-situ CO_2 measurement site locations, red dots are the currently active stations, blue dots are stations which have not provided data in over a year, image from (WMO, 2010)

The required precision for column-integrated CO_2 concentration data to be useful in constraining surface sources has been defined as approximately 2.5 ppm averaged over a month on an 8° x 10° footprint for land measurements (Rayner and O'Brien, 2001). This value is defined such that a satellite measurement system would exceed the capabilities of the current surface network if it could achieve this precision.

The 2.5 ppm minimum precision requirement to exceed the current measurement network defined by Rayner and O'Brien (2001) is insufficient to properly identify and quantify regional fluxes, in particular the so called 'missing terrestrial sink'. It is believed that a precision of much less than 1 ppm on a monthly and regional scale is more appropriate for total column measurements to be truly useful in discriminating and aiding in better quantifying the so called missing or residual sink (Heaps, 2007). In a report prepared for ESA on a potential CO_2 measuring LiDAR in space mission known as A-SCOPE the precision requirements were quoted at between 0.5 and 1.5 ppm with a bias requirement of between 0.05 ppm and 0.15 ppm (Ingmann et al., 2008). This stringent requirement on the bias originates from the need to measure relatively small variations of atmospheric CO_2 superimposed onto a sizable background concentration on a regional scale. For individual integrated measurements (over 50 km for example) it is expected that the measurement requirements for both the accuracy and precision would be much increased (relaxed) owing to the shorter spatial scale of the measurements.

There are a number of satellite instruments at present measuring CO_2 from space, including the SCIAMACHY instrument on board the ESA ENVISAT satellite (Bovensmann et al., 1999), the TES instrument onboard NASA's AURA satellite (Kulawik et al., 2010), the AIRS instrument onboard the NASA AQUA satellite (Chevallier et al., 2005), the IASI instrument onboard the METOP-A satellite and the GOSAT instrument launched by JAXA in January 2009 (Hamazaki et al., 2005). These systems use passive radiation either emitted by the atmosphere itself (thermal infrared) or from solar illumination (shortwave infrared). Some of these systems have shown the potential to meet the spatial coverage and accuracy requirements to improve flux estimates on continental scales beyond the capabilities of the surface network (Barkley et al., 2006; Buchwitz et al., 2006). They are however unable to meet the < 0.15 ppm accuracy objective required to aid in better quantifying the terrestrial sources and sinks (Chevallier et al., 2010; Hungershoefer et al., 2010). Passive systems in general have particular limitations which make meeting this objective difficult, for example shortwave infrared instruments are limited by their reliance on solar illumination which restricts their latitudinal coverage, and thermal infrared systems are not very sensitive to the lower atmosphere where the largest fluxes occur (Heaps, 2007; Hungershoefer et al., 2010). Furthermore, passive remote sensing systems involve retrieval complexities which suffer from aerosol contamination and radiation path length uncertainties.

An alternative method yet to be implemented is the use of active remote sensing for measuring total column CO_2 from space. One of the most promising active approaches is Total Column Differential Absorption LiDAR (TC-DIAL). TC-DIAL is theoretically able to measure atmospheric CO_2 from space with high accuracy without the latitudinal or diurnal constraints typical of passive systems. At present the technology (particularly the lasers) prevents the theoretical potential of TC-DIAL from being realised, however as technology developments continue the use of active remote sensing to complement the current measurement systems is becoming ever more feasible. The capability of a space-borne TC-DIAL instrument based on current technology for contributing to the current CO_2 measurement systems is investigated in detail in this thesis.

1.7 Modeling atmospheric carbon dioxide

There are two different approaches commonly used to derive CO_2 sources and sinks from available data, these are known as the *bottom-up* approach and the *top down* approach.

The bottom-up approach uses measured fluxes at particular locations (such as those from in-situ measurement sites), and extrapolates from them the approximate CO_2 concentrations at the undefined locations within the model. Statistical properties of the Earth's surface are used to define the interactions between the atmosphere and the biosphere. The uncertainties associated with this method are generally quite high owing to the large heterogeneity in space and time of the surface fluxes.

The inverse approach uses measurements from fixed locations on the Earth's surface to constrain a 3D atmospheric transport model to attain an optimal estimate of the underlying biospheric processes. This method provides a powerful technique for deducing fluxes on regional and global scales but is very sensitive to errors in both the transport model and the original measurements. The surface is generally split into large finite regions partly containing measurements used to provide a-priori values for the simulation. The 3D transport model is run forward in time to determine a future atmospheric CO_2 concentration distribution. A comparison is then made between the simulated future CO_2 concentration and a set of later in-situ measurements. A so called cost function is used to define the difference between the two, and the objective of the simulation is to minimise this function to achieve a reasonable approximation for the conditions which must have transpired for the following measurements to observe what they did. By consideration of the results, patterns can be identified which point towards the sources and sinks, however significant uncertainties in the derived fluxes occur as a result of transport model errors and measurement uncertainties. The uncertainties in both methods are heavily affected by the geographical distribution of the measurement sites used to constrain the models. The sparseness of the measurement network and its poor temporal sampling in many regions of the world has resulted in significant reliance on the realism of the computer models. Difficulties in siting and maintaining flask and IR gas analyser systems in remote or politically unstable regions points towards the need for a satellite remote sensing solution which can sample regions which are currently poorly sampled, including the tropics and the southern ocean.

1.8 Summary

Anthropogenic CO_2 is being released in significant quantities into the Earth's atmosphere as a result of energy production, cement production and land use change. The Earth's natural carbon cycle is removing approximately half of these emissions to the oceans and terrestrial biosphere but the exact nature and location of the uptake is still poorly understood. Using computer simulations it has been shown that if the atmospheric CO_2 continues to increase at the present rate there will be a significant and undesirable impact on the Earth's future climate. Current measurement systems including satellite observations and a comprehensive in-situ measurement network are unable to sufficiently constrain the surface fluxes leading to very large uncertainties in the derives estimates owing largely to their limited temporal and spatial coverage over important regions of the Earth's biosphere. Without this constraint it is difficult to accurately identify the mechanisms driving the exchanges of CO_2 between the atmosphere and biosphere. Understanding these mechanisms is essential to accurately predict the future of the Earth's climate and subsequently take informed action against such change.

The difficulty in constraining the CO_2 fluxes is partly due to the sparseness and uneven distribution of the in-situ measurement network making their data very difficult to interpret on a global scale. Simulation results using such data are very sensitive to errors in atmospheric transport models. Satellite remote sensing provides a much better distribution of data but integrated over a total column. Their measurements are generally less sensitive to surface fluxes and have errors which are larger than the requirement for accurately constraining regional sources and sinks. Furthermore present satellite remote sensing instruments have latitudinal constrains which prevent them from observing very high and low latitudes, and are often unable to view the tropics owing to the regular presence of cloud.

Additional methods of measurement are therefore needed which can achieve the accuracy, coverage and temporal resolution required to suitably constrain the carbon flux models. One such technique which has the theoretical potential to meet the required precision and temporal resolution is TC-DIAL. The TC-DIAL approach may be able to complement the existing measurement systems by measuring atmospheric CO_2 at all latitudes both day and night and by providing additional coverage over regions of particular interest such as the southern oceans and between patchy clouds in the tropics.

The capability of TC-DIAL for measuring atmospheric CO_2 from a low Earth orbiting satellite platform is investigated in detail in Chapter 5.

2. Total column differential absorption LiDAR for measuring atmospheric carbon dioxide from space

The atmospheric carbon and climate scientific communities have identified a strong need to better constrain terrestrial fluxes of CO_2 in poorly monitored regions, for example the southern oceans and tropics. The active remote sensing technique, differential absorption LiDAR (DIAL) has been shown through simulation to have the theoretical capability to complement the existing CO_2 measurement systems from a satellite platform by measuring CO_2 in poorly monitored regions of the Earth both day and night at all latitudes. At present, the current operational DIAL systems for measuring atmospheric CO_2 are limited to terrestrial instruments developed for technology and system demonstration purposes only and are not readily transferrable to a space-borne platform. The DIAL technique has however been the subject of many studies in the scientific literature which have investigated the challenges facing the development and operation of a satellite based DIAL system for measuring atmospheric CO_2. The studies have generally concluded that a total column version of a DIAL system (TC-DIAL) will provide a suitable combination of low measurement error with good system reliability (Ehret and Kiemle, 2005; Loth et al., 2005). The studies are also in agreement that the current challenges facing the future prospects of a TC-DIAL satellite instrument are largely related to the readiness of the technology on which they are based. This chapter describes the current level of development of terrestrial CO_2 DIAL systems and outlines the challenges facing the potential migration of such systems onto a satellite platform. This chapter also investigates the state of art technology which would form the key components of a space-borne TC-DIAL instrument.

2.1 Introduction to LiDAR and active remote sensing

Active remote sensing can be defined as the application of artificially generated electromagnetic radiation to remotely attain information on the nature of a substance. It has become frequently employed in medicine (x-rays, CAT scans, and ultrasound), architecture (3D mapping) and the manufacturing industry (quality control). It has also played an important role in recent history, particularly during the Second World War when sound waves were used to detect objects underwater such as mines and submarines (sonar) and radio waves were used to detect and monitor aircraft (radar).

LiDAR is a particular example of an active remote sensing technique. It uses wavelengths in and around the visible (including ultraviolet and near infrared) to obtain information on the environment. The name LiDAR is an acronym for Light Detection and Ranging and was chosen for consistency with the acronym for radar (Radio Detection and Ranging) by the US Navy. The measurement principle was first applied in the 1930's (prior to the invention of the laser), when attempts were made to measure air density profiles in the upper atmosphere using search lights to transmit light to a telescope some distance away. Thirty years later in 1960 the ruby laser was invented and the modern version of the LiDAR was conceived. This began with Fiocco and Smullin (Fiocco and Smullin, 1963) who published atmospheric observations using a ruby laser in 1963 (Weitkamp, 2005).

The success of a LiDAR instrument for making measurements of various kinds has often been connected to the capability of the technology at the time, in particular the lasers. LiDAR researchers were regularly involved in laser development as available commercial lasers which formed an integral part of their instruments often failed to meet technical requirements.

In its most basic form a LiDAR system consists of a transmitter and a receiver system accompanied by a series of electronics (Figure 2.1-1). The transmitter system is often driven by a laser owing to their capability to produce highly consistent monochromatic emissions which are desirable properties for an active remote sensing instrument. If a laser is used it is often accompanied by a beam expander to enable highly collimated beams which helps to minimise background noise.

The emission wavelength of a LiDAR system depends primarily on the type of laser used, however the output frequency may be shifted by an optical parametric oscillator should a wavelength be desired that current lasers alone cannot achieve (see section 2.4.4).

The first component of a LiDAR receiver system is a telescope which captures and focuses electromagnetic radiation. Depending on the purpose of the LiDAR the receiver diameter of the telescope can range from a few centimetres to over a meter. Following the capture of electromagnetic radiation a number of filters are often used to select a polarisation and wavelength before the signal passes on to the detector. The detector responds to the incident electromagnetic radiation by generation of an electric charge which is subsequently converted back into a light intensity using mathematical formulae which relate the two quantities for a particular detector (Weitkamp, 2005).

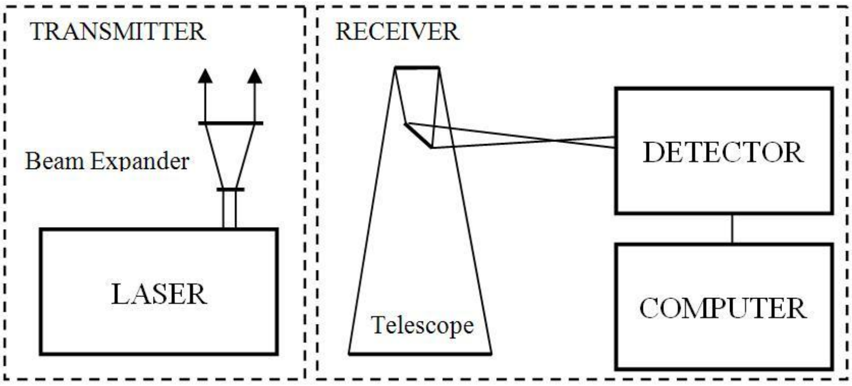

Figure 2.1-1 Principle configuration of a LiDAR system

Part of the electromagnetic radiation emitted by a LiDAR's transmitter system is returned to the receiver by scattering from various objects within the measurement environment, including solid bodies such as deliberately placed reflectors or atmospheric aerosols and molecules. The returning electromagnetic radiation contains information on the environment it has come into contact with and various LiDAR techniques are able to extract pieces of this information. The most basic information most LiDAR systems are able to obtain is the path length of the laser pulse or beam. This is achieved either by modulation of a continuous beam or by the emission of individual pulses combined with a measurement of the time delay between emission and reception (equation 7).

$$d = c(t_r - t_e) \qquad 7$$

where d is the average path length of the laser pulse in meters (from emission to reception), t_r is the time recorded at the reception of the temporal centre of the received pulse, t_e is the time recorded at the intensity peak of the laser emission and c is the speed of light in the medium it has propagated through (Approximately 2.99×10^8 ms^{-1} in the Earth's atmosphere).

Other information such the polarisation of the returning electromagnetic radiation and its absolute intensity can also be derived using a suitable LiDAR technique.

2.2 Differential absorption LiDAR

For measuring the concentrations of atmospheric gases (such as CO_2) a particular LiDAR technique known as differential absorption LiDAR (DIAL) is often employed. DIAL uses two separate laser emissions to derive a quantity known as the differential optical depth (DOD) of a gas at a particular wavelength (equation 8) (Bruneau et al., 2006).

$$\Delta\tau = \frac{1}{2}\ln\left(\frac{S_{off}}{S_{on}}\right) \qquad 8$$

where $\Delta\tau$ is the measured (one way) differential optical depth, S_{off} is the received light intensity from a laser emission which passes through the atmosphere without being absorbed by the atmospheric gas of interest, and S_{on} is the received light intensity from a laser emission which does get absorbed by the atmospheric gas of interest.

The two laser emissions produced for each DIAL measurement are known as *online* and *offline* (given as S_{on} and S_{off} in equation 8). The online wavelength is frequency tuned to be absorbed by an atmospheric constituent (such as CO_2) whereas the offline wavelength is frequency tuned to avoid absorption by the atmospheric constituent. The purpose of enabling only one of the emissions to be absorbed by the atmospheric gas of interest is to allow the offline emission to act as a reference intensity to compensate for the attenuation of the online signal by thin cloud and aerosol scattering. The result of the differential absorption is an intensity difference associated only with absorption by the atmospheric gas being measured. This concept is simplistically depicted in Figure 2.2-1.

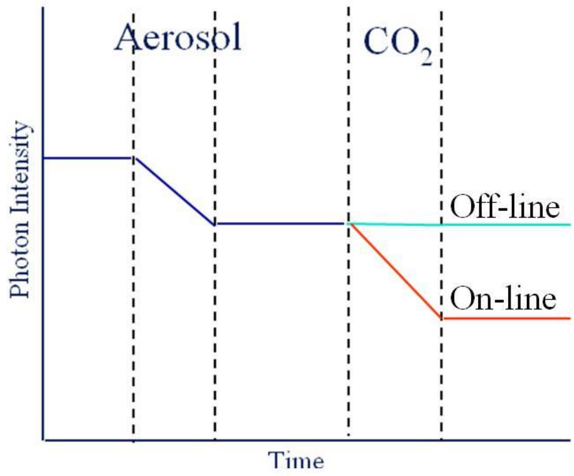

Figure 2.2-1 Diagram demonstrating the DIAL measurement principle by separation of the aerosol and CO_2 components

The measured DOD ($\Delta\tau$) provides information on the amount of absorption that has occurred by the gas of interest along the path of the laser emission. The DOD data collected by the instrument is used in a simple expression based on the Beer-Lambert law to derive the absolute concentration of the atmospheric gas encountered by the laser pulse or beam (equation 9).

$$n = \frac{\Delta\tau}{(\sigma_{on} - \sigma_{off})l} \qquad 9$$

where n is the atmospheric concentration of the measured gas in molecules cm^{-3}, the σ terms are the online and offline absorption cross sections for the gas at the wavelengths emitted by the laser, and l is the total path length of the lasers transmission through the atmosphere. The absorption cross section terms $(\sigma_{on}, \sigma_{off})$ are empirically derived, and equation 9 assumes the measured gas concentration n is constant along the path length l.

A weighting function containing information on the atmospheric state at the time of the measurement (pressure, temperature and water vapour concentrations) is often applied to derive a volume mixing ratio (VMR) in units of parts per million (ppm) to put the measured gas concentration into perspective with other atmospheric constituents (see Section 2.3). The weighting function forms the only DIAL retrieval component which involves information that is not captured by the DIAL measurement (aside from the spectroscopy) and as such contributes one of the largest sources of uncertainty to the CO_2 concentration measurement.

The DIAL retrieval of atmospheric concentrations is fundamentally simplistic as demonstrated by equations 8 and 9. Many other remote sensing techniques which can measure atmospheric CO_2 concentrations such as differential absorption spectroscopy have retrievals that are often under-defined problems at the measurement stage and therefore more complicated to solve (Platt and Stutz, 2008). An important advantage that DIAL systems have over passive remote sensing instruments (those which use solar illumination) is their ability to measure the precise path length of the electromagnetic radiation used to make the retrieval. The path length measurement (l) greatly improves the accuracy of the retrieval by better constraining the absorption calculation (equation 9). In addition DIAL systems are able to avoid uncertainties introduced by unexpected losses in signal intensity due to aerosols or thin cloud. The retrieval automatically accounts for the intensity difference by taking the ratio of two received signals (S_{on}, S_{off}) which have been subjected to the same scattering environment and responded to it in a very similar way.

At present the DIAL method is applied in a terrestrial setting for measuring atmospheric ozone and for monitoring industrial emissions such as sulphur dioxide (SO_2), nitrogen dioxide (NO_2) and carbon monoxide (CO) (Weitkamp, 2005). These measurements often use a specific DIAL technique known as dual wavelength Total Column DIAL (TC-DIAL).

A number of DIAL systems have recently been developed to demonstrate the technique for measuring atmospheric CO_2. Various methods have been employed including range resolved systems using atmospheric aerosols as scattering media (over very long integration times) which are able to determine the CO_2 concentration as a function of altitude, and total column systems using either aerosols or reflective targets as the scattering media to derive atmospheric concentrations of total columns (Abshire et al., 2008; Koch et al., 2008; Gibert et al., 2006).

The CO_2 DIAL systems demonstrated in the scientific literature use laser emissions in the short wave infrared (SWIR) region of the electromagnetic spectrum with wavelengths of either 1.6 µm (6367.223 cm^{-1}) or 2 µm (4875.749 cm^{-1}). These specific wavelengths are used for CO_2 measuring DIAL as they provide sufficiently strong absorption cross sections to enable a suitably large DOD to reduce error sensitivity, and have minimum interference from other atmospheric species (particularly water vapour) (Loth et al., 2005). Strong CO_2 absorption along the path of the laser emission (large DOD) is particularly important for statistically reducing the retrieval error. In general the larger the DOD (larger intensity gap between S_{off} and S_{on}) the less sensitive the retrievals are to uncertainties in the measured S_{off} and S_{on} quantities assuming the errors in S_{off} and S_{on} do not change and assuming S_{off} is the larger quantity of the two (as it is likely to be).

Figure 2.2-2 presents the spectral absorption lines at sea level for CO_2 and water vapour and highlights a particular spectral line identified as suitable for CO_2 DIAL determined by a feasibility study known as the FACTS report (Loth et al., 2005). The identified line is sufficiently free of absorption by atmospheric water vapour, is one the less temperature sensitive lines and is strong enough to provide sufficient CO_2 absorption to enable a suitably large DOD.

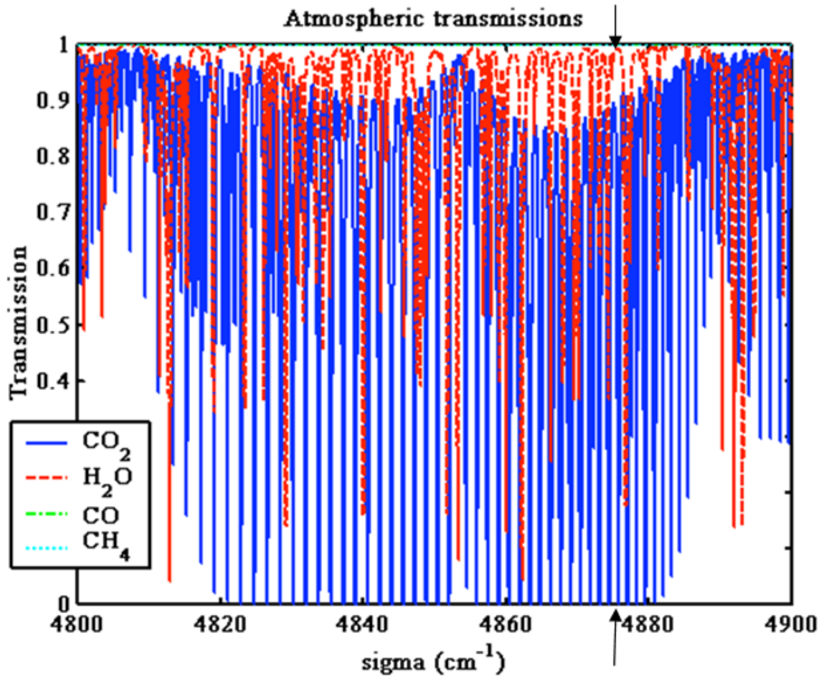

Figure 2.2-2 Carbon dioxide and water vapour absorption lines in the 2 µm region - arrows point to a suitable absorption line for CO_2 DIAL. Image from (Loth et al., 2005)

For TC-DIAL systems measuring atmospheric composition, accurate knowledge of the absorption features around the laser emission frequency is essential for performing accurate retrievals from the measured DOD $(\Delta\tau)$. CO_2 TC-DIAL measurements are made by recording the amount of light absorbed at a particular frequency and using an absorption cross-section (σ) derived in laboratory conditions for the gas being measured to convert this value into an atmospheric gas concentration (n). The amount of absorption (magnitude of the cross section) depends on the strength of the nearby absorption features, their proximity to the laser frequency and how they change as a function of atmospheric temperature and pressure. Quantifying the absorption expected from a measurement of received light intensity is required to interpret the DOD measurement and convert it into an atmospheric concentration.

The nature of the absorption features such as those observed in Figure 2.2-2 result from the interaction of electromagnetic radiation with particular configurations of atoms unique to individual gases. The study of the interaction between electromagnetic energy and matter is known as spectroscopy. The specific details of spectroscopy which gives cause to electromagnetic absorption lines are described by quantum mechanics and are beyond the scope of this chapter. In a simplistic sense molecules (such as CO_2) contain quantum mechanical energy transitions which allow electromagnetic radiation to be absorbed by the molecule and subsequently re-radiated or converted into thermal (kinetic) energy. This absorption can only occur at very specific frequencies of electromagnetic radiation known as the transition frequencies. The absorption occurs (in the short wave infrared) by stimulating the molecule into higher energy states known as rotational and vibrational states. The rotational state refers to the physical rotation of the molecule whilst the vibrational state refers to the relative vibrations of the atoms within the molecule (Figure 2.2-3) (Platt and Stutz, 2008). The rotational and vibrational transitions occur at different energies and are responsible for particular absorption line structures observed in the spectroscopy. The energies at which these transitions occur are summarised below.

- Vibrational transitions occur at around 0.1 eV, corresponding to wavelengths in the infrared.
- Rotational transitions occur at around 10^{-3} eV, corresponding to wavelengths in the microwave region.

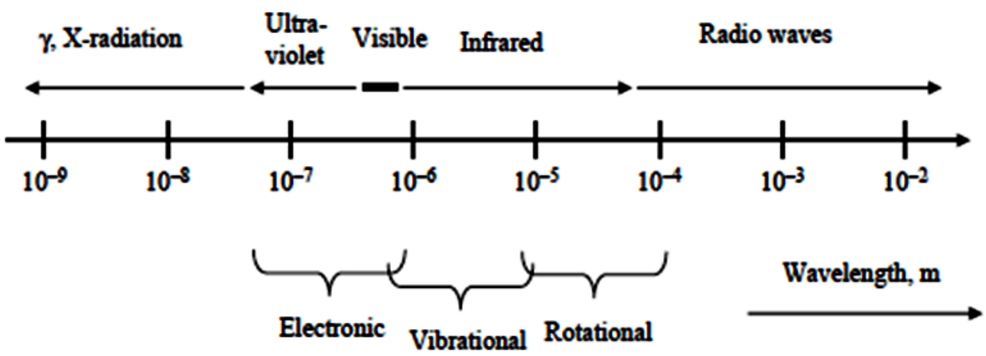

Figure 2.2-3 Quantum transitions as a function of wavelength

The vertical sensitivity of the TC-DIAL measurement is driven by changes in the shape and position of the spectral absorption lines as a function of altitude. The line profiles are very narrow at high altitudes, however lower down in the Earth's atmosphere a number of physical processes modify their shape and alter the cross section sampled by the laser emission. The changes in the spectral line shape and position is demonstrated in Figure 2.2-4 using a computer simulation of a single spectral line at a number of different altitudes above sea level.

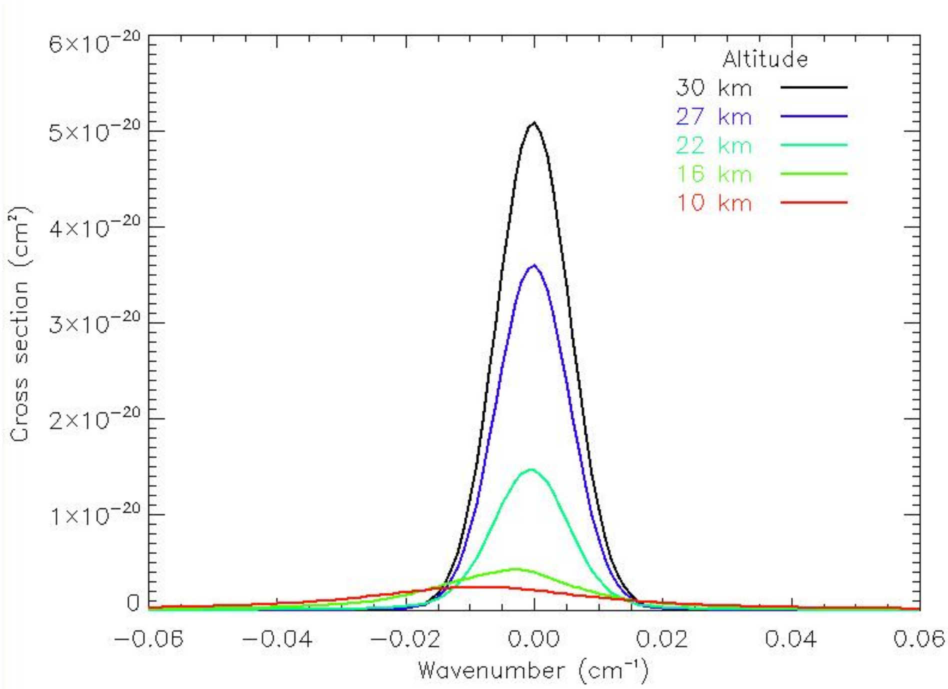

Figure 2.2-4 Spectral line widths for 5 altitudes generated using the TC-DIAL computer simulation (Chapter 3) with HITRAN 2008 parameters convolved with Voigt profiles

The two main drivers for the alteration of the shape and position of spectral absorption lines as a function of altitude are:

1. Doppler Broadening caused by Doppler shifts generated by the random velocities of atoms and molecules in the Earth's atmosphere. The energy driving the molecules is thermal and therefore the broadening magnitude is directly related to the square root of the atmospheric temperature (Platt and Stutz, 2008).

2. Pressure broadening caused by two similar effects known as impact pressure broadening and quasistatic broadening. Impact pressure broadening occurs as a result of a collision between the absorbing molecule and another molecule during the absorption process. The collision transfers energy between the colliding molecules changing the absorption frequency resulting in both a broadening and a shift of the absorption line in frequency space. Quasistatic broadening is caused by the influence of other molecules in the vicinity of the absorption molecule. This alters the energy levels of the absorbing molecule by proxy causing a change in the absorption frequency. This broadening is directly associated with the frequency of molecular collisions and therefore related to atmospheric pressure (Platt and Stutz, 2008).

Irrespective of the TC-DIAL systems measuring platform, a vertically emitted electromagnetic pulse or beam will pass through significant changes in atmospheric temperature and pressure along its journey. The changes in the shape of the sampled absorption line as a result causes a non linear sensitivity to the absorbing medium and introduces a retrieval dependency on ancillary data for the atmospheric state at the time of the measurement. For terrestrial systems, the atmospheric temperature and pressure may be measured in-situ and from it a reasonable approximation for its vertical structure may be inferred. The temperature and pressure information are applied in a computer model to derive a vertically resolved absorption cross section profile $(\sigma_{on}, \sigma_{off})$ for use in the retrieval.

One of the challenges facing many of the terrestrial CO_2 DIAL concepts is the lack of atmospheric backscattering which provides the atmospheric signal for the retrieval. In the short wave infrared (SWIR) region of the electromagnetic spectrum atmospheric scattering from aerosols is largely in the forward direction and therefore does not provide much signal for the receiver which is often co-located with the transmitter on the ground. The terrestrial DIAL systems measuring atmospheric CO_2 demonstrated in the scientific literature generally integrate their measurements over time periods of up to ten minutes to achieve sufficiently accurate results from atmospheric scattering (Gibert et al., 2006; Ismail et al., 2004). An alternative approach is to utilise the significantly stronger scattering created by the Earth's surface by mounting the instrument on an aircraft and pointing it toward the ground (Ehret et al., 2008). This methodology provides significantly improved retrievals owing to much greater signal being received at the detector and allows measurements to be integrated over seconds rather than minutes. Aircraft based TC-DIAL systems have demonstrated the feasibility of using a downward looking (nadir) system mounted on a moving platform for measuring total column atmospheric CO_2 and forms a natural first step toward a space-borne system.

2.3 Space-borne differential absorption LiDAR

With the carbon and climate modeling scientific communities requesting greater temporal and spatial coverage for atmospheric CO_2 measurements, the possibility of using TC-DIAL on a satellite platform to provide global measurements at all latitudes both day and night has recently been investigated in a number of feasibility studies and scientific papers (Dufour and Breon, 2003; Amediek et al., 2009; Ehret and Kiemle, 2005; Ismail et al., 2004; Loth et al., 2005). Many of the feasibility studies which have included literature reviews of the latest technology demonstrations have identified that dual wavelength TC-DIAL using a pulsed emission is one of the most suitable active remote sensing techniques for measuring atmospheric CO_2 from a satellite platform. Some of the studies have also shown through investigations using computer simulations that a dual wavelength TC-DIAL system has the theoretical capability to achieve high precision low biased measurements of atmospheric CO_2 from space if using the Earth's surface as the scattering medium.

From an orbiting platform a CO_2 TC-DIAL system would operate in principally the same way as it does in a terrestrial setting. Two laser emissions closely located in frequency space would be emitted almost simultaneously through the Earth's atmosphere and scattered by atmospheric aerosols and molecules, clouds and the Earth's surface. The scattered signals received at the detector would be used to derive a measurement of the total column DOD and a CO_2 retrieval would then be performed using ancillary data to derive the atmospheric concentration immediately beneath the satellite. Equations 10 to 12 have been suggested as a suitable method for deriving the CO_2 VMR from the received signal intensities S_{on} and S_{off} emitted from a satellite platform (Ingmann et al., 2008; Loth et al., 2005).

$$N_{CO_2} = \frac{\Delta\tau}{\int_{Surf}^{Sat} \nu(i)dp} \qquad (10)$$

$$\Delta\tau = \frac{1}{2}\ln\left(\frac{S_{off}E_{on}}{S_{on}E_{off}}\right) \qquad (11)$$

$$\nu(i) = \left[\frac{N_{av}}{(m_a g(i))\left(1 + \frac{m_w}{m_a}\rho_w(i)\right)}\right]\left(\sigma_{on}(i) - \sigma_{off}(i)\right) \qquad (12)$$

where N_{CO_2} is the column averaged dry air mole fraction CO_2 VMR, $\Delta\tau$ is the total column differential optical depth, S_{on} and S_{off} are the received online and offline intensities, E_{on} and E_{off} are the emitted online and offline intensities, ρ_w is the atmospheric water vapour mixing ratio, σ_{on} and σ_{off} are the absorption cross sections for the online and offline pulses, i represents atmospheric pressure levels, g is the acceleration due to gravity, m_a is the molar mass of dry air (0.029 kg), m_w is the molar mass of water vapour (0.018 kg) and N_{av} is Avogadro's number (6.022×10^{23} mol^{-1}).

The emitted and received intensity values $(S_{on}, E_{on}, S_{off}, E_{off})$ are the only quantities measured by the TC-DIAL instrument, the water vapour concentration (ρ_w) and the temperature and pressure information required to derive the absorption cross sections $(\sigma_{on}, \sigma_{off})$ for each pressure level (and at the surface) are ancillary data products obtained externally. The relationships between the absorption cross sections and the atmospheric temperature and pressure are described in section 0.

The laser emission wavelength is often referred to as an offset from the centre of a spectral absorption line. For a space borne 2 µm TC-DIAL system a laser offset of -0.1 cm^{-1} from the 4875.749 cm^{-1} spectral line has been suggested as a reasonable first approximation for the online laser frequency. The value of -0.1 cm^{-1} has been derived by the FACTS report using a computer simulation of a space borne TC-DIAL system (Bruneau et al., 2006; Loth et al., 2005).

For the 2 µm line sampled at -0.1 cm^{-1} from its centre, the vertical sensitivity profile (weighting function) generated by the broadening and shifting of the spectral line is presented in Figure 2.3-1.

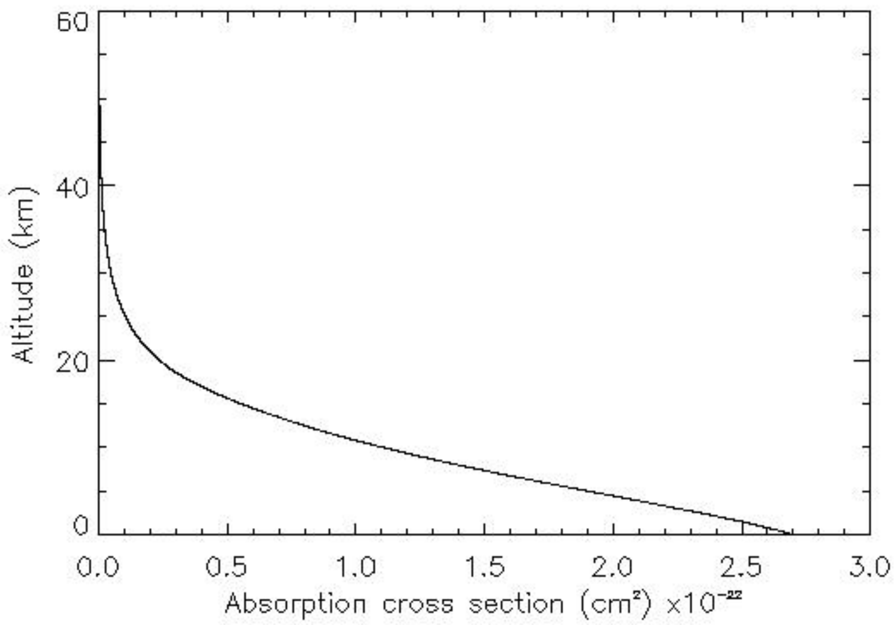

Figure 2.3-1 Vertical sensitivity profile for a TC-DIAL retrieval with a transmission frequency offset of -0.1 cm^{-1} from the centre of a 2 µm absorption line. Data generated by the TC-DIAL computer simulation (Chapter 3).

The exact frequency of the laser emission can be adjusted to alter the shape of the vertical sensitivity profile to suit the scientific objective. It is generally desirable for a space-borne CO_2 TC-DIAL system to have a high sensitivity near the Earth's surface where most of the fluxes occur, however optimising the magnitude of the measured DOD to reduce retrieval error is also of critical importance and is one of the primary drivers for the shape of the vertical weighting function. Fortunately, a weighting function favoring the surface is generally attained in the region surrounding the optimum laser frequency needed to produce a CO_2 retrieval with minimum error (see Chapter 5).

2.3.1 Errors associated with TC-DIAL migration from a terrestrial to a satellite platform

The causes of many of uncertainties associated with the retrieval of atmospheric gas concentrations from TC-DIAL atmospheric soundings are very similar for both terrestrial and space-borne systems. The key error sources for instruments in both environments include detector noise, inconsistencies in the laser emission properties (frequency, power and direction), and uncertainties in the spectroscopy and ancillary data. One of two exceptions to the systems similarities is the error associated with the ancillary data which is greatly amplified for a satellite based system owing to their reliance on numerical weather prediction models as opposed to in-situ measurements. It is clear from the feasibility studies in the scientific literature and the later chapters of this thesis that the migration from a terrestrial based dual wavelength TC-DIAL system to a space-borne system is likely to be closely connected to the future capability of Numerical Weather Prediction (NWP) models (Ingmann et al., 2008; Loth et al., 2005).

The required ancillary data products for atmospheric temperature, pressure and humidity are obtainable from meteorological forecasting centres such as the European Centre for Medium range Weather Forecasting (ECMWF) which operate an NWP model. The approximate uncertainties of these data are presented in Table 2.3.1-1.

Parameter	Uncertainty
Temperature	1 K
Surface pressure	0.5 – 1.5 hPa
Specific humidity	10%

Table 2.3.1-1 Approximate RMS errors for ancillary data required for TC-DIAL retrievals. Data from (Ingmann et al., 2008; Loth et al., 2005).

Many of the space borne TC-DIAL system concepts in the scientific literature suggest that a space-borne TC-DIAL system will operate most reliably by emitting the online and offline signals sequentially from a single laser. The simplicity of a single laser configuration introduces the benefit of greater system reliability but also causes a small temporal delay between the pulse pairs which forms an additional source of random error. The magnitude of the delay which depends on the rate at which the pulses are generated causes the signals to experience slightly different surface and atmospheric environments (Figure 2.3.1-1).

Minimising the delay between pulse emissions is achieved by transmitting the signals as quickly as possible, however the satellites high surface velocity (7 km s^{-1}) implies that a significant displacement between the online and offline footprint locations is difficult to avoid. The rate at which the laser emissions are generated is physically limited by the lasers Q-switching or mode-locking capabilities, and is fundamentally capped by the time the system has to wait for the previous pulse to clear the lower atmosphere in order to avoid cross-signal contamination (see Chapter 4).

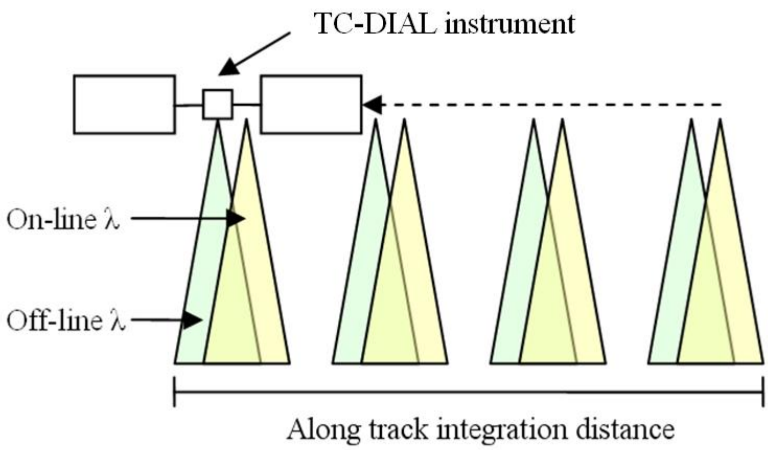

Figure 2.3.1-1 Representation of the space borne TC-DIAL measurement process showing four measurement pairs within an integration interval

The differences in the environments experienced by the online and offline signals introduce an error to the TC-DIAL retrieval which is unique to airborne and space-borne systems. The magnitude of the error depends on how far apart the surface footprints are and how heterogeneous the surface is. For the systems proposed in the scientific literature the small footprint deviation is likely to be one of the main sources of uncertainty associated with space-borne TC-DIAL retrievals (see Chapter 5).

Particular error sources such as the surface reflectance variability and uncertainties in the ancillary data have different levels of effect depending on how the TC-DIAL system is configured. TC-DIAL systems have a very large free parameter space which allows the instruments to be configured to best achieve a particular scientific objective (for example measuring carbon fluxes over tropical regions). There is a strong argument for a TC-DIAL system to be optimised for cloudy conditions (Houghton, 2005) which would lead to the system having a reduced integration path length. Such an instrument will inherently generate poorer retrievals than is necessary over clear sky conditions but may better achieve the science objective of having more accurate measurements between patchy clouds in the tropics (see Chapter 5).

The optimisation process of a TC-DIAL system is often carried out in the spectral domain as very small changes in laser frequency along the spectral absorption line have very large consequences on the optimum configuration of other free parameters. As an example of this effect, if the magnitude of the integration path length were to change then the optimum pulse repetition frequency would alter in response which would in turn affect the noise statistics per shot and lead to a change in the optimum DOD and therefore the laser frequency.

2.3.2 TC-DIAL detection techniques for a space-borne system

One of the most important components for determining the optimum TC-DIAL configuration is the choice of detection technique. There are two possible detection techniques which may be applied in a TC-DIAL system known as heterodyne detection and direct detection. Both techniques are applicable to terrestrial and space-borne environments, however their error behavior is sensitive to the nature of the scattering medium. The parameterisation of the error statistics detailed below for heterodyne and direct detection is specific to the condition of using the Earth's surface as the source of scattering.

Both detection techniques are sufficiently integrated into the TC-DIAL retrieval parameter space for them to require assessment in independently optimised conditions with the rest of the TC-DIAL system in order to allow a fair comparison of their relative capabilities. The choice of detection technique when both methods are under mutually optimised conditions enables the system to be streamlined toward the favourable technique, halving the systems overall parameter space. This study is carried out in Chapter 5.

Direct detection is technologically simpler than heterodyne detection and works by converting a received signal into photoelectrons at the detector and then digitising the signal either by photon counting or analogue to digital conversion. Its noise statistics for the detection of signals specifically scattered from a hard target such as the Earth's surface are given by equation 13.

$$SNR_{DD} = \frac{1}{\sqrt{F}} \sqrt{\frac{\eta N}{1 + (\eta N/M) + (N_B/N)}} \tag{13}$$

$$M = \left[1 + \frac{\pi A d\theta^2}{4\lambda^2}\right] \tag{14}$$

$$N_B = I_{sol} + \frac{1}{2F\eta}\left(\frac{\eta P_{NEP}}{hv}\right)^2 \delta t \tag{15}$$

where SNR_{DD} is the signal to noise ratio for direct detection, F is the excess noise factor which is an intrinsic property of the detector and its electronics, η is the quantum efficiency of the detector, N is the number of photons incident on the detector, N_B is the number of background photons from both solar illumination and detector noise, A is the area of the receiver aperture, θ is the full angle divergence of the laser beam, I_{sol} is the number of solar photons arriving on the detector, P_{NEP} is the detectors noise equivalent power, h is the Plank constant which is a value that relates a quantity electromagnetic energy with its frequency, v is the transmission frequency, δt is the length of the range gate in s, M is the number of individual light speckles on the surface of the detector and λ is the transmission wavelength (Bruneau et al. 2006; Loth et al., 2005).

The power measurement error (equation 13) affects both the online and offline measurements and is caused by internal detector noise creating uncertainties in the measured light intensity, and temporal and spatial fluctuations occurring as a result of an interference effect known as speckle.

Speckle occurs in all TC-DIAL measurements as a result of a coherent laser emission returning to the detector as a series of out of phase signals originating from various scattering objects on the Earth's surface. The interference pattern created across the face of the detector produces a fluctuating signal which leads to a random error in the measured intensity. The amplitude of the signals variability increases with the received power, and after a point no further improvement in retrieval error is gained by receiving a more powerful signal (Figure 2.3.2-1).

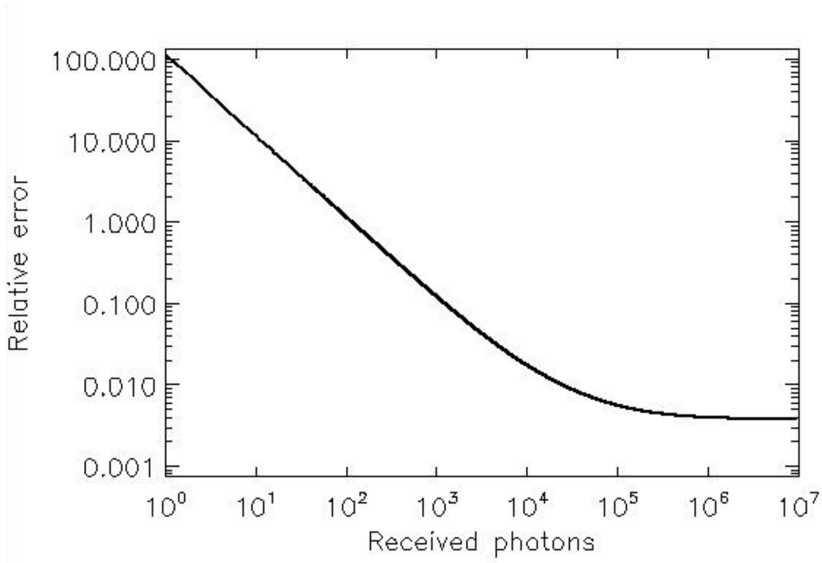

Figure 2.3.2-1 Direct detection relative error owing to detector noise as a function of received photon numbers

From equation 13 it can be seen that it is desirable to have a greater number of speckles (M) across the face of the detector as this reduces the magnitude of the signal variability. The number of speckles may be increased either by generating a larger surface footprint by increasing the beam divergence angle (θ) or by having a larger receiver mirror (A). The latter of the two is limited by the physical size and mass of the mirror as the instrument is required to be launched into orbit which presents tight constraints on the instruments overall mass and size. Increasing the divergence angle of the laser emissions is much easier to achieve, however one of the greatest assets of a TC-DIAL instrument is its narrow footprint so that it can see between patchy cloud, and increasing the beam divergence whilst keeping the mirror size constant results in a loss in signal arriving at the receiver. For these reasons the footprint diameter is generally limited.

In heterodyne detection the received signal from the Earth's surface is non-linearly mixed with an internal reference signal generated by the DIAL's laser (local oscillator). The output from this process is a high intensity difference frequency which carries information on the phase and amplitude of the received signal.

Heterodyne detection is particularly suitable for systems receiving very low intensity signals as the mixing process achieves very high (detector noise free) gain which can lift the signal above the detector noise. The expression that defines the relative error in the received signal for Heterodyne Detection (HD) may be simply given by equation 16.

$$SNR_{HD} = \frac{\sqrt{M}}{1 + (M/\gamma\eta N)} \qquad 16$$

where SNR_{HD} is the signal to noise ratio for HD, M is the number of speckle on the detector, γ is the heterodyne efficiency factor which refers to the efficiency of the heterodyne mixing process, η is the detector quantum efficiency and N is the number of photons incident on the detector (Bruneau et al. 2006; Loth et al., 2005).

For hard target returns (such as for a space-borne TC-DIAL system) the number of speckles is effectively limited to 1 owing to the heterodyne requirement for coherency in the mixing process. This severely limits the achievable SNR to unity and simplifies equation 16 to equation 17.

$$SNR_{HD} = \frac{1}{1 + (1/\gamma\eta N)} \qquad 17$$

Because of heterodyne detections capability to achieve noise free gain, its noise statistics are independent of detector NEP (above the shot noise limit) and as a consequence its SNR curve is almost completely flat (Figure 2.3.2-2) (Bruneau et al., 2006; Loth et al., 2005).

For a single sounding an SNR of 1 is far too low to make a useful measurement, however heterodyne detection can exploit its noise free gain characteristic by transmitting low powered pulses with a very high pulse repetition frequency (> 5 kHz) to statistically reduce the random error.

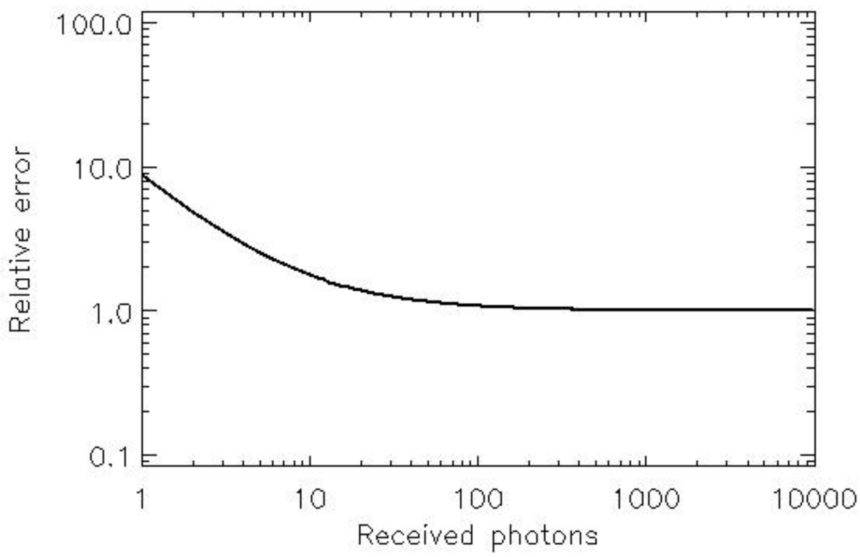

Figure 2.3.2-2 Heterodyne detection relative error owing to detector noise as a function of the number of photons detected

2.3.3 TC-DIAL orbit characteristics and path integration

Irrespective of the detection technique the precision of TC-DIAL measurements can be improved by the integration of multiple soundings. An appropriate length for the integration interval of a space-borne TC-DIAL system has been suggested independently of the instruments pulse repetition frequency (and of the detection technique) to be approximately 50 km (Ingmann et al., 2008, Loth et al., 2005). This length is defined based on a desire to achieve a spatial resolution which is sufficient to spatially resolve terrestrial sources and sinks of atmospheric CO_2. Aside from the spatial resolution argument however there is relatively little justification for the specific value of 50 km. The TC-DIAL surface integration distance is one of many free parameters in the system optimisation process and is investigated as a free parameter in Chapter 5.

One of the primary advantages of measuring from a satellite platform as opposed to from a terrestrial setting is the ability to frequently measure large regions of the Earth. Many passive satellite remote sensing instruments achieve good spatial coverage by having sufficiently wide surface swaths to allow daily measurements over much of the Earth's surface. For a TC-DIAL system on a satellite platform however the width of a single laser footprint on the Earth's surface represents the full swath width of the instrument, implying very little lateral measurement coverage as the satellite orbits the Earth. A single TC-DIAL measurement is approximately 50 km long by 180 m wide providing a very narrow swath. This is represented in Figure 2.3.3-1 using an orbital simulation.

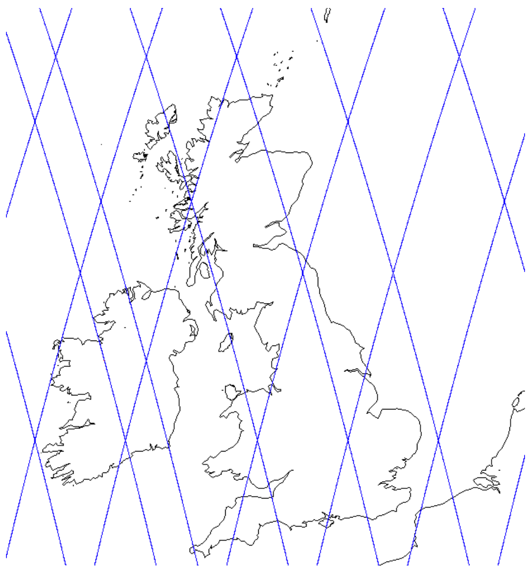

Figure 2.3.3-1 Spatial coverage over the UK for 7 days of laser soundings from a simulated satellite based TC-DIAL instrument, image generated using an orbital simulator described in Chapter 3.

The limited spatial coverage provided by a space-borne TC-DIAL instrument prevents the production of spatial data sets that cover the entire globe without interruption on a daily basis and may result in large errors when used with carbon flux models. However, the very narrow swath has a significant advantage in that it may allow the TC-DIAL instrument to make reasonably accurate measurements between patchy clouds. This is particularly beneficial in the tropics where there is currently poor measurement coverage and a lot of broken cloud.

A study to determine the precise advantage of TC-DIAL coverage over cloudy regions compared to current satellite remote sensing instruments is difficult owing to a need for two dimensional cloud data with a spatial resolution of less than 150 m. If this data series were available a more robust understanding could be developed for the advantages of the unusual viewing geometry provided by TC-DIAL.

A TC-DIAL system may be optimised to achieve a specific measurement objective such as measuring between clouds in some of the worlds tropical regions, however the optimum system configuration and its overall capabilities are heavily influenced by the technology on which the system is based. Limitations in the capability of the latest technology have been the main attributing factors for why TC-DIAL systems measuring atmospheric CO_2 are still in the terrestrial demonstration phase. The following section describes the currently available technology which may form the crucial components of a near future space-borne TC-DIAL system.

2.4 Lasers for space-borne TC-DIAL

Lasers are one of the principle components of modern LiDAR systems. They produce highly consistent, coherent and collimated monochromatic emissions and can be emitted as either a continuous beam or as individual pulses with a high pulse repetition frequency. There are many different types of laser which are suitable to form part of a LiDAR system. The type used determines a number of important parameters associated with the electromagnetic emission, including wavelength, power and emission type (pulsed or continuous).

A laser by definition is a device that generates and amplifies light and has following essential elements:

- A gain medium which consists of an appropriate collection of atoms, molecules and ions which can be excited into higher quantum mechanical energy levels
- A pumping process to excite the atoms
- A suitable optical feedback mechanism to allow the radiation to pass through the gain medium multiple times

The lasers gain medium contains a mixture of quantum mechanical energy levels arranged such that a process known as population inversion can occur. Materials are often selected (and in many cases doped) specifically to attain this essential energy level arrangement. The amplification of light within the laser depends on its ability to sustain the population inversion condition, and its efficiency and many of the emission properties are inextricably linked to the gain medium used (Siegman, 1986).

The complex arrangement of quantum mechanical energy levels within the gain medium is responsible for the precise frequency of the electromagnetic radiation emitted by the laser. The energy of each molecule within the gain medium is a discrete quantity which can only change in fixed amounts known as quantum mechanical transitions. The magnitude of the energy level transitions (gaps between the gain mediums molecular energy levels) relates to the frequency of emitted or absorbed electromagnetic radiation. This is described by Planck's law (equation 18).

$$\omega_{21} = \frac{E_2 - E_1}{\hbar} \qquad 18$$

$$\hbar = \frac{h}{2\pi} \qquad 19$$

where ω_{21} is known as the transition angular frequency (frequency of emitted or absorbed electromagnetic radiation), E_2 is the energy of the upper quantum level, E_1 is the energy of the lower quantum level, and h is Planck's constant which has a value of 6.626×10^{-34} J s.

An external source of energy, either electromagnetic or electrical with a specific magnitude to cause a quantum mechanical energy transition leads to the excitation of the gain medium's molecules to higher energy states (E_1 to E_2). Once excited the molecules very quickly decay back down to their original ground states with either the emission of electromagnetic radiation (spontaneous emission) or by heating the surrounding gain medium (nonradiative relaxation).

The process of providing very specific quantities of energy through a pumping mechanism and achieving electromagnetic emission is presented in Figure 2.4-1.

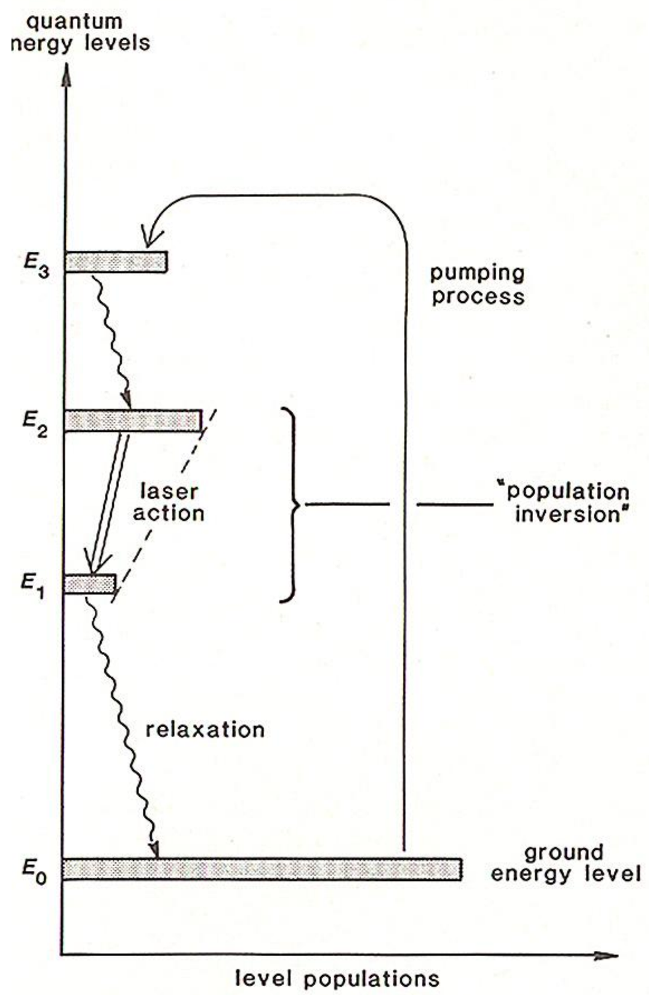

Figure 2.4-1 A four-level laser pumping system, image from (Siegman, 1986)

The most important form of emission which occurs within the gain medium of a laser is known as stimulated emission. This is responsible for the light amplification processes and the very high level of coherency in the resultant emission. Stimulated emissions occur when an external electromagnetic field such as the pumping energy or electromagnetic radiation from a previous relaxation process comes into contact with a molecule which is already in one of the higher energy states. If the frequency of the incident electromagnetic radiation matches the frequency of a molecule's energy above its ground state then a resonance condition is set up within the molecule and the electromagnetic wave passing by is amplified. The amplification (stimulated emission) has the same frequency and phase as the incident electromagnetic radiation making it coherent with other stimulated emissions within the gain medium.

The light amplification process within a laser is caused by numerous stimulated emissions occurring throughout the gain medium which are contained within the laser cavity. Sufficient pumping energy is required to ensure there are more molecules existing in an excited state than molecules existing in the ground state (population inversion). The population inversion condition must be maintained in order for the laser to produce a consistent emission. The laser's gain medium is continuously pumped with energy, either optically (sometimes using a diode laser) or electrically to maintain population inversion (Siegman, 1986).

The laser cavity which houses the gain medium has reflective surfaces at either end and stimulated emissions which initially travel within the cavity at random are soon focused into a collimated beam by the cavity mirrors. The beam bounces back and forth along the cavities length, consistently stimulating emissions which amplify the electromagnetic energy within the cavity. One of the cavities reflective surfaces is slightly transmissive and allows a portion of the electromagnetic radiation to escape through the laser aperture and out into the environment to form the laser emission (Figure 2.4-2).

Laser cavities have a range of different lengths and shapes. The length is particularly important as it defines the frequency modes transmitted by the laser. When the signal has developed into a beam propagating up and down the laser cavity a resonance condition is formed. This results in the generation of a standing wave constrained by the cavity walls (Figure 2.4-3).

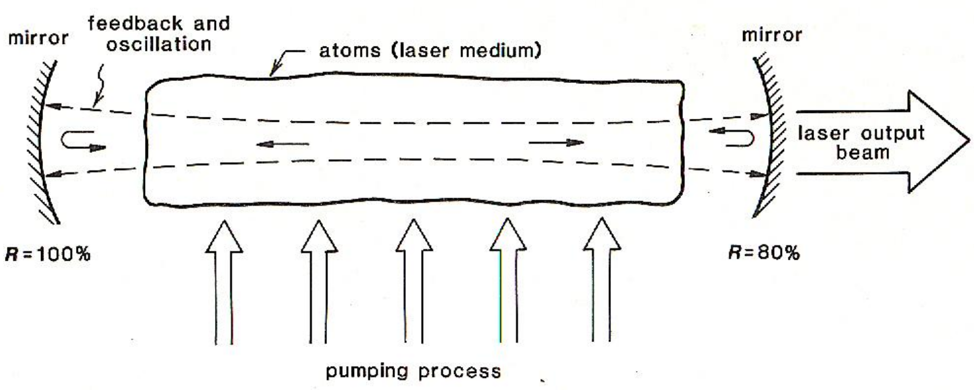

Figure 2.4-2 Example of standard laser cavity configuration, image from (Siegman, 1986)

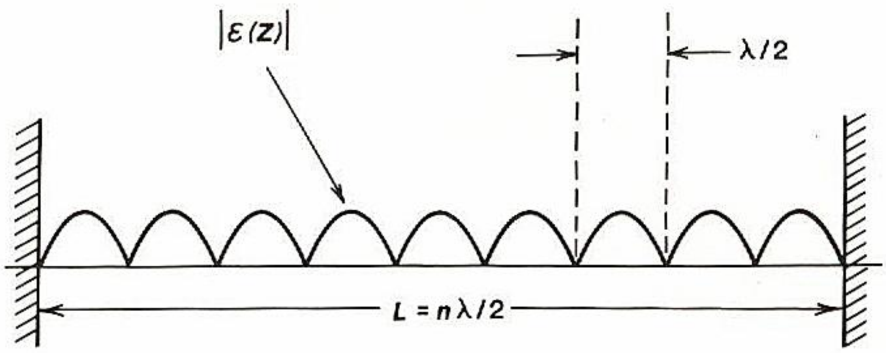

Figure 2.4-3 Standing wave in a laser cavity

The series of possible frequencies at which resonance can occur are known as axial-mode frequencies (equation 20). Frequencies between these points do not form the standing wave condition required to survive in the cavity and very quickly cancel themselves out.

$$\omega = 2\pi q\left(\frac{c}{2L}\right) \tag{20}$$

where ω is the axial mode angular frequency, q is an integer which refers to the mode number, c is the speed of light and L is the optical length of the laser cavity.

The distribution of frequencies amplified within the laser cavity is known as the gain curve. Within the gain curve are the axial mode frequencies which define the precise frequencies at which the electromagnetic radiation is amplified (Figure 2.4-4). The resultant laser emission is often a combination of these axial modes unless it is a single mode laser in which case only a single mode is excited and consequently emitted (Siegman, 1986).

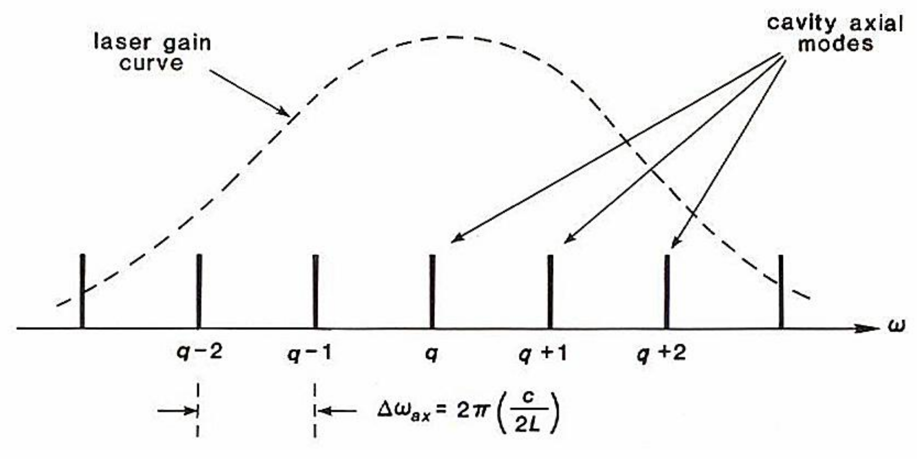

Figure 2.4-4 Axial modes at frequencies associated with resonance conditions within the laser cavity, image from (Siegman, 1986)

For a LiDAR system measuring atmospheric CO_2 from space (as is the interest here) the primary requirement for a laser is the ability to generate an emission with a specific SWIR wavelength of either 1.6 or 2 µm. Other important laser requirements have been defined in the FACTS report (Loth et al., 2005), which states that the laser must be capable of emitting with a power of no less than 1 W and have a spectral linewidth full width half maximum of no greater than 50 MHz. These loosely defined parameters are only three of many which must be suitable for a laser to function as part of a space borne CO_2 LiDAR system, but they provide a useful benchmark with which to filter out the immediately unsuitable laser systems from the available selection.

2.4.1 Semiconductor lasers

Semiconductor lasers are available for a range of emission wavelengths from 375 to 2680 nm. They are the smallest of all available laser systems as they use their own physical dimensions to act as the laser cavity. They are very energy efficient and have become well developed as a result of their applications in the telecommunications industry. They are frequently used as barcode readers, range finders and laser pointers, and have previously been developed for space applications. There is currently an extended cavity semiconductor laser monitoring the mirror positions in the orbiting IASI Michelson Interferometer.

Current semiconductor lasers are unsuitable for use as a primary laser source for a 1.6 or 2 μm space borne LiDAR system. They have been demonstrated to have the capability to achieve sufficient powers (kW) and a suitable spectral purity (<10 MHz), but these traits have not been found to exist in a single device. For example, an extended cavity semiconductor laser can achieve very good spectral purity (<10 MHz) but only with mW powers, whilst a normal (Fabry-Perot) semiconductor laser can achieve kW powers but with relatively poor spectral purity (around 300 MHz). Several laboratories are working on developing diode arrays which may be able to combine good spectral purity with high power. In the future these may provide a feasible source of electromagnetic radiation for a space borne LiDAR system, but at present semiconductor lasers do not fully meet the requirements. It is likely because of this that there has been no demonstration to date of a semiconductor laser operating as part of a LiDAR system measuring atmospheric composition (Loth et al., 2005).

2.4.2 Fibre lasers

Fibre lasers use doped optical fibres as the active gain medium and are often pumped by semiconductor lasers. They are largely used in industry for laser cutting, welding and folding of metals as they can achieve very high emission powers owing to their fibres having a high surface to volume ratio allowing efficient cooling. There have been many technology demonstrations of fibre lasers operating in the 2 µm region (Jackson and King, 1998; Hayward et al., 2000; El-Sherif and King, 2003), but there are no examples of one operating as part of an atmospheric composition LiDAR system. There has however been a direct detection differential absorption LiDAR system demonstrated successfully using a 1.6 µm fibre laser, providing an indication of their potential as part of terrestrial LiDAR systems (Abshire et al., 2008).

Numerous demonstrations in the scientific literature indicate that fibre laser technology has the capability to achieve sufficient power requirements for applications in 2 µm LiDAR systems, with powers around 5 W having been demonstrated. Fibre laser technology at 1.6 and 2 µm requires further development and demonstration however, particularly with regard to their sensitivity to radiation conditions typical of the space environment. Efforts are currently being conducted to test fibres in irradiated conditions to assess this effect.

2.4.3 Crystal lasers

Crystal lasers at 1.6 and 2 µm use materials such as YAG or YLF doped with thulium or holmium as their gain media. This laser technology has been demonstrated more than any other laser type at 1.6 and 2 µm, and multiple terrestrial LiDAR systems are being developed using Tm:YAG as their laser source (Koch et al., 2008; Gibert et al., 2006). Spectral linewidths of less than 10 MHz and transmission powers of around 1 W have been reported, and crystal lasers have previously been developed for space applications, including the 0.532/1.064 µm Nd:YAG laser which is part of the CALIOP LiDAR on board the Calipso instrument.

Crystal lasers are the most suitable laser source at present for application in a 1.6 or 2 µm LiDAR system, and this is reflected by their frequent and successful use in terrestrial LiDAR developments. Their power and spectral capabilities have already been demonstrated in the scientific literature as being suitable for terrestrial LiDAR systems, and their high energy efficiency and superior robustness over the alternatives make them particularly attractive for space operation.

2.4.4 Optical parametric oscillators

An optical parametric oscillator (OPO) is a device consisting of a non-linear crystal and an optical resonator which shifts the frequency of incident electromagnetic radiation. The frequency shift is achieved by optical resonance within an optical resonator on two components of the same beam separated by the crystals birefringent property. The two individual waves which oscillate within the optical resonator have frequencies which add up to the frequency of the incident wave (conservation of energy). The wave with the desired frequency and the wave known as the residual wave leave the crystal at different angles allowing the wave with the desired frequency to be isolated.

The OPO's output frequency may be selected by altering the phase matching condition within the crystal. This is achieved by small changes in the lights path length through the crystal either by thermal expansion or by adjusting the crystals orientation to the incident beam. Generally OPO's are used to access specific wavelengths that lasers cannot obtain alone, and for the 1.6 µm region an OPO provides the best results for a laser operating as part of a LiDAR system (Loth et al., 2005). Its ability to select a very specific wavelength is highly desirable, particularly in the 1.6 µm region which requires the spectral absorption line to be sampled at its maximum point (at sea level).

2.5 Detectors for space-borne TC-DIAL

Electromagnetic radiation emitted by a laser system on board a low Earth orbiting TC-DIAL instrument is scattered by the Earth's surface and returned back to the TC-DIAL receiver approximately 2.5 milliseconds later. The receiver telescope focuses the electromagnetic radiation onto a detector inside the instrument which generates an electric charge in response. The charge generated is quantified and recorded by the onboard electronics and either processed onboard or transmitted to a ground station where it is converted into a light intensity value. The semiconductor detector which reacts to the electromagnetic radiation is generally defined in terms of its quantum efficiency (QE), its noise equivalent power (NEP) and its internal gain. The QE refers to the efficiency of the conversion process from incident electromagnetic radiation to electrical charge in the detector, the NEP is defined as the signal power that gives a signal to noise ratio of 1 for a 1 Hz bandwidth and has units of $WHz^{-1/2}$ and the internal gain refers to the amplification of the received signal within the detector.

For the 1.6 and 2 µm regions of the electromagnetic spectrum semiconductor detectors are often made out of indium gallium arsenide (InGaAs) as they are sensitive to these regions of the SWIR. Until recently avalanche photo diodes (APD) were most suitable for 1.6 µm detection as they provided reasonably low NEP and an internal gain of approximately 10. For the 2 µm region PIN (Positive-Intrinsic-Negative) diodes were the only available choice with no internal gain and a relatively poor NEP. Recent developments in detector technology however has improved InGaAs semiconductor detector capability, enabling low NEP and high QE for both the 1.6 and 2 µm regions of the electromagnetic spectrum. The new detectors which are currently in the development stage exceed the capabilities of alternative detection methods and have been selected as the most suitable detectors for a future TC-DIAL system by the FACTS report (Loth et al., 2005). The new InGaAs detectors are most beneficial for 2 µm detection as the old 2 µm InGaAs PIN diodes had no internal gain and therefore had a heavy dependency on a pre-amplifier to boost the signal which added a lot of noise. The new detectors have a very large (2×10^3) internal gain system which removes the need for the preamplifier and therefore greatly improves 2 µm detection. One of the new 2 µm InGaAs semiconductor detectors is currently being applied in a terrestrial LiDAR instrument under development at NASA Langley (Refaat et al., 2004).

A semiconductor detector (such as InGaAs) is a substrate containing suitably located quantum mechanical energy levels known collectively as the valence band which are situated somewhere between the ground state energy level of the material and the conduction band (where electrons and associated holes are free to conduct) (Figure 2.5-1).

In a photo-conductive detector incident electromagnetic radiation with the appropriate frequency is able to excite electrons and holes from the valance band into the conduction band to form a temporary electrical current in the semi-conductor. A small bias is applied across the detector to produce an electric field which attracts the free electrons to the detector anode and the holes left behind (positive charge in a molecule owing to a missing electron) to the detector cathode. The generated current is proportional to the intensity of the incident electromagnetic radiation allowing the light intensity to be inferred from the measured electrical current across the detector.

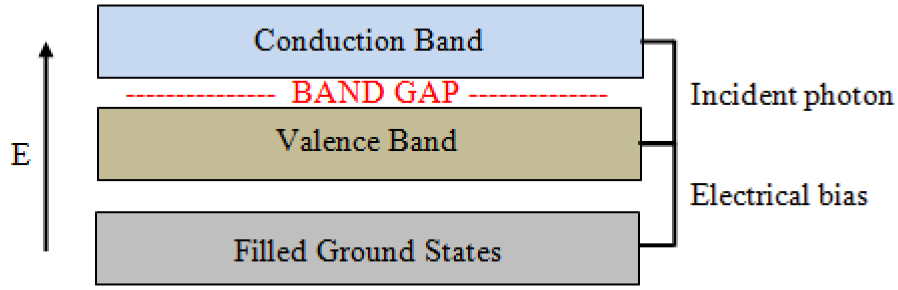

Figure 2.5-1 Basic semiconductor band structure

InGaAs detectors are manufactured using a process known as liquid phase epitaxy which allows a seamless connection between the various layers of material which make up the detector. The layers are doped such that they contain either an abundance of electrons (N-type) or an abundance of positive charge carriers known as holes (P-type) (Figure 2.5-2).

The precise doping of the two materials and the presence of the P-N junction between the layers provides the required quantum mechanical energy level structure for detection of a given frequency of electromagnetic radiation. InGaAs detectors can be tuned so that their peak sensitivity is situated over the wavelength of interest. The tuning is achieved by adjusting the relative contribution of indium and gallium within the InGaAs lattice (Abedin et al., 2004) (Figure 2.5-3).

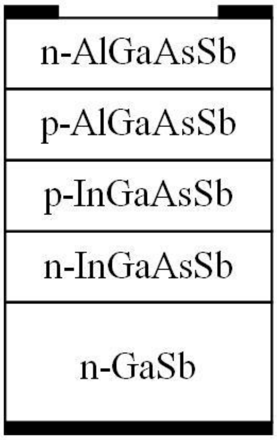

Figure 2.5-2 InGaAs phototransistor structure, image is reproduction of a figure from (Refaat et al., 2004)

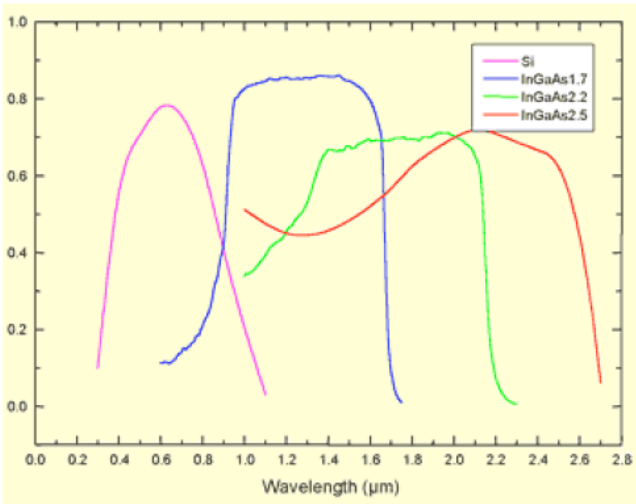

Figure 2.5-3 Quantum efficiencies for various InGaAs lattice ratios, image from (Loth.C et al., 2005)

2.6 Summary

The active remote sensing technique TC-DIAL has been the focus of a number of feasibility studies that have investigated the application of TC-DIAL as a CO_2 measurement system on a low Earth orbiting satellite platform. The studies have reviewed the latest technology (at the time of writing) which could be used to build a TC-DIAL instrument, and have applied computer simulations using parameters based on definitions for this technology to show that TC-DIAL is a promising approach for use as a space-borne instrument for measuring atmospheric CO_2.

The TC-DIAL approach is most desirable as an addition to the current CO_2 measurement systems owing to its potential to provide accurate measurements at all latitudes with no diurnal constraints. The main limitations indicated by the feasibility studies are the capabilities of the laser and detector technology and the reliance on relatively inaccurate ancillary data. Recent developments in detector technology have significantly improved the theoretical capability of CO_2 TC-DIAL, which is particularly notable for the 2 μm region which is greatly aided by the high internal gain of the new detector technology which removes the dependency on a noisy preamplifier. The significant improvement achieved by the recent detector advances in the 2 μm region has presented a particular scientific interest in 2 μm TC-DIAL. Until recently the APD 1.6 μm detectors were preferable over the 2 μm PIN diode detectors owing to their superior NEP, gain and QE, and as such 1.6 μm appeared to be the most suitable wavelength for measuring atmospheric CO_2. Because of the new interest in 2 μm TC-DIAL this wavelength is focused on in this thesis.

Lasers that operate at 2 μm are currently being developed and demonstrated. At present crystal lasers offer the best overall solution, combining suitable power, narrow emission linewidth, high energy efficiency and space operational heritage. These lasers provide the required specifications to function as part of a TC-DIAL system but further developments are still required to ensure they can maintain their desirable properties for long periods of time under space conditions.

It is clear from the technology reviews that significant improvements are being made toward there being suitably capable technology available to form an operational space-borne TC-DIAL system, however further work and demonstration in an appropriate system configuration which fairly represents a space-borne system is still required.

In addition to the technology demonstrations, computer simulations have also been used in both feasibility studies and scientific papers to define the capability of instruments under various conditions. The most comprehensive investigation of TC-DIAL as a space-borne remote sensing instrument was carried out by a feasibility study known as the FACTS report. The computer simulations carried out in the FACTS report were used to optimise a theoretical TC-DIAL system based on out of date 2 μm detector technology and spectroscopy (HITRAN 2004). The simulations also omitted a number of free parameters such as integration path length and the instruments pulse repetition frequency in the optimisation process. A suitable continuation of this research is to apply the same computer simulation methodology using up-to-date detector technology parameters and spectroscopy with particular consideration for some of the parameters which may be primarily driven by a science objective. To perform the study a suitably representative computer simulation of the physical processes associated with the measurement of total column CO_2 by a TC-DIAL instrument in low Earth orbit is required. The following chapter details a novel computer simulation written for the purpose of expanding on the current understanding of the capabilities of CO_2 measuring TC-DIAL.

3. Space-borne Total Column Differential Absorption Lidar computer simulation

The Total Column Differential Absorption LiDAR (TC-DIAL) simulator (TCDS) is a computer model written in the programming language IDL. The model objective is to investigate the capability of a space-borne TC-DIAL system for measuring atmospheric carbon dioxide, and to examine the components of the system which contribute to the uncertainty of atmospheric retrievals performed using its measurements. The core of the TCDS is the propagation of photons through a simulation of the Earth's atmosphere, including interactions with clouds, aerosols and carbon dioxide. The model also simulates photon interaction with the Earth's surface and the detection process onboard the satellite instrument (Figure 3-1).

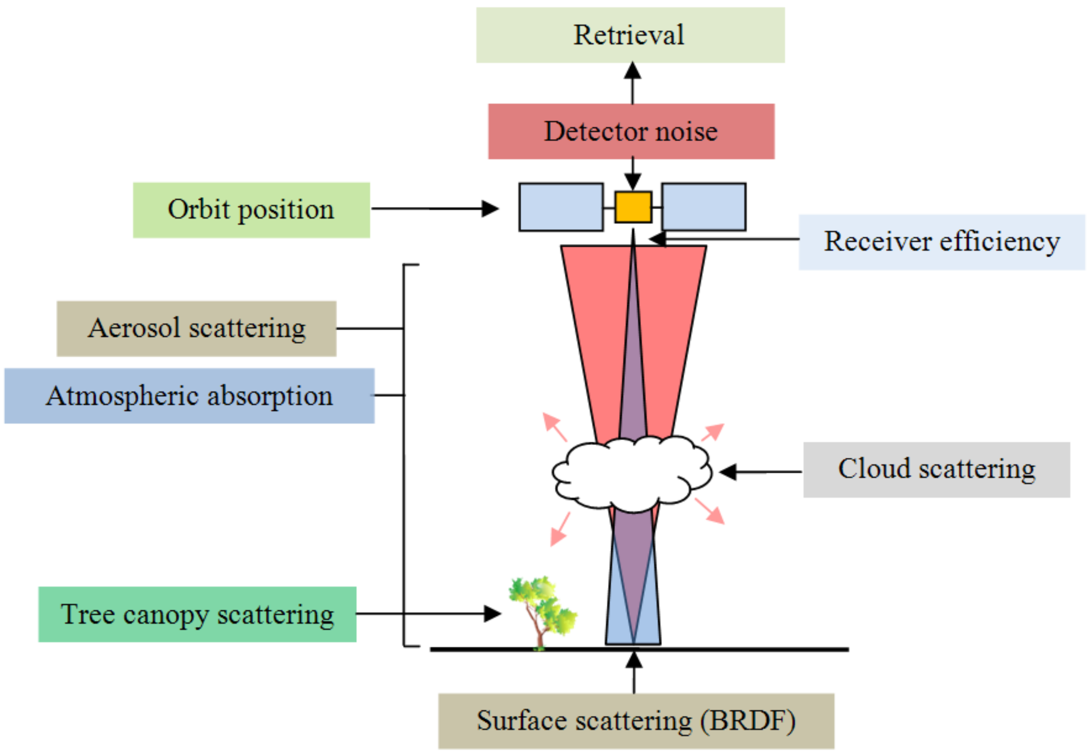

Figure 3-1 A depiction of the key physical processes modeled by the TCDS

The design priority for the TCDS is computational efficiency as large numbers of iterations are required for the analysis of various system components.

Other important design considerations are:

- Batch processing capability for executing large iterative simulations
- Multi-threading capability to optimise available processing resources
- Flexibility for investigating many different facets associated with TC-DIAL systems
- Portability so that it may be run on many different systems

The TCDS comprises of multiple sub procedures responsible for simulating individual physical processes associated with TC-DIAL systems. Figure 3-2 provides a schematic representation of the structure of the TCDS. The CORE procedure at the centre of the schematic is the main executable which calls and links all of the sub procedures.

Each TCDS simulation is configured by two input text files known as the *control* and *variable* files. The control file contains switches which enable or disable various model components and the variable file contains definitions for the models physical parameters.

The TCDS uses three major nested loops to iteratively run simulations known as *orbit*, *batch* and *contour*. The batch and contour loops incrementally adjust preselected variables to generate a data series of system responses, and the orbit loop works in conjunction with an orbit simulation to produce a series of retrievals using a realistic orbit track.

The TCDS and its input text files are duplicated to allow the model to utilise the multiple processor capability of modern computer servers. The model copies are either linked together to contribute towards a common simulation, or configured independently to work on separate projects simultaneously.

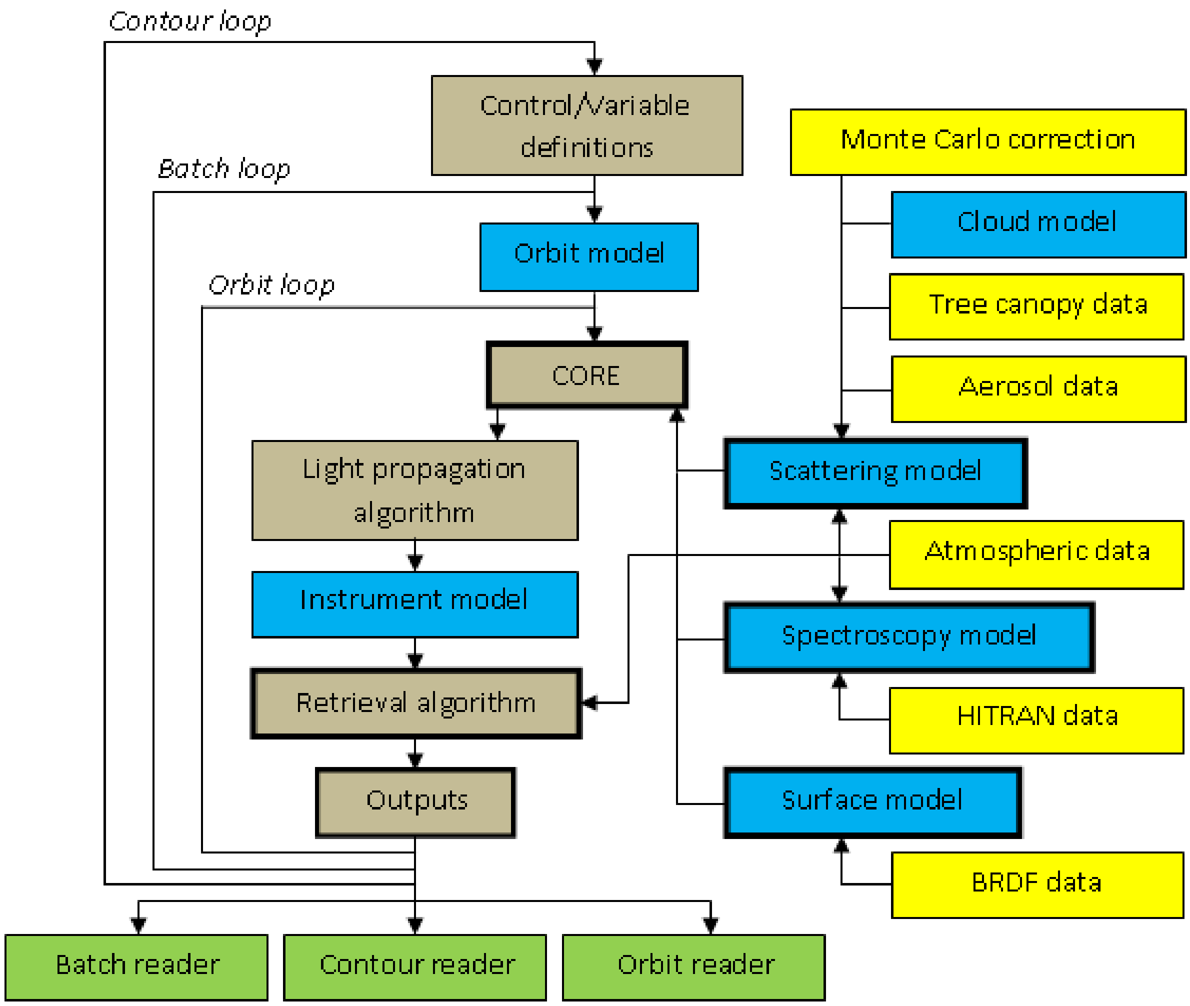

Figure 3-2 Schematic representation of the TC-DIAL simulator. Blue boxes represent physical models, yellow boxes represent data sources, green boxes represent ancillary programs and light brown boxes are uncategorised model components. Boxes with thick borders are components that require specific input from other model components.

3.1 Model components

The following section describes the physics and application of the procedures displayed in Figure 3-2.

3.1.1 Light propagation algorithm

The photon positions are controlled by two arrays known as *up* and *down.* Each of their array elements represents an individual atmospheric altitude and photons are able to move between them to simulate their vertical propagation through the Earth's atmosphere.
The photons initially enter the model via the top element of the down array and are moved along by one array element per time step. The photons calculated to scatter backward are transferred to the same indices of the upward array and begin the process of moving in the opposite direction (Figure 3.1.1-1).

The scattering process occurs in both directions allowing previously scattered photons to scatter back into their original direction at a later point in time. This system creates a multiple scattering environment within the field of view (FOV) of the TC-DIAL receiver.

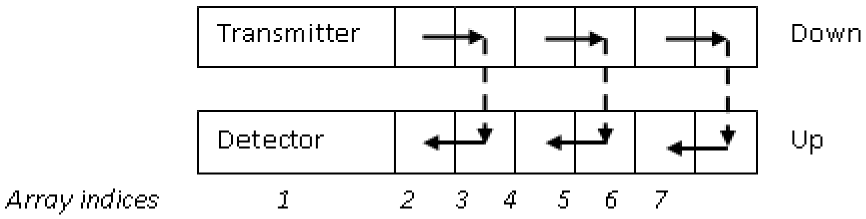

Figure 3.1.1-1 Diagram representing basic photon propagation mechanism in the TCDS. Only single backscattering events are portrayed for 3 downward photons

The series of calculations that govern the propagation of photons through the up and down arrays are given by equations 21 to 28.

Equations 21 and 22 determine the quantity of photons that pass through an atmospheric level without being absorbed by CO_2.

$$C_u = U - AU \qquad 21$$

$$C_d = D - AD \qquad 22$$

where U is the up array containing upward propagating photons, D is the down array containing downward propagating photons, A is an array of atmospheric absorption fractions and C_u and C_d are the photon quantities in the up and down arrays which pass through without being absorbed by CO_2.

Equations 23 to 26 determine the quantity of photons scattered in the up and down arrays for the backward and loss directions, with the loss direction accommodating photons that scatter outside of the instrument's field of view. Any photons calculated as being lost are ultimately removed from the system via equations 27 and 28.

$$R_{uB} = C_u S_u \tag{23}$$

$$R_{uL} = C_u S_{uL} \tag{24}$$

$$R_{dB} = C_d S_d \tag{25}$$

$$R_{dL} = C_d S_{dL} \tag{26}$$

where the R terms are the quantities of photons scattered, the S terms are the pre-calculated scattering fraction arrays, the subscripts u and d refer to the up and down arrays and the subscripts B and L refer to the backward and loss scattering directions.

Equations 27 and 28 determine the quantity of photons that continue in their respective directions having taken into account both scattering and absorption processes. These expressions generate the new up and down arrays for the following time step.

$$U = C_u + R_{dB} - R_{uB} - R_{uL} \tag{27}$$

$$D = C_d + R_{uB} - R_{dB} - R_{dL} \tag{28}$$

Upon calculation of the new up and down arrays their contents are shifted by a single array element to simulate the propagation of light. When the photons reach the first element of the upward array they are recorded as having reached the satellite detector.

The process of applying equations 21 to 28 and then shifting the arrays continues until sufficient iterations have occurred for all photons in the model to either return to the satellite or leave the system.

The number of levels the atmosphere is split into is determined by the model control files, however a standard resolution is approximately 10 m. The atmospheric properties which affect the propagation of light through the atmosphere are scaled via sampling and interpolation to match the model resolution (see Section 3.2).

3.1.2 Atmospheric data

The Earth's atmosphere is modeled in the TCDS using vertically resolved profiles of temperature, pressure and water vapour. These profiles are obtained from reference atmospheres for the MIPAS satellite instrument (Remedios et al., 2007), and samples of these profiles are presented in Figure 3.1.2-1.

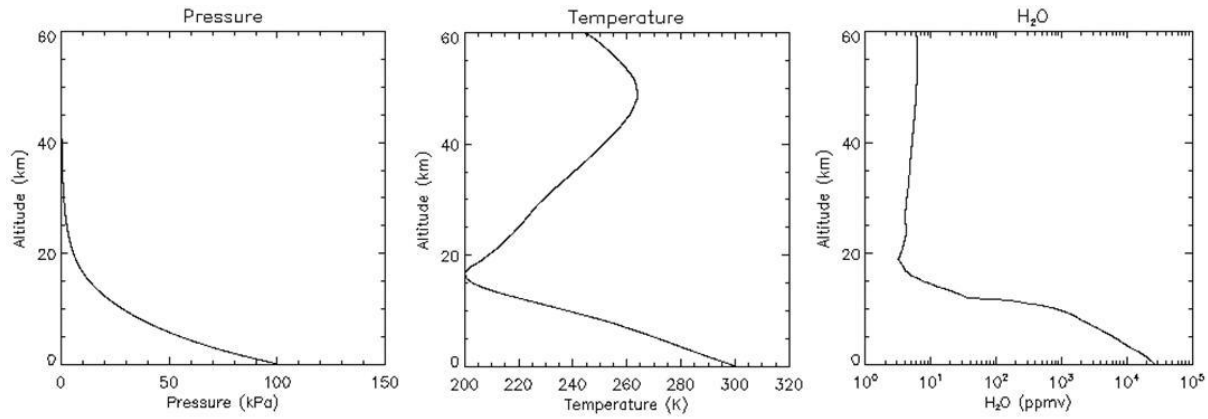

Figure 3.1.2-1 Example profiles that define the Earth's atmosphere in the TCDS (profiles for July and 45° N)

The MIPAS profiles are available for a series of latitude bands at 1 km vertical resolution. The TCDS automatically selects the appropriate version for a given simulation based on the measurements location on the Earth's surface. Upon selection of the appropriate version the TCDS alters the profile's sampling to match the model sampling through interpolation (Section 3.2.1).

The atmospheric profiles read into the model are required by many of the TCDS sub procedures. Their applications within the TCDS include the computation of the atmospheric absorption spectroscopy and the determination of the molecular scattering coefficients. The profiles are either configured as idealistic with no associated uncertainties, or include errors to represent limited knowledge in the atmospheres state and composition. For ideal simulations the TCDS employs identical profiles for both the light propagation algorithm and the retrieval process. This ensures there are no uncertainties in the state of the atmosphere when the measurement is made.

For the simulation of more realistic TC-DIAL systems, uncertainties in the knowledge of the physical properties of the Earth's atmosphere are accounted for. The uncertainties are introduced to the model by modifying the atmospheric profiles used by the light propagation algorithm whilst leaving the profiles used by the retrievals unaltered. The difference results in a retrieval error which is quantifiable as a function of profile uncertainty.

3.1.3 Aerosol and molecular scattering

Electromagnetic radiation propagating through the Earth's atmosphere is frequently scattered by aerosols and atmospheric molecules. The frequency of the scattering and therefore its magnitude as a function of distance has a very strong wavelength dependency. For shortwave infrared (SWIR) radiation from a TC-DIAL system both molecular and aerosol scattering processes are sufficiently strong to be of relevance.

Close to the Earth's surface where there is an abundance of particulate matter, scattering of SWIR electromagnetic radiation is predominantly caused by aerosols, however at higher altitudes where aerosols are in much lower concentrations molecular scattering dominates (Figure 3.1.3-1).

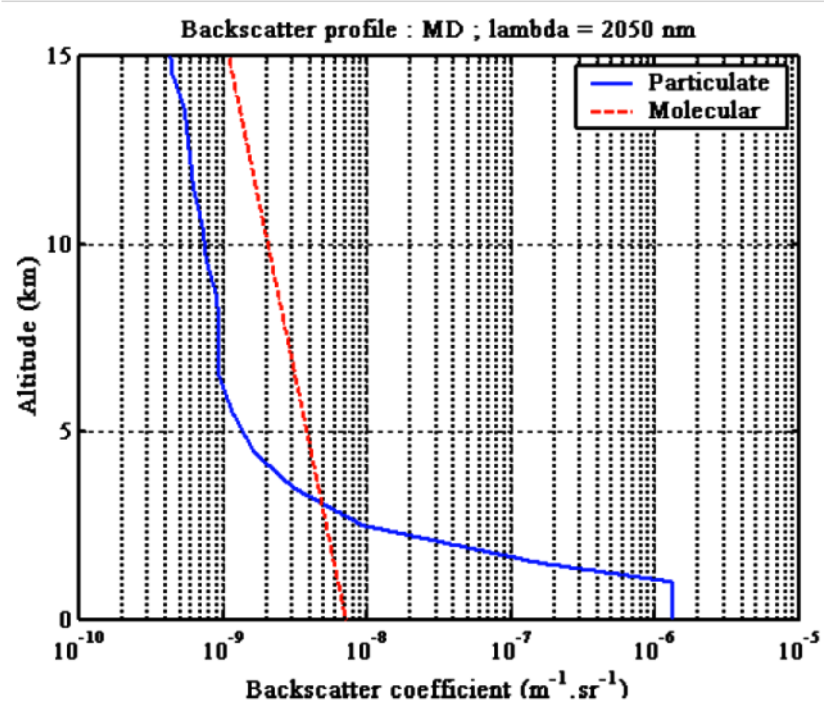

Figure 3.1.3-1 Molecular and particulate matter backscatter coefficients as a function of altitude for 2 µm radiation. Image from the FACTS report (Loth et al., 2005).

For a space-borne TC-DIAL system which transmits electromagnetic energy through the Earth's atmosphere as a collimated beam, any aerosol or molecular scattering leads to a partial deflection of energy away from the detector's field of view. Such a loss in received signal decreases the signal-to-noise ratio and ultimately increases the retrieval error.

Owing to their capability to influence the retrieval, both molecular and aerosol scattering components are considered important parameters in the performance of a TC-DIAL system and as such are included as physical processes in the TCDS.

3.1.3.1 Molecular scattering

Atmospheric molecular scattering occurs when the loosely bound outer electrons of molecules in the Earth's atmosphere are forced to oscillate in the presence of an electromagnetic wave. The generated electron oscillation matches the frequency of the incident wave and transmits at the same wavelength in various directions. This process is known generally as an elastic scattering event, as the majority of the scattered energy is radiated away from the molecule (dipole) at the same wavelength, and very little is absorbed and released as thermal energy.

The probability distribution function describing the direction of light scattered by a molecule approximated as a perfect dipole (such as N_2 and O_2) is known as the Rayleigh phase function and is shown in Figure 3.1.3.1-1.

A dipole moment is generated within a molecule by an external electromagnetic field. The orientation of the scattering plane relative to the electromagnetic fields polarisation determines the appearance of the phase function in the scattering plane. Plotted in two dimensions (as in Figure 3.1.3.1-1) the Rayleigh scattering phase function is a cross sectional representation of a three dimensional phase function (McCartney, 1976).

For a nadir LiDAR system the scattering plane may be defined as the horizontal cross section of the laser beam in the atmosphere. Using this definition a transverse linearly polarized laser transmission will generate a dipole oscillation that is parallel to the scattering plane. The TCDS uses this definition to determine the directional probability of molecular scattering.

The Rayleigh scattering phase function is given by equation 29.

$$P_R(\theta) = \frac{3}{4}(1 + \cos^2\theta) \tag{29}$$

where θ is the subtended scattering angle from the incident vector to the scattering vector. The magnitude of the phase function is plotted in Figure 3.1.3.1-2.

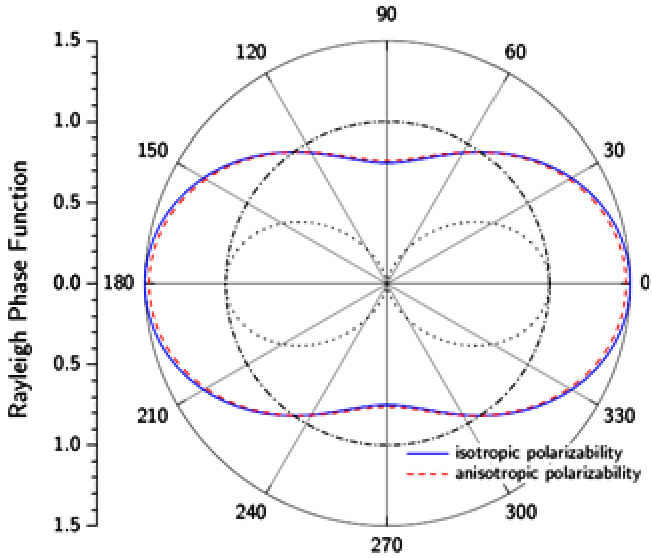

Figure 3.1.3.1-1 The Rayleigh phase functions for light polarized parallel to the scattering plane (dotted line), light polarized perpendicular to the scattering plane (dot-dashed line) and unpolarized light (solid line). Image from (Hönninger, 2002).

The Rayleigh scattering coefficient defines the fraction of scattered light per unit length. The expression for the scattering coefficient is given by equation 30.

$$\sigma_r(a) = \frac{128\pi^5 {\alpha_{vol}}^2 K N(a)}{\lambda^4} \qquad 30$$

where σ_r is the Rayleigh scattering coefficient as a function of altitude a in m^{-1}, N is the number of scattering molecules, α_{vol} is the atmospheric polarisability factor which for air is approximately 1.7×10^{-20}, λ is the wavelength of the light being scattered in m, and K is the Kings correction factor which compensates for atmospheric depolarisability and has a value of approximately 1.038 for air (Sneep, 2004).

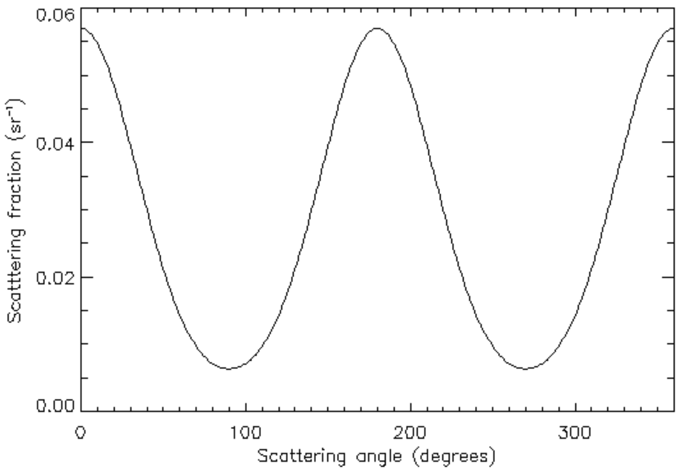

Figure 3.1.3.1-2 Magnitude of the Rayleigh phase function as a function of scattering angle from the incident vector

The number of scattering molecules N is calculated as a function altitude using a form of the ideal gas equation (equation 31).

$$N(a) = \frac{P(a)}{RmT(a)} \tag{31}$$

where N is the number of molecules per cubic meter as a function of altitude a, R is the gas constant with a value of $8.314 \text{ J mol}^{-1} \text{ K}^{-1}$, P is the atmospheric pressure in Pa and T is the atmospheric temperature in K which are both defined as a function of altitude from MIPAS reference atmosphere profiles, and m is the average mass of an atmospheric molecule which for the TCDS is a weighted average of the mass of oxygen and nitrogen at 5×10^{-26} kg.

3.1.3.2 Aerosol scattering

Aerosol scattering is the interaction of electromagnetic radiation with dielectric particulate matter and is often mathematically defined by Mie theory (McCartney, 1976). An important requirement for the application of Mie theory is that the propagating wavelength must be of similar size to the scattering particle. For near infrared electromagnetic radiation and much of the particulate matter in the Earth's atmosphere this condition is met.

The calculation of the Mie scattering phase function is computationally expensive and considered impractical for use in the TCDS which has design emphasis on efficiency. The most computationally efficient alternative is to use look up tables containing pre-calculated Mie scattering phase functions, however these have the potential restrict the models operational flexibility. To avoid any such restrictions the TCDS uses a more computationally efficient approximation for the Mie scattering phase function known as the Henyey-Greenstein (H-G) phase function.

The H-G phase function provides a good approximation for the forward scattering component of the Mie phase function but poorly represents the backscatter component (Cornette, 1992). A modified version of the H-G phase function which models the backscatter more realistically is used in the TCDS (equation 32).

$$P_{HG}(\theta, g) = \frac{3}{2}\frac{1-g^2}{1+g^2}\frac{1+\cos(\theta)^2}{[1+g^2-2g\cos(\theta)]^{3/2}} \qquad 32$$

where P_{HG} is a modified version of the H-G phase function, g is the asymmetry factor, and θ is the scattering angle subtended from the incident vector. The asymmetry parameter is obtained from the radiative transfer model SCIATRAN, which is given as an average value for a typical mixture of atmospheric aerosols as a function of altitude (Rozanov et al., 2005).

The magnitude of the H-G phase function generated using equation 32 is presented in Figure 3.1.3.3-1.

3.1.3.3 Application of atmospheric scattering

To incorporate molecular and aerosol scattering processes into the light propagation algorithm, the TCDS requires unitless vertically resolved profiles of atmospheric scattering fractions in the up and down directions. These profiles are generated using the scattering coefficients and phase functions described in sections 3.1.3.1 and 3.1.3.2.

The aerosol scattering coefficient profile obtained from the radiative transfer model SCIATRAN is interpolated at the beginning of each TCDS simulation to obtain the same vertical sampling as the TCDS in order to correctly interface with the model.

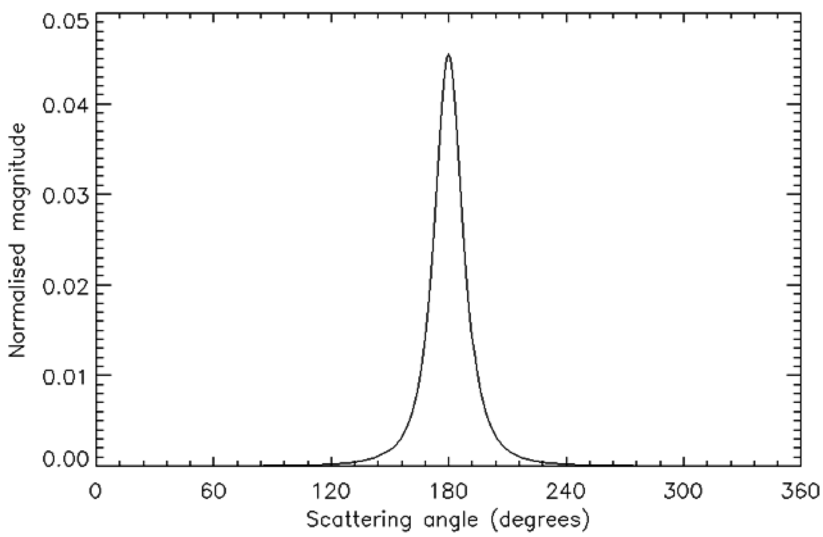

Figure 3.1.3.3-1 Magnitude of the H-G phase function as a function of scattering angle

To determine the fraction of radiation scattered in a particular direction at each atmospheric level the phase functions are integrated (Henyey Greenstein) or averaged (Rayleigh) over a series of angle ranges (Figure 3.1.3.3-2). The ranges are split into up, down and loss components. The down scattering component uses the angle formed between the scattering event and the edge of the detectors FOV on the Earth's surface ($\emptyset_D$), the up component uses the angle formed between the scattering event and the edge of the satellites receiver mirror ($\emptyset_U$), and the loss component uses all remaining angles to accommodate scattering out of the system. The up, down and loss components are derived for both forward and backward scattering events resulting in a total of six scattering profiles.

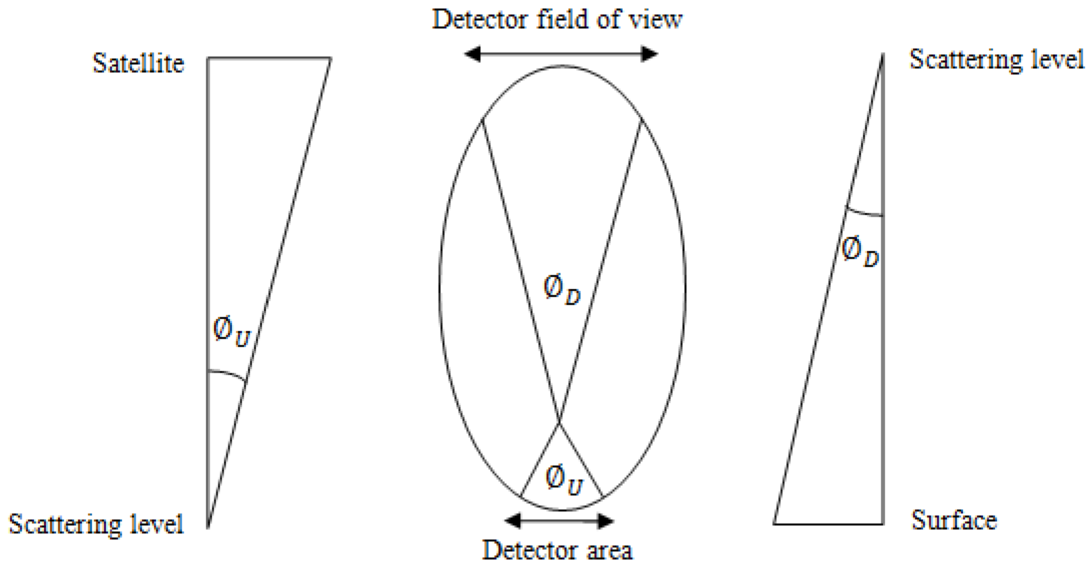

Figure 3.1.3.3-2 The three scattering regions of a H-G phase function used by the TC-DIAL simulator (centre), the geometry of scattering towards the detector (left), and the geometry of scattering towards the surface (right).

The angles over which the up and down scattering phase functions are integrated or averaged over are calculated by equations 33 and 34.

$$\emptyset_D(a) = \tan^{-1}\left(\frac{l(a)}{D_s}\right) \tag{33}$$

$$\emptyset_U(a) = \tan^{-1}\left(\frac{L - l(a)}{D_m}\right) \tag{34}$$

where $\emptyset_D$ is the angle in degrees created between the scattering event and the radius of the surface footprint, l is the altitude of the atmospheric level at level index a, D_s is the diameter of the surface footprint, $\emptyset_U$ is the angle in degrees created between the scattering event and the radius of the receiver mirror, L is the satellite orbital altitude and D_m is the diameter of the receiver mirror.

The directional scattering fractions for the up, down and loss components are determined for the H-G phase function by integrating over the angles that lie within the extremes of $\emptyset_D$ and $\emptyset_U$. This process is carried out using equations 35 to 37.

$$C_{DHG}(a) = \int_{0}^{[\emptyset_D(a)/2]} P(\theta)\, d\theta + \int_{360-[\emptyset_D(a)/2]}^{360} P(\theta)\, d\theta \tag{35}$$

$$C_{UHG}(a) = \int_{180-[\emptyset_U(a)/2]}^{180+[\ \emptyset_U(a)/2]} P(\theta)\, d\theta \tag{36}$$

$$C_{LHG}(a) = \int_{0}^{360} P(\theta)\, d\theta - C_{DHG}(a) - \ C_{DHG}(a) \tag{37}$$

where C_{DHG}, C_{UHG} and C_{LHG} are the down, up and loss scattering fractions respectively for H-G scattering, and P is the H-G scattering phase function.

The directional scattering fractions for the up, down and loss components are determined for the Rayleigh phase function by averaging over the angle ranges that lie within the extremes of $\emptyset_D$ and $\emptyset_U$. This process is carried out using equations 38 to 45.

$$C_{DR}(a) = \frac{\left[\sum_{0}^{n=[\emptyset_D(a)/2]} P(n) + \sum_{360-\ [\emptyset_D(a)/2]}^{360} P(n)\right] O_D(a)}{\emptyset_D(a)} \tag{38}$$

$$C_{UR}(a) = \frac{\sum_{k=180-[\emptyset_U(a)/2]}^{k=180+[\ \emptyset_U(a)/2]} P(k) O_U(a)}{\emptyset_U(a)} \tag{39}$$

$$C_{LR}(a) = \frac{\sum_{0}^{t} P(t)\, O_L(a)}{360 - (\emptyset_U(a) + \emptyset_D(a))} \tag{40}$$

$$\theta_D = \tan^{-1}\left(\frac{D_s}{2l(a)}\right) \tag{41}$$

$$\theta_U = \tan^{-1}\left(\frac{D_m}{2\big(L - l(a)\big)}\right) \tag{42}$$

$$O_D(a) = 2\pi\,(1 - \cos\theta_D) \qquad 43$$

$$O_U(a) = 2\pi\,(1 - \cos\theta_U) \qquad 44$$

$$O_L(a) = 4\pi - (O_U + O_D) \qquad 45$$

where C_{DR}, C_{UR} and C_{LR} are the down, up and loss scattering fractions respectively for Rayleigh scattering, n are the array indices for the downwards component of the phase function, k are the array indices for the upwards component of the phase function, t are the array indices which are not covered by the indices n and k, O_D, O_U and O_L are the down, up and loss solid angles respectively and P is the Rayleigh scattering phase function.

The final scattering fractions for use in the light propagation algorithm combine both the molecular and aerosol scattering components. The backscatter versions of these profiles are calculated using equations 46 to 48.

$$S_{UB}(a) = \sigma_r(a)\sigma_{HG}(a)C_{Ur}(a)C_{UHG}(a)d \qquad 46$$

$$S_{DB}(a) = \sigma_r(a)\sigma_{HG}(a)C_{Dr}(a)C_{DHG}(a)d \qquad 47$$

$$S_{LU}(a) = \sigma_r(a)\sigma_{HG}(a)C_{Lr}(a)C_{LHG}(a)d \qquad 48$$

where S_{DB}, S_{UB} and S_{LB} are unitless scattering profiles for the down, up and loss scattering components for backward scattering. σ_r and σ_{HG} are the Rayleigh and H-G scattering coefficient profiles in m^{-1}, d is the atmospheric interval step size in m, and C_{Fr}, C_{Ur}, C_{Lr}, C_{DHG}, C_{BHG} and C_{LHG} are the up, down and loss directional scattering fraction profiles for the Rayleigh and H-G scattering phase functions.

The S_{DB}, S_{UB} and S_{LB} arrays are applied in the light propagation algorithm to calculate the magnitude of scattering in the backward direction. Forward scattering arrays are similarly determined but using inverted phase functions for the calculations of C_D, C_U and C_L.

The final scattering profiles are displayed in Figure 3.1.3.3-3 for both the forward and backward directions.

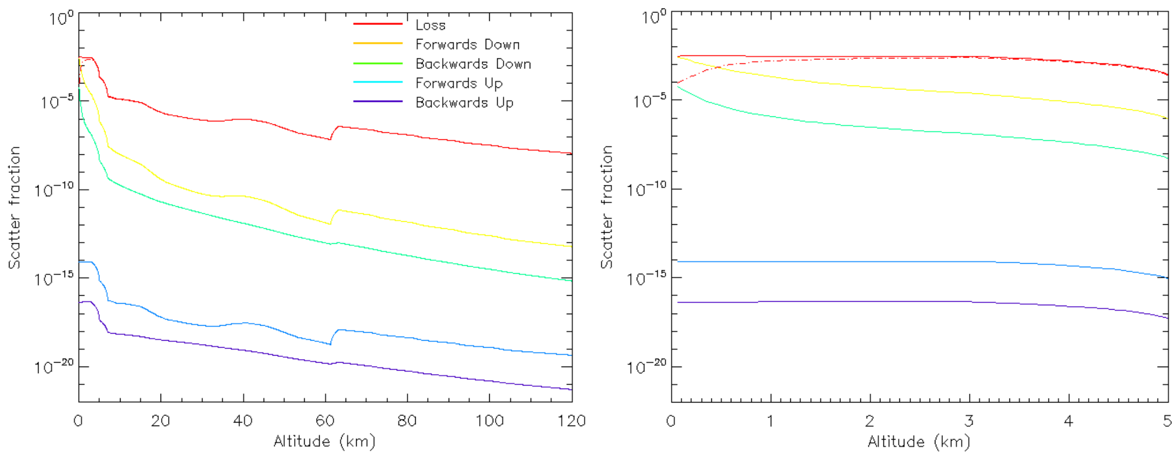

Figure 3.1.3.3-3 Scattering fraction profiles generated and used by the TCDS (left) and a close up of the profiles near to the Earth's surface (right).

As shown in Figure 3.1.3.3-3, the backscatter in the upward direction is the least efficient of the scattering components. The very small solid angle between the scattering event and the instruments receiver mirror combined with the use of the backward portion of the H-G phase function allows very little signal to arrive back at the detector from atmospheric scattering.

The loss component is the dominant scattering process owing to its solid angle accommodating a significant majority of both the H-G and Rayleigh phase functions. Near to the Earth's surface the loss scattering fraction splits into two separate components displayed as solid and dashed lines in Figure 3.1.3.3-3. The dashed line represents the loss for the downward scattering direction and the solid line represents the loss for the upward scattering direction. The separation is caused by a 180° difference in the orientation of the H-G phase function with respect to the Earth's surface. For the downward loss component the strong frontal area of the H-G phase function is pointing toward the surface and begins to be taken over by the forward-down scattering component as the light approaches the ground. The switch over from down-loss to down-forward is caused by an increase in the solid angle between the scatterer and the surface footprint. For the upward scattering direction the same effect occurs but on the rear of the H-G phase function and as such the majority of the scattering remains with the loss component (Figure 3.1.3.3-4).

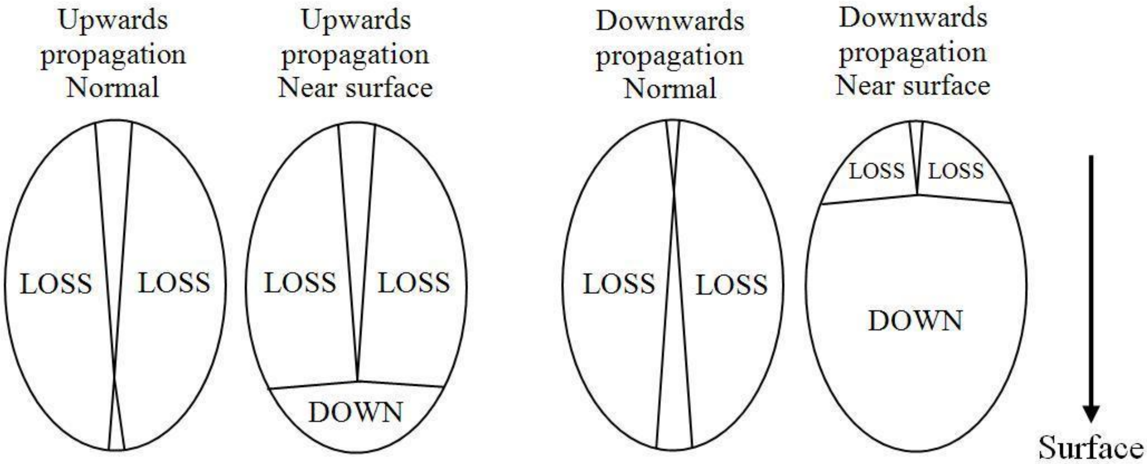

Figure 3.1.3.3-4 Orientation of the upward and downward H-G phase functions at an intermediate altitude and near to the Earth's surface. The phase functions are separated into loss and down regions to show the importance of the phase functions orientation to the Earth's surface

3.1.3.4 Validation of scattering model

The TCDS scattering algorithm has been partially validated by comparison of its backscatter coefficients with those from the ESA-RMS model presented in the FACTS report (Loth et al., 2005). The backscatter coefficients for 2 µm electromagnetic radiation scattering in the Earth's atmosphere are shown for both models in Figure 3.1.3.4-1.

The ESA-RMS aerosol composition used to produce the backscatter coefficient profile presented in the FACTS report (and reproduced here) is not provided. The aerosol configuration extracted from SCIATRAN and used in the TCDS is classed as a summer scenario, with 10 km visibility in the boundary layer and 50 km visibility in the troposphere.

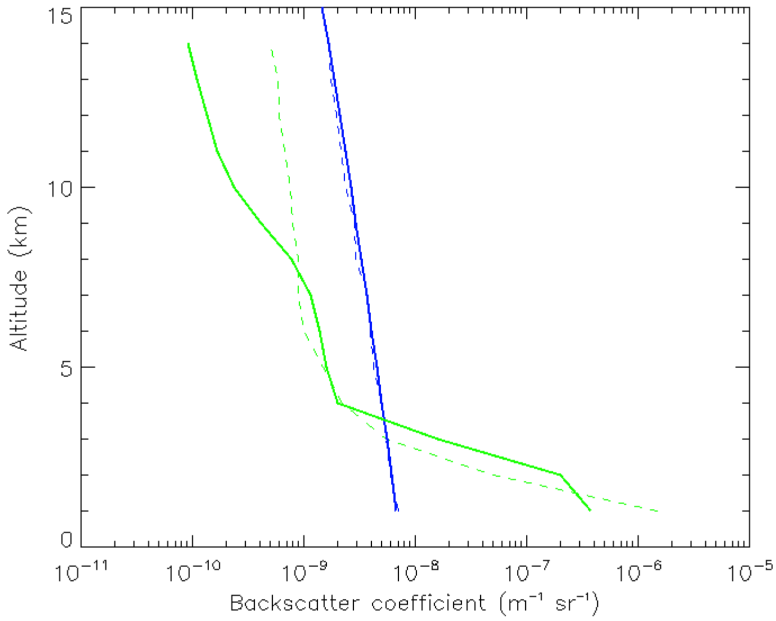

Figure 3.1.3.4-1 Backscatter coefficients generated by the TCDS scattering algorithm (solid lines) and the ESA-RMA model (dashed lines) for molecular scattering (blue) and aerosol scattering (green).

A reasonable agreement is shown in Figure 3.1.3.4-1 between the TCDS and the ESA-RMS scattering models providing a level of confidence in the TCDS scattering algorithm. Some discrepancy between the aerosol components is expected as the models likely utilise different scattering coefficient profiles. The magnitude of the aerosol discrepancy is within normal variations of atmospheric concentration.

Figure 3.1.3.5-1 presents the backscatter coefficient profile used in the TCDS for the comparison plot.

3.1.3.5 Monte Carlo scattering correction

The TCDS scattering algorithm is fundamentally limited to operating in two dimensions owing to the nature of the light propagation algorithm on which it is based. This limitation imposed on the models realism by the incomplete geometry renders it inaccurate at reasonably high optical depths (> 0.5). To compensate for this inaccuracy correction factors are derived using a novel Monte Carlo simulation which accommodates multiple atmospheric scattering in three dimensions (see Section 3.3.1). The correction factors are applied in the TCDS scattering algorithm by adjusting the previously calculated scattering fractions.

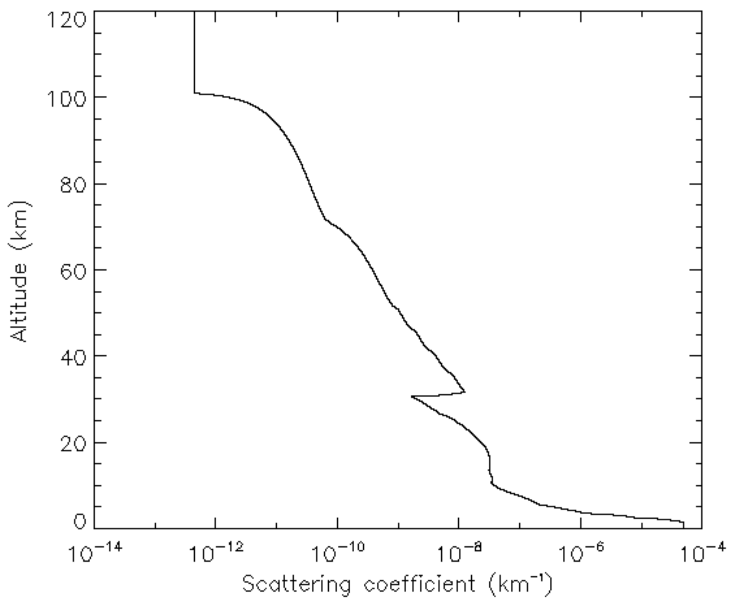

Figure 3.1.3.5-1 Scattering coefficient from SCIATRAN as a function of altitude for a summer scenario with a boundary layer visibility of 10 km and a troposphere visibility of 50 km

For the forward and backward scattering directions the correction factors are applied in the TCDS scattering algorithm by multiplying the derived scattering fraction by the appropriate corrective factor (equations 49 to 54). For the loss component which acts as a form of attenuation, the correction factors are initially modified to correspond to an adjustment in signal attenuation as opposed to an adjustment in signal transmission (as they are derived – see Section 3.3.1) (equations 55 to 58).

$$S_{DB}(a) = S_{DB}(a)C_{DB}(a) \qquad 49$$

$$S_{UB}(a) = S_{UB}(a)C_{UB}(a) \quad 50$$

$$S_{DF}(a) = S_{DF}(a)C_{DF}(a) \quad 51$$

$$S_{UF}(a) = S_{UF}(a)C_{UF}(a) \quad 52$$

$$S_{LU}(a) = S_{LU}(a)C_{UF2}(a) \quad 53$$

$$S_{LD}(a) = S_{LD}(a)C_{DF2}(a) \quad 54$$

$$C_{UF2}(a) = \frac{1 - \left(1 - A_{a/c}(a)\right) C_{UF}(a)}{A_{a/c}} \quad 55$$

$$C_{DF2}(a) = \frac{1 - \left(1 - A_{a/c}(a)\right) C_{DF}(a)}{A_{a/c}(a)} \quad 56$$

$$A_a(a) = O_L(a)\sigma_{HG}(a) \quad 57$$

$$A_c(a) = O_L(a)\omega l\beta_{ext}\ (a) \quad 58$$

where the S terms are the scattering fractions, the C terms are the correction factors, A_a is the scattering attenuation caused by losses from aerosol scattering, A_c is the scattering attenuation caused by losses from cloud scattering, the subscripts D and U refer to the downward and upward scattering directions, the subscripts F and B refer to the forward and backward scattering components, the subscript 2 refers to the modified correction factors, the index a refers to the atmospheric level, the term O_L is defined in Section 3.1.3.3, σ_{HG} is the H-G scattering coefficient, ω is the single scattering albedo for cloud, l is the length of the atmospheric level in m and β_{ext} is the extinction coefficient for cloud in units of m^{-1}.

3.1.4 Atmospheric absorption

The absorption of electromagnetic energy by atmospheric CO_2 is calculated for each atmospheric level in the TCDS using a form of the Beer-Lambert law (equation 59).

$$A_i = \frac{I_i}{I_{i-1}} = e^{-n_i \sigma_i l} \qquad 59$$

where A_i is the absorption fraction used in the TCDS light propagation algorithm, I_i is the intensity of light after having passed through the absorbing medium with atmospheric level index *i*, I_{i-1} is the incident light arriving from the previous atmospheric level, *n* is the atmospheric concentration of CO_2 in molecules cm^{-3}, σ is the absorption cross section in cm^2, and l is the length of the atmospheric level in cm.

The Beer-Lambert equation is depicted diagrammatically in Figure 3.1.4-1.

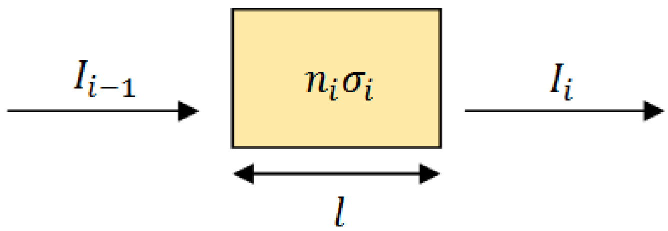

Figure 3.1.4-1 Depiction of the Beer-Lambert law

Equation 59 is applied for each atmospheric level to derive a vertical profile of absorption fractions for use in the TCDS light propagation algorithm (see Section 3.1.1).

3.1.5 Absorption spectroscopy

Particular wavelengths of electromagnetic energy are strongly absorbed by gases in the Earth's atmosphere. The magnitude of the absorption is determined by the strength of absorption lines and their proximity in frequency space to the transmitting wavelength. The HITRAN 2008 database (Rothman et al., 2009) is used to obtain these data in order to parameterise a spectroscopy model to simulate the intensity and shape of absorption lines as a function of altitude. A pre-processed array of spectral line strengths and broadening coefficients around the 2 µm region are generated from the HITRAN data for quick look-up by the TCDS.

Figure 3.1.5-1 shows the range of absorption lines selected for quick access by the TCDS for both the online and offline wavelengths. The x axis is centered on an appropriate online wavenumber of 4875.749 cm^{-1}.

The TCDS absorption spectroscopy model calculates vertically resolved absorption cross sections by convolving Voigt lineshapes onto the HITRAN line centres (Mitchell, 1971).

The expression for the Voigt lineshape is given by equation 60.

$$V(x) = \frac{fy}{\pi} \int_{-\infty}^{\infty} \frac{e^{-t^2}}{(x-t)^2 + y^2} dt \qquad 60$$

where

$$f = \frac{1}{\Delta_D} \qquad 61$$

$$y = \frac{\Delta_L}{\Delta_D} \sqrt{\ln 2} \qquad 62$$

$$x = \frac{\sigma - \sigma_o}{\Delta_D} \sqrt{\ln 2} \qquad 63$$

$$\Delta_L = H_{ref}\left(\frac{P}{101325}\right)\left(\frac{296}{T}\right)^{1/2} \quad (64)$$

$$\Delta_D = 2\sigma_o\sqrt{\frac{2kT\ln(2)}{mc^2}} \quad (65)$$

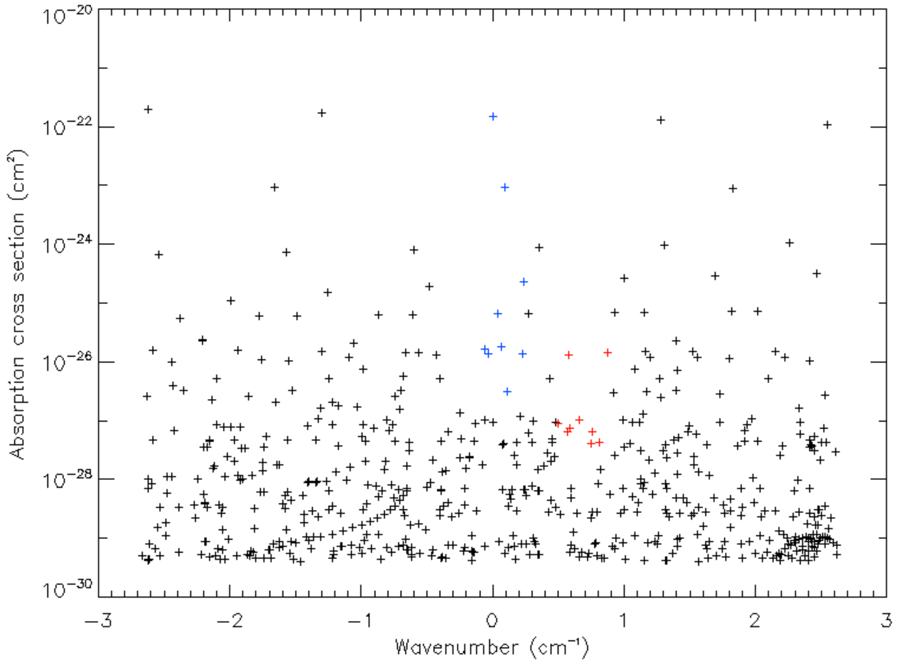

Figure 3.1.5-1 HITRAN 2008 spectral line strengths centred on 4875.749cm^{-1}. Blue and red crosses indicate the online and offline absorption lines simulated in the TCDS.

H_{ref} is the Lorentz spectral lines half width at half maximum for a reference temperature and pressure. For HITRAN and therefore the TCDS these are 101325 Pa and 296 K. σ is the wavenumber of the laser transmission, σ_o is the wavenumber of the spectral line centre, P is the atmospheric pressure and T is the atmospheric temperature and k is Boltzmann's constant, c is the speed of light and m is the mass of the absorbing particle.

The absorption lines at surface temperature and pressure are plotted in Figure 3.1.5-2 as a transmission spectrum. The data are generated using the TCDS absorption spectroscopy model.

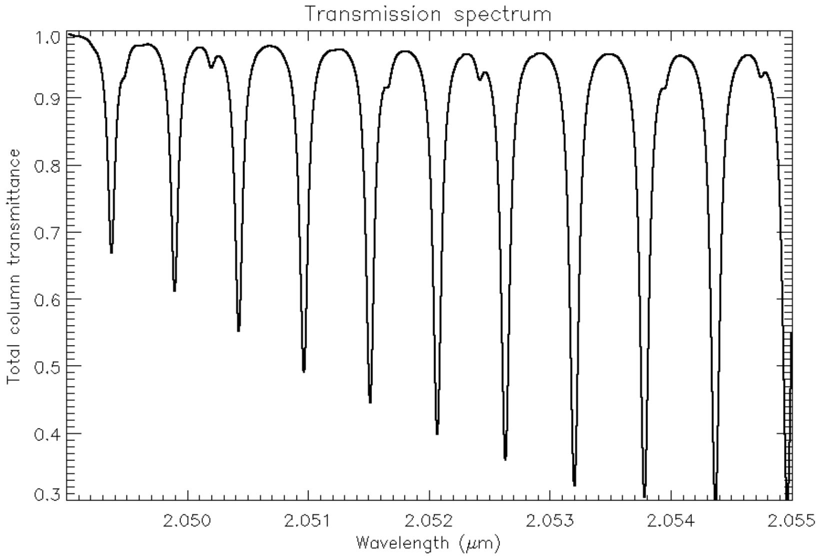

Figure 3.1.5-2 Transmission spectrum generated by the TCDS using HITRAN 2008 spectral lines for single nadir TC-DIAL sounding through 120 km of atmosphere

3.1.5.1 Validation of absorption model

The TCDS absorption algorithm has been partially validated by comparison of its simulated measurements with those from another LiDAR simulator presented in the FACTS report (Bruneau et al., 2006; Loth et al., 2005). To allow a fair comparison the TCDS instrument is configured identically to the specification of the FACTS simulated instrument.

Figure 3.1.5.1-1 presents the received intensities at the detector for the online and offline transmissions generated using the TCDS and the FACTS LiDAR simulator.

The relevant feature of Figure 3.1.5.1-1 is the separation between the online and offline received intensities. The intensity difference at the top and bottom of both plots is very similar indicating a good agreement between the two absorption models. The exact shape of the lines is expected to differ owing to the models using different atmospheric profiles (particularly aerosol).

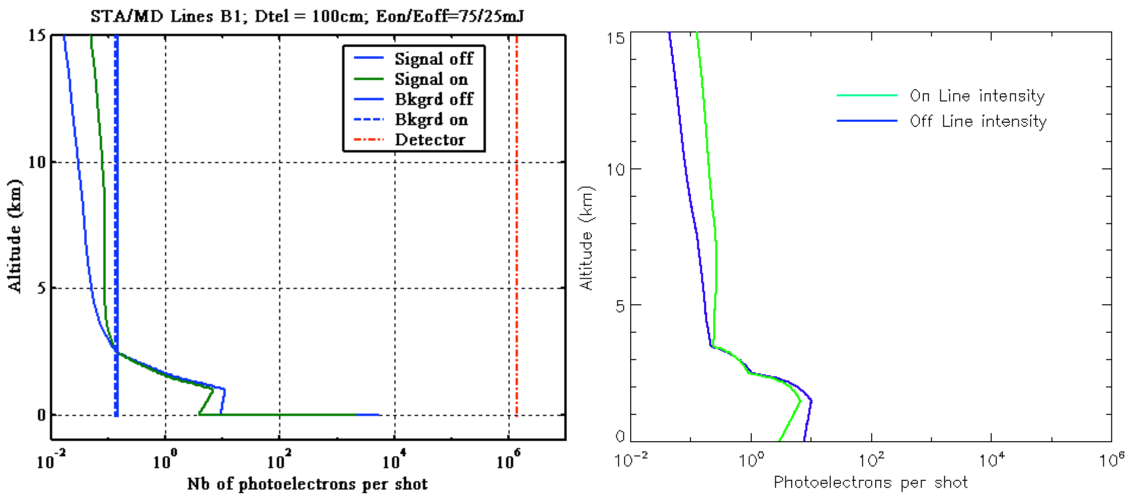

Figure 3.1.5.1-1 Comparison of received intensities generated using the FACTS LiDAR simulator (left) and the TCDS (right). (see text for details)

A further demonstration of the TCDS compatibility with the FACTS simulator is presented in Figure 3.1.5.1-2, which shows the optical depth as a function of altitude from a TCDS simulation next to the optical depth taken from a figure in the FACTS report using the same online frequency offset of -0.1cm^{-1}.

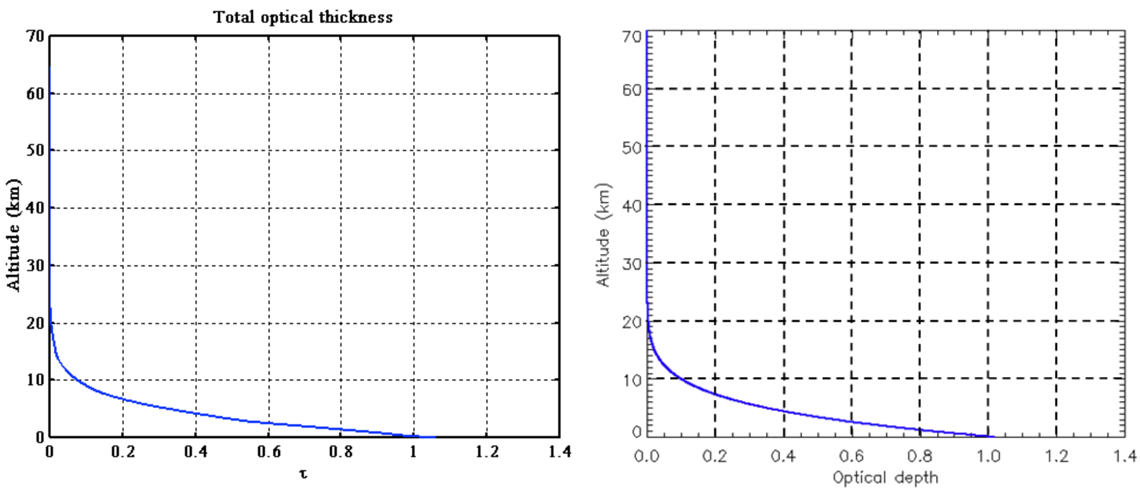

Figure 3.1.5.1-2 Comparison of atmospheric optical depths generated using the FACTS LiDAR simulator (left), and the TCDS (right). (see text for details)

The magnitude of the simulated optical depth is a direct consequence of the models absorption spectroscopy, therefore the agreement shown in Figure 3.1.5.1-2 provides confidence in the TCDS absorption spectroscopy algorithm if it is assumed that the FACTS simulator is correct.

3.1.6 Carbon dioxide retrieval

The retrieval of atmospheric CO_2 from simulated TC-DIAL soundings is calculated using equations 66 to 68 (Ehret et al., 2008; Loth et al. 2005; Bruneau et al. 2006).

$$N_{CO_2} = \frac{\Delta\tau}{\int_{Surf}^{Sat} \nu(l)dl} \tag{66}$$

$$\Delta\tau = \frac{1}{2}\ln\left(\frac{S_{off}E_{on}}{S_{on}E_{off}}\right) \tag{67}$$

$$\nu_p(i) = \left[\frac{N_{av}}{(m_a g)\left(1 + \frac{m_w}{m_a}\rho_w(i)\right)}\right]\left(\sigma_{on}(i) - \sigma_{off}(i)\right) \tag{68}$$

where N_{CO_2} is the CO_2 volume mixing ratio (VMR), $\Delta\tau$ is the total column differential optical depth, S_{on} and S_{off} are the received online and offline intensities, E_{on} and E_{off} are the transmitted online and offline intensities, k is the Boltzmanns constant, T is the atmospheric temperature, P is the atmospheric pressure, ρ_w is the atmospheric water vapour mixing ratio, σ_{on} and σ_{off} are the absorption cross sections for the online and offline pulses, l is the orbital altitude, i represents atmospheric pressure levels, m_a is the molar mass of dry air (0.029 kg), m_w is the molar mass of water vapour (0.018 kg), and N_{av} is Avogadro's number (6.022×10^{23} mol^{-1}). The weighting function ν_p is the pressure weighting function which is commonly used in DIAL studies owing to most atmospheric models using a vertical co-ordinate based on pressure. The pressure weighting function is used on the assumption that the atmosphere is hydrostatic, which over the length of a TC-

DIAL measurement (50 km) is true (Loth et al., 2005). The TCDS error studies use the pressure weighting function to maintain equivalence to other TC-DIAL studies.

The pressure, temperature and water vapour terms in the weighting functions (Equation 68) are vertically resolved profiles obtained from MIPAS reference atmospheres (Remedios et al., 2007). The absorption cross sections for the retrieval (σ_{on} and σ_{off}) are obtained from the TCDS absorption spectroscopy model.

The received intensities S_{on} and S_{off} provide the only information available to the TC-DIAL retrieval regarding the probed volume of atmosphere. Any modulation in the ratio of their intensities which does not arise from atmospheric CO_2 absorption creates errors in the total column differential optical depth. Uncertainties in the atmospheric state (i.e. temperature, pressure and water vapour) at the time of the measurement also result in a retrieval error as incorrect information is used to derive the CO_2 concentration.

The derivation of the retrieval error in the TCDS accommodates both of these error sources by subtracting the original CO_2 concentration from the retrieved CO_2 concentration (equation 69).

$$\left(\Delta N_{CO_2}\right)_{retrieved} = \left(N_{CO_2}\right)_{retrieved} - \left(N_{CO_2}\right)_{real} \qquad 69$$

where ΔN_{CO_2} is the retrieval error.

3.1.7 Detector noise

The TC-DIAL detection system introduces uncertainty to the CO_2 retrievals by adding background noise (dark current) to the received signals.

The detector noise for direct and heterodyne detection techniques are defined for atmospheric and surface signals using equations 70 to 76.

$$SNR_{DD} = \frac{1}{\sqrt{F}} \sqrt{\frac{\eta S}{1 + (\eta S/M) + (N_B/S)}} \tag{70}$$

$$SNR_{HD} = \frac{\sqrt{M}}{1 + (M/\gamma\eta S)} \tag{71}$$

$$M_{DDatm} = \left[1 + \frac{\pi A d\theta^2}{4\lambda^2}\right] \sqrt{1 + \left(\frac{2\delta R}{c\tau_C}\right)^2} \tag{72}$$

$$M_{HDatm} = \sqrt{1 + (2\delta R/c\tau_C)^2} \tag{73}$$

$$M_{DDsurf} = \left[1 + \frac{\pi A d\theta^2}{4\lambda^2}\right] \tag{74}$$

$$M_{HDsurf} = 1 \tag{75}$$

$$N_B = I_{sol} + \frac{1}{2F\eta}\left(\frac{\eta P_{NEP}}{h\upsilon}\right)^2 \delta t \tag{76}$$

where F is the excess noise factor, η is the quantum efficiency of the detector, S is the number of photons simulated to have been received by the detector, N_B is the number of background photons from both solar illumination and detector noise, γ is the heterodyne efficiency factor, A is the area of the receiver aperture, θ is the full angle divergence of the laser beam, δR is the length of the range gate in m, I_{sol} is the number of solar photons arriving on the detector, P_{NEP} is the detectors noise equivalent power, h is the Plank constant, υ is the transmission frequency, δt is the length of the range gate in s, and λ is the transmission wavelength (Bruneau et al., 2006; Loth et al., 2005).

The reciprocal of equations 70 and 71 provide one standard deviation relative errors for the offline and online received signals. These are used to define the detector noise either as a fixed quantity or to constrain a probability density function to form a random noise scenario.

For simulations where multiple retrievals are integrated the random noise mode is used to avoid a bias in the results. For individual simulations where consistency is required the fixed errors are used.

The noise is added to the received signal intensities using equations 77 and 78.

$$S_{off} = S_{off} \pm \frac{S_{off}}{SNR_{off}} \tag{77}$$

$$S_{on} = S_{on} \pm \frac{S_{on}}{SNR_{on}} \tag{78}$$

where S_{off} and S_{on} are the offline and online received signal intensities, and SNR_{off} and SNR_{on} are the signal to noise ratios calculated for either heterodyne or direct detection.

3.1.8 Transmission waveform

The shape of the laser pulse transmitted by a TC-DIAL instrument is approximated in the TCDS as a skewed normal distribution (equation 79).

$$f(x) = \frac{2\alpha}{2\pi b^2} e^{\left(\frac{(x-a)^2}{2b^2}\right)} \int_{-\infty}^{\alpha x} e^{\left(\frac{(\alpha x-a)^2}{2b^2}\right)} dx \tag{79}$$

where α is the skew parameter set as 3, a is the centre position of the Gaussian distribution and b is the standard deviation (Azzalini, 1985).

The waveform is generated at high resolution and then sampled to match the temporal resolution of the simulated instrument.

The received waveforms for detector sampling times of 100, 50 and 10 ns are presented in Figure 3.1.8-1.

For simulations where the temporal sampling is equal to or wider than the FWHM of the pulse, the TCDS is automatically configured to transmit a single intensity unit only. This simplification saves on the processing time required to generate and subsequently sample the transmission waveform.

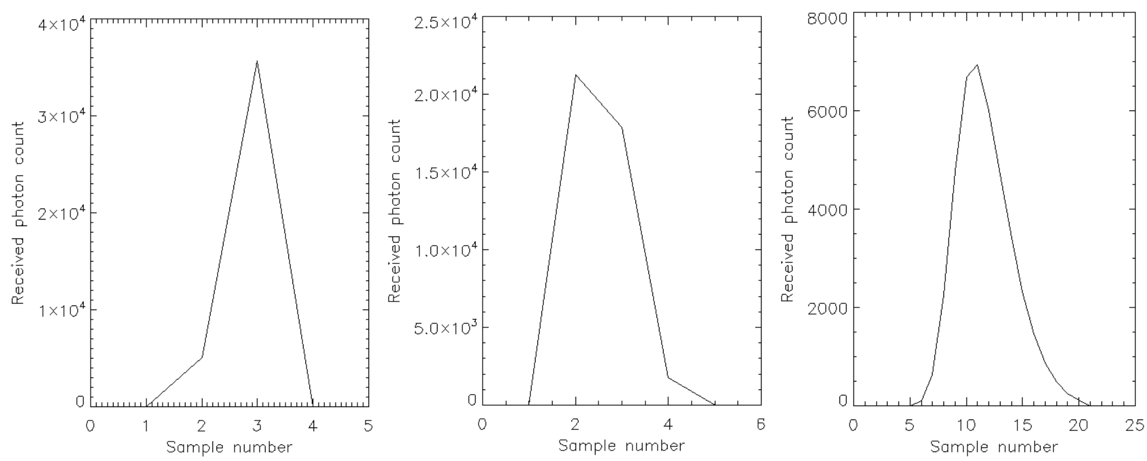

Figure 3.1.8-1 Received pulse waveforms for 3 temporal integration times of 100, 50 and 10 ns (from left to right), for a 100 ns FWHM simulated skewed laser transmission generated using the TCDS computer model, sample numbers refer to the model sample numbers and therefore each increment refers to a single temporal integration interval.

3.1.9 Cloud model

Approximately 70% of the Earth's surface is covered by cloud which acts as a scattering medium at the wavelength transmitted by a 2 µm TC-DIAL instrument (Wylie and Eloranta, 2007). Atmospheric scattering causes part of the laser energy to be removed from the detectors FOV. Such a reduction in the received signal intensity from the Earth's surface results in an increase in retrieval error.

In principle cloud scattering may be positively utilised in conjunction with surface scattering to form a vertically resolved retrieval if the conditions are correct. However a significant reduction in the signal received from the surface will occur and the merit of poor vertically resolved retrievals may be very limited.

To quantify the effect of cloud presence in the instruments FOV a cloud algorithm is written and incorporated into the TCDS.

The radiative properties of liquid water clouds in the TCDS are calculated by equations 80 to 82.

$$\frac{\beta_{ext}}{\mathrm{LWC}} = a_1 {r_e}^{b_1} + c_1 \tag{80}$$

$$1 - \omega = a_2 {r_e}^{b_2} + c_2 \tag{81}$$

$$g = a_3 {r_e}^{b_3} + c_3 \tag{82}$$

where β_{ext} is the extinction coefficient, LWC is the liquid water content of the cloud, ω is the single-scattering albedo, g is the asymmetry parameter and r_e is the radius of the water droplet. a, b, and c are wavelength dependant coefficients which are given in Table 3.1.9-1 for the 2 µm region (Hu and Stamnes, 1992).

	1	2	3
a	2150	0.004	-0.358
B	-1.150	0.688	-0.640
c	14.20	-0.004	0.925

Table 3.1.9-1 Water cloud coefficients for the 2 µm region

The directional interaction of electromagnetic energy with water cloud droplets may be mathematically described by Mie theory. As described in section 3.1.3.2 for aerosol scattering the TCDS uses a more computationally efficient approximation for the Mie scattering phase function known as the Henyey-Greenstein (H-G) approximation. For cloud modeling the same approach is taken and the H-G phase function is determined using equation 32.

Cloud scattering fraction profiles are generated using the same process described in section 3.1.3.3, and are added to the aerosol scattering fraction arrays for the up, down and loss directions. Figure 3.1.10-1 presents the scattering fraction profiles in the presence of optically thin cloud for each directional component used by the TCDS light propagation algorithm. The cloud layer is 1.6 km thick and starts at approximately 700 m altitude.

3.1.10 Solar illumination

During daylight hours solar illumination of the Earth's surface introduces background noise to received TC-DIAL signals. To determine the magnitude of the retrieval error incurred by the signal contamination, solar illumination is included in the TCDS.

The solar illumination of the Earth's surface is introduced to the daylight TC-DIAL measurements using 2 µm surface radiance data obtained from SCIATRAN. The intensity of the solar energy arriving on the TC-DIAL receiver is calculated using equation 83.

$$I_{sol} = 2\pi RABS_U \quad 83$$

where I_{sol} is the solar intensity received at the satellite detector, R is the solar radiance data obtained from SCIATRAN for a surface albedo of 1 in units of $\mathrm{s^{-1}\ nm^{-1}\ cm^{-2}\ sr^{-1}}$, A is the area of the laser footprint on the Earth's surface in cm^2, B is the bandwidth of the receiver filter in nm, and S_U is the unitless backscatter fraction profile which defines surface scattering toward the detector.

The calculated solar intensity scattered into the instruments FOV is added to the received laser intensity for all daylight measurements. The intensity difference is not initially accounted for in the retrieval and if uncorrected would lead to a slight bias in the measurement.

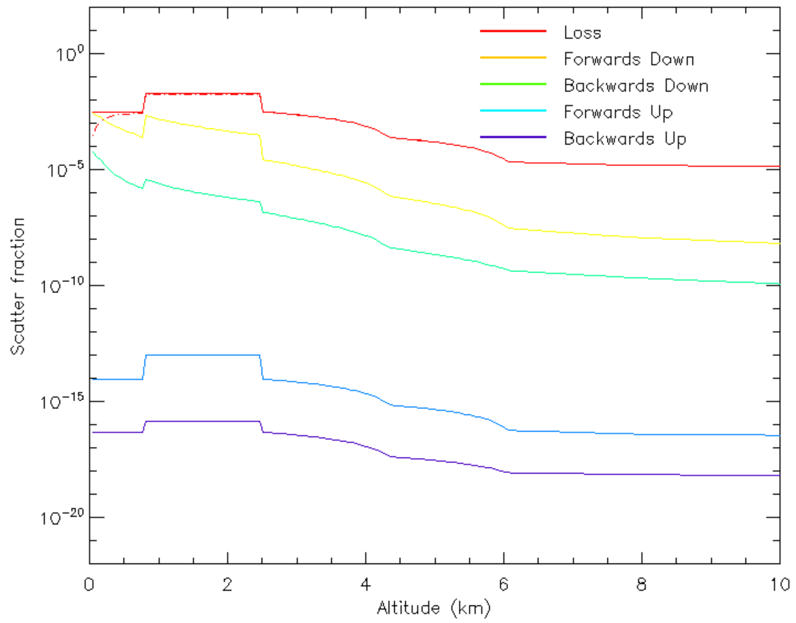

Figure 3.1.10-1 TCDS directional scattering components with standard aerosol profiles and optically thin cloud at 700 m to 2300 m altitude.

3.1.11 Orbit simulation

An orbit simulation is written and incorporated into the TCDS to realistically capture the variety of surface types encountered within an integrated series of TC-DIAL soundings.

The orbit simulation provides an approximation for the footprint locations on the Earth's surface for each laser transmission, taking account of orbital attitude and instrument pulse repetition frequency.

3.1.11.1 Orbit geometry derivation

The orbit simulator is written with the assumption that the TC-DIAL satellite follows a perfectly circular orbit about the Earth with no variation in altitude. This simplification is a suitable approximation for modeling a low earth orbiting (LEO) satellite and aids in reducing the complexity of the orbit simulator's geometry. Small deviations from a realistic orbit track are expected in the simulation owing to LEO satellites not following a perfectly circular orbit on account of the Earth being slightly non-spherical. Such small errors in the surface track are however unimportant for the purpose and application of the orbit simulator in the TCDS. The application of the simulator is to generate an approximation for TC-DIAL footprint separation and ground track orientation in order to obtain a realistic surface reflectance distribution as a function of time.

The orbit is first defined as a flat circle in the x-y plane consisting of individual satellite positions corresponding to laser emissions. Equations 84 and 85 define these positions in two dimensions as a function of angle θ.

$$x = (R_e + R_s)\sin(\theta_i) \qquad 84$$

$$y = (R_e + R_s)\cos(\theta_i) \qquad 85$$

$$\theta_i = \left(\frac{2\pi i}{T f_{prf}}\right) \quad 86$$

where R_e is the radius of the Earth, R_s is the satellite altitude above the surface of the Earth, θ_i is the angle of declination for a given transmission index i, T is the orbital period and f_{prf} is the instrument pulse repetition frequency.

The orbit is made three dimensional by tilting it out of the x-y plane using the orbital inclination angle φ (equations 87 to 93).

$$L = y^2 - 2y^2 \cos(\varphi) \quad 87$$

$$\omega = \frac{1}{2}(180 - \varphi) \quad 88$$

$$\delta y = L \cos(\alpha) \quad 89$$

$$Y = y + \delta y \ \text{ for } y \geq 0 \quad 90$$

$$Y = y - \delta y \ \text{ for } y < 0 \quad 91$$

$$z = L \sin(\alpha) \text{ for } 90^{\circ} > \alpha \geq 270^{\circ} \quad 92$$

$$z = -L \sin(\alpha) \text{ for } 270^{\circ} > \alpha \geq 90^{\circ} \quad 93$$

where z is the position of the satellite in the z axis and Y is the position of the satellite in the y axis following the orbit tilt.

Figure 3.1.11.1-1 displays the geometry used to define the terms in equation 87 to 93, and Figure 3.1.11.1-2 presents the x-y plane projections of the satellites orbital positions before and after the orbit tilt process.

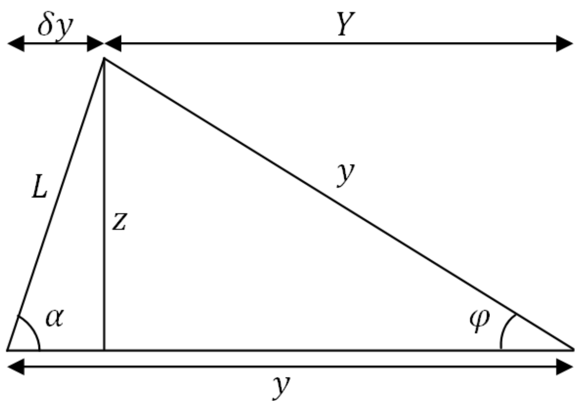

Figure 3.1.11.1-1 Geometry used to define orbit tilt out of the x-y plane

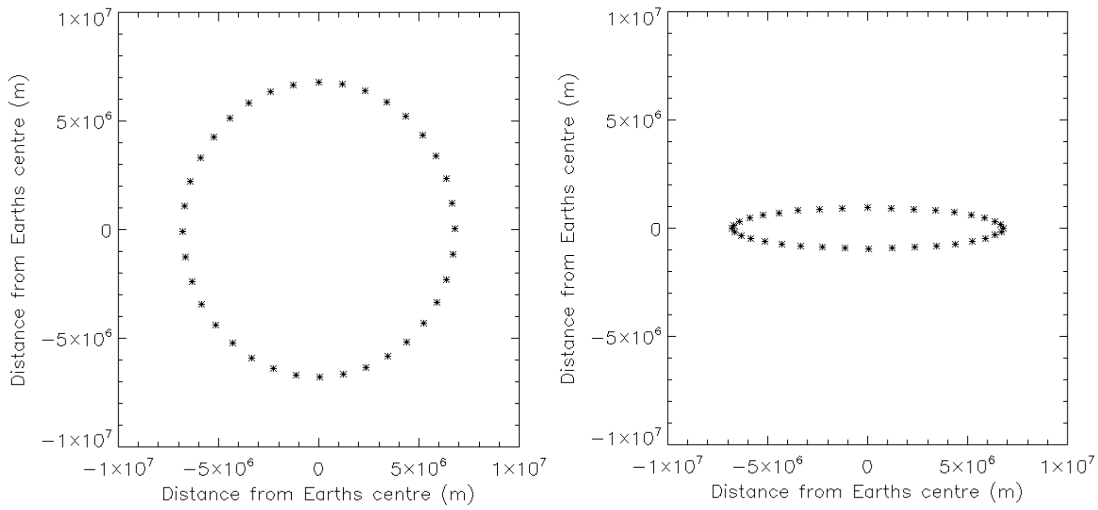

Figure 3.1.11.1-2 Satellite positions in the x-y plane for flat and tilted circles

The co-ordinate system is changed to introduce the Earth's rotation. This allows the use of longitude and latitude as definitions for the measurement locations (Equations 94 to 96).

$$r = \sqrt{x^2 + Y^2 + z^2} \tag{94}$$

$$\emptyset_{sp} = \cos^{-1}\left(\frac{Z}{r}\right) \tag{95}$$

$$\theta_{sp} = \tan^{-1}\left(\frac{Y}{x}\right) + \omega t \qquad (96)$$

where r is the distance from the centre of the Earth to the satellite, $\emptyset_{sp}$ is the zenith angle, θ_{sp} is the azimuth angle, ω is the angular velocity of the Earth's rotation and t is the time elapsed since the beginning of the simulation.

A three dimensional representation of the satellite position in space is given in Figure 3.1.11.1-3. The surface track produced by this orbit is shown in Figure 3.1.12-1.

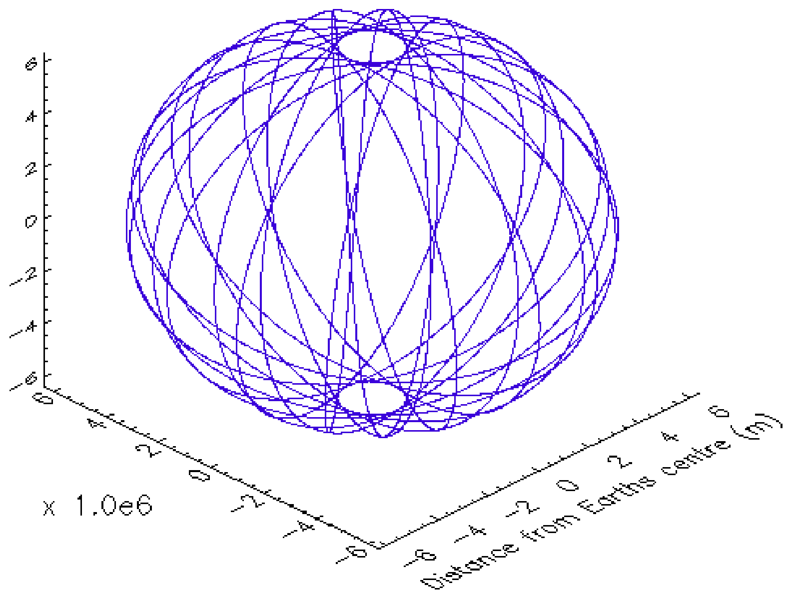

Figure 3.1.11.1-3 Satellite positions in three dimensional space using the centre of the Earth as a reference point for an 82 degree inclined low Earth orbit

3.1.12 Surface model

The Earth's surface is represented in the TCDS as a global map of surface reflectivity calculated using a hotspot modified bi-directional reflectance distribution function (BRDF). The function is parameterised using the 500 m resolution MODIS BRDF data product MCD43A1.5 (Strahler et al., 1999). The MCD43 product has been shown to have an RMS error of 0.0130 (equivalent to <5%) from continuous field measurements of surface albedo (Salomon et al., 2006).

The BRDF method provides the TCDS with realistic surface reflectivity at 2 µm for the viewing and illumination geometries of a spaceborne TC-DIAL system.

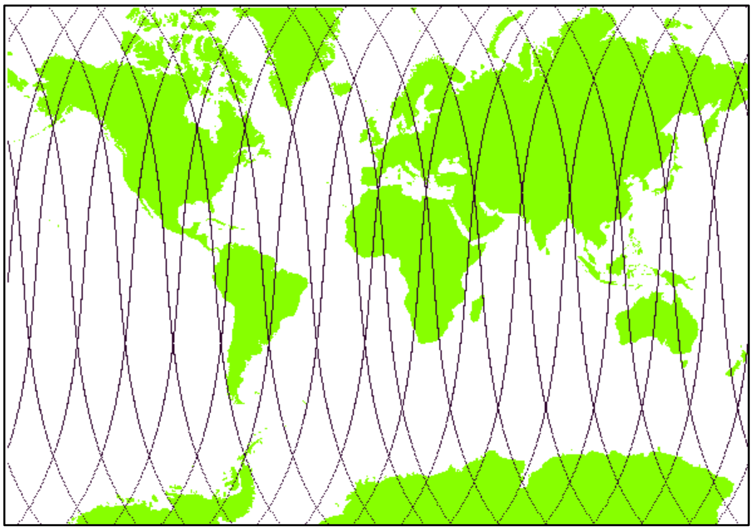

Figure 3.1.12-1 Measurement positions for a TC-DIAL system in an 82 degree inclined low Earth orbit

3.1.12.1 Ross-Li BRDF

The TCDS uses a particular form of BRDF known as the Ross-Li model which allows the use of MODIS parameterisation.

The Ross-Li model is defined as the sum of three parameters f_{iso}, f_{geo} and f_{vol} which combine to give the surface reflectivity R (Equation 97). f_{vol} and f_{geo} have associated kernels which provide the BRDF's directional components (Wanner et al., 1995).

$$R(\theta,\vartheta,\varphi,\Lambda) = f_{iso} + f_{vol}(\Lambda)K_{vol}(\theta,\vartheta,\varphi) + f_{geo}(\Lambda)K_{geo}(\theta,\vartheta,\varphi) \qquad 97$$

where K_{geo} and K_{vol} are the geometric and volumetric kernels.

The volumetric kernel (equation 98) is modified to account for the hotspot effect (Maignan et al., 2003) which occurs when the observation systems viewing geometry is the same as the illumination geometry. For a spaceborne nadir TC-DIAL system this effect occurs with every sounding as the transmitter and receiver are co-aligned.

$$K_{vol} = \frac{4}{3\pi}\left[\frac{1}{\cos\theta_s + \cos\theta_v}\right]\left[F_{hs}\left(\left(\frac{\pi}{2} - \varepsilon\right)\cos\varepsilon + \sin\varepsilon\right)\right] - \frac{1}{3} \qquad 98$$

where,

$$\cos\varepsilon = \cos\theta_s\cos\theta_v + \sin\theta_s\sin\theta_v\cos\varphi \qquad 99$$

$$F_{hs} = \left(1 + \frac{1}{1 + \varepsilon/0.03}\right) \qquad 100$$

θ_s is the illumination azimuth angle, θ_v is the viewing azimuth angle and φ is the illumination zenith angle.

The geometric kernel is given by equation 101.

$$K_{geo} = O(\theta,\vartheta,\varphi) - \sec\theta - \sec\vartheta + \frac{1}{2}(1 + \cos\varepsilon)\sec\theta\sec\vartheta \qquad 101$$

where

$$O = \frac{1}{\pi}(t - \sin t \cos t)(\sec\theta + \sec\vartheta) \tag{102}$$

$$\cos t = \frac{2\sqrt{D^2 + (\tan\theta \tan\vartheta \sin\varphi)^2}}{\sec\theta + \sec\vartheta} \tag{103}$$

$$D = \sqrt{\tan^2\theta + \tan^2\vartheta - 2\tan\theta \tan\vartheta \cos\varphi} \tag{104}$$

$$\cos\varepsilon = \cos\theta \cos\vartheta + \sin\theta \sin\vartheta \cos\varphi \tag{105}$$

3.1.12.2 Global surface reflectivity map

A global map of surface reflectivity is required by the TCDS to simulate the interaction of laser light with the Earth's surface over entire TC-DIAL LEO orbits. The MODIS data product MCD43A1.5 provides the required parameters to describe the reflectance properties of the entire Earth's surface at the desired wavelength. The data is obtained in granular format and combined into a single global data set of surface BRDF parameters using a TCDS auxiliary program. Multiple data sets are generated in this fashion and superimposed to remove cloudy data. The resultant cloud cleared BRDF map is re-projected onto a cylindrical grid from its native sinusoidal format to allow for faster grid referencing.

Equation 97 is applied to each MODIS data point to generate the surface reflectivity map used in the TCDS. Ocean scenes are an exception as they are not available within the 2 µm MODIS data product. For ocean scenes a value of 0.025 sr^{-1} is used as the mean reflectivity from POLDER data, and a random variability is added to it. The standard deviation of the variability (0.0016 sr^{-1}) is obtained from MODIS 1.6 µm data which includes ocean scenes. It is therefore assumed that the ocean variability at 2 µm is similar to the variability at 1.6 µm on a 500 m resolution scale.

Figure 3.1.12.3-1 and Figure 3.1.12.3-2 present 2 µm surface reflectance maps of Europe and South America generated by the TCDS.

3.1.12.3 Validation of surface reflectance

The TCDS surface model is partially validated by comparison of the surface reflectivity values it produces with those obtained from the POLDER instrument as presented in the FACTS report (Loth et al., 2005).

The POLDER instrument is a spaceborne wide field of view imaging radiometer which provides global measurements of spectral and directional scattering characteristics of the Earth's surface. The POLDER data products are validated against in-situ surface reflectivity campaigns (Lacaze, 2005).

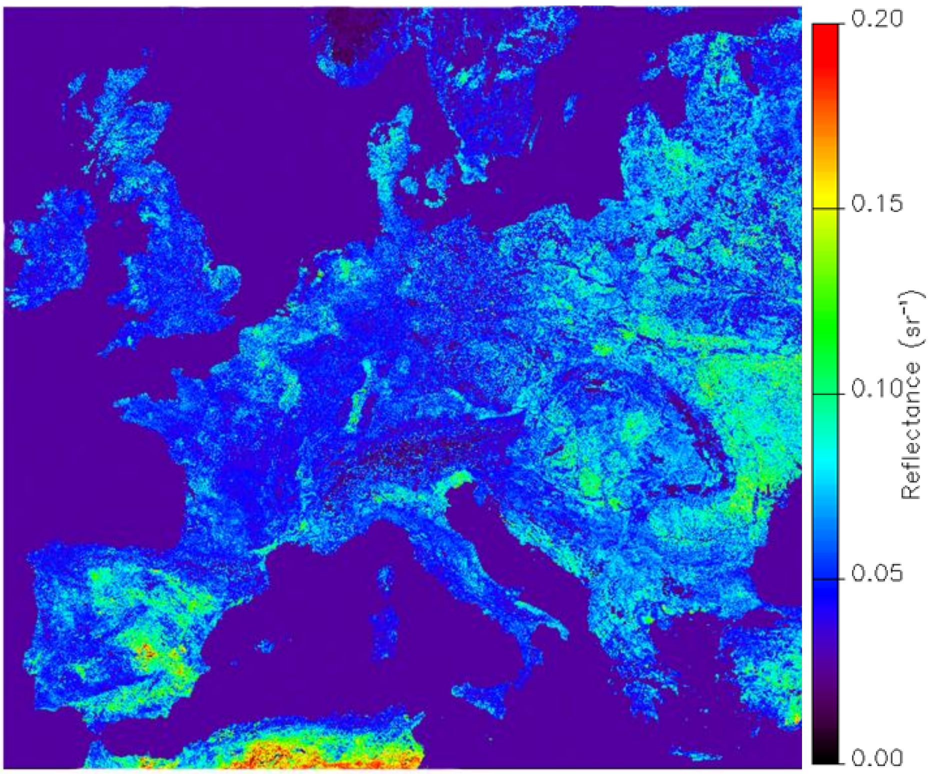

Figure 3.1.12.3-1 500 m resolution surface reflectivity map of Europe for a 2 µm nadir TC-DIAL system, data from MODIS, produced using TCDS algorithm

The TCDS data are separated into geographic regions of vegetation, desert and snow, and the mean reflectance within each region are calculated and compared to the POLDER equivalents obtained from the FACTS report. Table 3.1.12.3-1 presents the results of the comparison.

Region	POLDER	TCDS
Vegetation	0.03	0.027
Desert	0.22	0.224
Snow	0.015	0.017

Table 3.1.12.3-1 Polder and TCDS surface reflectivity comparison

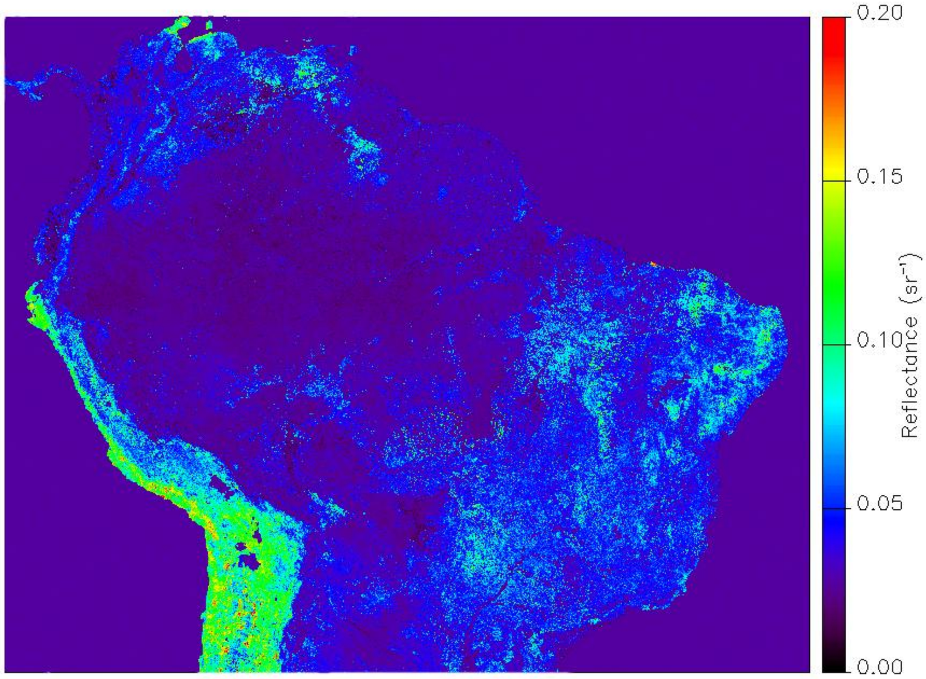

Figure 3.1.12.3-2 500 m resolution surface reflectivity map of South America for a 2 µm nadir TC-DIAL system, data from MODIS, produced using the TCDS

3.1.13 Tree canopy

Tree canopies scatter TC-DIAL signals prior to their contact with the Earth's surface leading to a reduction in the intensity of the returning waveform via two principal mechanisms. Firstly the canopy removes part of the pulse energy from the instrument FOV by sideways scattering, and secondly the waveform energy distribution is extended in time beyond the range of the temporal integration interval of the TC-DIAL instrument. The loss of received signal from both mechanisms leads to an increase in retrieval error.

The returning waveform is distributed across the full height of the scattering tree and therefore contains information on the tree canopy's height and thickness. If the instruments temporal sampling is sufficiently fast to capture this information then the TC-DIAL system has the potential to measure biomass as well as atmospheric CO_2.

To perform an assessment on the effect of tree canopies on TC-DIAL retrievals a vertically resolved tree canopy profile is included in the TCDS.

The data for the tree canopy is obtained from the University College London (UCL) in the form of vertically resolved scattering fractions (Disney et al., 2010). The tree canopy profile is sampled to match the sampling used by the TCDS simulation in order to correctly interface with the TCDS scattering model.

Figure 3.1.14-1 shows the UCL broadleaf tree canopy data used by the TCDS.

3.1.14 Pre-processing algorithm

For performing large and complicated simulations, data may be pre-processed in preparation to significantly reduce the processing load required by the computer model. For the TCDS which has a very large number of potential configurations, generating specific data sets prior to each simulation is an impractical process. Instead, the TCDS incorporates a novel pre-processing algorithm which searches a binary coded database of previously run model configurations and reads in the associated data only if the exact same configuration has been run before. If there are no previously generated data then the simulations physical models are applied and the data is added to the database at the end.

The pre-processing algorithm is particularly beneficial for batch and contour simulations in which some model components remain unchanged whilst others vary. The algorithm has the capability to select and read in data only for those components that are non variable within the simulation.

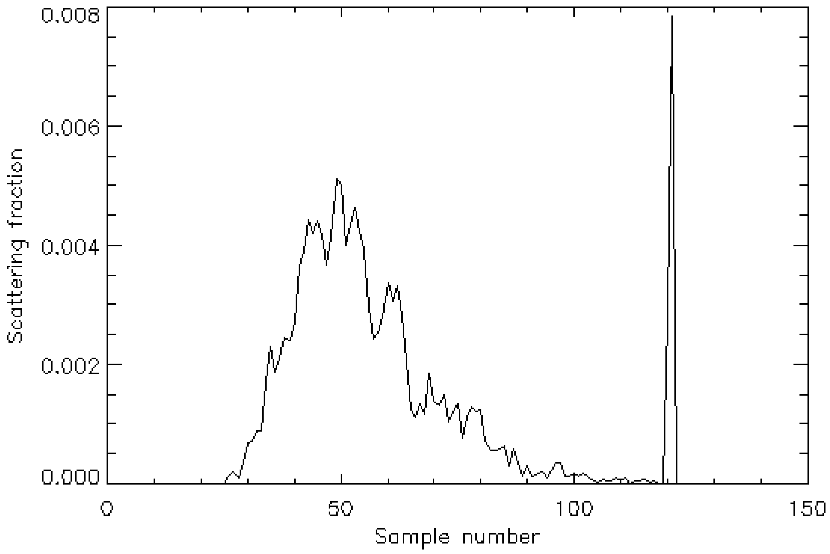

Figure 3.1.14-1 UCL broadleaf tree canopy scattering fraction data used by the TCDS. The surface feature can be easily discriminated from the canopy feature when using very small spatial samples

3.2 Atmospheric profile interpolation

The TCDS requires the vertical resolution of the atmospheric profiles to match the temporal sampling of the TC-DIAL instrument being simulated. This requirement is inherent in the model design which ensures maximum efficiency by running the model at the resolution of the simulated instrument. Real TC-DIAL systems generally require their temporal sampling to be finer than the native resolution (1 km) of the TCDS atmospheric profiles. The TCDS profiles are therefore interpolated to achieve the desired resolution.

The interpolation algorithm used by the TCDS is a modified linear interpolation routine that provides a faithful reproduction of the shape and content of the original profile. Alternatives such as quadratic and polynomial interpolation were found to be unsuitable owing to their incompatibility with the profile shapes leading to spectroscopic artifacts in the simulation results.

3.2.1 Linear interpolation

Linear interpolation links together adjacent points in a data series by straight lines. If the linearly interpolated profile contains nonlinearities then errors are introduced in the interpolated profile. The atmospheric profiles in the TCDS are all nonlinear and therefore require the use of a special form of linear interpolation to minimise these errors.

The nonlinearity errors introduced through the use of normal linear interpolation on the TCDS atmospheric profiles are well within their natural variability and therefore may be ignored for single simulations, however during comparisons of instrument configurations in which the instrument sampling changes, any unwanted variation in atmospheric composition leads to unexpected errors in the results.

Figure 3.2.1-1 provides an example of the over estimation introduced by linear interpolation of a nonlinear function. The red filled area shows the over estimation and the green filled area shows the under estimation. As the red is larger than the green the interpolation of the centre data point is over estimating its true value.

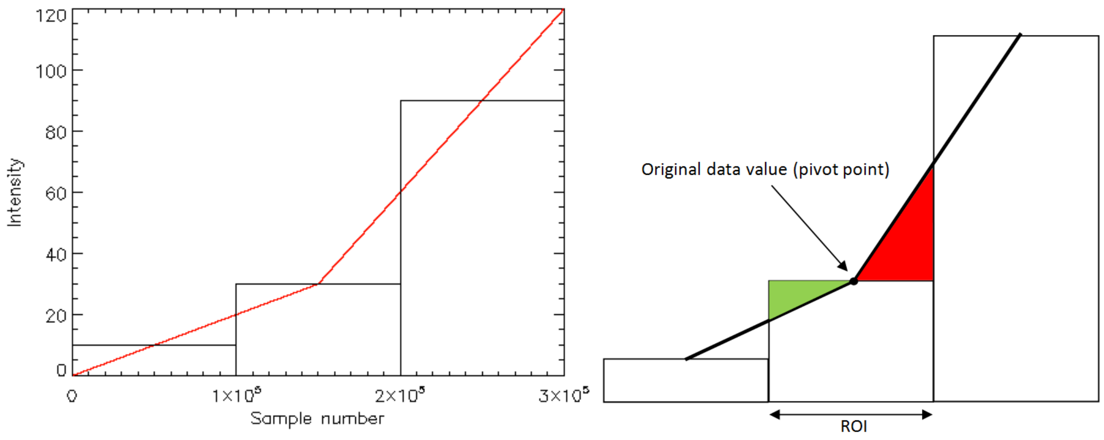

Figure 3.2.1-1 Non-linearity of an atmospheric profile (left), and the driving mechanism for the non-linearity error (right)

3.2.2 Correction algorithm

The interpolation correction algorithm calculates the extent of the misrepresentation within the region of influence (ROI) displayed in Figure 3.2.2-1 and compensates by altering the magnitude of the centre point (pivot point).

The expressions used to correct for the misrepresentation created by the linear interpolation are given by equations 106 to 109.

$$\mathrm{O}_1 = \frac{1}{4}\left(\frac{A_2 - A_1}{2}\right) \quad 106$$

$$\mathrm{O}_2 = \frac{1}{4}\left(\frac{A_1 - A_0}{2}\right) \quad 107$$

$$\mathrm{D} = (\mathrm{O}_2 - \mathrm{O}_1) \quad 108$$

$$\mathrm{A}_2^{new} = \mathrm{A}_2^{old} \pm \mathrm{D} \quad 109$$

where O_1 and O_2 are the areas of the green and red triangles in Figure 3.2.1-1. A_0 , A_1 and A_2 are the values of the original profile, with A_1 being the centre column and A_0 and A_2 being the data points on either side. Figure 3.2.2-1 defines the terms used for equations 106 to 109.

The expressions which form the corrective algorithm given as equations 106 to 109 are applied within an iterative loop to correct all data points in the profile.

The interpolated profiles are heavily over sampled to accommodate all possible resolutions and to reduce sampling errors in the corrective process. The profiles are later sampled to attain the temporal resolution of the simulated instrument.

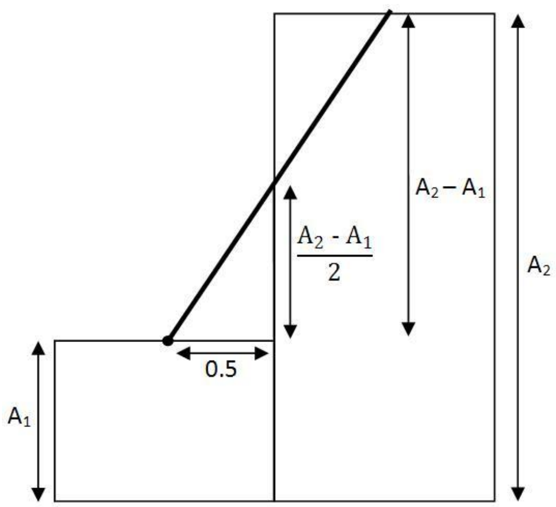

Figure 3.2.2-1 Diagram showing terms used in the interpolation correction algorithm

The effect of applying equations 106 to 109 is shown on the left of Figure 3.2.2-2. The interpolated line is reduced so that it correctly represents the original value over its region of influence.

The error distributions for the normal and corrected linear interpolations are presented on the right panel of Figure 3.2.2-2.

The sampling errors in the corrected profiles reduce as greater numbers of samples are used which is a convenient result as the profiles are required to be over interpolated so that they are ready for sampling later in the TCDS. The error improvement achieved by using the corrective algorithm is from approximately $0.1\ \%$ to less than $10^{-4}\ \%$.

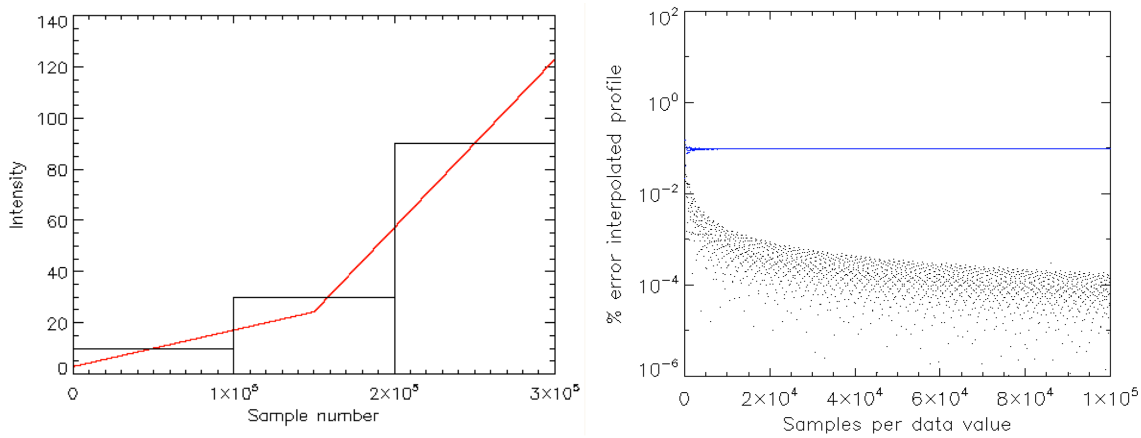

Figure 3.2.2-2 Interpolated line following the application of the corrective procedure (left), and the error distribution for normal linear interpolation (blue) and corrected interpolation (black) as a function of sample numbers.

3.3 Monte Carlo scattering model

The TCDS light propagation algorithm is a two dimensional (2D) simulation of photon propagation through the Earth's atmosphere. The 2D nature of the simulation requires the TCDS to use a simplified scattering system limited to only calculating atmospheric scattering events inside the detectors FOV. Any photons that are scattered outside detectors FOV are considered lost without any possibility of returning. This lack of consideration for the scattering activity outside the detectors FOV renders the TCDS scattering model inaccurate in conditions where the atmospheric optical depth is sufficiently high for there to be a reasonable probability of secondary scattering occurring within the temporal integration time of the TC-DIAL instrument. Furthermore, under multiple scattering conditions the average scattering phase function becomes less pronounced in the forward direction and more homogenous, rendering the phase function used in the TCDS inaccurate in conditions where there is a high probability of multiple scattering occurring within a single atmospheric level.

To accommodate multiple scattering in three dimensions whilst maintaining the efficiency of the simulation, a look up table is derived containing correction factors for both the forward and backward scattering components. The factors are derived for a range of optical depths and scattering angles using a novel Monte Carlo simulation.

3.3.1 Monte Carlo algorithm

To provide statistics on three dimensional scattering for TC-DIAL viewing geometry a Monte Carlo model for tracing the progress of individual photons in the presence of a scattering medium has been developed.

The TCDS Monte Carlo algorithm operates by simulating the propagation of photons in discrete spatial steps through three dimensional (3D) space. At particular moments in time determined by the magnitude of the scattering coefficient, a propagating photon is scattered away from its incident vector at an angle defined by a probability density function. The process of move and scatter continues until the photon has left a finite region of space and its final position and displacement vector are recorded. When enough photons are simulated the statistics of the scattering events are analysed and correction factors for the TCDS scattering model are derived.

Under standard atmospheric conditions with a normal level of aerosol and no cloud cover the Earths atmospheric optical depth for 2 μm electromagnetic radiation is too low for multiple scattering to occur within a single atmospheric level (vertical sampling of a typical TC-DIAL instrument). Correction factors derived under such conditions will always have a value of 1 leaving the TCDS scattering model unaltered. Only under significant scattering conditions such as cloud and dense aerosol are the derived correction factors likely to be of relevance. As such the Monte Carlo scattering algorithm is restricted to simulating only particulate matter and cloud (using the H-G phase function, see Section 3.1.3.2).

3.3.1.1 Scattering distance and propagation

The probability of a scattering event occurring in a single propagation step within a region of aerosol or cloud in the Monte Carlo simulation is given by equation 110.

$$P = 1 - (\omega l_m \beta_{ext})^{1/S} \qquad 110$$

where P is the scattering probability for an individual atmospheric propagation step, l_m is the length the TCDS atmospheric level in m, ω is the single scattering albedo, β_{ext} is the extinction coefficient in m^{-1} and S is the number of step intervals simulated in the Monte Carlo algorithm for a single TCDS atmospheric level. The single scattering albedo and extinction coefficient values are obtained directly from the cloud and aerosol components of the TCDS to help retain equivalence between the TCDS and Monte Carlo models for comparison and validation purposes.

The step intervals in the Monte Carlo model are calculated parallel to the incident vector allowing them to be dynamic in their direction of travel. The spatial flexibility introduced helps reduce the possibility of sampling artifacts manifesting in the results. Typically, the step intervals are set to 0.25 m in length when the TCDS is operating at 15 m resolution as a suitable compromise between realism and computational efficiency.

For each spatial step travelled a linear random number generator is applied in conjunction with the scattering probability P to determine if scattering will occur. If it does then its position is noted and a further simulation is run to determine the distance the photon will subsequently travel before it reaches another scattering event. Once these two distances are recorded the directional scattering algorithm is enabled (Section 3.3.1.4). If the photon manages to reach the end of the atmospheric level with or without scattering it is removed from the system and the model is reset ready for another photon to begin.

3.3.1.2 Henyey-Greenstein (H-G) probability density function

The scattering angle subtended from the incident vector for each scattering event is determined using a probability density function (PDF) derived from the H-G phase function. The PDF is generated by an iterative binning process in which the 2D TCDS phase function in units of sr^{-1} (see Section 3.1.3.2) is binned into a phase function in units of degrees. The result is a 2D PDF representing a 3D phase function (Figure 3.3.1.2-1).

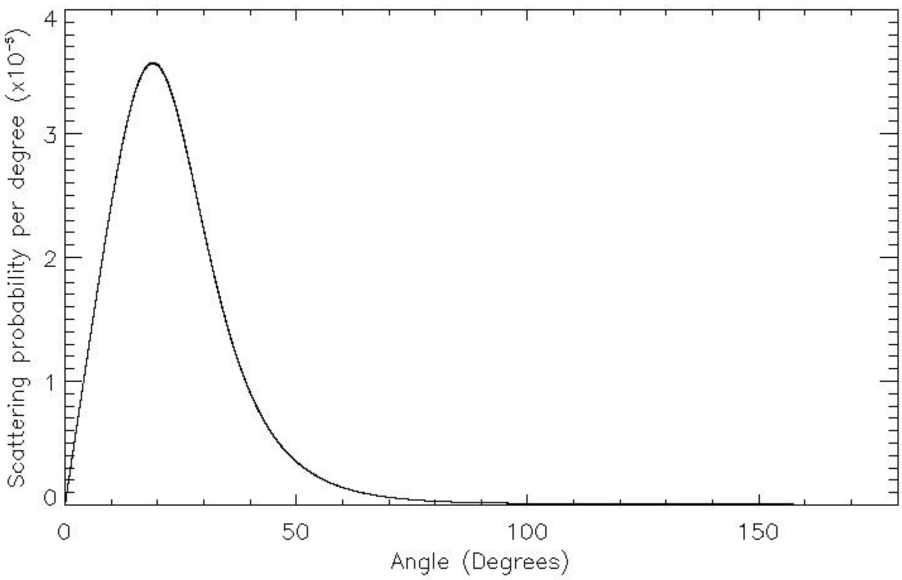

Figure 3.3.1.2-1 2D representation of a 3D H-G PDF generated by the TCDS Monte Carlo algorithm

The shape of the profile presented in Figure 3.3.1.2-1 appears contradictory to the original H-G phase function as its peak amplitude is not in the forward direction. This unexpected appearance is explained by considering the spatial distribution of the H-G phase function in three dimensions. Near the phase functions peak in 3D the available surface area per degree is very small and as such the spatial density of scattering directions is relatively high. Around the sides of the phase function however the available surface area per degree becomes significantly larger and the spatial density drops (see Figure 3.3.1.2-2). The 2D phase function in Figure 3.3.1.2-1 accommodates this automatically through the binning process. When plotted in 3D using the Monte Carlo algorithm, the resulting distribution correctly represents the original TCDS phase function with the expected forward dominant peak (Figure 3.3.1.4-8).

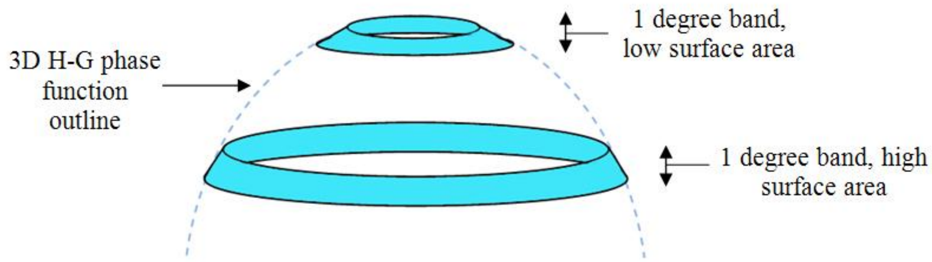

Figure 3.3.1.2-2 Two 1 degree bands of a 3D H-G phase function at different scattering angles demonstrating the surface area difference responsible for the shape of the 2D H-G PDF

3.3.1.3 Random angle generator algorithm

The scattering events in the Monte Carlo simulation are required to be random, mutually exclusive, and appropriately weighted to correctly represent the H-G PDF. The Monte Carlo algorithm meets these requirements by generating a random distribution of scattering angles using a random angle generator (RAG) algorithm. The RAG algorithm produces random numbers using a linear random number generator seeded by the computer server's system clock to ensure exclusivity. The distribution is then weighted using an array known as the *collection* array, which contains values corresponding to the scattering angles. The more likely scattering angles (determined by the H-G PDF) occupy more of the available space within the collection array and therefore present a larger target area (higher probability) to a generated random number (Figure 3.3.1.3-1). The resultant distribution of angles produced by the RAG algorithm is correctly weighted by the H-G PDF as presented in Figure 3.3.1.3-2.

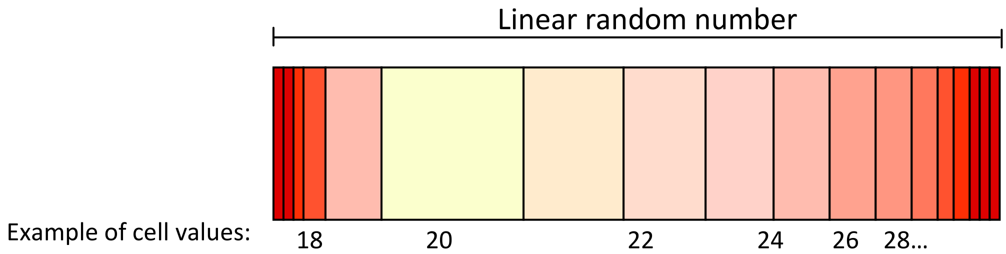

Figure 3.3.1.3-1 Collection array weighted by the H-G PDF. The width of the cells provide the weighting

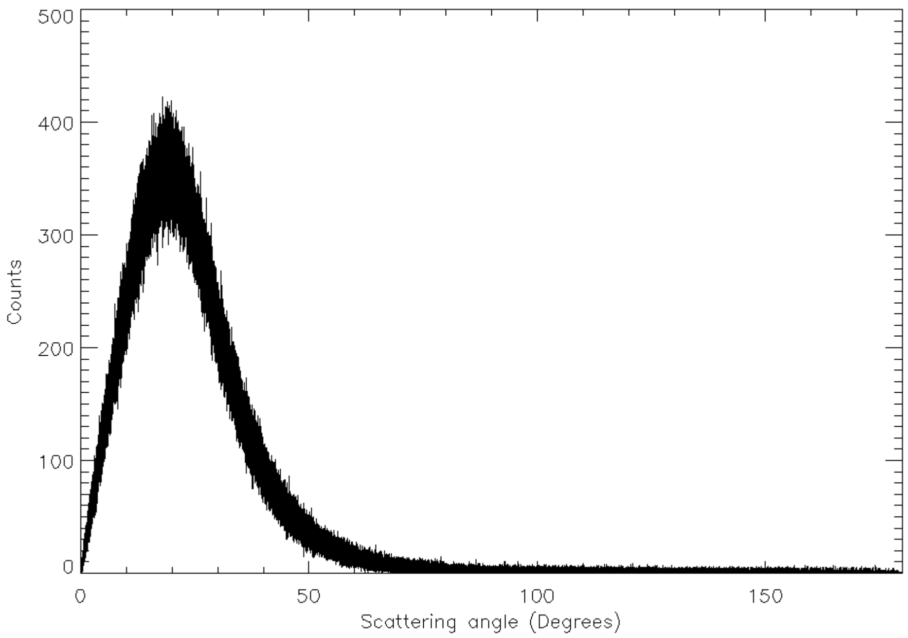

Figure 3.3.1.3-2 Histogram of 10,000,000 angles generated using the RAG algorithm

3.3.1.4 Directional scattering algorithm

The 3D Monte Carlo scattering algorithm separates the scattering vector into two angular components. The vertical component θ is based on the H-G PDF and is randomly derived for each scattering interval. The horizontal component φ forms a ring about the incident vector with equal probability in all directions owing to the phase functions axial symmetry (Figure 3.3.1.4-1).

The positions of the scattered photons are defined and recorded in a fixed reference frame where the x-y plane is parallel to the Earth's surface. A dynamic reference frame is also used when calculating the new travel vector following a scattering event which is defined by the z axis being parallel to the previous travel vector (vector prior to scattering).

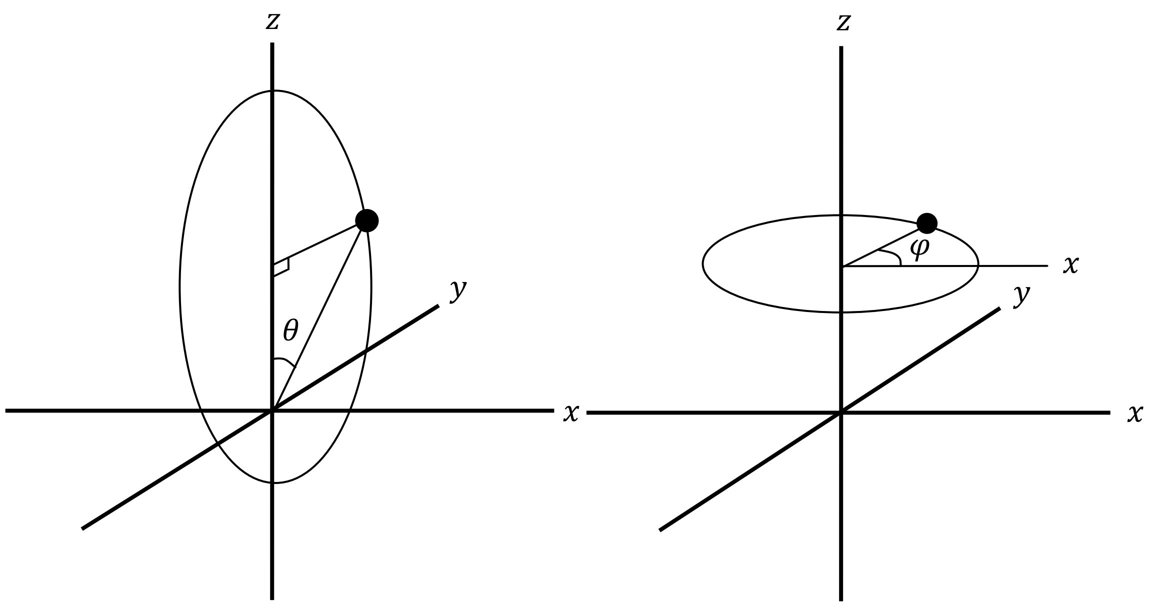

Figure 3.3.1.4-1 Definition of the scattering components used in TCDS Monte Carlo algorithm presented in a fixed reference frame. Black dot indicates the position of a scattered photon

In Cartesian co-ordinates the position of a scattered photon along its original travel vector is defined in the fixed reference frame by equations 111 to 115.

$$x_0 = L\cos\varphi_0 \qquad 111$$

$$y_0 = L\sin\varphi_0 \qquad 112$$

$$z_0 = D_2\cos\theta_0 \qquad 113$$

$$D_2 = D_1\cos\theta_1 \qquad 114$$

$$L = D_2\sin\theta_0 \qquad 115$$

where x_0, y_0 and z_0 are the Cartesian positions of a scattered photon along its original direction of travel (as if it hadn't scattered), and forms the end point of the D_2 vector. θ_1 is the angle subtended from the previous travel vector to the new travel vector in the dynamic reference frame and is determined by the RAG algorithm. θ_0 is the angle subtended from the z axis to the original travel vector in the fixed reference frame and is derived from the previous scattering event. φ_0 is the horizontal angle subtended from the x axis to the original travel vector in the dynamic reference frame and is also obtained from the previous scattering event. D_1 is the distance the photon has travelled along its new travel vector and is calculated by the distance scattering algorithm (see Section 3.3.1.1), and D_2 is the equivalent distance the photon has travelled along its original travel vector. Figure 3.3.1.4-2 diagrammatically defines the terms used to calculate D_2 in the dynamic reference frame and x_0, y_0 and z_0 in the fixed reference frame.

The length D_2 defines the distance the photon has travelled along its original vector as if it hadn't scattered. Its direction forms the axis of symmetry for the H-G phase function. At the end of D_2 (x_0, y_0, z_0) a line may drawn perpendicular to the D_2 vector to form the radius of the H-G phase function for a scattering event at that position (see Figure 3.3.1.4-3).

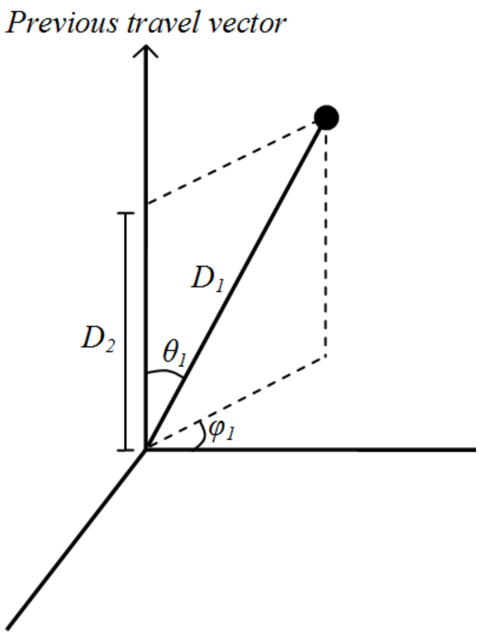

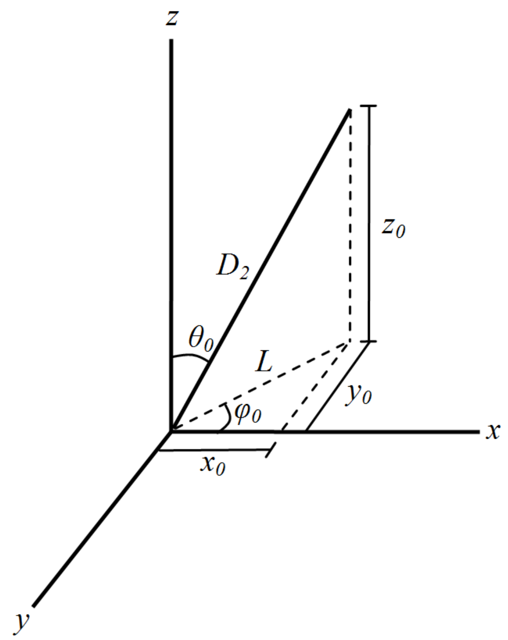

Figure 3.3.1.4-2 Left - Dynamic reference frame scattering geometry, black dot indicates final position of the photon following a scattering event. Right - Fixed reference frame scattering geometry

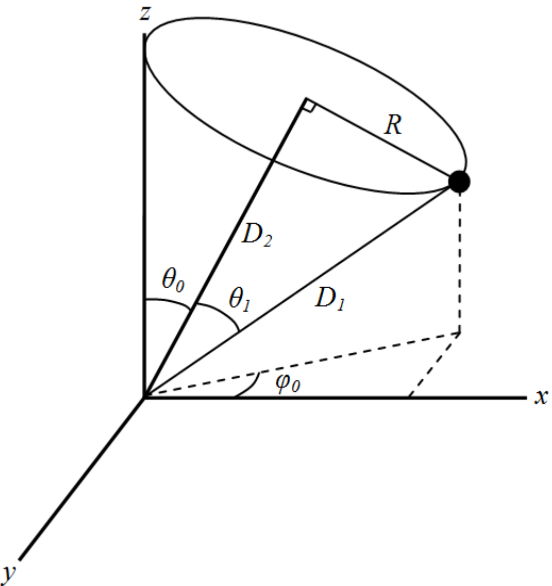

Figure 3.3.1.4-3 Fixed reference frame scattering geometry showing a ring of the H-G phase function, black dot indicates final position of a photon. The axis origin is defined as the position of the last scattering event.

The circle radius in Figure 3.3.1.4-3 is calculated by equation 116.

$$R = \sqrt{D_1^{\ 2} - D_2^{\ 2}} \qquad 116$$

D_1 is determined by the distance scattering function (see Section 3.3.1.1) and D_2 is calculated from D_1 using equation 114.

To determine the position of the scattered photon the circle about the end of the D_2 vector must first be defined. For mathematical convenience the circle is initially defined in the x-y plane using Cartesian co-ordinates (equations 117 and 118).

$$x_c = R \sin \theta_c \qquad 117$$

$$y = R \cos \theta_c \qquad 118$$

where x_c and y define the position of the circle in the x-y plane, and θ_c is the angle from the x axis in the x-y plane. θ_c is random between 0 and 2π owing to the H-G phase functions symmetry creating an equal probability of scattering occurring in all directions.

The circle is tilted out of the x-y plane using the same principle employed by the orbit simulator algorithm (see Section 0). The extent of the tilt is defined by the angle θ_1 (see Figure 3.3.1.4-4).

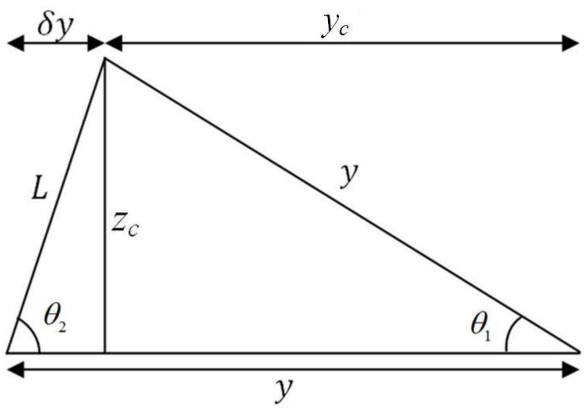

Figure 3.3.1.4-4 Circle tilt geometry used to tilt the H-G phase function ring out of the x-y plane

Equations 119 to 125 are used to determine the y_c and z_c values within the tilted circle. The y_c and z_c values are relative to the centre of the circle (axis origin) and therefore have no knowledge of their position with respect to the tip of the D_2 vector.

$$L = y^2 - 2y^2 \cos(\theta_1) \quad 119$$

$$\omega = \frac{1}{2}(180 - \theta_1) \quad 120$$

$$\delta y = L\cos(\theta_2) \quad 121$$

$$y_c = y + \delta y \ \text{ for } y \geq 0 \quad 122$$

$$y_c = y - \delta y \ \text{ for } y < 0 \quad 123$$

$$z_c = L\sin(\theta_2) \text{ for } 90^{\circ} > \alpha \geq 270^{\circ} \quad 124$$

$$z_c = -L\sin(\theta_2) \text{ for } 270^\circ > \alpha \geq 90^\circ \quad (125)$$

The previous calculations assume the tilt occurs using the x axis as a pivot. The final stage of the scattering algorithm rotates the tilted circle about the z axis so that it has the correct orientation to intersect the D_2 vector in the fixed reference frame (as in Figure 3.3.1.4-3). Equations 126 to 130 calculate the final x_1, y_1 and z_1 co-ordinates for the photon position by first rotating the circle through an angle φ_1, and then adding the resultant position to the end of the D_2 vector (x_0, y_0, z_0).

$$x_1 = r\cos\varphi_1 + x_0 \quad (126)$$

$$y_1 = r\sin\varphi_1 + y_0 \quad (127)$$

$$z_1 = z_c + z_0 \quad (128)$$

$$r = \sqrt{x_c^{\,2} + Y^2} \quad (129)$$

$$\varphi_1 = \tan^{-1}\left(\frac{x_c}{Y}\right) \quad (130)$$

where x_1, y_1 and z_1 are the final positions of the photon following the scattering event and form the starting position for the next scattering event (if the photon remains within the boundaries of the atmospheric cell).

The Monte Carlo algorithm requires the redefinition of φ_0 and θ_0 for the initial geometry of the next scattering process.

The new travel vector in the fixed reference frame is defined by the difference between the new photon position following scattering and the old photon position prior to scattering (equations 131 to 133). For the first scattering event the previous photon position is always the origin (0,0,0), for all other scattering events it is defined as (x_p , y_p , z_p).

$$x_{diff} = x_1 - x_p \tag{131}$$

$$y_{diff} = y_1 - y_p \tag{132}$$

$$z_{diff} = z_1 - z_p \tag{133}$$

where x_{diff} , y_{diff} and z_{diff} are the distances in Cartesian co-ordinates which form the resultant travel vector. From these values the required φ_0 and θ_0 terms are derived (equations 134 to 139).

$$\theta_0 = \cos^{-1}\left(\frac{z_{diff}}{h}\right) \tag{134}$$

$$\varphi_0 = \tan^{-1}\left(\frac{x_{diff}}{y_{diff}}\right) \text{ for } x_{diff} > 0 \text{ and } y_{diff} > 0 \tag{135}$$

$$\varphi_0 = \tan^{-1}\left(\frac{y_{diff}}{x_{diff}}\right) + \frac{\pi}{2} \text{ for } x_{diff} > 0 \text{ and } y_{diff} < 0 \tag{136}$$

$$\varphi_0 = \tan^{-1}\left(\frac{x_{diff}}{y_{diff}}\right) + \pi \text{ for } x_{diff} < 0 \text{ and } y_{diff} < 0 \qquad 137$$

$$\varphi_0 = \tan^{-1}\left(\frac{y_{diff}}{x_{diff}}\right) + \frac{3\pi}{2} \text{ for } x_{diff} < 0 \text{ and } y_{diff} > 0 \qquad 138$$

$$h = D_1 = \sqrt{x_{diff}^{\ 2} + y_{diff}^{\ 2} + z_{diff}^{\ 2}} \qquad 139$$

where φ_0 is the angle of the photons travel vector in the x-y plane, and θ_0 is the angle subtended from the z axis to the photons new travel vector. Figure 3.3.1.4-5 presents the geometry used for this calculation.

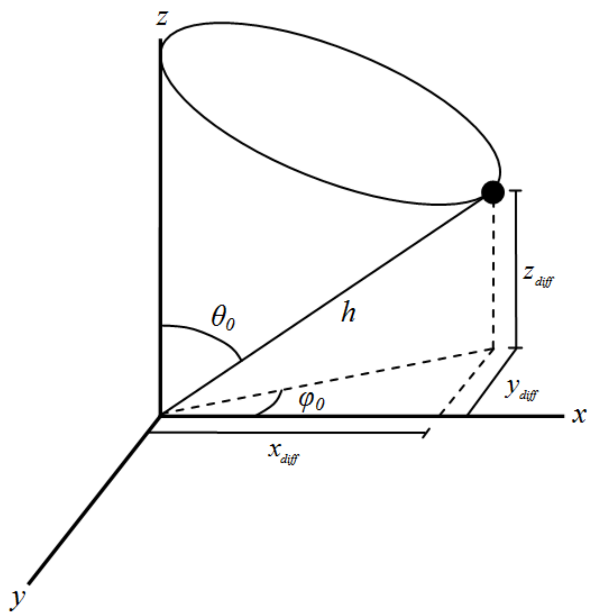

Figure 3.3.1.4-5 Scattering geometry defining the direction of photon propagation following a scattering event in the fixed reference frame

The Monte Carlo algorithm is repeated until either the photon reaches the end of the atmospheric cell or the maximum number of scattering events is reached. Figure 3.3.1.4-6 diagrammatically demonstrates a series of calculations used to determine the scattering positions during a Monte Carlo simulation. The images in Figure 3.3.1.4-6 are taken from a scattering algorithm fidelity test in which all possible angle configurations were tested to detect any errors in the process.

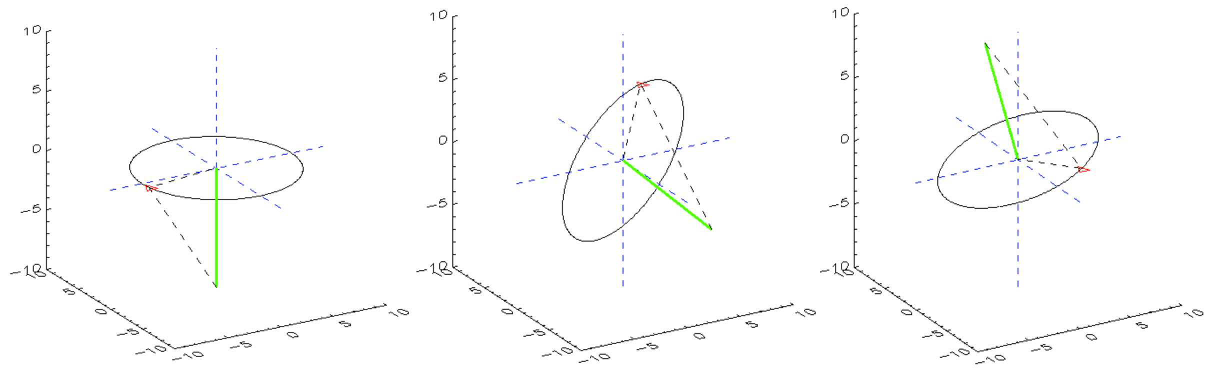

Figure 3.3.1.4-6 Scattering algorithm calculations depicted geometrically in 3D space. Green lines represent the incident vector, circles represent a ring about the H-G scattering phase function, and red triangles indicate the scattering position (relative to the origin)

The results from two Monte Carlo simulations are presented in Figure 3.3.1.4-7. The cloud optical depth used for these simulations was set very high (> 1) for demonstration purposes.

The primary output from the Monte Carlo algorithm is a two dimensional array of photon positions (in the x-y plane) at the top and bottom of the atmospheric cell. Figure 3.3.1.4-8 presents a histogram of this data from the simulation of 100,000 photons for the forward direction, combined with a cross section of the histogram revealing the dominant forward scattering peak of the 3D H-G PDF.

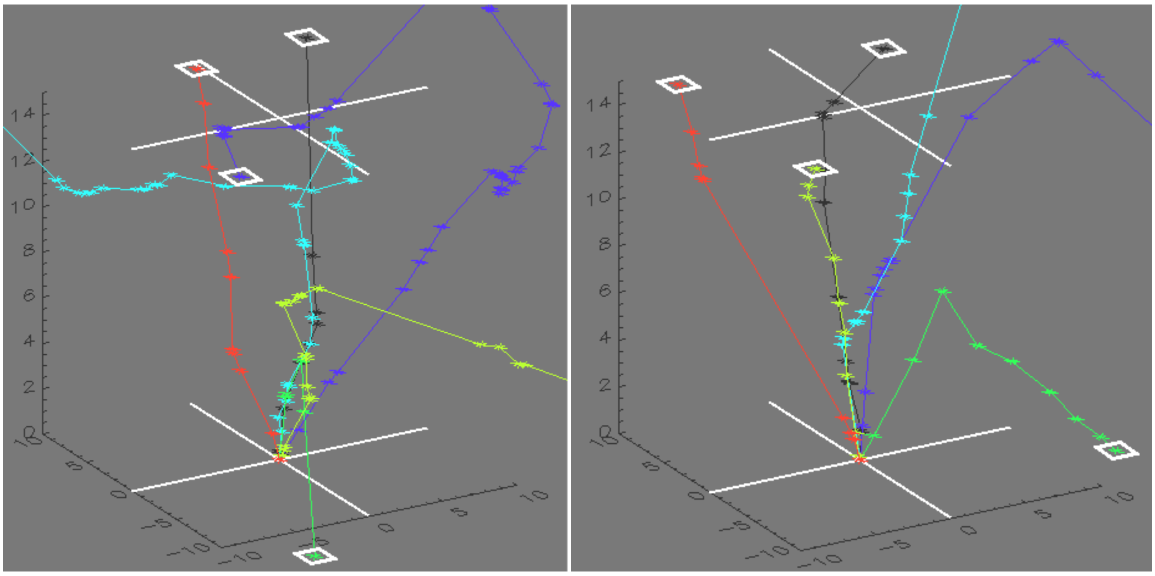

Figure 3.3.1.4-7 3D representation of two groups of 6 photons propagating through a very thick layer of cloud, data generated by the TCDS Monte Carlo model, white squares indicate photon exit points

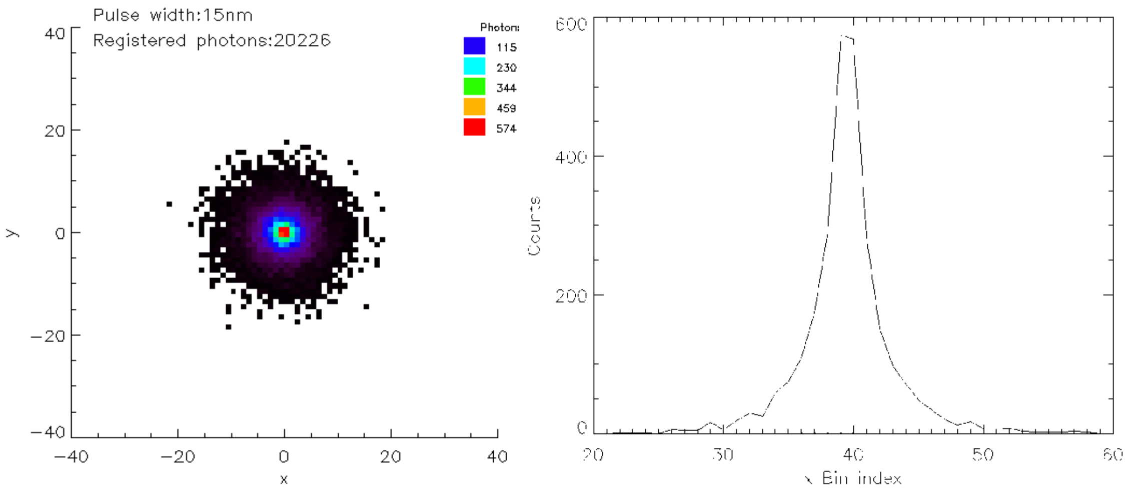

Figure 3.3.1.4-8 Left – Monte Carlo simulation results showing the number of photons leaving at the top of an atmospheric cell in the x-y plane. Right – A cross section at y = 0 of the histogram demonstrating the dominant forward peak of the H-G phase function.

3.3.1.5 Photon detection

Upon leaving the scattering environment at the top or the bottom of the atmospheric level the recorded photons are classified into *lost*, *forward* and *backward* components. The forward component consists of photons that have reached the far end of the atmospheric level and are identified by their final z values exceeding the top of the atmospheric cell (15 m by default). The backward component consists of photons that have turned back on their original vector by at least 90° and are identified by having negative final z values. The loss component accommodates the few photons that never leave the cloud layer within the time limit of the simulation.

The forward and backward components are further subcategorised into being *inside* or *outside* the detectors FOV. For the downward component the FOV is defined as the surface footprint of the laser transmission whilst for the upward component it is defined as the area of the receiver mirror on the satellite instrument. The magnitude of the two FOV's differ but the determination of whether a photon lies inside or outside is the same. Photons are classified as being inside the FOV if their projected travel vector intersects with the FOV surface area. Equations 140 to 143 are used to determine the point of intersection as a distance vector from the centre of the FOV. If the intersection distance is smaller than the FOV radius then the photon is classified as being inside.

$$x_p = L\cos(\varphi_1) + x_f \qquad 140$$

$$y_p = L\sin(\varphi_1) + y_f \qquad 141$$

$$L = \left(z_f \pm A\right)\tan(\theta_1) \qquad 142$$

$$R = \sqrt{{x_f}^2 + {y_f}^2} \qquad 143$$

where x_p and y_p are the projected positions of the photon in the x-y plane, x_f, y_f and z_f are the final positions of the photon after leaving the atmospheric level, L is the distance from the centre of the FOV in the x-y plane, A is the distance from the surface to the top of the cloud layer or from the satellite to the top of the cloud layer, R is the distance from the centre of the beam to the photons projected position in the x-y plane, and θ_1 is the final recorded scattering angle subtended from the z axis in the fixed reference frame (see Figure 3.3.1.5-1).

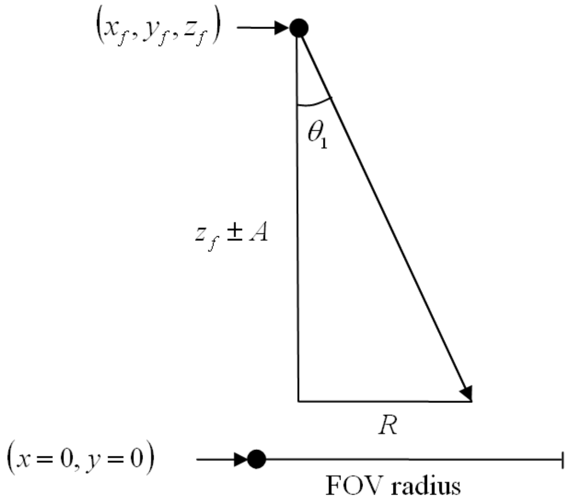

Figure 3.3.1.5-1 Geometry used to determine exiting photon categorisation. In the case shown the end of the projected vector lands within the FOV radius and is therefore classified as being *inside*.

A final classification is applied to the photons that have remained inside the detectors FOV which accounts for the temporal sampling of the TC-DIAL instrument. The filter condition for the photon being classified as *detected* is that the photon must reach either end of the atmospheric level within a given time window.

The time filter is applied in the Monte Carlo algorithm in the form of a distance filter, where photons that have a cumulative travel distance of more than 1.5 times the instruments vertical resolution are marked as *undetected*, and photons that have a cumulative travel distance of less than 1.5 times the vertical resolution are marked as *detected*. The factor of

1.5 is based on the distance a photon can travel before the main pulse leaves the sample of interest. On average the pulse will be approximately in the middle of the atmospheric level when a scattering event occurs, therefore a photon can travel up to an average of 1.5 times the length of the atmospheric sample for it to be detected in the same temporal sample as the main pulse (see Figure 3.3.1.5-2).

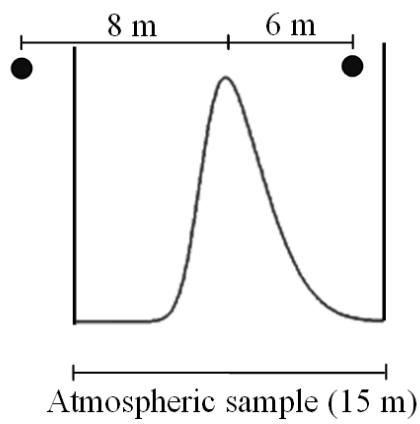

Figure 3.3.1.5-2 Depiction of a transmission pulse in the centre of an atmospheric temporal sample with two multiple scattered photons depicted as black dots. The photon on the right is within the temporal window and therefore detected, the photon on the left is not and is therefore filtered out.

The distribution of photons received on the far side of the atmospheric cell is presented in Figure 3.3.2-1 for filtered and non filtered conditions.

3.3.2 Validation of scattering models

The Monte Carlo simulation requires validation in order to be used in confidence with the TCDS scattering algorithm. Two separate methodologies are applied to perform this validation. The first is a direct comparison of the Monte Carlo results with the single scattering regime of the TCDS scattering algorithm to demonstrate the consistency between the models. Secondly the multiple scattering processes of the Monte Carlo algorithm are validated against a series of tests in which the outcomes are known. This provides confidence in the multiple scattering algorithm which cannot be validated by comparison with the single scattering TCDS model.

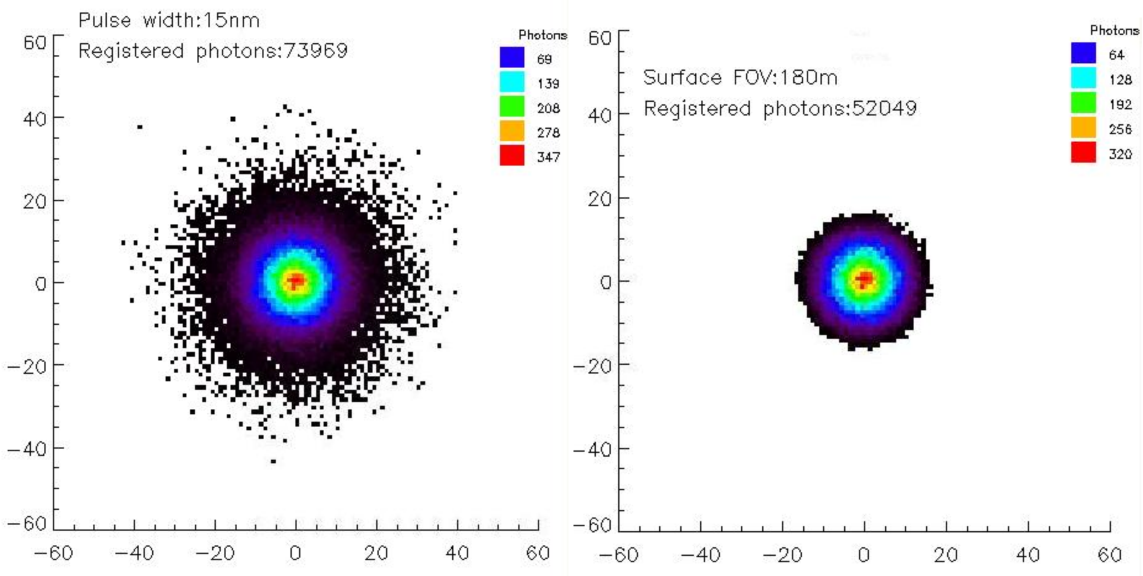

Figure 3.3.2-1 Left – Unfiltered photons leaving the atmospheric cell in the x-y plane. Right – time and FOV filtered photons leaving the atmospheric cell in the x-y plane.

3.3.2.1 Directional scattering algorithm

The Monte Carlo model and the TCDS scattering algorithm are required to produce the same results under the same conditions for there to be confidence in the derived correction factors. To ensure such consistency is present a comparison study between the two models is undertaken. The Monte Carlo simulation is written with a mode of operation designed to mimic the scattering processes of the TCDS. This special TCDS emulation mode is specifically designed not to interfere with the Monte Carlo scattering mechanism to ensure the model operates normally in 3D. The only intervention applied is a limit on the Monte Carlo scattering model to only one scattering event per photon. This is sufficient to realistically emulate the TCDS scattering model which is fundamentally limited to the simulation of one scattering event per atmospheric level.

For comparison purposes the TCDS model is configured with no aerosol in the atmosphere and only a single cloud layer 15 m thick on a 15 m wide spatial resolution. The absence of any other scattering media ensures the isolation of the system from external scattering influences. The cloud optical depth is set so that there is no possibility of multiple scattering occurring to guarantee reliable TCDS results.

The number of photons remaining in both models is defined by the field of view (FOV) of the TC-DIAL instrument. For backward scattered photons the FOV is determined by the solid angle from the centre of the cloud to the detector on the satellite instrument, and for forward scattered photons the FOV is determined by the solid angle from the centre of the cloud to the surface footprint.

A series of simulations are run using the TCDS for a range of receiver angles to determine the number of photons remaining within the FOV. The same FOV conditions are applied to five Monte Carlo simulations each containing 10,000,000 photons. The percentage difference between the photon numbers calculated to have remained in the FOV by the TCDS and the Monte Carlo model are plotted in Figure 3.3.2.1-1 and Figure 3.3.2.1-2 for the forward and backward scattering directions with the coloured lines corresponding to individual simulations.

Despite propagating 10,000,000 photons for each Monte Carlo simulation, the backscatter of the H-G PDF is so weak that less than 100 photons are received over a 6° angular swath in the backward direction, and only approximately 10 within a 1° angular swath. The sampling error in the backward direction is therefore expected to be very high and not indicative of a physical difference between the two models. This hypothesis is verified by the sampling errors quickly saturating as the viewing angle increases, particularly in the forward direction. In the rear direction the saturation of the error reaches an average of approximately 0.8% at 90°, which is significantly larger than the saturated error in the forward direction which has an average of approximately 0.01% at 90°. The difference between the magnitudes of the two errors at 90° is a result of the errors propagating through the angles and continuing to have influence on the result.

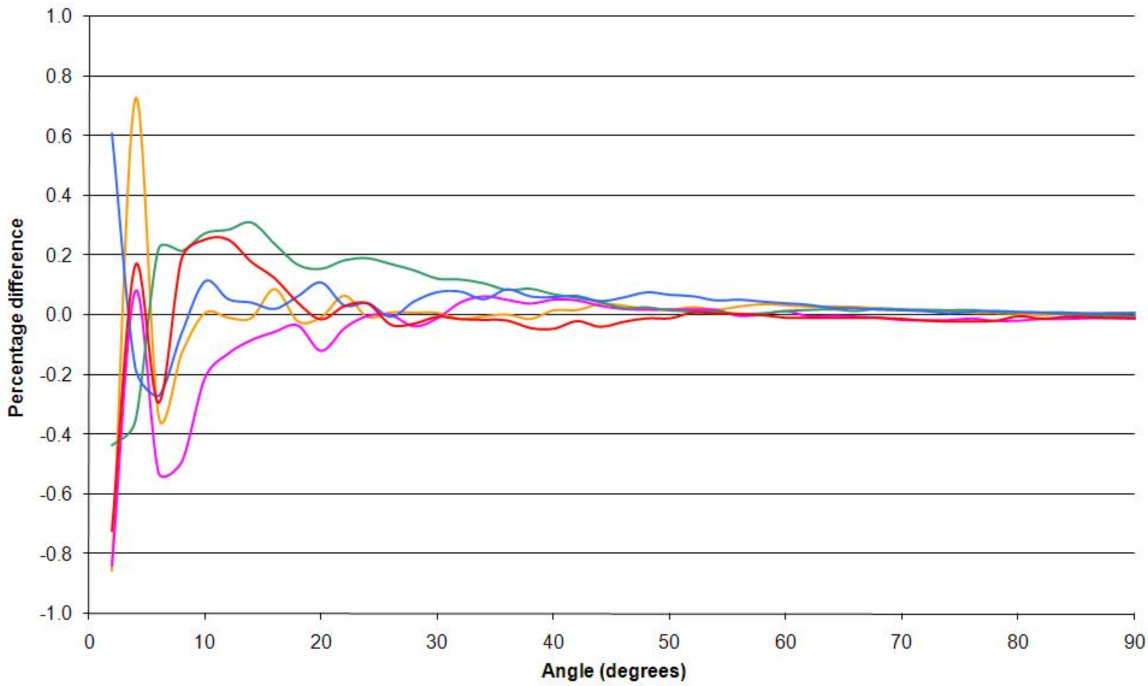

Figure 3.3.2.1-1 Percentage error for the number of photons received in the forward direction between the Monte Carlo model and the TCDS as a function of subtended viewing angle

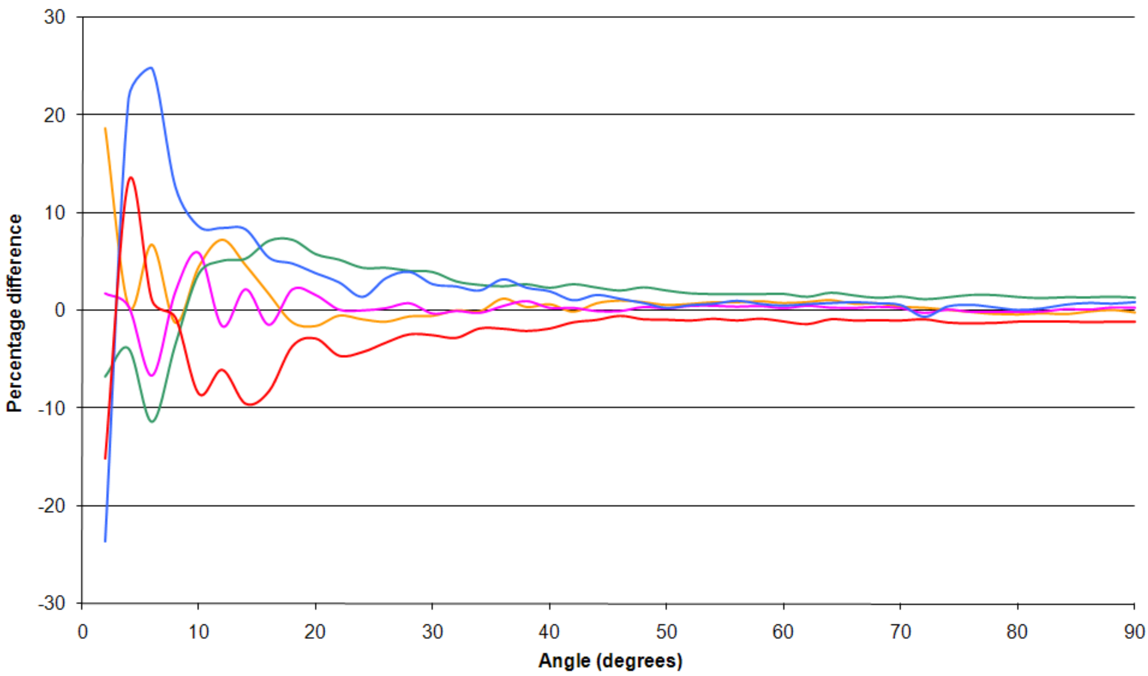

Figure 3.3.2.1-2 Percentage error for the number of photons received in the backward direction between the Monte Carlo model and the TCDS as a function of subtended viewing angle

The general bias observed in many of the results is caused by the error propagation effect. In the rear direction only 20,000 photons are received over a 90° angular swath and as such the measurements remain very sensitive to both sampling errors and a propagating bias. In the forward direction however the number of photons received over a 90° angular swath is approximately 9,000,000, and therefore the forward measurements are significantly less sensitive to a previous bias and sampling errors.

3.3.2.2 Continuity of the dynamic reference frame

The comparison of the TCDS and Monte Carlo models has demonstrated the equivalence of their scattering algorithms and proven that the Monte Carlo algorithm for a single scattering event is working correctly. It has not however validated the Monte Carlo models multiple scattering mechanism. The progression from single scattering to multiple scattering in the Monte Carlo model is the inclusion of a dynamic reference frame in which the subsequent scattering vectors are computed. To ensure this mechanism is working as it should, a series of tests are run to determine if the dynamic reference frame is correctly calculating the scattering vectors. During these tests the initial scattering angles are fixed so that the photons are immediately scattered away from the origin before being scattered again to return them to a reasonable vector so that they may be captured for observation. The last few scattering events are random and follow the ordinary scattering procedure. By this method the phase function has been forced to be recalculated in a different reference frame, and by observing the results and comparing them to the mathematical theory the fidelity of the algorithm may be proven.

The first test involves initially scattering the photons away from the origin along the four main axes before scattering them vertically so that their reference frames are parallel with the z axis again. The first scattering angle is 85° from the z axis, and the distance to scattering is set to 30 m. The position in the x-y plane for each test should theoretically be 29.8 m along each of the main axes. The results from this test agree with the theory and are presented in Figure 3.3.2.2-1.

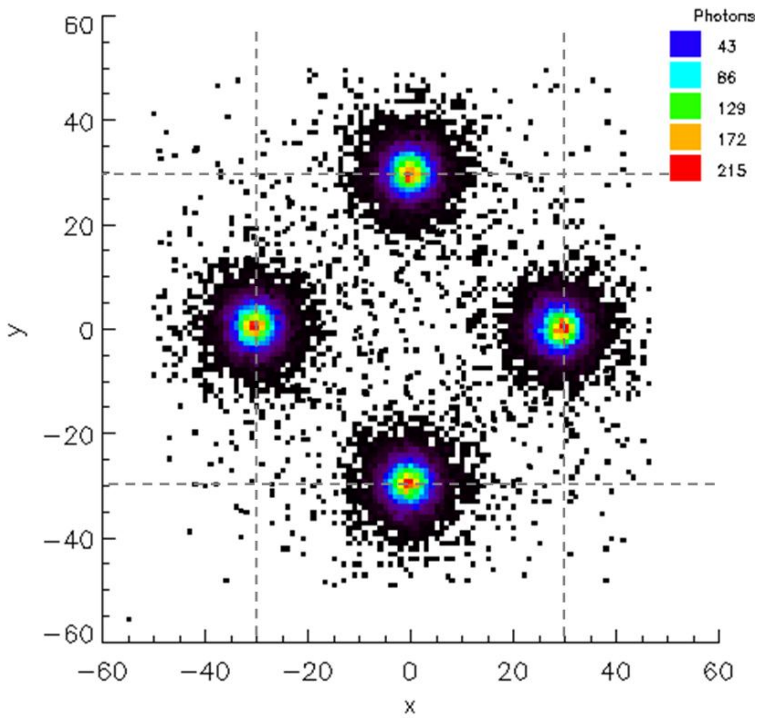

Figure 3.3.2.2-1 Monte Carlo simulation results for the first algorithm fidelity test, the grey lines indicate the theoretical position for the centre of each distribution.

The second and third tests involve initially scattering the photons away from the origin at a 45° angle over a distance of 10.6 m before scattering them in the opposite direction at 90°. The theory indicates that the centre of the phase function will approximately line up with the x-y origin, and that the resultant distribution observed in the histogram will resemble a flat oval with a slight radial distortion. The shape of the distribution is driven by the recording system accepting photons as having left the system at any point beyond 15 m on the z axis. This detection principle implies that photons are detected at variable z positions and as such the resulting image in the x-y plane is expected to appear as if the distribution is being viewed slightly side on (and not as a flat projection). Furthermore, the longer path length experienced by some of the photons to reach 15 m on the z-axis implies that multiple scattering is more likely to occur on one side of the distribution than the other, and therefore it is also expected that the distribution will appear less defined and more spread out on one side. Figure 3.3.2.2-2 and Figure 3.3.2.2-3 present the results from the second and third algorithm fidelity tests. The results agree with the theory.

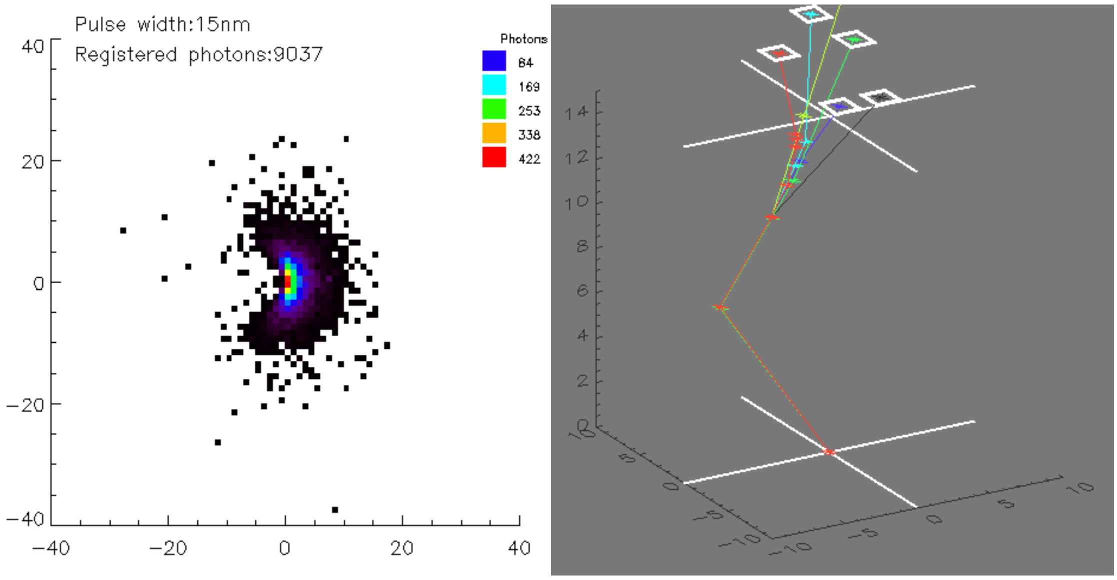

Figure 3.3.2.2-2 Monte Carlo simulation results for the second algorithm fidelity test. Left – histogram in the x-y plane showing received photons correctly distributed and centred on the x-y origin. Right – 3D plot of photon positions within an atmospheric cell presenting the test geometry.

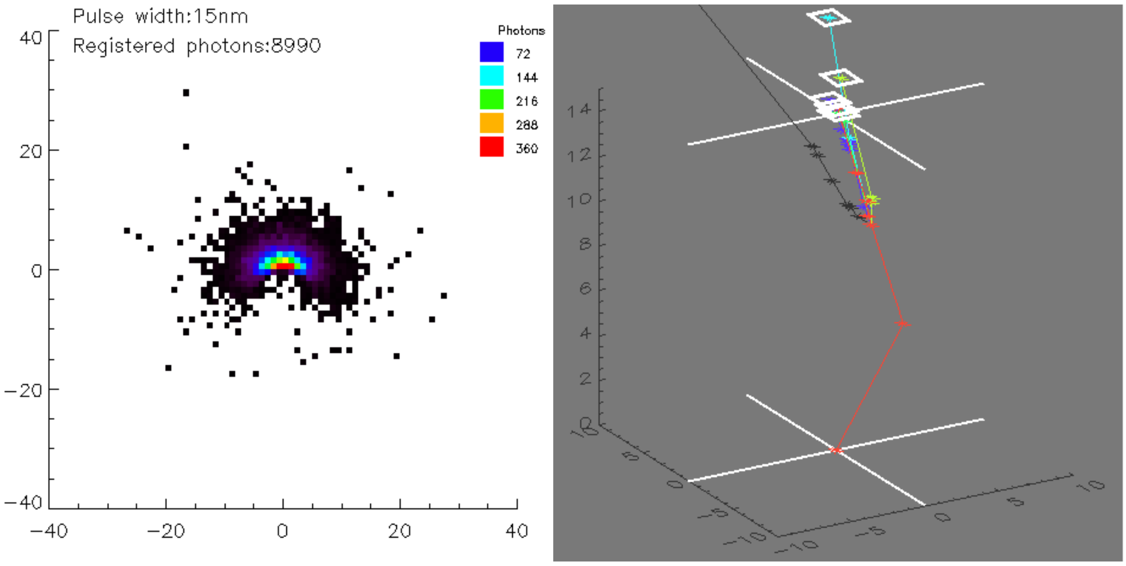

Figure 3.3.2.2-3 Monte Carlo simulation results for the second algorithm fidelity test. Left – histogram in the x-y plane showing received photons correctly distributed and centred on the x-y origin. Right – 3D plot of photon positions within an atmospheric cell presenting the test geometry.

3.3.3 Derivation of correction factors

The correction factors for the TCDS scattering model are derived for a range of scattering angles and scattering probabilities to cover the full range of permissible scattering conditions. 70,000,000 photons are simulated for each angle and coefficient scenario resulting in a total of 7×10^9 photons over a range of 5 scattering probability values and 20 angle values. The number of photons remaining inside the detector FOV for both the Monte Carlo model and the TCDS are recorded and compared. The correction factors for the forward and backward scattering directions are derived using equations 144 to 147.

$$C_{FU}(\theta_U, \sigma) = M_{FU}(\theta_U, \sigma)/T_{FU}(\theta_U, \sigma) \qquad 144$$

$$C_{BU}(\theta_U, \sigma) = M_{BU}(\theta_U, \sigma)/T_{BU}(\theta_U, \sigma) \qquad 145$$

$$C_{FD}(\theta_D, \sigma) = M_{FD}(\theta_D, \sigma)/T_{FD}(\theta_D, \sigma) \qquad 146$$

$$C_{BD}(\theta_D, \sigma) = M_{BD}(\theta_D, \sigma)/T_{BD}(\theta_D, \sigma) \qquad 147$$

where C is the correction factor, M is the number of photons that have remained inside the FOV from the Monte Carlo simulation, T is the number of photons that have remained within the detectors FOV from the TCDS simulation, θ is the angle subtended from the vertical to the edge of the FOV beginning at the scattering media, σ is the scattering coefficient, subscripts F and B refer to the forward and backward scattering components and subscripts U and D refer to the upward and downward scattering directions.

The correction factors are linearly interpolated to attain approximations for the factors between the data values obtained from the simulations. For very small angles (< 1°) the correction factors are highly linear and therefore suitably approximated by linear extrapolation.

The correction factors derived for both the forward and backward scattering components are presented in Figure 3.3.3-1 and Figure 3.3.3.1-1. The scattering probabilities define the probability of a photon scattering within the 15 m atmospheric cell.

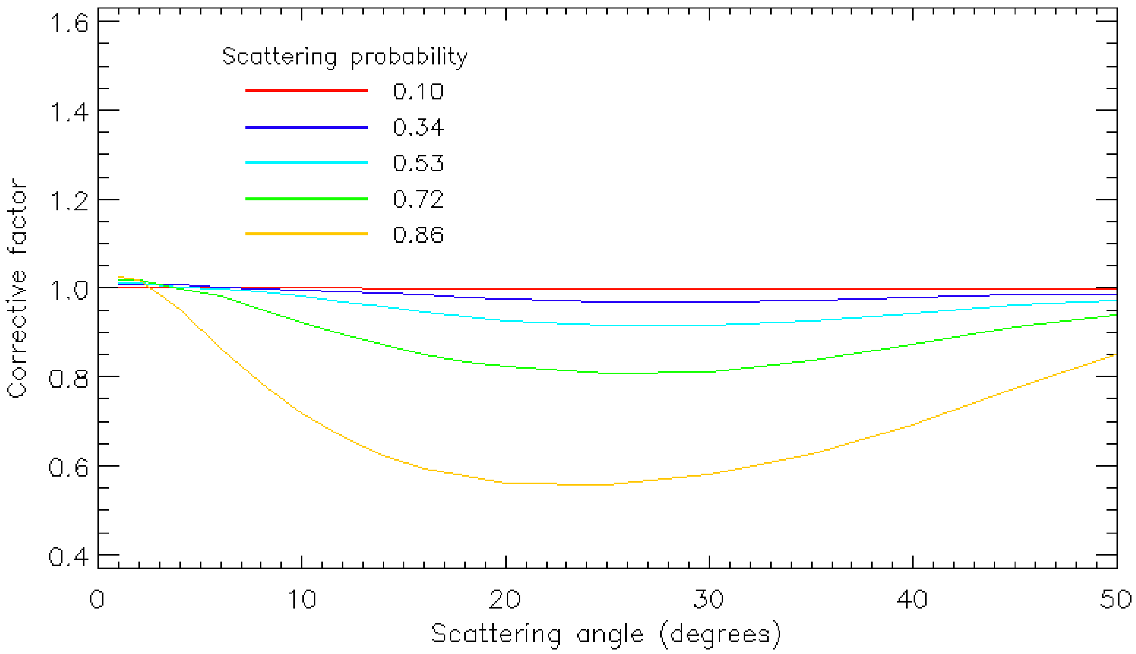

Figure 3.3.3-1 Correction factors as a function of scattering angle (angle from the vertical) for 5 scattering probability conditions for the forward scattering direction

3.3.3.1 Analysis of results

Correction factors with values greater than one imply the TCDS is underestimating the number of photons inside the detectors FOV, and factors with values less than one imply the TCDS is overestimating the number of photons inside the detectors FOV. The cause of the corrective factor distributions presented in Figure 3.3.3-1 and Figure 3.3.3.1-1 are described for both scattering components below.

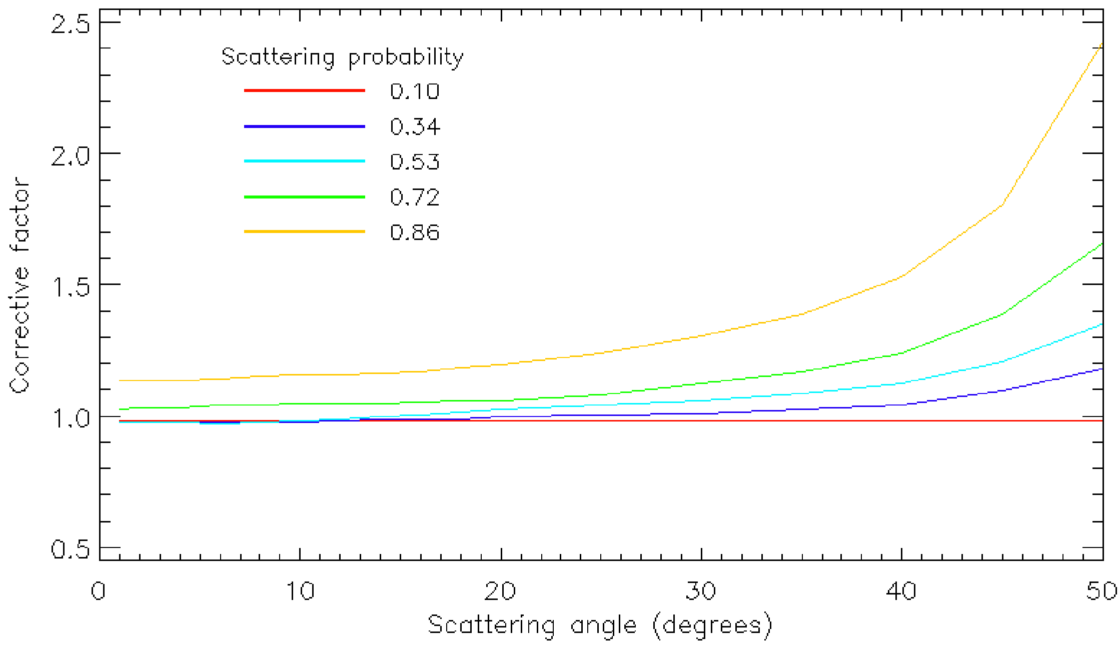

Figure 3.3.3.1-1 Correction factors as a function of scattering angle (angle from the vertical) for 5 scattering probability conditions for the backward scattering direction

The correction factors for the forward scattering component indicate that the TCDS generally overestimates the number of photons remaining inside the detectors FOV (except at very small angles). The overestimation is caused predominantly by the negative gradient of the H-G phase function as the scattering angle widens away from the forward peak. The shape of the PDF implies there is a higher probability that multiple scattered photons will scatter out of the detector FOV than back into it. The imbalance between these probabilities implies a net loss in the photons remaining in the detector FOV, particularly when there is a large chance of multiple scattering occurring. Furthermore, the TCDS scattering probability is calculated based on the length of the atmospheric level (15 m), however in the Monte Carlo simulations the photons path length varies depending on its initial scattering angle (see Figure 3.3.3.1-2). The longer path length introduced by the first scattering event sending the photon away from the vertical provides a greater opportunity for secondary scattering to occur. The effect of increasing the probability of multiple scattering through an increased path length amplifies the loss of photons from the FOV and further increases the gap between the TCDS scattering algorithm and the 3D Monte Carlo model.

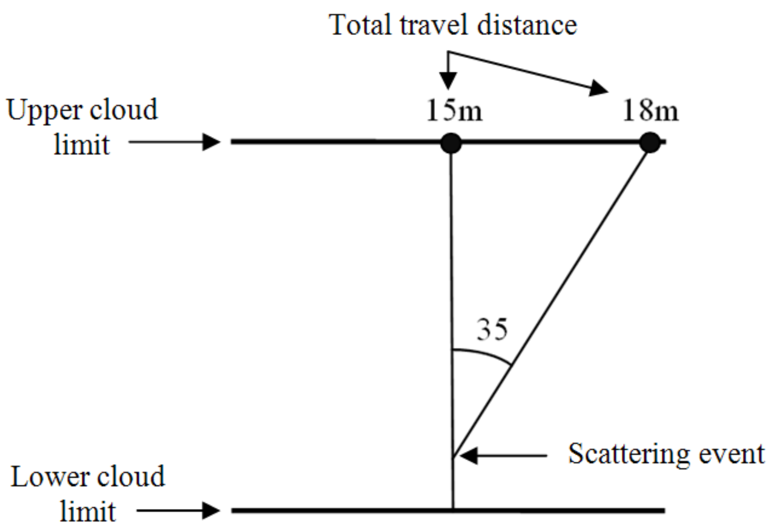

Figure 3.3.3.1-2 Longer path length caused by initial scattering introduces a greater probability for secondary scattering compared to photons that travel unimpeded through the cloud layer

From approximately 20° to 25° onwards the forward correction factors begin to tend towards unity. The change in direction is caused by the recapturing of previously lost photons from the dominant forward peak of the H-G phase function. The loss of photons at the edge of the FOV through multiple scattering reduces as the FOV widens towards the wings of the H-G PDF. This reduction in scattering probability occurs in conjunction with the more significant recapturing of multiple scattered photons from the forward dominant peak as the capturing angle widens.

At very narrow viewing angles (< 3°) the forward scattering correction factors are slightly positive, implying the TCDS scattering algorithm is underestimating the number of photons returning to the satellite. The underestimation is caused by a difference in the viewing geometry between the two models. The TCDS uses a fixed scattering position at the top of the cloud layer for all scattering events, forcing a fixed viewing geometry to the target FOV. The Monte Carlo simulation however is more realistic by allowing the scattering to occur at any point within the cloud. The average lower altitude of the scattering positions in the Monte Carlo model allows a slightly wider range of possible scattering angles that will remain within the FOV.

The correction factors for the backward scattering component imply the TCDS generally underestimates the number of photons remaining inside the detectors FOV. The primary cause of the underestimation is the two models having different definitions of the detector FOV. The FOV for the TCDS is defined as an angle subtended over part of the H-G phase function, whereas in the Monte Carlo model it is defined as a physical area some distance away. As the FOV increases the target area for the Monte Carlo simulation increases as well, presenting a larger target for multiple scattered photons to scatter into. This effect isn't seen in the forward scattering component as strongly as the photons are initially travelling towards the FOV when they enter the cloud layer. It is most notable in the rear direction as there are fewer photons initially scattering backwards, and any small perturbation by multiple scattering leads to the production of a relatively significant corrective factor.

3.4 Summary

The TCDS computer model has been written to provide a tool which can be applied in an iterative manner to assess the parameter space surrounding the accuracy of atmospheric retrievals performed by a TC-DIAL system. To achieve this objective the dependant parameters for TC-DIAL retrievals are efficiently simulated using well established and documented physical principles, including spectroscopy, atmospheric scattering and surface interaction in the form of a bidirectional reflectance distribution function. The computational efficiency of the model is the main design priority and ancillary algorithms including the Monte Carlo algorithm and the pre-processing algorithm were developed to allow large numbers of iterations to be carried out efficiently whilst maintaining the models flexibility. The most important components of the TCDS (spectroscopy, surface interaction and atmospheric scattering) have been partially validated, often using comparisons with equivalent results presented in the FACTS report. This method provides a level of total model fidelity as they often require the combination of multiple model components to produce the final results.

As well as being computationally efficient the TCDS has been written to be easy and quick to use, utilising separate text files containing switches and variables to quickly adjust internal parameters. This capability is considered essential because of the large number of TC-DIAL parameters which require an adjustment facility.

The application of a Monte Carlo model to provide a more realistic representation of atmospheric scattering is employed to enable particular studies associated with cloud and dense aerosol to be representative of reality. Without this particular consideration for the missing scattering mechanisms in the TCDS scattering algorithm studies involving scattering media with optical depths > 0.5 would have incurred errors.

The TCDS is used in its entirety to investigate the TC-DIAL parameter space and to perform specific studies on sources of CO_2 retrieval error in Chapters 4, 5, 6 and 7.

4. The use of cloud statistics for the determination of the pulse repetition frequency for a heterodyne detection TC-DIAL system

A space-borne TC-DIAL instrument based on current technology is required to emit multiple online and offline pulses for each atmospheric measurement made in order to statistically reduce the retrieval errors to a suitable level. The rate at which pulses are emitted is known as the pulse repetition frequency (PRF) and is one of many parameters that affect the overall precision of both heterodyne and direct detection TC-DIAL retrievals over an integrated series of measurements. For direct detection an optimum PRF exists for a given system configuration and in Chapter 5 it is shown that for a system based on current technology the optimum PRF lies in the region of 10 to 50 Hz. For heterodyne detection however the PRF is required to be as large as possible (> 5 KHz) owing to its very high single sounding retrieval error caused by a phenomenon known as speckle (see Chapter 2). The frequent presence of cloud in the Earth's atmosphere presents restrictions on the usable pulse repetition frequencies above approximately 5 kHz for a space-borne TC-DIAL system owing to the possibility of an effect known as cross signal contamination occurring in the Earth's atmosphere (described below). For direct detection the usable PRF's are too low to present concern in this respect; however for heterodyne detection where the required PRF's are generally greater than 5 kHz, cross signal contamination is a high possibility.

For a space-borne TC-DIAL system cross signal contamination can occur when a LiDAR pulse is given insufficient time to clear the lower atmosphere before another pulse is emitted. The upward travelling pulse returning to the satellite is likely to pass through a scattering medium (such as cloud) at some point along its journey. During its propagation through the scattering medium the returning signal may encounter the next pulse travelling in the opposite (downward) direction. If this eventuality were to occur the backscatter of the much stronger downward pulse would combine with the upward pulse causing an undefined increase in signal intensity. A small amount of compensation is afforded to the upward pulse owing to it also backscattering within the cloud and therefore losing some of its energy to the scattering medium, however the downward pulse is inherently more powerful having not scattered from the Earth's surface or encountered as much atmosphere. As a consequence of the power imbalance between the two pulses, the backscatter from the downward pulse has a much stronger influence on the upward pulse than vice versa. The effect of this contamination in the received pulse intensities is ultimately a bias in the CO_2 retrieval which cannot be reduced through averaging over multiple measurements. Figure 4-1 demonstrates the cross signal contamination process.

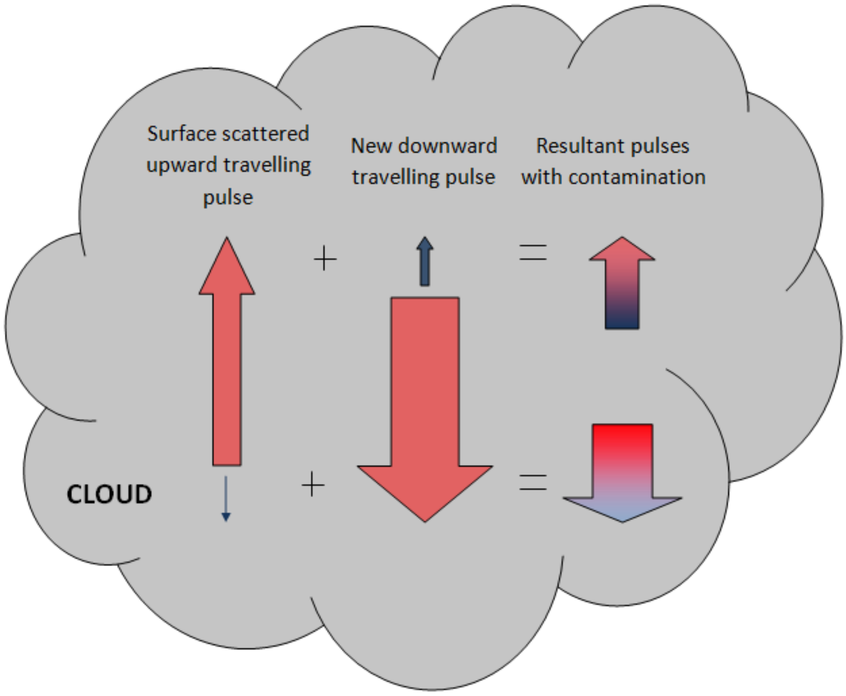

Figure 4-1 Diagrammatic representation of cloud scattering leading to cross signal contamination, red arrows represent original signals, blue arrows represent backscattered signals and arrow widths represent signal intensities

A PRF of 5 kHz is considered to be the minimum frequency at which cross signal contamination may occur. This value is defined based on its equivalence to a signal crossover altitude of approximately 15 km. Above 15 km clouds and aerosols which have strong scattering capabilities at 2 µm are very rare (see Chapter 3) and therefore there is little possibility of cross signal contamination occurring above this altitude.

The conversion from PRF to signal cross over altitude is presented in equation 148.

$$A = \frac{c}{4\mathrm{PRF}} \tag{148}$$

where A is the signal cross over altitude in m, c is the speed of light at $2.998 \times 10^8\ ms^{-1}$ and PRF is the instruments pulse repetition frequency in Hz. The factor of 4 accommodates two conversions, first it accounts for the PRF representing the pulse repetition frequency for the pulse pairs and not the individual soundings, implying that the temporal gap between the online and offline emissions is half of the temporal gap between each pulse pair. Second the altitude from the surface is half of the spatial distance between the online and offline pulses owing to the first pulse having reflected off the Earth's surface prior to crossing over with the second pulse in the atmosphere.

The relevance of cross signal contamination for heterodyne detection TC-DIAL retrievals and its implications on the system's PRF may be determined by comparing the magnitude of the bias associated with cross signal contamination with the retrieval error imposed by a reduction in signal intensity caused by the presence of cloud. If the retrieval error incurred by the reduction in signal intensity over a 50 km integration distance is greater than the bias caused by cross signal contamination then a process of cloud avoidance would be required as opposed to a careful selection of the instruments PRF. It is the purpose of this chapter to determine the relevance of cross signal contamination in the Earth's atmosphere, and if required suggest appropriate PRF windows to minimise the possibility of its occurrence.

4.1 Methodology

Using global statistics on cloud thickness and altitude it is possible to determine the most suitable PRF's for use by a heterodyne detection system which will minimise the possibility of cross signal contamination in the atmosphere. Heterodyne detection is relatively insensitive to minor reductions in signal intensity and as such can perform measurements reasonably well under light cloud conditions. For this reason separating optically thin from optically thick clouds is an important first step in order to quantify the gain achieved by avoiding cross signal contamination. Using the TCDS (see Chapter 3) it is possible to quantify the retrieval error associated with both a reduction in signal intensity owing to the presence of thin cloud and the retrieval error introduced by cross signal contamination in the Earth's atmosphere for a given cloud optical depth.

To provide suitable cloud properties with which to constrain the TCDS model, a scientific paper detailing global cloud statistics is used as the reference case (Wylie and Eloranta, 2007). Wylie et al. 2007 compare data obtained from the Geoscience Laser Altimeter System (GLAS) with data from the High Resolution Infrared Radiation Sounder (HIRS) Pathfinder to determine height resolved global cloud cover for both optically thin and optically thick cloud. The GLAS instrument incorporates a LiDAR system allowing vertical profiles of cloud optical depth to be derived along a single laser footprint track 70 m wide (similar viewing geometry to space-borne TC-DIAL). The HIRS instrument provides much more complete spatial data sets of global monthly averages owing to its 20 km wide surface swath but provides very little information regarding the clouds vertical profile or altitude. The combination of data from the two instruments provides a global picture of cloud cover containing average vertical profiles and altitude statistics for both optically thin and optically thick clouds.

The results presented by Wylie et al. 2007 show that approximately 70% of the Earth's surface is covered by some form of cloud, ranging from very dense cumulus cloud near the surface, to very fine and thin cirrus cloud in the stratosphere. With such a high percentage of the Earth's surface covered by some form of cloud at any moment in time a TC-DIAL's system configuration is required to accommodate the possibility that clear sky measurements will be regularly interrupted (see Chapter 5).

Of the 70% global cloud cover a significant proportion (approximately 35%) is defined as having an optical depth in the short wave infrared (1 μm) of less than 3. This statistic implies that around 25% of the Earth's surface is covered by optically thin cloud (optical depth of < 3) which for heterodyne TC-DIAL LiDAR system is likely to be sufficiently low for measurements to be performed with reasonable precision. The statistic also implies that approximately 45% of the Earth's surface is covered with optically thick cloud (optical depth

> 3) which is likely to be too dense to form a heterodyne TC-DIAL retrieval owing to insufficient signal intensities arriving from the surface.

To demonstrate the retrieval error introduced by measuring through optically thin cloud a TCDS simulation is run with a heterodyne configuration given in Table 5.2-2 with a PRF of 5 kHz and an integration distance of 50 km (see Chapter 3). The simulation is run with a liquid water cloud layer present in the atmosphere at an altitude of 3 km with a range of optical depths from 0.1 to 3.0 using the TCDS batch mode of operation. The TCDS Monte Carlo correction factors for multiple scattering are enabled to allow optical depths in excess of 1 to be realistically simulated (see Chapter 3).

The retrieval errors associated with the reduction in signal intensity caused by the presence of cloud cover are determined by calculating the retrieval error difference between measurements made with and without cloud cover in the scenes using heterodyne detection noise statistics. For the retrieval errors associated with cross signal contamination the errors are calculated by simulating multiple pulses in the Earth's atmosphere simultaneously with the appropriate temporal spacing and recording the error incurred by the presence of undetermined increases in the returning signal intensities. For these simulations the detector noise is disabled in order to determine the retrieval error caused only by the signal contamination. Identical simulations are also run for a direct detection system (configured as in Table 5.2-2) for comparative purposes.

4.2 Results

The results of the simulations for the retrieval errors associated with the loss of signal intensity caused by cloud in a heterodyne detection TC-DIAL instruments field of view are presented in Figure 4.2-1. The results demonstrate the large difference in the sensitivities of direct and heterodyne detection TC-DIAL in the presence of cloud, with heterodyne detection being shown to be less sensitive to a decrease in signal intensity from the surface. Heterodyne detections relative insensitivity to a signal reduction is a result of a relatively high PRF dampening the additional retrieval error introduced by a decrease in signal to noise ratio. A reduction in signal intensity per shot for heterodyne detection results in a relatively minor climb of the heterodyne error curve and as a consequence has little effect on the overall retrieval error (see Chapter 7). For direct detection the addition of the retrieval error is not as well dampened owing to it having a PRF of only 13 Hz and as such the system is significantly more sensitive to a minor reduction in signal intensity.

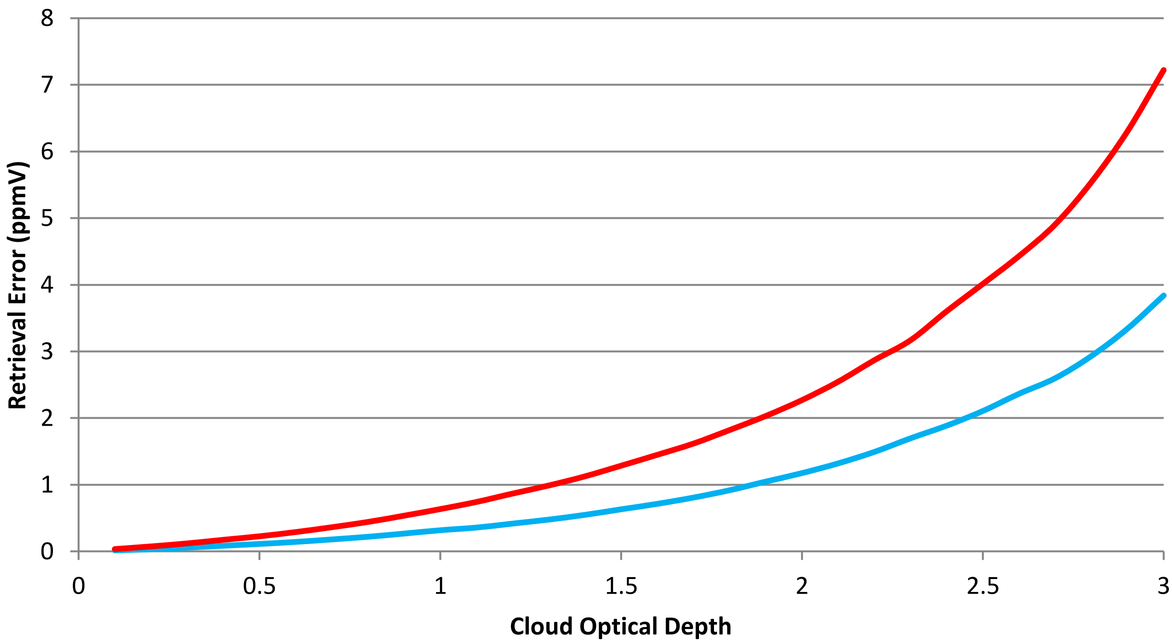

Figure 4.2-1 CO_2 retrieval errors as a function of cloud optical depth for direct (red) and heterodyne (blue) detection space-borne TC-DIAL instruments. Data generated by the TCDS (see Chapter 3) for instruments configured using parameters in Table 5.2-2 for a 50 km integration distance.

Figure 4.2-1 demonstrates that heterodyne detection errors over regions of relatively thin cloud are sufficiently small to warrant a system configuration which allows such measurements to be possible in order to avoid the loss of up to 25% global coverage. To enable heterodyne detection to perform measurements through thin cloud the system must be configured to minimise the possibility of cross signal contamination within the Earth's atmosphere. To ensure the risk of signal contamination is minimised the system must operate a PRF corresponding to an altitude at which cloud is relatively rare. Results presented by Wylie et al. 2007 provide a useful statistic for the frequency of clouds at different altitudes around the globe and are presented in Figure 4.2-2.

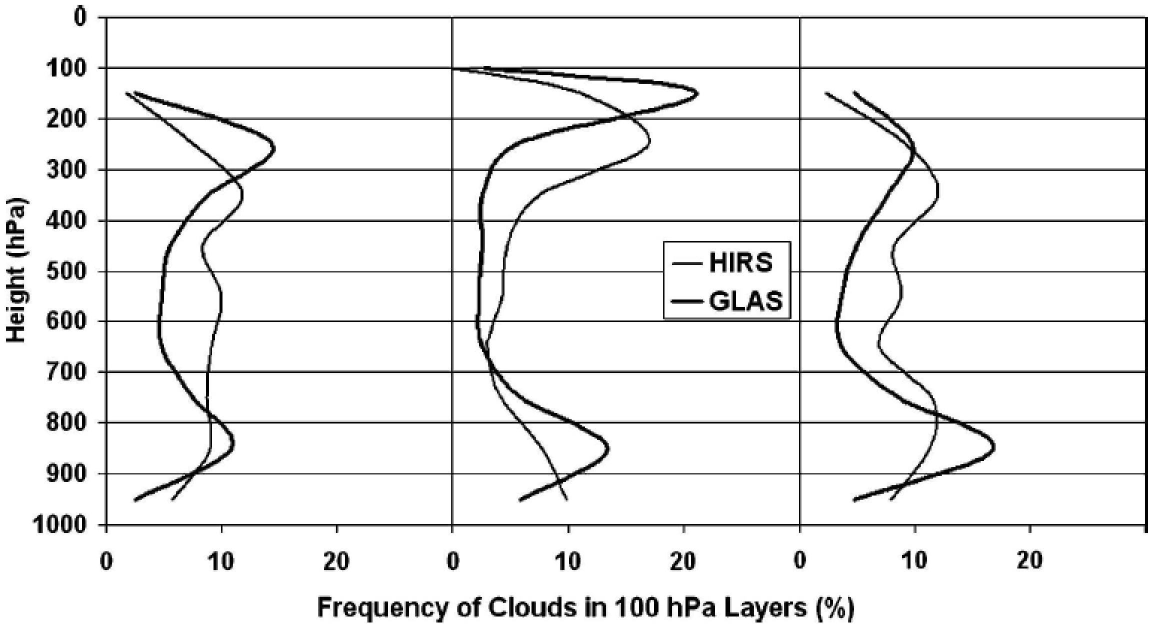

Figure 4.2-2 Vertical profile of cloud top heights from GLAS and HIRS measurements performed during 01 Oct to 16 Nov 2003, image from Wylie et al. 2007

As shown by Wylie et al. 2007 and demonstrated in Figure 4.2-2 the majority of clouds exist below 3 km and between 7 and 15 km. As a result of this information it is clear that PRF's corresponding to altitudes in excess of 15 km or between 3 and 7 km will result in the least possibility of cross signal contamination. The operating PRF for a heterodyne detection TC-DIAL system must therefore be limited to two possible regions if measurements are to be made under cloudy conditions. The possible PRF regions are 5 and 15 kHz which correspond to 15 and 5 km altitudes respectively. Of the two possibilities a PRF of 5 kHz (15 km) would most likely avoid cross signal contamination owing the signal cross over altitude being above the vast majority of clouds in the Earth's atmosphere, however the retrieval error at 5 kHz is approximately 0.11 ppm higher than at 15 kHz under optimised conditions (see Chapter 5). At a PRF of 15 kHz a reasonable possibility remains for cross signal contamination in the atmosphere owing to its cross over altitude being at 5 km, however for the 30% of clear skies and a significant proportion of the 35% of thin cloudy skies around the Earth a 15 kHz system benefits from the 0.11 ppm retrieval error reduction gained by having a higher PRF.

Figure 4.2-3 presents the results from simulations performed to determine the retrieval error associated with cross signal contamination in the Earth's atmosphere for a space-borne heterodyne detection TC-DIAL instrument. Included in Figure 4.2-3 is the retrieval error associated with the signal loss caused by the presence of cloud in the instruments field of view (red line) as presented in Figure 4.2-2. The significant retrieval error difference presented in Figure 4.2-3 between the two sources of error demonstrates the importance of avoiding cross signal contamination, with errors climbing as high as 20 ppm for cloud optical depths which in the absence of cross signal contamination would have an error of no more than 3 ppm.

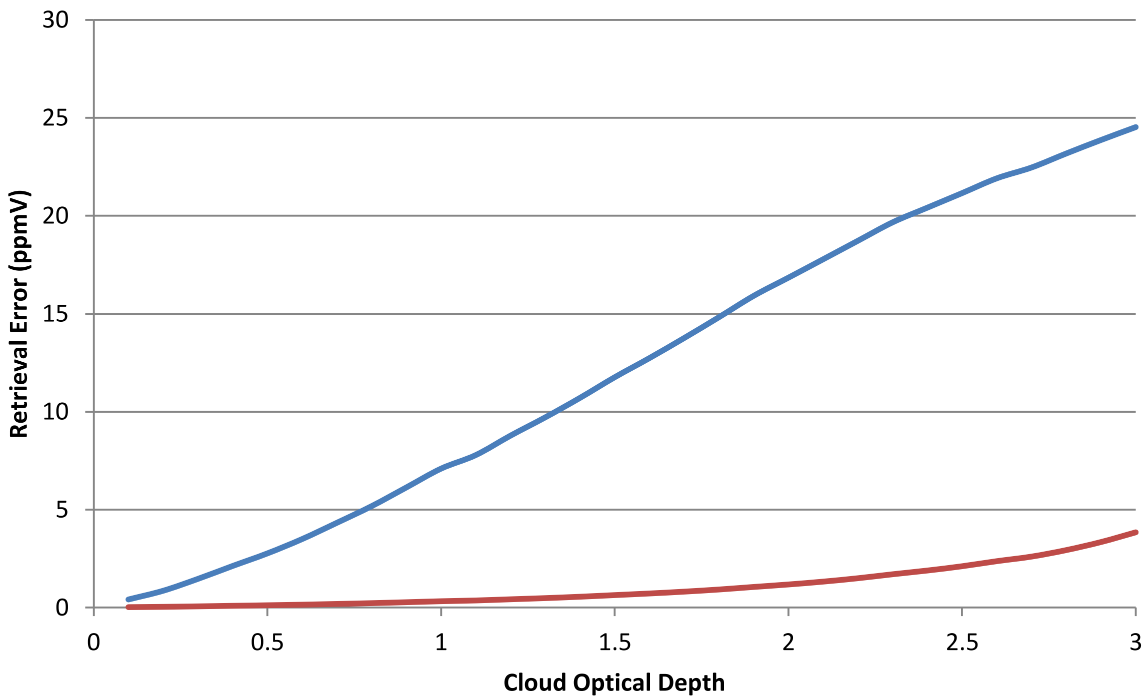

Figure 4.2-3 Retrieval error associated with cross signal contamination in the Earth's atmosphere (blue) and retrieval error associated with a signal intensity reduction owing to the presence of cloud in the Earth's atmosphere for a space-borne heterodyne detection TC-DIAL instrument configured as in Table 5.2-2, data produced by the TCDS (see Chapter 3)

In addition to performing simulations for 5 kHz PRF the retrieval errors associated with cross signal contamination were also investigated for 10 and 15 kHz PRF's. The results from the simulations were too similar to be plotted with retrieval errors differing by no more than 0.001 ppm. The very close similarity between the retrieval errors implies that in the context of heterodyne detection TC-DIAL the cross signal contamination is independent on the magnitude of the PRF. The cause of the error similarity between different PRF's is a result of the TC-DIAL retrieval errors being dependent only on the differences between the signal contamination and the original signal from the Earth's surface, and not dependant on the absolute magnitude of the single sounding emission power. This effect is produced by the intensity of the signal contamination changing in proportion to the signal intensity originating from the Earth's surface.

The magnitude of the TC-DIAL retrieval error associated with individual soundings as a result of cross signal contamination is dependent on the order in which the signal contamination occurs. Figure 4.2-4 presents the relationships between cloud optical depth and the number of photons detected at the satellite for the online (blue) and offline (red) signals originating from both cloud scattering (light colours) and surface scattering (dark colours) events.

The signal contamination of the surface scattered online and offline pulses is caused by the next pulse, and therefore in Figure 4.2-4 the offline surface signal (dark red) is contaminated by the online cloud scattered signal (light blue) and vice versa. As seen in Figure 4.2-4 the offline signal returning from the Earth's surface is the strongest of the surface scattered signals and is contaminated by the online cloud backscatter which is the strongest of the cloud scattered signals (owing to the emission power ratio favoring the online pulse). The opposite situation occurs for the offline contamination of the online pulse in which both signals are the weakest of their respective pairs. As a result of the strong pulse being contaminated by the strong cloud signal, and the weak pulse being contaminated by the weak cloud signal, the overall retrieval error incurred for both the online and offline signals are quite similar (see Figure 4.2-5).

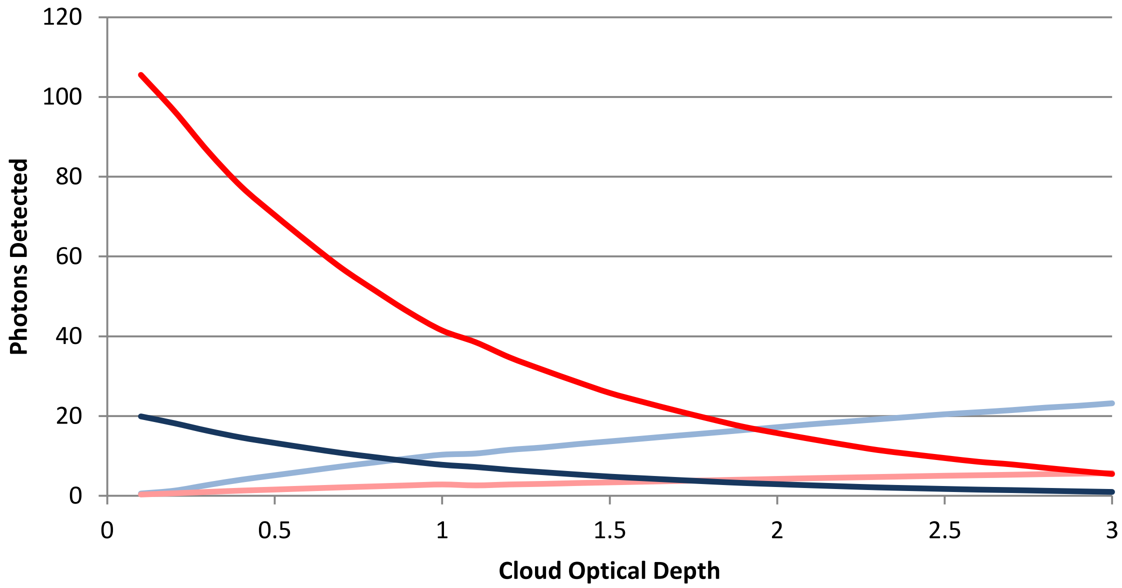

Figure 4.2-4 Number of photons detected from online (blue) and offline (red) TC-DIAL soundings scattered from the Earth's surface (dark) and cloud (light) for a heterodyne detection instrument operating at 5 kHz PRF for a range of cloud optical depths

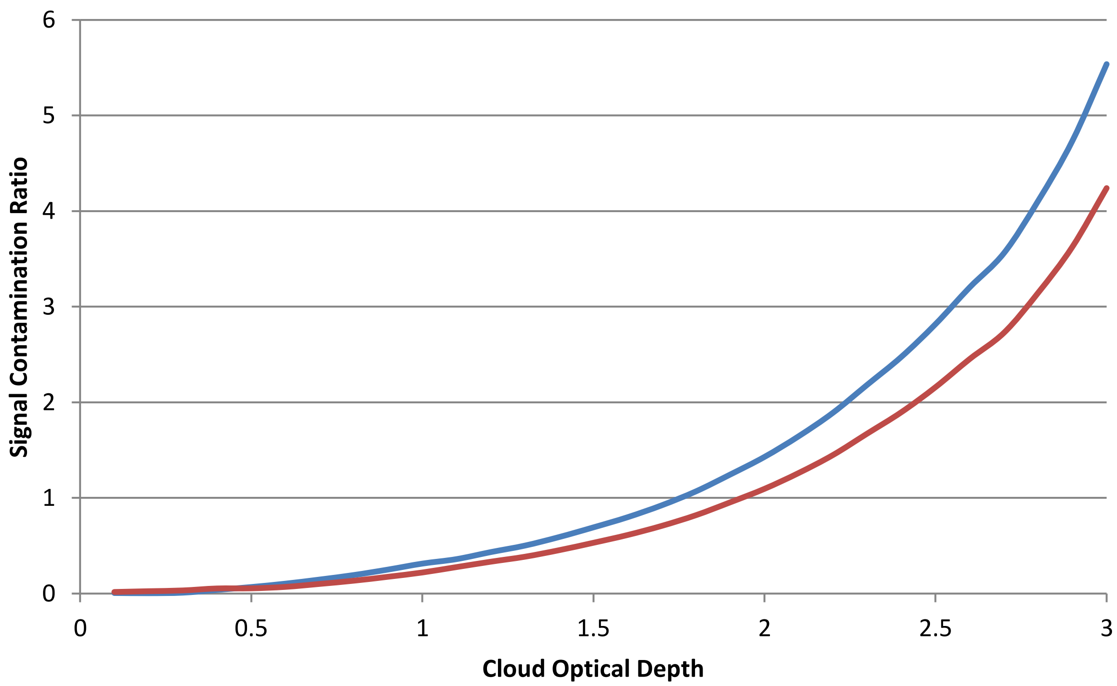

Figure 4.2-5 Signal contamination ratio (contamination/original) for the online (blue) and offline (red) TC-DIAL pulses for a range of cloud optical depths

One of the critical elements in defining the magnitude of the retrieval errors incurred by cross signal contamination is the emission power ratio between the online and offline signals (as demonstrate by the error similarity in Figure 4.2-5). The optimum system configuration for heterodyne detection has an emission power ratio of 6 to 1 in favour of the online wavelength, implying that the contamination of the offline signal is significantly greater than the contamination of the online signal. The imbalance between the online and offline signal modifications is largely the cause of the retrieval error, and therefore if cross signal contamination were an unavoidable source of error it would be become one of the drivers for a heterodyne systems configuration. As it is however the error associated with cross signal contamination may be avoided by selecting a suitable PRF, and therefore the relationship between the cross signal contamination error and the emission power ratio has no effect on the optimum system configuration (except for the PRF).

4.3 Summary

A heterodyne detection TC-DIAL system is required to operate with a very high PRF, which presents the possibility of cross signal contamination occurring when measurements are made through thin cloud. A paper by Wylie et al. 2007 has provided global cloud statistics which state that approximately 70% of the Earth's surface is covered by some form of cloud, and 35% of this consists of cloud with an optical depth of < 3. It has been shown in this chapter through computer simulation that a heterodyne system based on current technology is relatively insensitive to signal attenuation by thin cloud and incurs additional errors associated with cloud cover of less than 4 ppm through a cloud with an optical depth of up to 3. It has also been shown that for a cloud optical depth of 2, an uncertainty of approximately 16 ppm would be additionally introduced to the overall retrieval error should cross signal contamination occur. Based on this information it is concluded that avoidance of cross signal contamination is important in order for a heterodyne detection system to be able to see through thin cloud and gain up 25% global coverage.

Using the aforementioned cloud statistics provided by Wylie et al. 2007, the altitudes at which cloud is most infrequent have been identified and converted into the associated PRF's of 5 and 15 kHz.

Closer investigations into the causes of the errors associated with cross signal contamination have revealed that the emission power ratio is a driver for the magnitude of the contamination, and that by careful selection it would be possible to reduce the impact of the contamination for the appropriate altitude of cloud (such as 5 km). However, cross signal contamination may be avoided by careful selection of the PRF, and the emission power ratio is one of many parameters which are used in the optimisation of a TC-DIAL system which guarantee a permanent improvement in retrieval uncertainty. Based on these facts the emission power ratio is not used to minimise the cross signal contamination error.

Through investigation into the sources of the TC-DIAL retrieval uncertainty by cross signal contamination it has been shown that the uncertainty is applied to the retrieval unevenly between the online and offline signals. The uneven distribution of the uncertainty is a result of both the emission power ratio favoring the online signal and to a lesser extent the altitude of the clouds. At higher altitudes the backscatter from clouds is dominated by the online signal owing to its much greater emission power. However the scattering from the Earth's surface (and potentially very low clouds) is much stronger for the offline signal owing to the online signal having been strongly absorbed by atmospheric CO_2.

Compensation for the errors introduced by cross signal contamination is likely to be difficult. The most obvious methodology would be to utilise information collected by the TC-DIAL instrument from previous pulses to compensate for the proceeding contamination. However, although the TC-DIAL instrument collects information on the signal intensity received from cloud scattering in the previous pulse, the signal received is likely already contaminated from the pulse before that, rending it almost impossible to distinguish the scattering caused by the cloud against the scattering from the surface, particularly as cloud is spatially and temporally highly dynamic.

5. Optimisation of a current technology space-borne TC-DIAL instrument for measuring atmospheric carbon dioxide

The active remote sensing technique TC-DIAL has been put forward as a potentially suitable instrument for complementing the existing CO_2 measurement systems by measuring total column atmospheric CO_2 from a low Earth orbiting satellite platform at all latitudes both day and night. Feasibility studies have explored this possibility by investigating much of the parameter space surrounding TC-DIAL retrieval errors through the computer simulation of instruments parameterised with definitions for the latest technology at the time of writing. Despite the thoroughness of the research conducted to date the findings of the reports and papers in the scientific literature (in particular the optimisation of the systems) often include what is now out of date technology, especially with regard to the detector technology which has recently improved (Ehret and Kiemle, 2005; Loth et al., 2005). In addition the feasibility studies have often failed to demonstrate the relative importance of some of the key instrument parameters and sources of error in influencing the systems optimisation strategy such as the integration path length, instrument pulse repetition frequency and spectral dependency of some of the ancillary data products used in the retrieval.

This chapter builds on previous work by focusing on particular aspects of the TC-DIAL retrieval parameter space to demonstrate the importance of key error sources that are not yet fully realised in the context of defining the optimum system configuration. This chapter also introduces novel investigations into the effect of the systems integration distance on the systems optimum configuration, the definition of the systems optimum pulse repetition frequency (PRF) and a demonstration of the importance of spectrally dependent ancillary data in the system optimisation process. The conclusions drawn from the individual studies point toward an optimum TC-DIAL system configuration based on current technology and an approximation for the retrieval error capability of such a system.

Throughout this chapter references are made to particular aspects of the optimisation process that are currently inaccurately derived or incomplete in the scientific literature followed by descriptions of how they are improved in this thesis to derive a more accurate and in some cases better justified optimum system configuration.

5.1 Key sources of error for space-borne TC-DIAL retrievals of atmospheric CO_2

The dominant error sources affecting CO_2 TC-DIAL retrievals from a space-borne platform are determined by the instrument configuration and the capability of the technology the system is based on. This section defines the approximate magnitudes of the main TC-DIAL retrieval error sources for a system based on current technology to ascertain the error drivers and the technology development priorities. Upon determination of the approximate error magnitudes the overall system optimisation strategy is investigated and determined for two different science driven scenarios known as the clear sky optimisation scenario and the cloudy sky optimisation scenario (see section 5.2).

5.1.1 Primary TC-DIAL retrieval error dependencies and parameter space

The accuracy and precision of TC-DIAL CO_2 retrievals depends on the magnitude of uncertainties that affect the parameters used to determine the atmospheric concentration from the measurements made. The first uncertainty in the measurement process is introduced to the system through the received online and offline signal intensities which form the differential optical depth (DOD) (equation 149).

$$\Delta\tau(R) = \frac{1}{2}\ln\left[\frac{S_{off}(R)E_{on}}{S_{on}(R)E_{off}}\right] \qquad 149$$

where $\Delta\tau$ is the total column differential optical depth, S_{on} and S_{off} are the online and offline received signal intensities, and E_{on} and E_{off} are the online and offline emission intensities (Bruneau et al., 2006).

The signal intensities S_{on} and S_{off} are determined by the measurement of the electrical current generated on the instrument's detector. The detector noise (dark current) adds a fluctuation to both the online and offline received signal intensities which propagate through as an error in the measured DOD. Other key errors which adversely affect the magnitude of the received online and offline signals are the surface reflectance variability between the online and offline signals and the laser frequency stability which are described and quantified in sections 5.1.2 and 5.1.3.

The relative error in the measured DOD may be given by equation 150 (Bruneau et al., 2006).

$$\frac{\sigma(\Delta\tau)}{\Delta\tau} = \frac{1}{2\Delta\tau}\left\{\left[\frac{\sigma(S_{on})}{S_{on}}\right]^2 + \left[\frac{\sigma(S_{off})}{S_{off}}\right]^2\right\}^{1/2} \qquad 150$$

where the left hand term in equation 150 is the relative error for the measured DOD.

The minimisation of the DOD error function is a critical system design requirement for achieving the optimum measurement precision. The error function may be adjusted either by altering the magnitude of the measured DOD (τ) or by altering the error associated with the measured signal intensities (S_{on} & S_{off}).

The magnitude of the measured DOD may be defined by selection of the laser emission frequency (Figure 5.1.1-1). Moving the emission frequency closer to the spectral line centre increases the magnitude of the DOD and therefore (as shown by equation 150) decreases the DOD's relative error.

A consequence of increasing the magnitude of the DOD however is a reduction in the received online signal intensity due to greater absorption by atmospheric CO_2. A reduction in the signal intensity at the receiver implies a smaller signal to noise ratio (SNR) and therefore an increased retrieval error via detector noise. A balance between the magnitude of the DOD, the error introduced by detector noise and the parameters which influence the intensity of the received signal (surface reflectance, emission power and pulse repetition frequency) is required to optimise the accuracy and precision of the CO_2 retrievals.

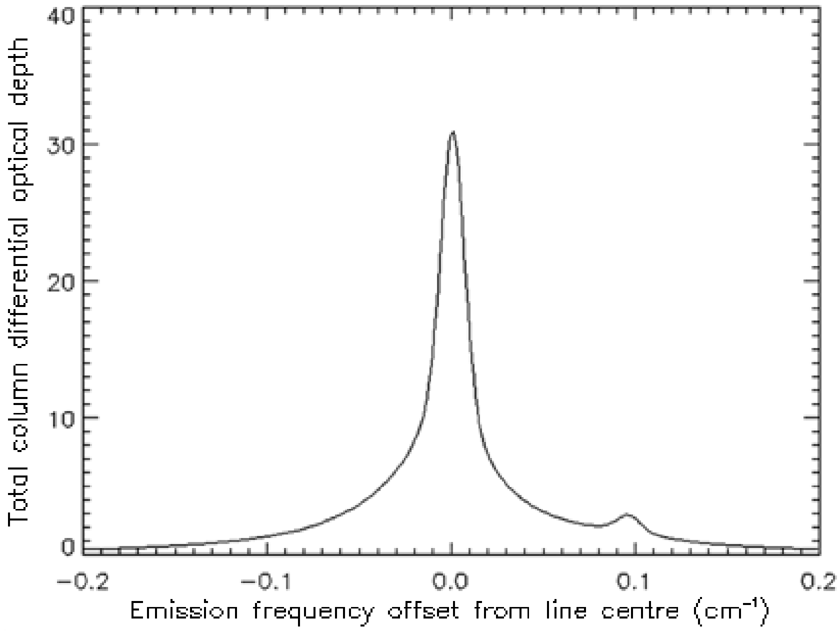

Figure 5.1.1-1 Total column optical depth as a function of online emission frequency offset from the centre of the 4875.748957 cm^{-1} (2 µm) spectral absorption line – image produced by the TCDS (Chapter 3)

The optimisation process for the measured DOD depends greatly on the detection technique employed owing to significant differences in the detector noise statistics between heterodyne and direct detection. The magnitude of the DOD error caused by both detection techniques forms a significant component of the overall retrieval error, and the systems sensitivity to particular error dependant parameters significantly varies depending on the technique used. No obvious superiority between the two techniques exist which would allow one of the techniques to be immediately omitted, therefore independent consideration of both detection methods for the DOD optimisation is required to assess their relative capabilities and optimisation conditions (see sections 5.1.5 and 5.2).

In addition to the DOD measurement containing uncertainties, the process of converting the DOD into an atmospheric concentration in ppm introduces further sources of error. Equation 151 presents the weighting function calculation which translates the measured DOD into an atmospheric VMR.

$$\nu(i) = \left[\frac{N_{av}}{(m_a g(i))\left(1 + \frac{m_w}{m_a}\rho_w(i)\right)}\right]\left(\sigma_{on}(i) - \sigma_{off}(i)\right) \tag{151}$$

where ν is the weighting function used in the CO_2 retrieval, i represents atmospheric pressure levels, g is the acceleration due to gravity (9.81 ms^{-2}), m_a is the molar mass of dry air (0.029 kg),), m_w is the molar mass of water vapour (0.018 kg), ρ_w is the atmospheric water vapour mixing ratio, σ_{on} and σ_{off} are the absorption cross sections for the online and offline pulses and N_{av} is Avogadro's number (6.022×10^{23} mol^{-1}) (Bruneau et al. 2006; Loth et al., 2005).

The atmospheric temperature, pressure and water vapour concentration values which are used to define the weighting function and the absorption cross sections are most likely to be determined for the entire Earth from numerical weather prediction models which have reasonably high levels of uncertainty (Table 2.3.1-1). The uncertainties in the NWP derived atmospheric properties are translated into an error in the derived CO_2 concentration via two separate routes. First the real atmospheric water vapour concentration (ρ_w) is misrepresented in the weighting function by the uncertainties in the NWP model, and the difference incurred between the real concentration and that used in the retrieval generates an error in the derived VMR. Secondly some of the atmospheric properties derived from the NWP model are used to constrain a spectroscopy model to define the absorption cross section profiles (σ_{on} & σ_{off}). In the presence of atmospheric profile uncertainties the absorption calculation incorrectly determines the concentration of atmospheric CO_2 present for a given quantity of absorption.

The errors introduced to the weighting function by uncertainties in the ancillary data are separate from those introduced in the measurement process onboard the satellite (Figure

5.1.1-2), however the relatively large magnitude of the ancillary data errors and their spectral dependency (particularly temperature and pressure) introduce a strong influence on the optimum configuration of the satellite instrument. In the scientific literature the spectral dependency of the ancillary data is commented on as being relevant to the systems configuration (Loth et al., 2005). However it has never been demonstrated in the process of determining the optimum configuration and as such its importance in this context has never been properly explored (section 5.2).

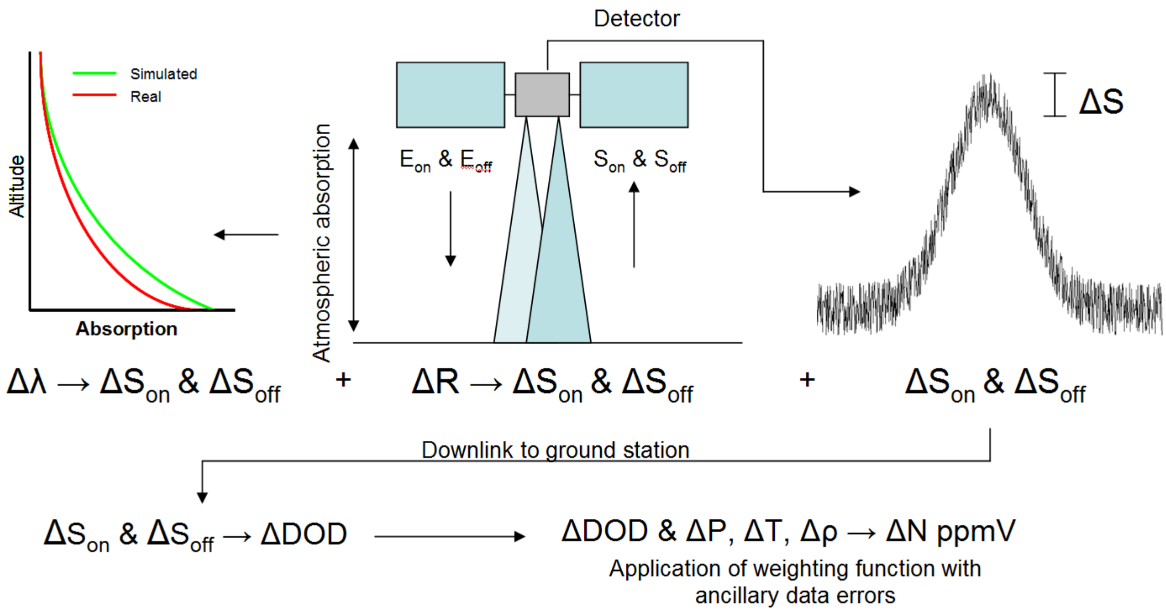

Figure 5.1.1-2 Diagram representing the key sources of error for a space-borne TC-DIAL system, including laser frequency uncertainty (Δλ), surface reflectance variability (ΔR), detector noise and errors associated with ancillary data.

In addition to the omission of the spectral dependency of some of the key parameters in the optimisation process, the computer simulations performed and described in the scientific literature use spectroscopy parameters obtained from either the HITRAN 2000 or the HITRAN 2004 databases which have since been superseded by a more accurate and complete database (Rothman et al., 2009; Loth et al., 2005; Ehret and Kiemle, 2005). Since the publication of HITRAN 2004 significant improvements have been made in HITRAN's 2 μm spectroscopy by the addition of thousands of extra spectral lines and adjustments to the existing spectral lines (Toth et al., 2007). As a result of the missing and inaccurate data in their spectroscopy the previous studies reported in the literature have not realistically represented the effects of the spectroscopy in the region surrounding the 4875.74896 cm^{-1} spectral line on the systems configuration. Figure 5.1.1-3 demonstrates the difference between the HITRAN 2004 and HITRAN 2008 databases by comparing their line strengths and positions in the vicinity of the 4875.749 cm^{-1} spectral line.

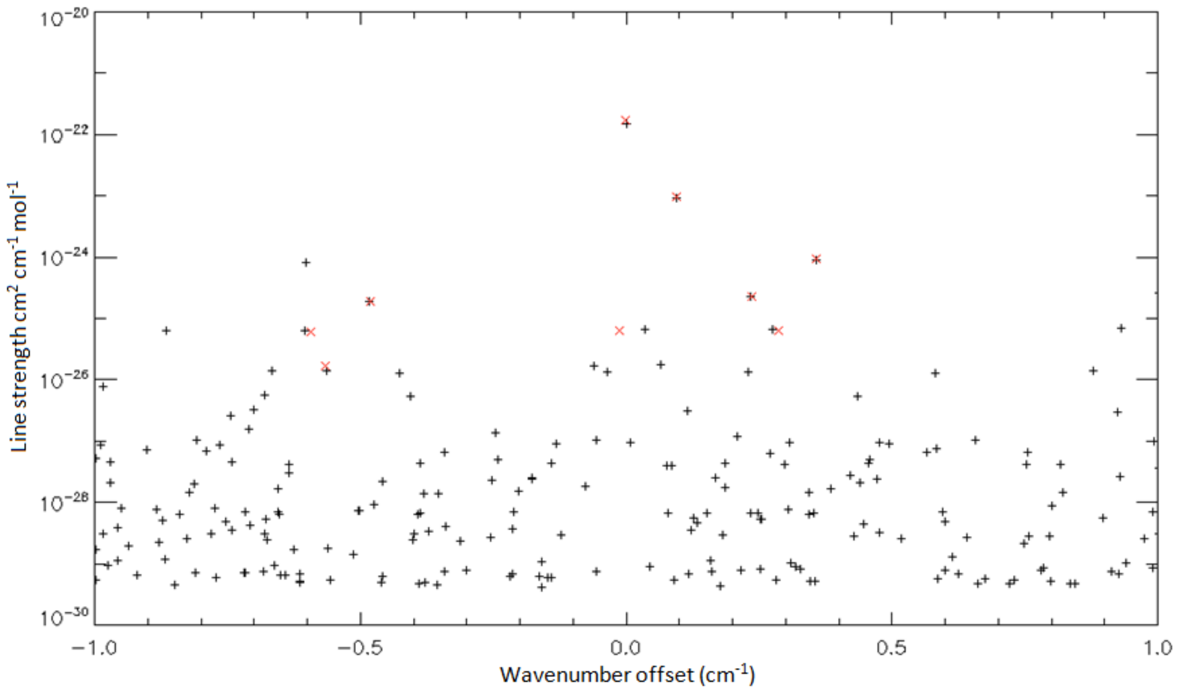

Figure 5.1.1-3 Spectral absorption coefficients as a function of wavenumber offset from the 4875.749 cm^{-1} spectral absorption line, black markers represent HITRAN 2008 (used by the TCDS), red markers HITRAN 2004.

The importance of including all relevant secondary spectral lines in the optimisation process for a TC-DIAL system is demonstrated in Figure 5.1.1-4, which shows the magnitude of the retrieval error difference between simulations that consider 1 and 9 of the most relevant spectral lines in the vicinity of the 4875.749 cm^{-1} spectral line for various detector NEP values. The simulations for the data presented in Figure 5.1.1-4 were produced using the TCDS computer model (Chapter 3) in its contour mode of operation with a system configuration given in Table 5.2-2.

As demonstrated by the change in the error magnitude as a function of laser emission frequency in Figure 5.1.1-4, without consideration for the secondary spectral lines the optimum system configuration would be incorrectly derived as it would not be properly influenced by all of the absorption features. The studies performed in this chapter use HITRAN 2008 for their spectroscopy to achieve a more complete picture of the influence that secondary spectral lines have on the optimisation process.

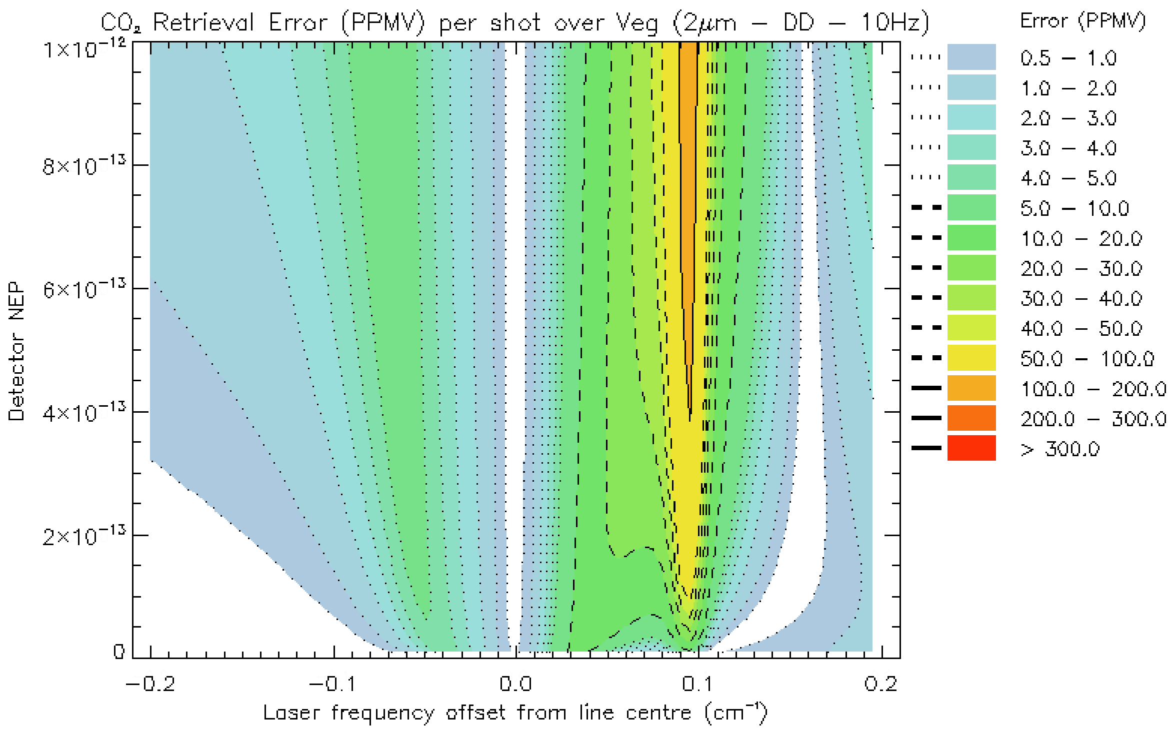

Figure 5.1.1-4 TC-DIAL retrieval error difference for a single sounding as a function of laser frequency offset from the centre of the 4875.749 cm^{-1} spectral line and detector NEP, showing the retrieval error incurred by omitting 8 of the 9 most relevant spectral lines for direct detection

The full parameter space surrounding TC-DIAL retrieval errors is extensive and much of it is unconstrained implying it can be adjusted to provide a more precise retrieval for either a given scientific objective or a given technology. Figure 5.1.1-5 presents a diagrammatic representation of the most important region of the TC-DIAL retrieval parameter space with particular focus on the number of photons received on the detector.

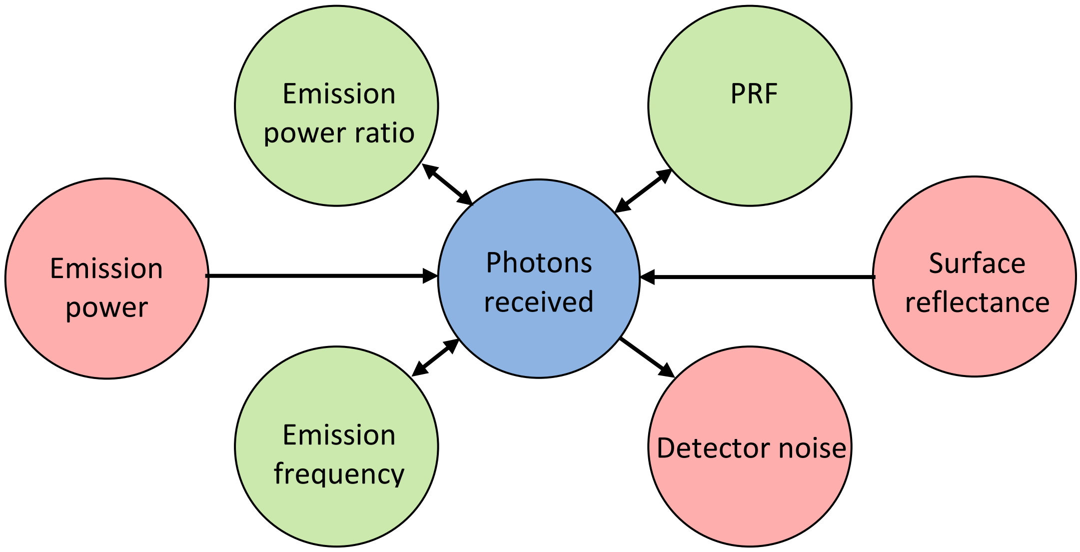

Figure 5.1.1-5 Diagram representing parameter space dependency on the received photons for a space borne TC-DIAL system, arrows indicate the direction of the dependency. Red circles are constants defined by technology parameters and green circles are adjustable parameters which are used in section 5.2 to optimise the system.

Figure 5.1.1-5 demonstrates that the number of received photons is heavily modulated by an extensive array of parameters. One of the most significant sources of uncertainty in the retrieval process is the error introduced to the DOD by the detector noise. It is generally desirable to receive as many photons as possible on the detector to attain a high signal to noise ratio (SNR), however for a satellite based system where available power is limited, reducing the number of photons received per sounding by rationing the available power over a greater number of soundings per measurement (increasing the PRF) can statistically improve the overall retrieval accuracy beyond the negative effects of a decreased SNR. In addition to this, the online and offline wavelengths can be emitted with different powers (E_{on} & E_{off}) to increase the magnitude of the DOD by adjusting the emission power ratio. This can statistically reduce the DOD error as shown by equation 150 despite the negative effect it has on the offline SNR. Both the emission power ratio and the pulse repetition frequency are therefore closely coupled parameters to the detector noise as they can both independently improve the retrieval accuracy but can also have negative consequences on the number of received photons at the detector.

Figure 5.1.1-6 and Figure 5.1.1-7 demonstrate the importance of using the online to offline emission power ratio as a free parameter in the optimisation process for heterodyne and direct detection by showing the TC-DIAL retrieval error as a function of emission power ratio and laser frequency offset from the 4875.748957 cm^{-1} spectral line (see Section 2.2). Figure 5.1.1-6 and Figure 5.1.1-7 demonstrate the presence of a spectral dependency associated with the emission power ratio as well as there being an optimum value made visible by the closing contours for both direct and heterodyne detection.

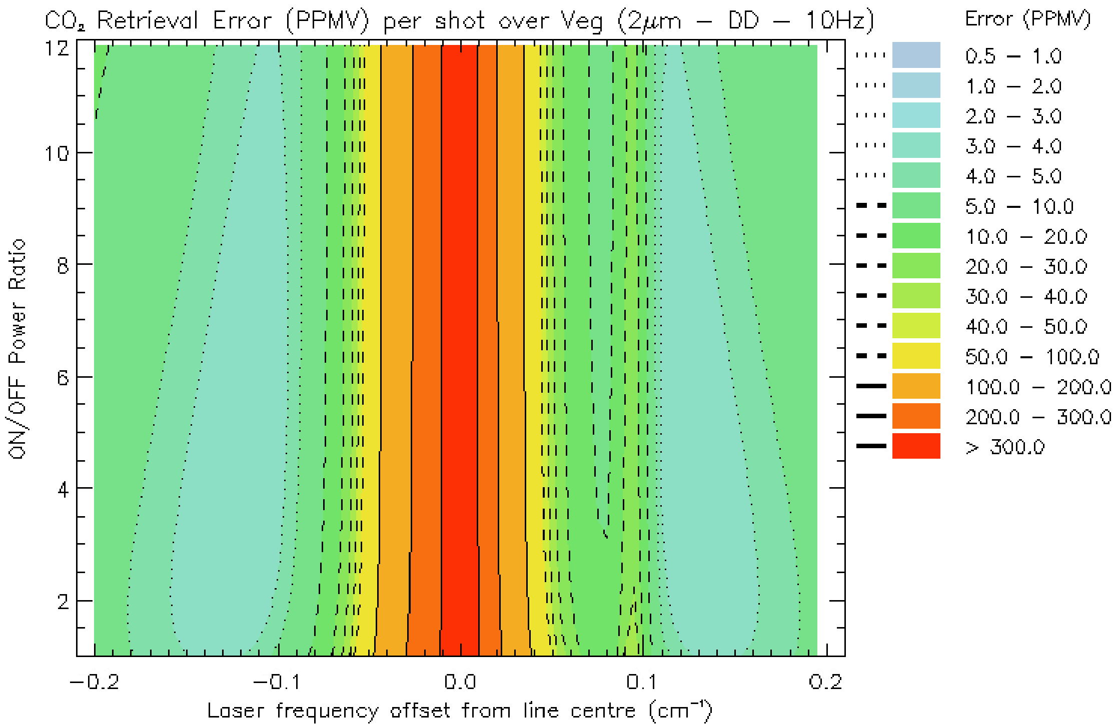

Figure 5.1.1-6 TC-DIAL retrieval error for a single sounding as a function of laser frequency offset from the centre of the 4875.748957 cm^{-1} spectral line and emission power ratio for a direct detection system over vegetation

The final system parameter which strongly influences the optimum system configuration is the laser emission frequency (particularly for the online pulse) which has indirect effects on the retrieval precision through its influences on the magnitude of the DOD and the number of received photons on the detector.

The strong sensitivity of the dependant parameters to the spectroscopy including the secondary spectral lines shown in Figure 5.1.1-4, Figure 5.1.1-6 and Figure 5.1.1-7 demonstrate that the optimisation process is required to include all of the relevant spectral lines to allow the system to be correctly influenced by the absorption features.

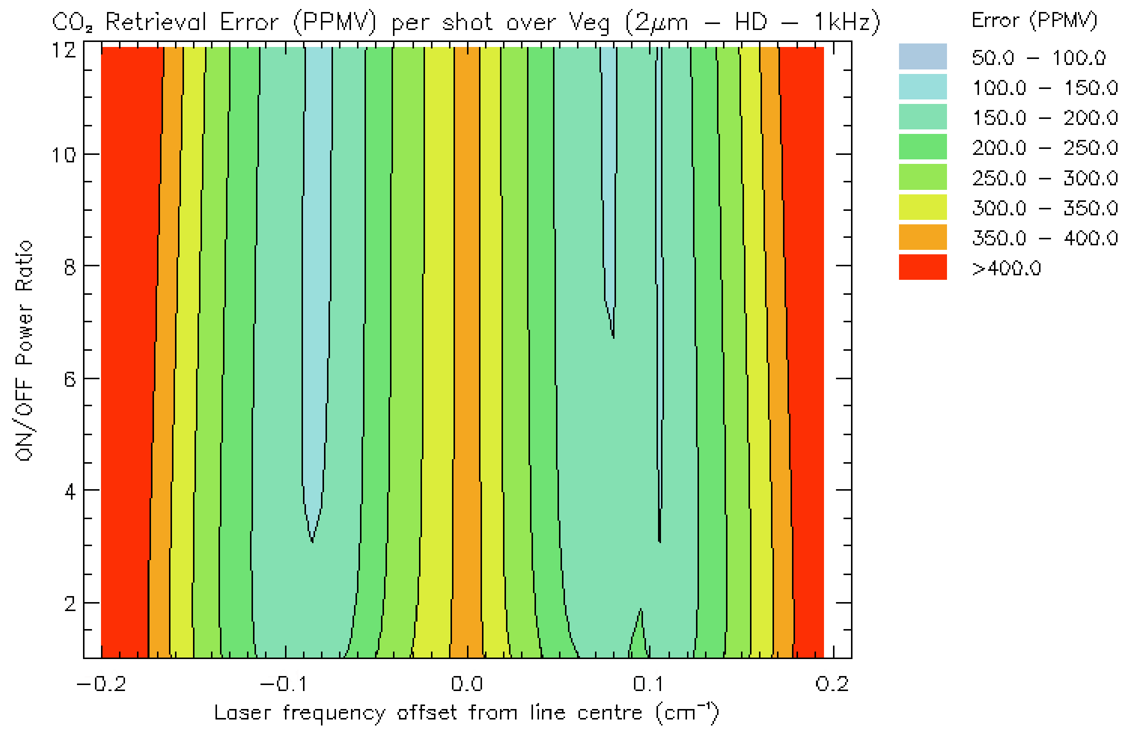

Figure 5.1.1-7 TC-DIAL retrieval error for a single sounding as a function of laser frequency offset from the centre of the 4875.748957 cm^{-1} spectral line and emission power ratio for a heterodyne detection system over vegetation

The relationships between the received photons, the emission power ratio, the PRF and the emission frequency form the primary adjustable parameter space which can be used to optimise a TC-DIAL system (see section 5.2). These parameters are presented as green circles in Figure 5.1.1-5.

The parameter space elements given as red in Figure 5.1.1-5 are considered fixed quantities as they are largely technology dependant and therefore unchangeable by instrument design. Of the red parameters displayed in Figure 5.1.1-5 the surface reflectance is the most unavoidable and has the largest effect on the retrieval error owing to its significant influence on the number of photons received at the detector during the mission. The number of photons received from desert scenes is over 7 times as many as those seen over vegetation and ocean scenes which in turn are over twice as many as those received from snow and ice scenes. The data presented in Figure 5.1.1-8 to Figure 5.1.1-10 show the approximate number of photons received on a space-borne TC-DIAL instruments detector for 3 different emission powers and 3 different surface types to demonstrate the relative importance of emission power and surface reflectance. The data for Figure 5.1.1-8 to Figure 5.1.1-10 were generated using the TCDS computer model to simulate a few days of surface reflectance measurements from the perspective of a TC-DIAL instrument in low Earth orbit (see Chapter 3). Each surface biome is separated from the series of measurements using a MODIS surface type map which is plotted for the entire Earth in Figure 5.1.1-11 (Strahler et al., 1999).

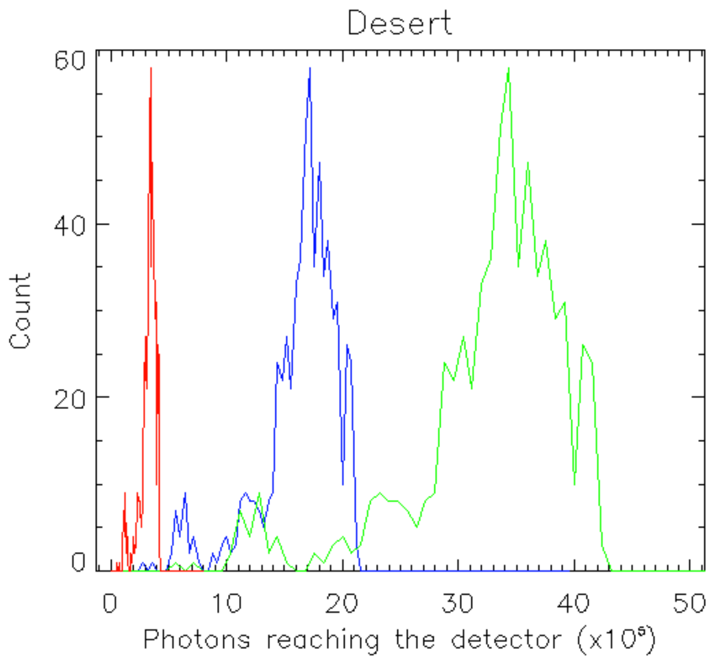

Figure 5.1.1-8 Histogram of surface reflectance's for the desert biome obtained from a simulated low Earth orbiting TC-DIAL instrument using the TCDS, red = 1 W, blue = 5 W and green = 10 W emission power

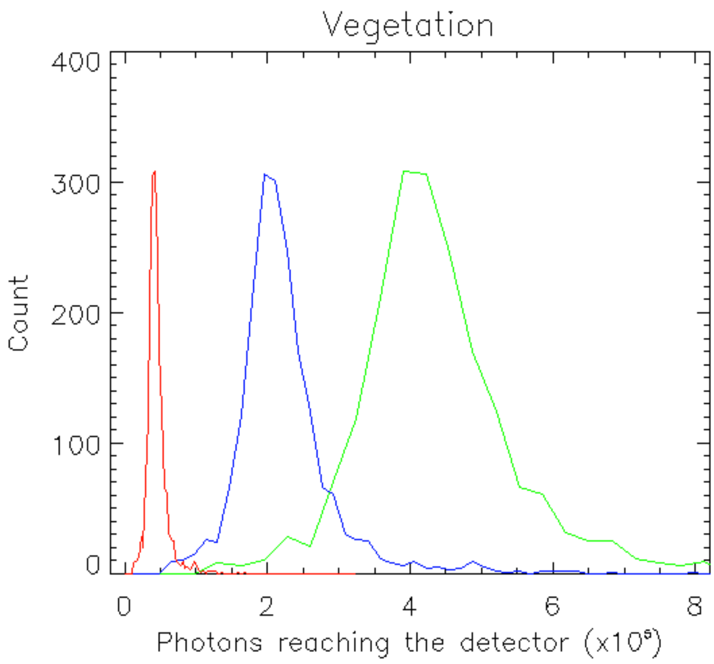

Figure 5.1.1-9 Histogram of surface reflectance's for the vegetation biome obtained from a simulated low Earth orbiting TC-DIAL instrument using the TCDS, red = 1 W, blue = 5 W and green = 10 W emission power

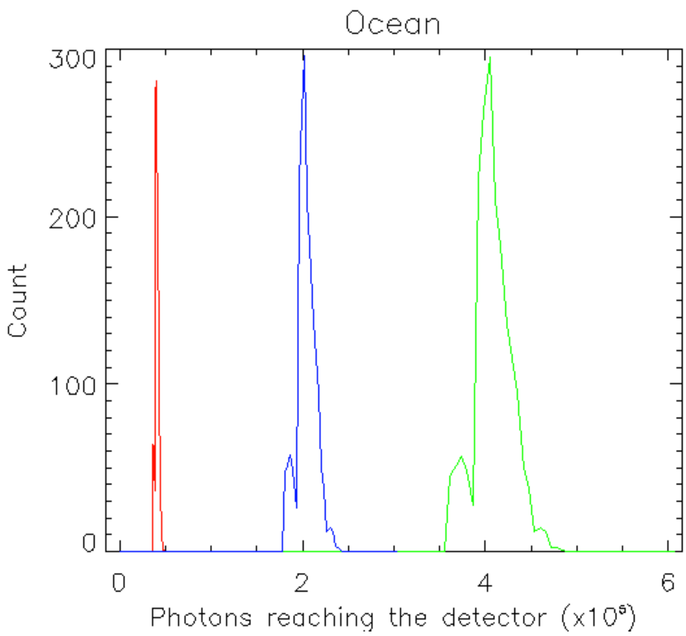

Figure 5.1.1-10 Histogram of surface reflectance's for the ocean biome obtained from a simulated low Earth orbiting TC-DIAL instrument using the TCDS red = 1 W, blue = 5 W and green = 10 W emission power

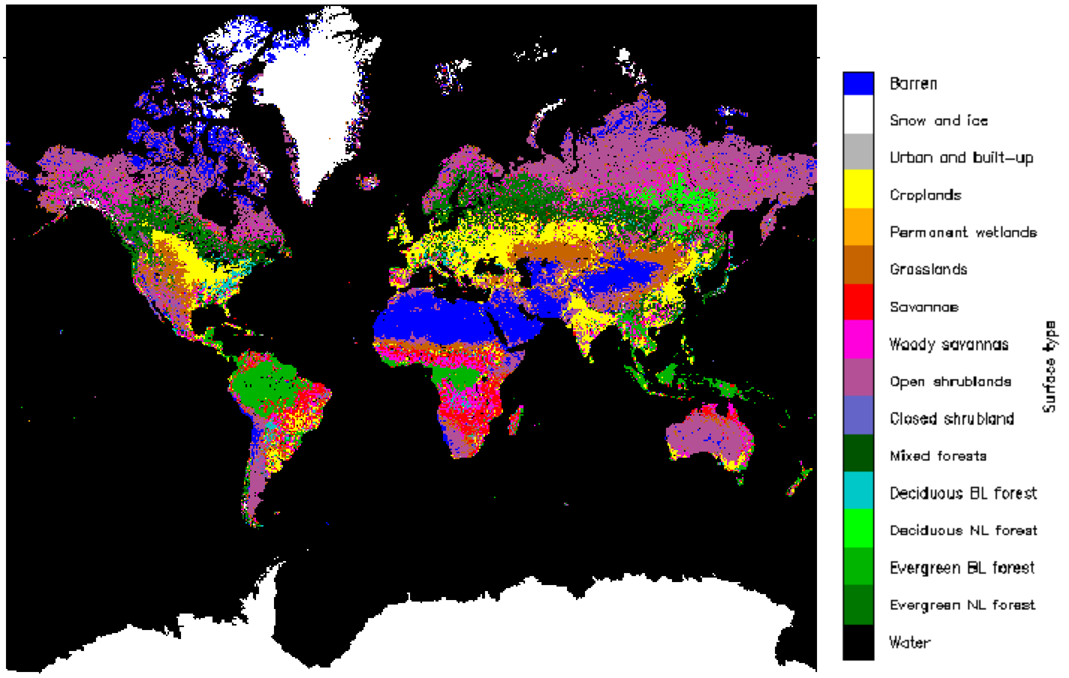

Figure 5.1.1-11 Land type map generated from MODIS surface type data

The difference observed in Figure 5.1.1-8 to Figure 5.1.1-10 for the number of received photons over each of the main biomes is significant, and no other individual parameter has such an unavoidable influence on the accuracy of the measured DOD. Figure 5.1.1-12 and Figure 5.1.1-13 demonstrate the effect that measurements over different surface biomes have on the precision of the DOD by showing the retrieval error difference between measurements made over snow and desert scenes as a function of laser emission frequency and emission power for direct and heterodyne detection. The contours in Figure 5.1.1-12 and Figure 5.1.1-13 show that there is a significant spectral dependency associated with the surface biome and therefore a strong influence on the optimum DOD. The results in Figure 5.1.1-12 and Figure 5.1.1-13 also demonstrate that the magnitude of the emission power plays a much less dominant role after approximately 0.5 W (at < 0.7 cm^{-1}) in comparison to the errors introduced by the difference in the surface reflectance between desert and snow scenes.

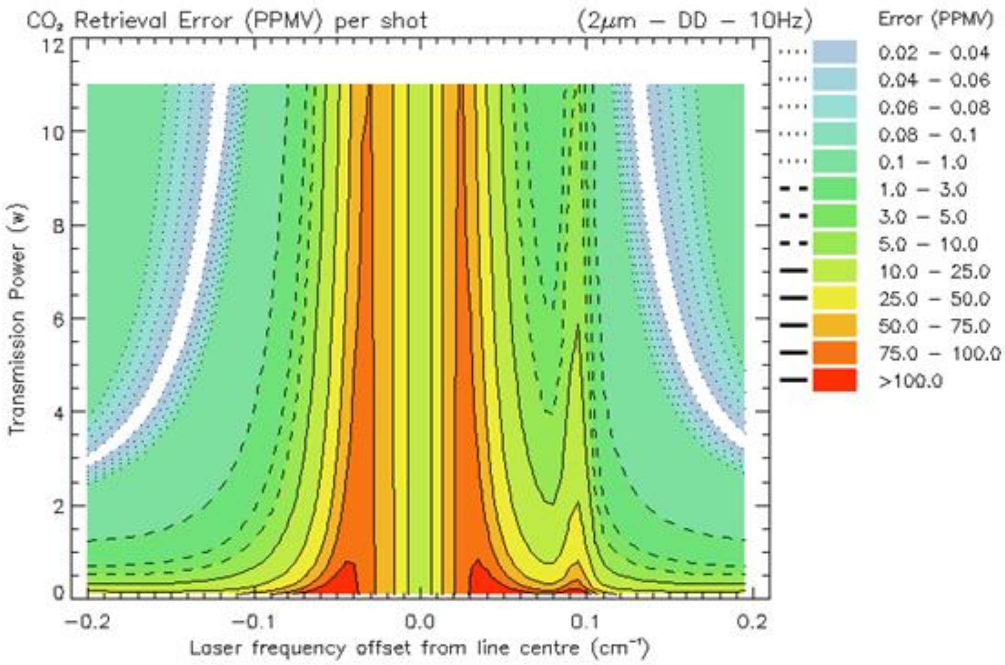

Figure 5.1.1-12 Retrieval error difference between snow and desert surface types as a function of laser frequency offset from 4875.748957 cm^{-1} spectral line and emission power for a direct detection TC-DIAL instrument parameterised using the system definition given in Table 5.2-2

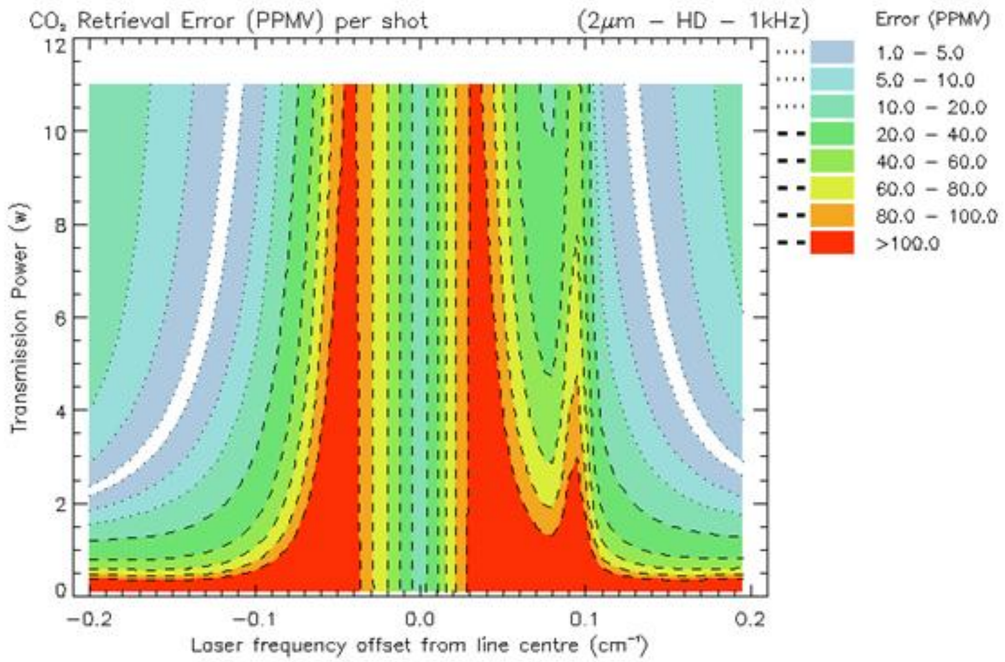

Figure 5.1.1-13 Retrieval error difference between snow and desert scenes as a function of laser frequency offset from 4875.748957 cm^{-1} spectral line and emission power for a heterodyne detection TC-DIAL instrument parameterised using the system definition given in Table 5.2-2

The magnitude of the effect that surface reflectance has on the retrieval accuracy implies that a TC-DIAL system is required to be optimised for one particular biome. For a 5 W emission power at approximately -0.8 cm^{-1} from the 4875.749 cm^{-1} line centre the retrieval error difference between snow and desert scenes for a direct detection TC-DIAL system operating at 10 Hz PRF is shown in Figure 5.1.1-12 to be approximately 4 ppm.

Both vegetation and ocean surface reflectances are conveniently very similar for a 2 µm TC-DIAL system, and this fact coupled with their importance to the global carbon cycle (see Chapter 1) implies a TC-DIAL system would likely be optimised for these two biomes.

5.1.2 Laser frequency stability

Amongst the technical requirements for a laser to perform as part of a TC-DIAL system is its ability to maintain a consistent emission frequency throughout the mission lifetime (>1 year). Frequency locking techniques have been developed and demonstrated as part of terrestrial DIAL systems (Koch et al., 2008; Gibert et al., 2006) (see Chapter 2), and identifying the errors likely to be incurred for a given frequency uncertainty provides perspective on the frequency locking capabilities of such laser developments. The laser frequency uncertainty is one of many spectrally dependant parameters within the TC-DIAL system which is required to be accommodated in the system optimisation process in order to influence the magnitude of the DOD (see Section 5.2).

The error introduced by a frequency deviation is investigated in this section as a function of laser frequency. The results are generated using the TCDS computer model in its contour mode of operation in two dimensions by iteratively adjusting both the laser frequency and its frequency modulation (see Chapter 3). The frequency adjustment is applied in the TCDS spectroscopy model by adding a frequency offset to the sampling position of the spectral absorption line. The absorption coefficients derived for the retrieval are left unaltered, and the resulting difference between the absorption in the physical simulation and the coefficients in the retrieval lead to a realistic representation of the measurement error incurred for a given frequency deviation.

The frequency stability simulations are run twice to determine the importance of considering multiple spectral absorption lines. The first simulation uses only the 4875.749 cm^{-1} (2 μm) spectral line whilst the second simulation uses nine of the most dominant spectral lines in the vicinity of the 4875.749 cm^{-1} spectral line. To isolate the frequency uncertainty error in the retrievals the simulations are run in the absence of any other source of error. The results are presented in Figure 5.1.2-1 and Figure 5.1.2-2 for the single and multiple spectral line simulations and Figure 5.1.2-3 for the difference between the two for simulations using systems configured as in Table 5.2-2 for soundings integrated over 50 km.

The results from the frequency stability study show a significant error dependancy on both the emission frequency and the position of secondary spectral absorption lines as demonstated by Figure 5.1.2-3. The magnitude of the errors observed are driven by the gradient of the spectral absorption lines in the frequency domain.

The absorption line features evolve as they pass through the atmosphere as a function of altitude including broadening and shifting. The change in the line shapes with altitude introduces a level of smearing in the error as a function of spectral position.

To attain a reasonable differential optical depth the emission frequency must be in the vicinity of ± 0.1 cm^{-1} from the centre of the 4875.749 cm^{-1} spectral line, however the results presented in Figure 5.1.2-2 suggest that the -0.1 cm^{-1} option is more favourable owing to the presence of secondary spectral absorption lines on the positive side of the 4875.749 cm^{-1} spectral line.

Random frequency uncertainties with a standard deviation of 1.9 MHz have been reported in the literature for a frequency locked crystal laser operating as part of a CO_2 DIAL system (Koch et al., 2008). Using the TCDS the retrieval errors expected to be incurred from the use of such a laser in a TC-DIAL system are calculated at approximately 0.4 ppm per sounding. Over a typcal integration distance of 50 km an error of 0.4 ppm per shot constitutes a measurement uncertainty of approximately 0.05 ppm for direct detection (10 Hz PRF). For heterodyne detection most random errors (aside from the detector noise) become significantly reduced by the very high pulse repetition frequency of the instrument and as a consequence have no discernable effect on the precision of the retrieval.

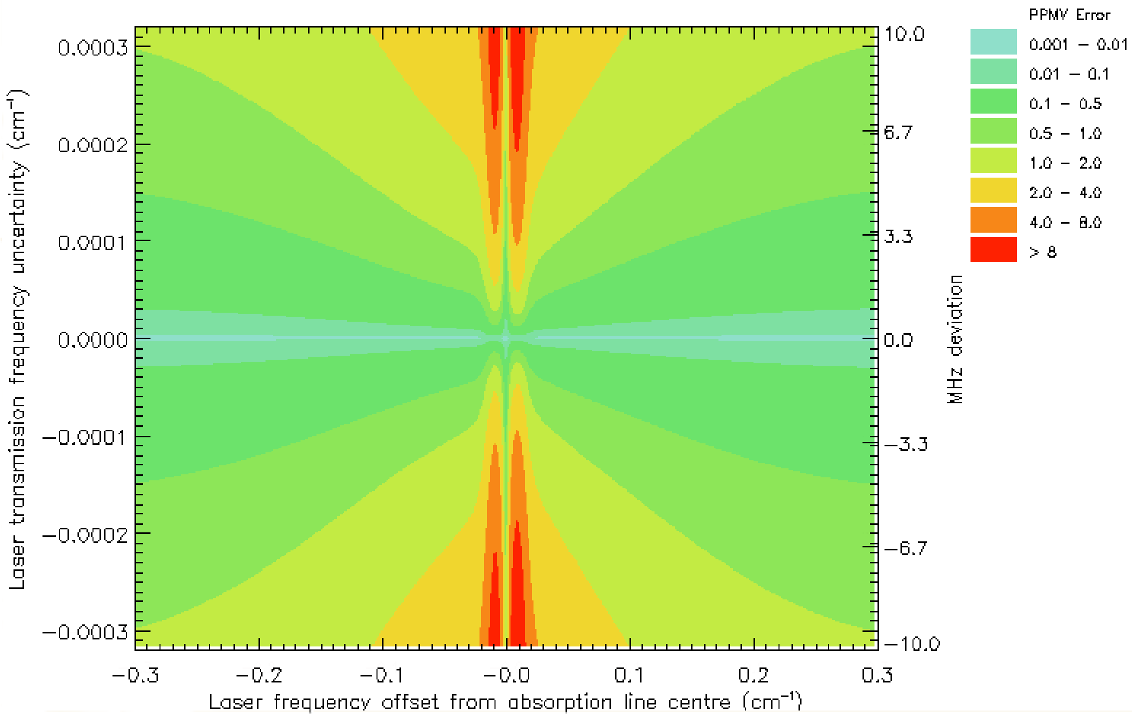

Figure 5.1.2-1 TC-DIAL retrieval error as a function of laser frequency uncertainty and laser frequency offset from an absorption line centre (1 spectral line)

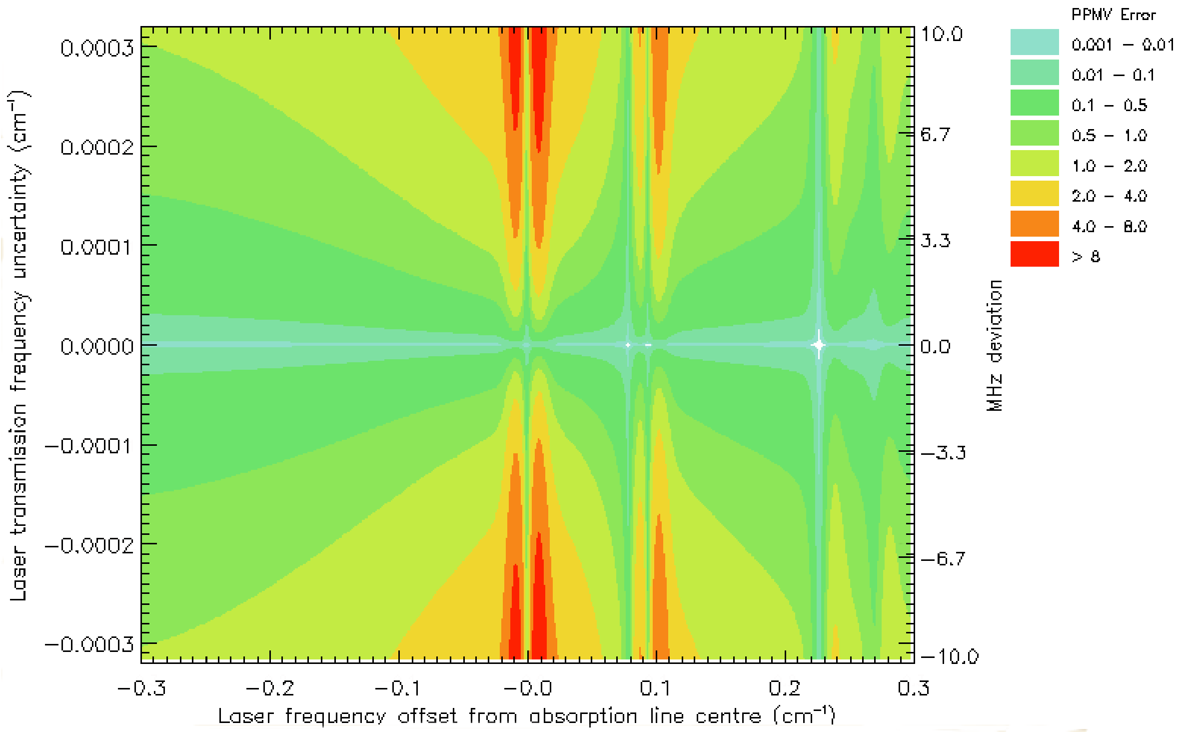

Figure 5.1.2-2 TC-DIAL retrieval error as a function of laser frequency uncertainty and laser frequency offset from an absorption line centre (9 spectral lines)

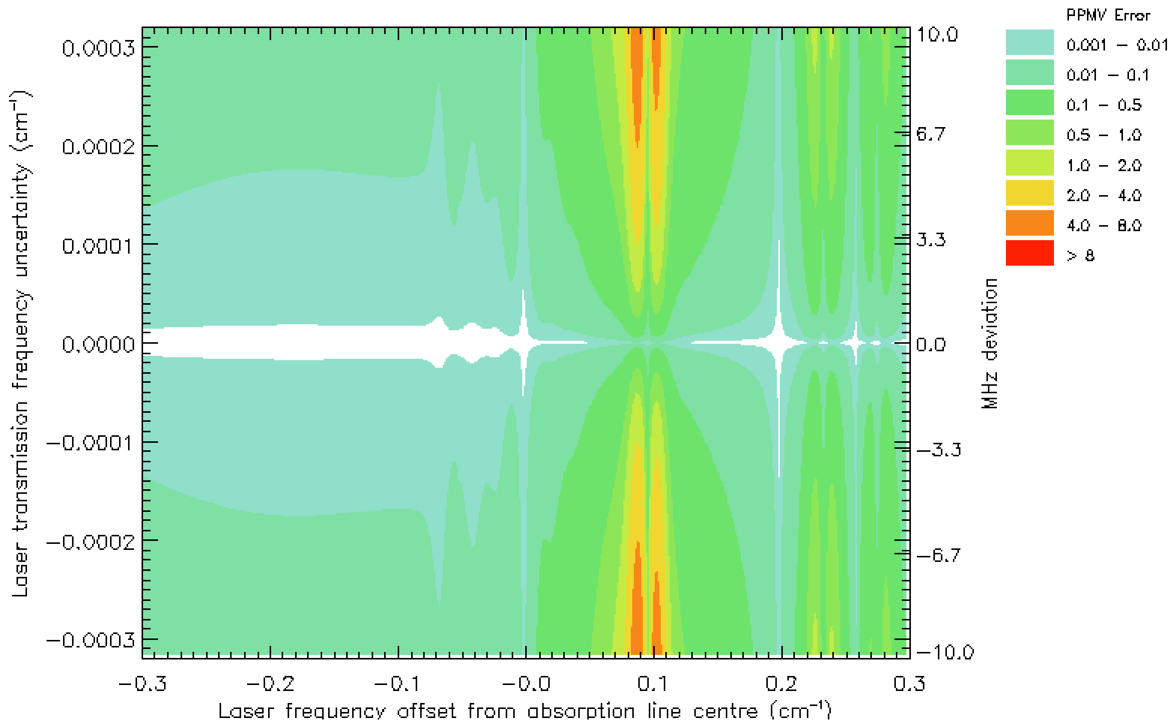

Figure 5.1.2-3 TC-DIAL retrieval error as a function of laser frequency uncertainty and laser frequency offset from an absorption line centre (difference between 1 and 9 lines)

5.1.3 Surface reflectance variability

The spatial variability of the Earth's surface reflectance introduces differences to the scattered intensities of the consecutively emitted online and offline LiDAR signals. The signal intensity differences incurred between the slightly offset online and offline footprints lead to uncertainties in the retrieved atmospheric CO_2 concentrations. The retrieval uncertainty introduced by the surface reflectance variability is one of the key error sources affecting space-borne TC-DIAL retrievals and as such is required to be included in the overall retrieval error budget.

The spatial offset between the laser emissions is caused primarily by two independent factors. First a temporal delay between laser emissions caused by the system waiting for the previous pulse to clear the lower atmosphere to avoid cross signal contamination results in a surface footprint separation of approximately 1.5 m owing to the satellites high orbital velocity (7 km s^{-1}) . Secondly, low amplitude vibrations within the satellite platform can lead to an effect known as laser pointing jitter which can introduce a further random offset between the online and offline surface footprint locations. Chapter 6 describes a study to determine an approximation for the magnitude of the retrieval errors incurred by surface reflectance variability over agriculture for the 2 µm wavelength. The results suggest an approximate random error of 0.19 ppm for 50 km's of measurements at 50 Hz PRF for a footprint separation of 10 m. A study in the scientific literature investigating the same effect but for the 1.6 µm wavelength over many different surface biomes derives a similar error of approximately 0.22 ppm (average) over the same number of soundings (Amediek et al., 2009). It was suggested by Amediek et al. 2009 that the footprint collocation ambiguity is likely to be much less than 10 m, and state that a 10 m overlap used in their study is an upper bound estimate. For the TC-DIAL error studies carried out in this chapter the retrieval errors are intended to correspond to the most likely error for a current technology system as opposed to an upper bound limit, and therefore a 5 m footprint overlap is assumed to be a more realistic surface footprint offset for use in this thesis. Chapter 6 determines an approximation for the retrieval errors incurred by a 5 m footprint separation and arrives at a value of 2.1 ppm per sounding.

5.1.4 Ancillary data

Ancillary data is required to provide information on the state of the atmosphere for the TC-DIAL retrieval. For satellite based dual wavelength TC-DIAL systems this data is likely to be derived from NWP models which have relatively high levels of uncertainty for this application. In addition to the high levels of uncertainty the limited spatial resolution of the NWP derived atmospheric properties (> 20 km) prevent the data from being able to be used as a random source of error over much of the measurement interval, implying the retrieval becomes heavily dependent on the accuracy of the data.

To determine the influence uncertainties in the ancillary data have on the system optimisation process the errors for the atmospheric properties are defined in frequency space to allow their influence on the optimum system definition alongside other spectrally dependant sources of error.

The uncertainties in the atmospheric pressure are introduced to the TCDS by applying an offset to the surface pressure used in the physical simulation. The offset in the surface pressure results in a difference between the pressure profiles used to define the spectroscopy for the retrieval and the profiles used in the actual simulation. The retrieval error introduced by surface pressure uncertainties is plotted in Figure 5.1.4-1 as a function of both surface pressure uncertainty and laser emission frequency.

The spectral dependency in the pressure uncertainty causes an increase in retrieval error as the laser frequency moves away from the centre of the spectral absorption line. The relationship displayed in Figure 5.1.4-1 implies that a lower DOD value will introduce a greater pressure error and therefore have the effect of pulling the optimum system toward the centre of the spectral line. For a surface pressure uncertainty of 1 hPa (0.1%) (Ingmann et al., 2008; Loth et al., 2005) the retrieval error per atmospheric measurement is approximately 0.59 ppm. This value is in good agreement with an equivalent figure derived by the TC-DIAL simulator in the FACTS report which derives a value of approximately 0.56 ppm for the same quantity of error. These two values are not expected to entirely agree owing to differences in their spectroscopy databases as the FACTS simulator uses HITRAN 2004 and the TCDS uses HITRAN 2008.

The magnitude of the temperature uncertainty for a space borne TC-DIAL system relying on NWP data is defined by the Aperge NWP model for a -0.1 cm^{-1} offset from the primary 2 µm spectral absorption line (4875.749 cm^{-1}). The error determined for temperature profile predictions by the Aperge NWP model arrives at a value of approximately 0.34 ppm per measurement. In order to incorporate this single uncertainty figure into the TCDS to become spectrally resolved for use in the system optimisation process the error defined by the Aperge NWP model is used as a normalisation coefficient to modify a spectrally resolved temperature error profile generated by the TCDS (see Chapter 3). The error profile initially generated by the TCDS uses a value of 1 K for the uncertainty in the temperature profile in order to attain the required spectral dependency. The temperature error profile produced from this process is presented in Figure 5.1.4-2.

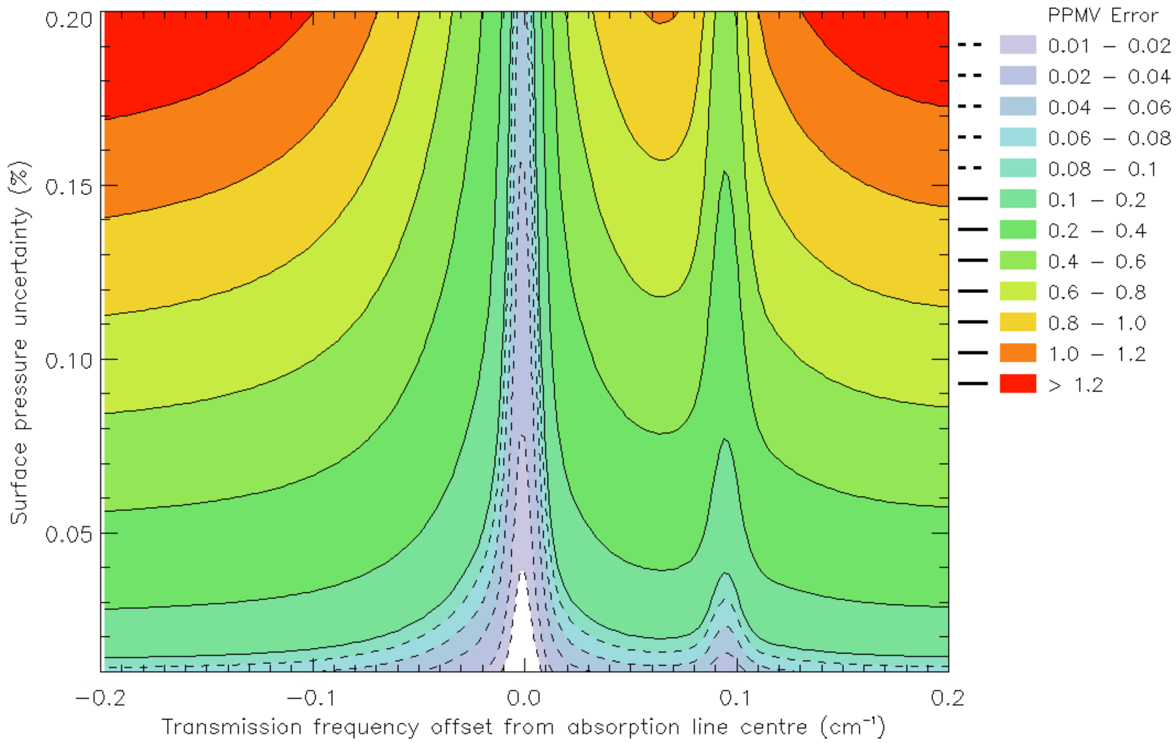

Figure 5.1.4-1 CO_2 retrieval error as a function of atmospheric pressure uncertainty and laser emission frequency for a single sounding

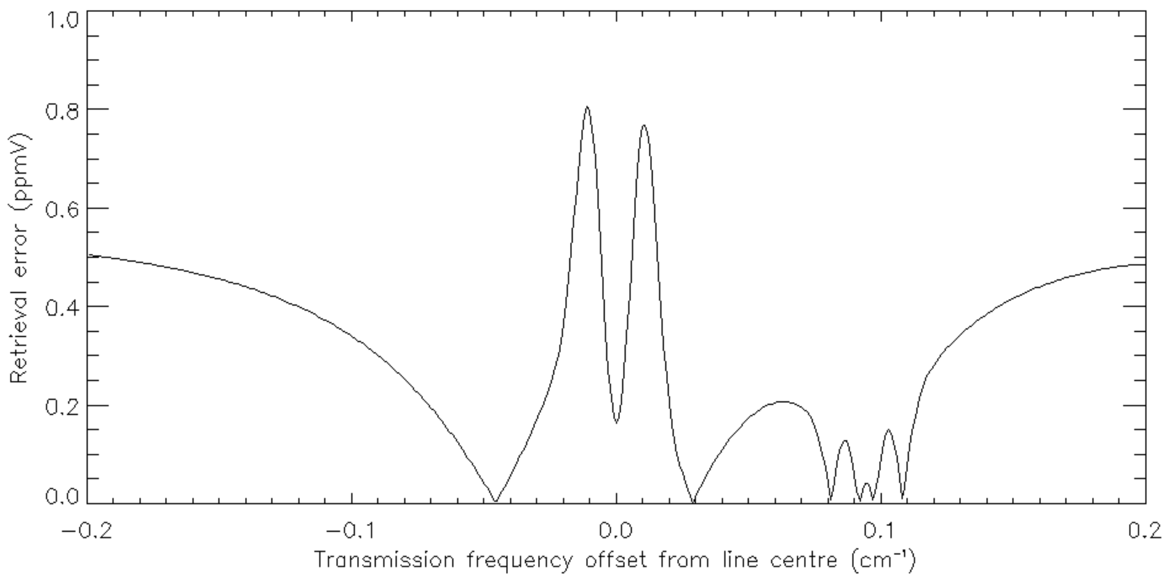

Figure 5.1.4-2 CO_2 retrieval error as a function of emission frequency offset for an atmospheric temperature error defined by the Aperge NWP model and expanded in the spectral domain by the TCDS (see Chapter 3)

The final ancillary data product used in the retrievals weighting function which contains a source of uncertainty is the atmospheric water vapour concentration. The water vapour parameter does not contain a significant spectral dependency owing to the laser frequency having been deliberately chosen to avoid water vapour absorption features. For this reason the water vapour uncertainty contribution is therefore accepted into the TCDS as a single uncertainty value defined by the FACTS report as approximately 0.13 ppm (Loth et al., 2005).

All three of the ancillary data errors are introduced to a TCDS optimisation algorithm described in Section 5.2. The temperature and pressure errors are introduced as spectrally resolved profiles in order to correctly influence the optimum laser emission frequency and therefore the magnitude of the DOD.

5.1.5 Detector noise

The primary driver for the total column DOD error is dependent on the detection technique employed by the system. For direct detection the error is highly sensitive to the magnitude of the detectors noise equivalent power (NEP) whereas for heterodyne detection the error is more sensitive to the magnitude of the instruments PRF. The following section details the noise characteristics introduced by both detection techniques in preparation for the optimisation process in Section 5.2.

5.1.5.1 Direct detection

The expressions defining the relative error in the measurement of the received signal intensities for direct detection is given by equations given in Section 2.3.2. Defining the error dependencies of the various terms within these functions is important for understanding their relevance to a current technology TC-DIAL system and to ascertain potential technology development priorities. To suitably compare the dependant parameters with an appropriate perspective they are plotted in two dimensions against each other with a region of interest highlighted to demonstrate the current capability of technology and a reasonable expectation of improvement in the near future.

The contributions to the measurement error by the detector efficiency and the number of incident photons received on the detector are plotted in Figure 5.1.5.1-1 for the system defined in Table 5.2-2.

A realistic detector efficiency range is presented in Figure 5.1.5.1-1 covering 0.7 (current capability) to 0.9 (an assumed level of improvement), and a realistic range for the incident photon numbers is also presented covering 0.5×10^4 to 5.0×10^4 assuming a 10 Hz PRF, a 5 W emission power and a range of reflectances spanning the main surface types on the Earth. The surface reflectances are derived using the TCDS orbit simulator in conjunction with its BRDF model to derive the number of photons returning to the detector for a given emission energy (see Chapter 3). The limits used in Figure 5.1.5.1-1 are based on current technology specifications with extensions to accommodate possible improvements in the future. The PRF optimisation process generally limits the number of received photons to the indicated window to statistically improve the retrieval accuracy (see section 5.2).

Figure 5.1.5.1-1 demonstrates that neither parameter is particularly dominant when viewing a large portion of the parameter space, however when constraining the window to a technologically constrained region it is clear that the number of received photons plays a much more dominant role over the detector efficiency owing to the large range of surface reflectances around the Earth.

The retrieval error is presented with respect to the detector efficiency and detector NEP in Figure 5.1.5.1-2. The constraining window in Figure 5.1.5.1-2 ranges from 0.7 to 0.9 for the detector efficiency, and 3×10^{-14} to 6×10^{-13} for the detector NEP. The limits for the detector NEP are obtained from two potential detector technologies. The larger value of the two is based on the previous 2 μm detectors quoted for application in a TC-DIAL system by the FACTS report which has recently been superseded by new InGaAs semiconductor detectors currently in development (Refaat et al., 2004). The new InGaAs semiconductor detectors have been quoted to have NEP values of approximately 5×10^{-14} which has been extend in the constraining window to 3×10^{-14} to allow room for improvement. Despite the generous technologically constrained window in Figure 5.1.5.1-2 the detector NEP is always the dominant parameter, with detector efficiency only beginning to play a role as the NEP increases beyond the window.

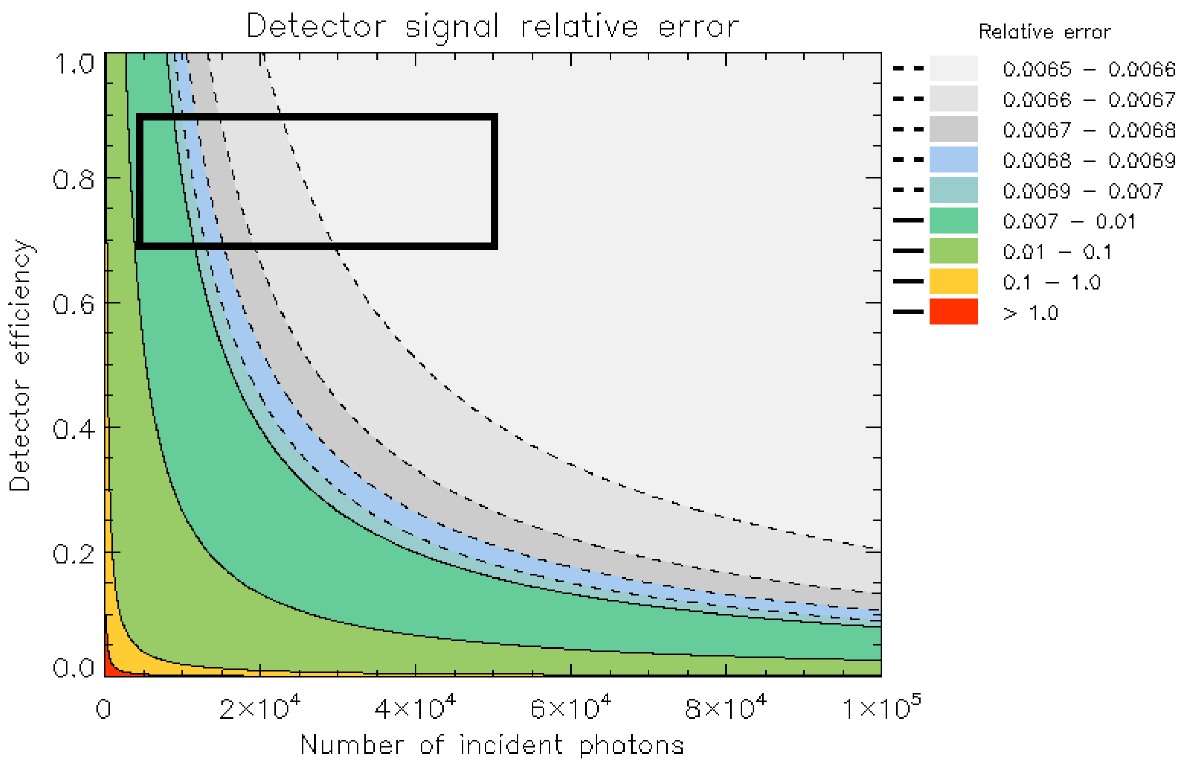

Figure 5.1.5.1-1 CO_2 retrieval error for a TC-DIAL system as a function of detector efficiency and number of incident photons with black box representing a region of current to future technology capability for a single sounding

In addition to Figure 5.1.5.1-2 indicating that the detector NEP is significantly more dominant than the detector efficiency across the range indicated, it also shows that decreasing the NEP much further beyond the latest technology will yield relatively little improvement in the retrieval accuracy for the TC-DIAL system simulated.

The significance of the recent InGaAs semiconductor developments for a 2 μm direct detection system is best demonstrated in Figure 5.1.5.1-3 which also highlights the lack of subsequent improvement that would be made by increasing the NEP much further for a current technology TC-DIAL system.

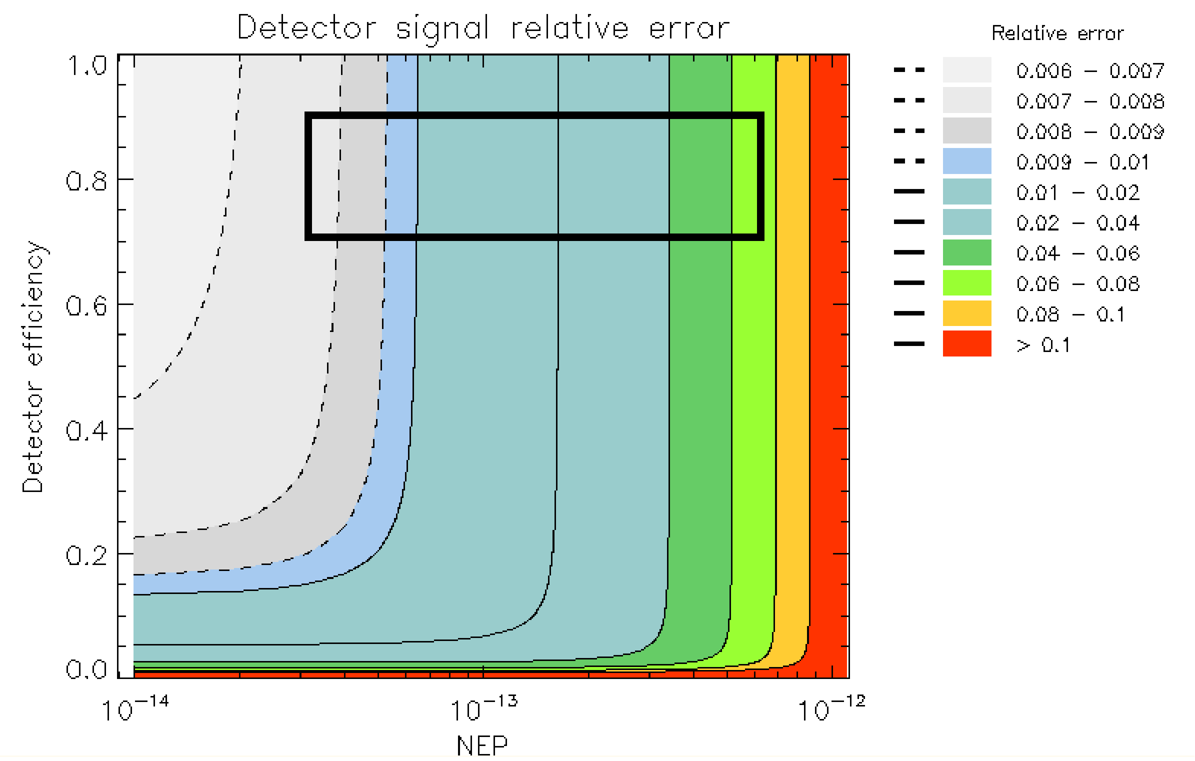

Figure 5.1.5.1-2 CO_2 retrieval error for a TC-DIAL system as a function of detector efficiency and detector NEP with black box representing a region of current to future technology capability

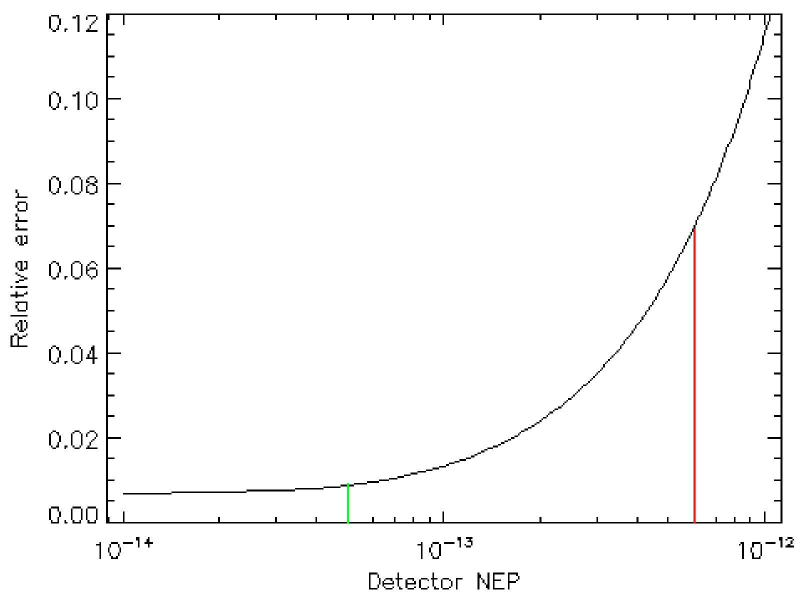

Figure 5.1.5.1-3 CO_2 retrieval relative error as a function of detector NEP showing new InGaAs detector NEP (green) and old detector NEP (red) suggested by the FACTS report

The significant improvements to TC-DIAL accuracy achieved by the recent advancements in InGaAs semiconductor technology have implications on a direct detection systems optimal configuration. The optimum TC-DIAL configuration is required to be recalculated for each major technology advancement to ensure the best retrievals possible are achieved.

To demonstrate the importance of the detector NEP on the optimum system configuration the TCDS computer model (see Chapter 3) has been employed to produce a spectrally resolved contour plot of retrieval error as a function of detector NEP for direct detection (Figure 5.1.5.1-4). The results in Figure 5.1.5.1-4 show that a change in detector NEP introduces a nonlinear change in retrieval error as a function of laser emission frequency from the spectral line centre. The implication of this relationship is that the optimum configuration will shift in the spectral domain when the value of the detector NEP changes and as such will influence the magnitude of the DOD and therefore the optimum system configuration.

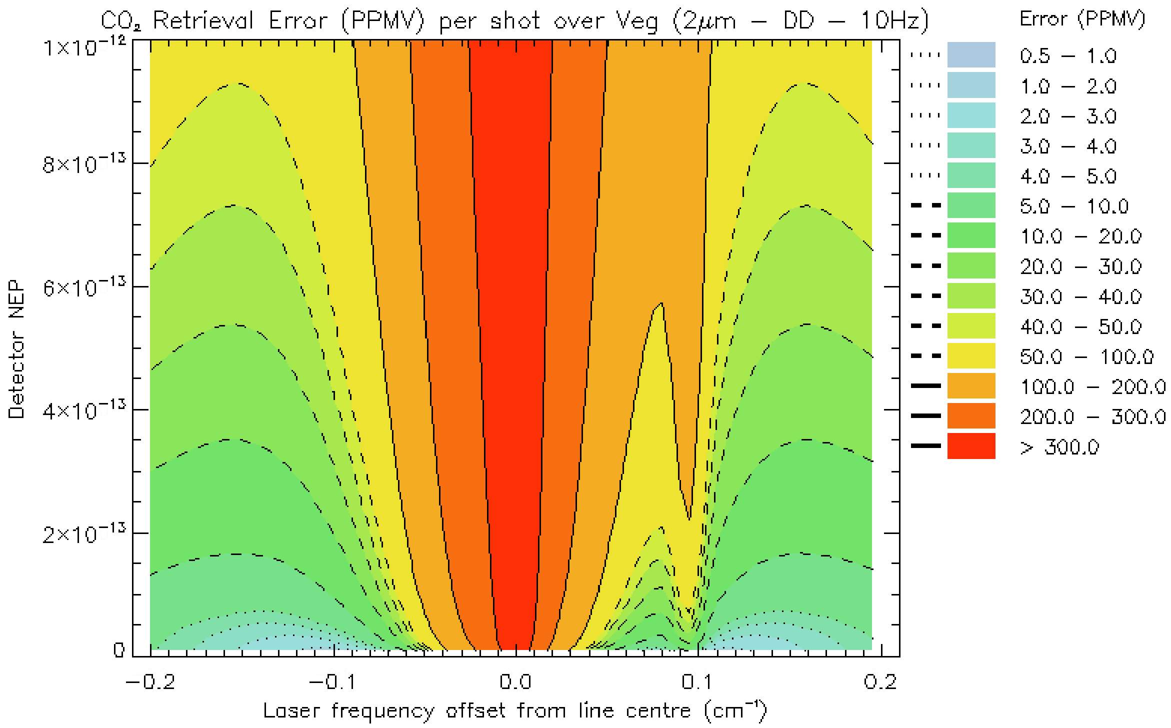

Figure 5.1.5.1-4 CO_2 retrieval error for a single sounding as a function of detector NEP ($WHz^{-0.5}$) and laser emission frequency offset from the 4875.748957 cm^{-1} spectral line for direct detection

At the current level of detector development receiving more photons on the detector has become a priority, and this has been partly demonstrated in Figure 5.1.5.1-1 where detector efficiency is superseded by the number of received photons. The relationship between the detector NEP and the number of received photons is further demonstrated in Figure 5.1.5.1-5 which shows that although the detector NEP and number of received photons can be adjusted to achieve improvements in retrieval uncertainty, within the technologically constrained window the number of received photons becomes ever more dominant as the detector NEP is improved (made smaller).

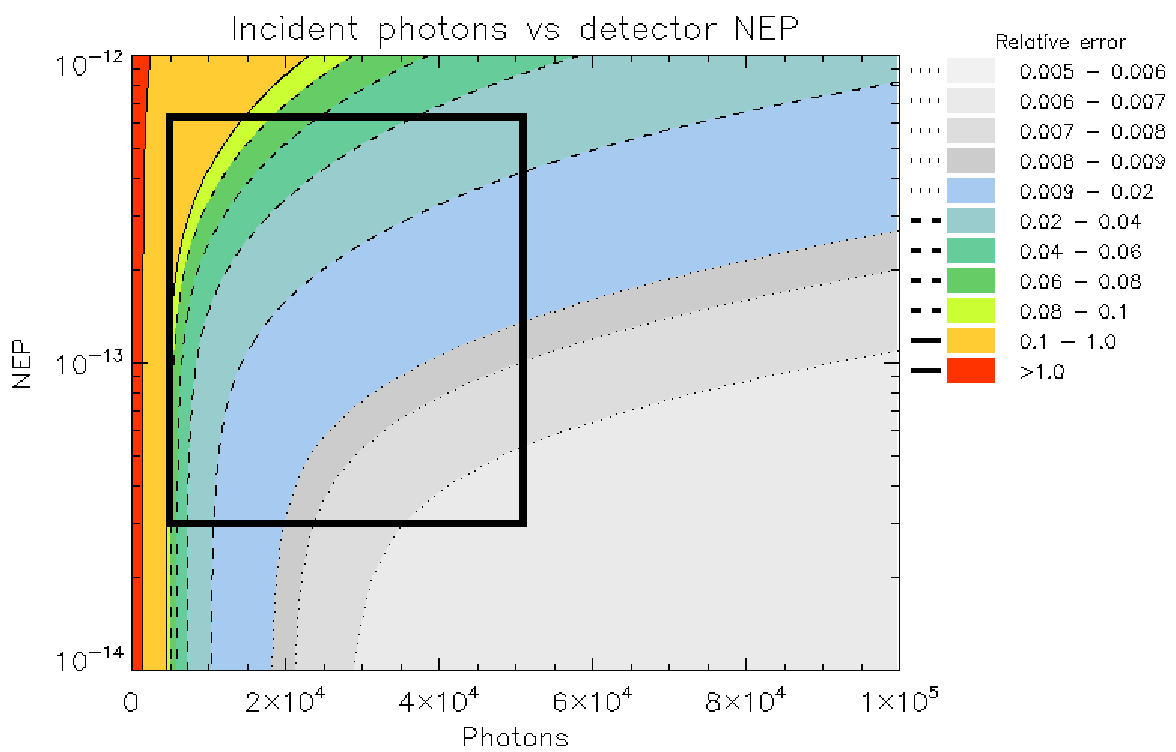

Figure 5.1.5.1-5 CO_2 retrieval error as a function of detector NEP and number of received photons with black box representing a region of current technology capability

In conclusion, it is clear from comparing the dependant parameters for the retrieval error associated with the direct detection of LiDAR signals received from the Earth's surface that the detector NEP and efficiency have reached a level of development that make them less of an influence on the overall retrieval error. Improvements in the detector NEP beyond the demonstrated capabilities of the InGaAs semiconductor detectors currently being developed would yield relatively little improvement in retrieval accuracy if laser emissions cannot exceed 5 W. The primary parameter now driving the error in the measured DOD is the magnitude of the received signal intensity which is heavily dependent on the surface reflectance and the emission power. Emitting a greater signal intensity is therefore a highly desirable technological advancement for direct detection, however this is physically limited by the availability of power onboard the satellite and the capability of the laser system to sustain a 5 W emission for over a year. Emitting 2 µm laser pulses at 5 W on a satellite system is currently a technological challenge, and therefore assumed as a fixed quantity for a near future TC-DIAL system in this thesis.

The number of photons received on the instruments detector for a given emission power can be influenced by adjusting the PRF. Increasing the PRF allows more pulses to be integrated over during a single measurement which has the effect of statistically reducing the random errors associated with the retrieval. An undesirable consequence of increasing the PRF is a decrease in the available energy per pulse which causes a decrease in the measurements SNR. Optimisation of a direct detection system therefore requires attention to the PRF as a free parameter. Despite the PRF's influence on the systems configuration and overall retrieval error the current scientific literature that reports on TC-DIAL system optimisation does not demonstrate the PRF as a free parameter in their simulations (Ehret and Kiemle, 2005; Loth et al., 2005).

Using the TCDS computer simulation the effect of the PRF on the systems optimum configuration is determined by varying the instruments emission power through a wide range of values to simulate the retrieval precision for pulse energies associated with various PRF's. The retrieval precision for each of the PRF simulations is then statistically reduced using Gaussian error statics (equation 152) to emulate the error associated with the series of soundings.

$$E_{ppmv} = \frac{\varepsilon_{ppmv}}{\sqrt{f_{prf}}} \qquad 152$$

where E_{ppmv} is the retrieval error integrated over a second, ε_{ppmv} is the one standard deviation retrieval error for a single sounding derived by the TCDS and f_{prf} is the instruments PRF.

The results of the PRF simulations are presented in Figure 5.1.5.1-6 for a TC-DIAL system configured similarly to the specifications given in Table 5.2-2 to provide a realistic demonstration of the retrievals PRF dependency.

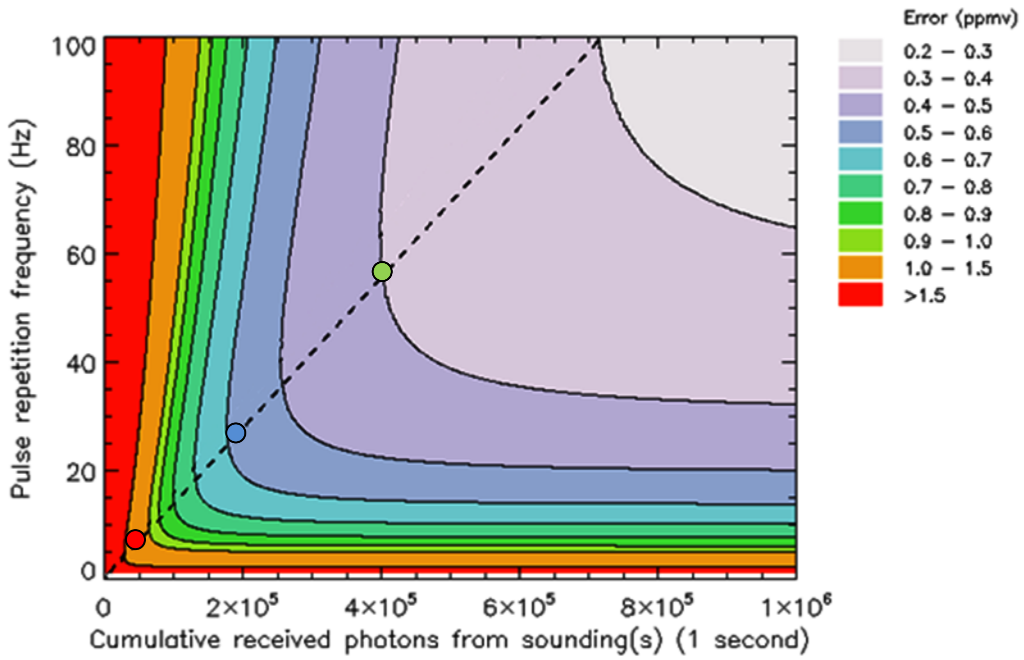

Figure 5.1.5.1-6 CO_2 retrieval errors incurred by errors in the measured DOD for direct detection as a function of instrument pulse repetition frequency and number of received photons, dashed line shows optimum PRF, coloured points are for various emission powers over vegetation, red = 1 W, blue = 5 W, green = 10 W

The shape of the contours in Figure 5.1.5.1-6 indicate the existence of an optimum PRF for a given received photon intensity for direct detection. The presence of an optimum exists as a consequence of the saturation of the direct detection error curve as displayed in Figure 2.3.2-1. The optimum value of the PRF increases in magnitude until the received signal intensity from a single sounding begins to move up the error curve beyond the saturation point. Once the error has begun to climb the curve an increase in the instruments PRF results in a significant increase in the integrated retrieval error.

Achieving an optimum system for direct detection therefore requires the PRF, the DOD and their dependant parameters to be configured such that the overall system error for a given scientific objective is minimised. For direct detection the PRF has been shown to be one of the primary adjustable parameters in the optimisation process and is treated as such in the determination of the optimum system in section 5.2.

5.1.5.2 Heterodyne detection

The expressions defining the relative error in the measurement of the received signal intensities for heterodyne detection is given by equations in Section 2.3.2. The internal gain mechanism achieved by the heterodyne mixing process onboard the satellite instrument implies the noise expression is independent on the detector NEP (assuming a reasonable detector is used) and as such is only dependant on the received photon intensity and the detector efficiency. Figure 5.1.5.2-1 presents the relationship between the number of received photons and the detector efficiency for a heterodyne system. The perfect symmetry in Figure 5.1.5.2-1 occurs as a result of how the axes have been scaled, however following the application of a very high PRF to achieve sufficiently low SNR the number of photons per sounding received on the detector is likely to only number in the hundreds. The detector efficiency region in Figure 5.1.5.2-1 of 0.7 to 0.9 is very close to being completely straight and therefore has no significant effect on the retrieval accuracy in comparison to the number of received photons. A sharp gradient in the retrieval error only appears at very small received photon numbers, and as such the optimisation of a heterodyne TC-DIAL system lies in achieving the highest possible PRF to statistically reduce the random errors incurred by speckle (see Chapter 2). The limiting factor for heterodyne detection is the ability of the laser to achieve and sustain a very high PRF (> 5 kHz) with sufficient power to exceed the shot noise limit.

Using the TCDS computer simulation as described in section 5.1.5.1 the effect of the PRF on a heterodyne systems optimum configuration is determined. The results of the simulations are presented in Figure 5.1.5.2-2.

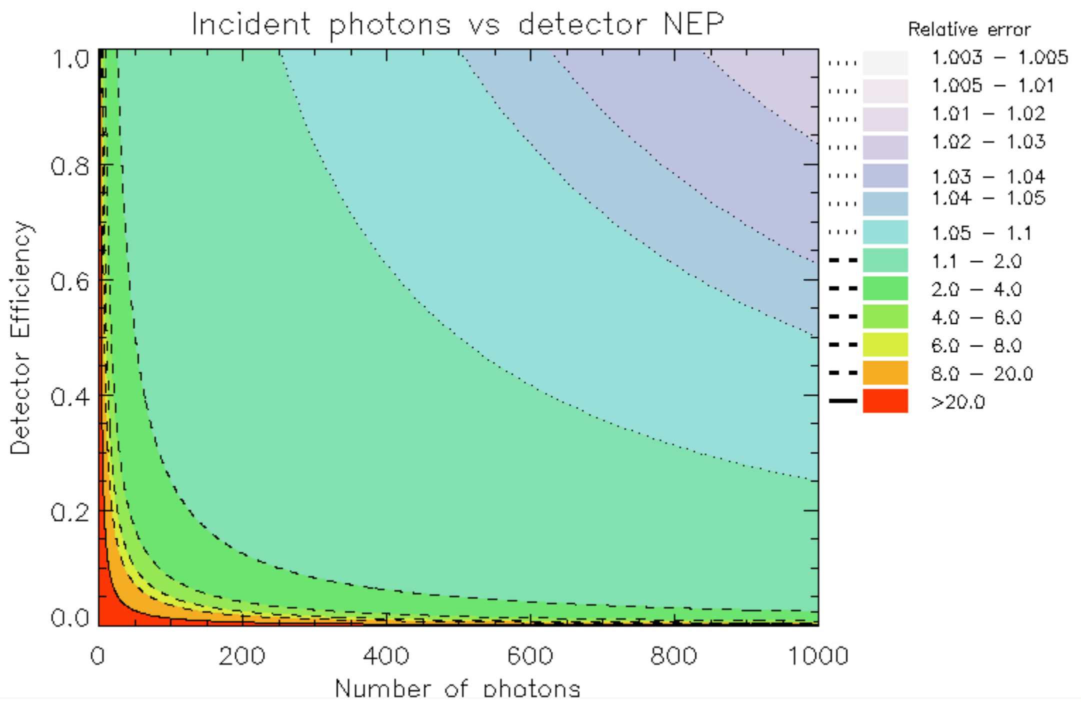

Figure 5.1.5.2-1 CO_2 retrieval error for a TC-DIAL system as a function of detector efficiency and number of incident photons for heterodyne detection

As demonstrated by the open contours of Figure 5.1.5.2-2 for heterodyne detection there is no optimum PRF for a given number of received photons. The heterodyne detection error curve increases at around 100 photons (see Figure 2.3.2-2), however a very large positive increment in PRF must occur for the number of photons per shot to reduce by a meaningful amount and climb the error slope. As a consequence even when receiving tens of photons per shot causing the SNR to be very low, the overall error in the retrieval is still lower than when the system receives hundreds of photons per shot. For heterodyne detection the PRF is therefore not an adjustable parameter in the optimisation process and instead is required to be as large as possible. The maximum PRF a suitable laser can achieve will restrict the maximum operational PRF of the LiDAR system, however the statistical presence of clouds at particular altitudes in the Earth's atmosphere has been found to limit the PRF's to particular windows to reduce the possibility of cross signal (online to offline) contamination within the Earth's atmosphere (see Chapter 4). The PRF's for heterodyne detection are therefore limited to the regions of 5 kHz or 15 kHz to minimise the probability of cross signal contamination.

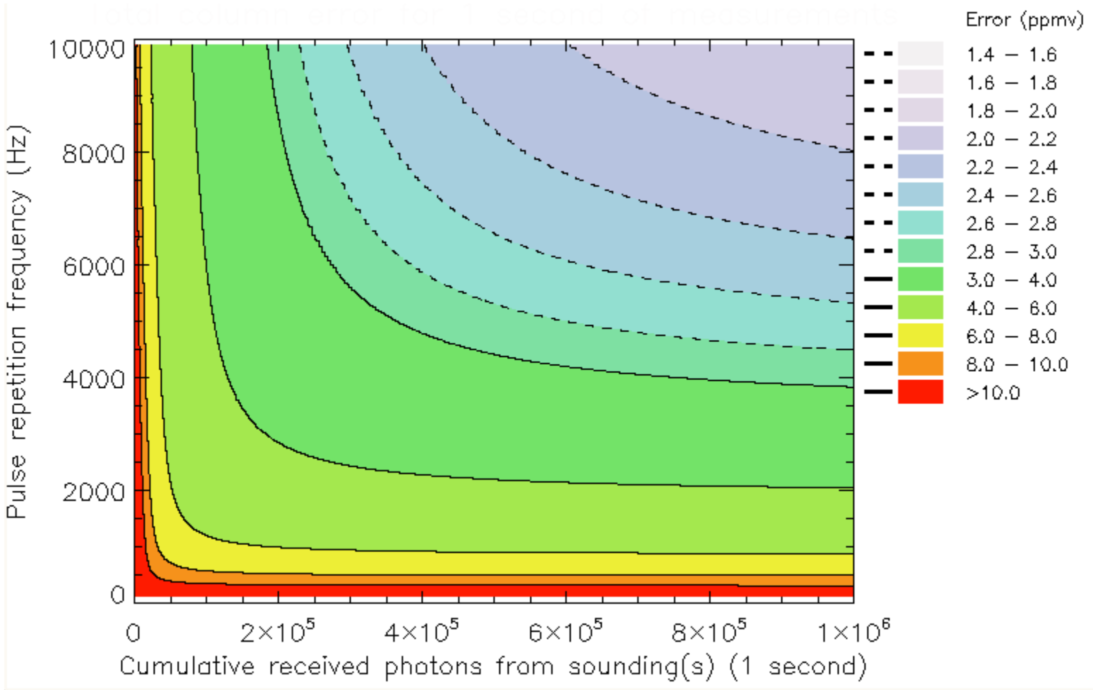

Figure 5.1.5.2-2 CO_2 retrieval errors incurred by errors in the measured DOD for an unoptimised heterodyne detection system as a function of instrument pulse repetition frequency and number of received photons

5.2 Optimisation of a 2µm space-borne TC-DIAL instrument for clear sky and cloudy sky scenarios

The retrieval errors associated with measurements from a space-borne TC-DIAL system have an expansive parameter space which (in many cases) can be adjusted to minimise retrieval errors for given circumstances. Studies in the scientific literature (particularly the FACTS report) have explored many of the relationships governing the accuracy of TC-DIAL retrievals under idealistic (clear sky) conditions (Ehret and Kiemle, 2005; Loth et al., 2005).

As discussed throughout section 5.1 however, much of the previous work carried out in determining the optimum system configuration is based in part on what is now out of date technology and incomplete spectroscopy. Furthermore the current scientific literature does not explicitly demonstrate the use of the instruments PRF and integration distance in the determination of the optimum system, nor do they quantify the relative contributions of each individual parameter in the optimisation process to ascertain their actual relevance.

The following section determines through computer simulations parameterised with the latest technology definitions (Table 5.2-2) and accommodating many of the most relevant dependant parameters the optimum TC-DIAL instrument configuration. The optimisation process is performed for two measurement scenarios known as the clear sky scenario and the cloudy sky scenario. The clear sky scenario refers to the optimisation of a TC-DIAL instrument in the presence of many of the key error sources to achieve the best possible retrievals under clear sky conditions. The cloudy sky scenario refers to a system configured in anticipation of optically thick patchy clouds below the satellite which would cause regular interruptions of its view to the surface along its measurement track.

The clear sky scenario (as named here) is the concept generally used in the optimisation of 2 µm TC-DIAL systems in the scientific literature with integration distances of approximately 50 km (Ehret and Kiemle, 2005; Loth et al., 2005; Bruneau et al., 2006; Ingmann et al., 2008). Such clear sky conditions are however quite rare over 50 km distances, particularly over regions of current scientific interest such as the tropics. It is likely that a system optimised for such idealistic conditions will fail to properly represent the ideal system configuration required for best observing CO_2 fluxes in the most important regions of the Earth's terrestrial and marine biospheres.

The cloudy sky scenario which is investigated in this section assumes the integration path length of the instrument is an unknown quantity and derives the optimum system configuration for a number of possible integration distances ranging from 1 second (7 km) to 7 seconds (50 km). A comparison between the systems is then carried out to identify the differences in optimum configuration and instrument capability to ascertain the merit of optimising for cloudy conditions.

To perform the optimisation studies the TCDS computer model is used in its contour mode of operation to iterate through all permutations of instrument configuration within realistic limits determined by current technology capabilities. The relevance of the error sources and the adjustable dependant parameters are investigated during the optimisation process with the aim of understanding their relative importance in determining the accuracy of the TC-DIAL retrievals. Particular attention is paid towards the instruments PRF, integration path length and ancillary data as these parameters are yet to be properly investigated as critical elements in a TC-DIAL systems optimisation.

The optimum simulations are run for direct detection and heterodyne detection separately in order to compare their capabilities under mutually optimised conditions and to ascertain independently how their parameters affect their associated retrievals. The system configurations used for the following simulations are given in Table 5.2-2

The simulated satellite instrument for the optimisation process is fixed in its orbit above an area of the Amazon rainforest with a reflectance which is representative of the mean global reflectance of vegetation for a 5 W emission. The derived system configurations from the following studies are therefore optimised specifically for vegetation and ocean biomes only owing to their similar surface reflectances.

The instruments PRF and integration distance affect the retrieval by statistically reducing the random errors through multiple measurements of the same (or very similar) environments. The error reduction is applied in the simulations using Gaussian error statistics given by equation 152 for all random errors (ancillary data errors are systematic). The Gaussian method of error reduction is also used when combining individual random errors in the process of determining the overall retrieval error. The use of a quadratic relationship causes additional error components in some of the simulations to create very little additional error to the overall retrieval. The quadratic combination of errors with very different magnitudes which causes this effect is particularly notable for heterodyne detection.

5.2.1 Optimum system for direct detection

For direct detection the dependant parameters investigated in the optimisation process are the laser emission frequency, the online and offline emission power ratio and the instruments PRF. The sources of uncertainty included in the simulations which influence the optimum system definition are the ancillary data errors (pressure, temperature and humidity), the surface reflectance variability error, the laser frequency stability error and the detector noise.

Figure 5.2.1-1 presents the direct detection retrieval error relationship for an online to offline emission power ratio of 5:1 in the presence of detector noise only. Figure 5.2.1-2 presents the same relationship but for an emission power ratio of 4.7:1 in the presence of detector noise and frequency stability errors, and finally Figure 5.2.1-3 presents the same relationship again but for a power emission ratio of 5:1 in the presence of detector noise, frequency stability, surface reflectance variability and ancillary data errors.

The results presented in Figure 5.2.1-1 to Figure 5.2.1-3 are optimised for their emission power ratios and plotted to demonstrate the evolving relationships between the PRF and laser frequency.

Figure 5.2.1-1 to Figure 5.2.1-3 diagrammatically present the optimum system configurations at various levels of error contribution. The closed contours presented demonstrate the presence of single and well defined optimum values in both the laser frequency and PRF domains.

The results from Figure 5.2.1-1 to Figure 5.2.1-3 are presented in tabular form in Table 5.2.1-1.

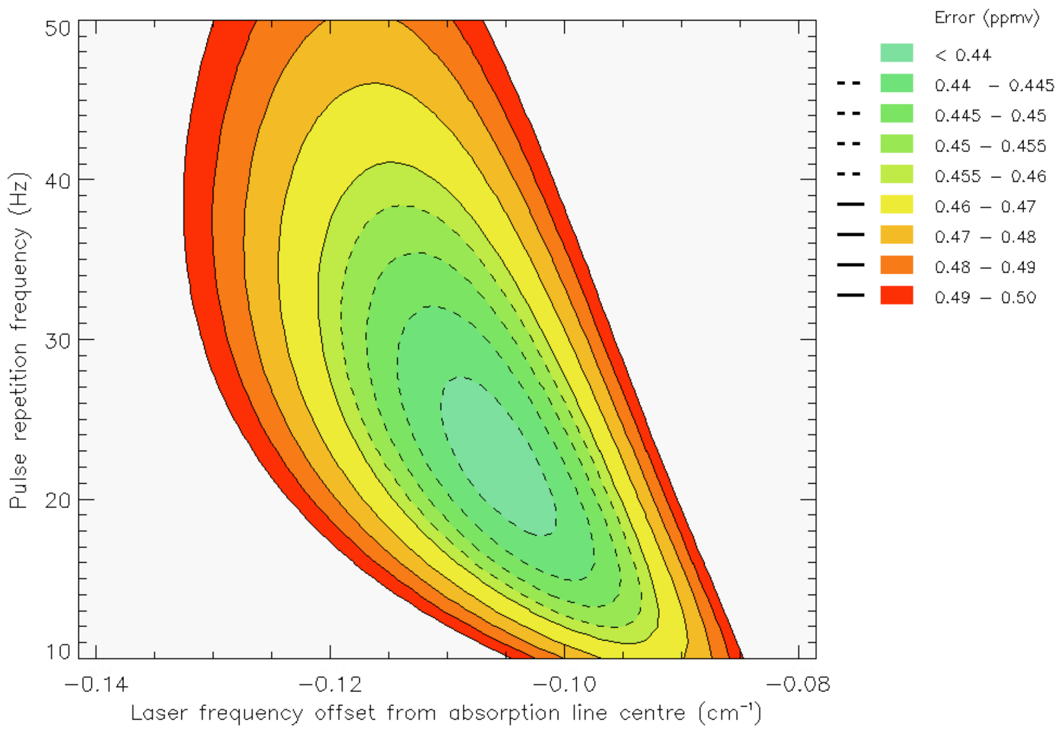

Figure 5.2.1-1 CO_2 retrieval error showing optimum laser frequency offset and PRF for a direct detection TC-DIAL system subjected to detector noise only with an online to offline laser power emission ratio of 5:1 and integrated over 1 second

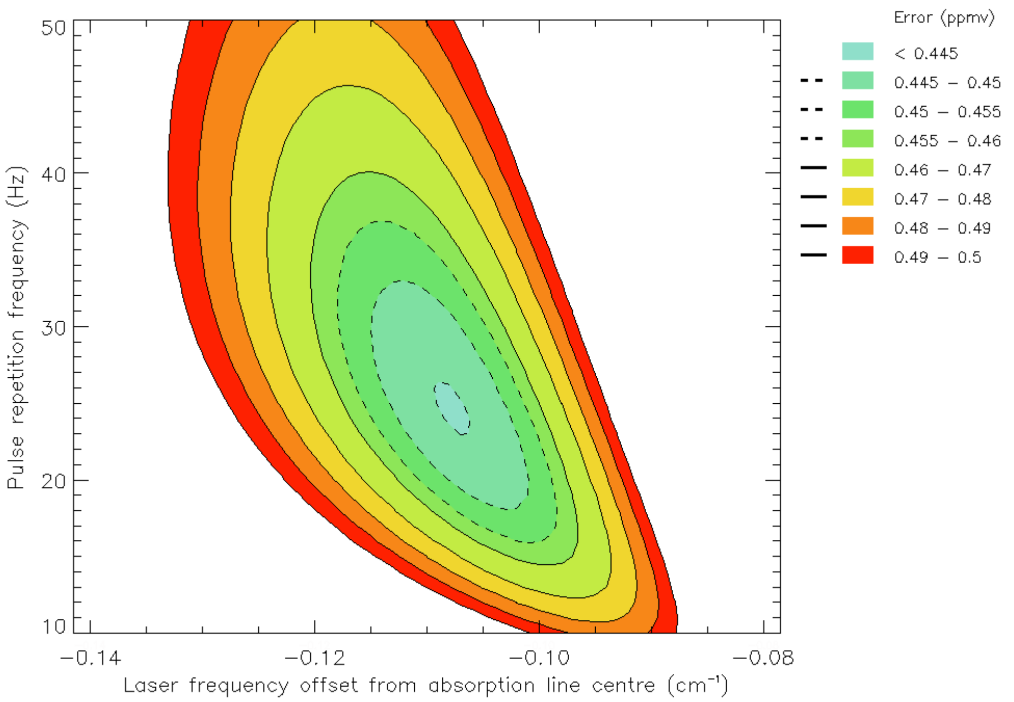

Figure 5.2.1-2 CO_2 retrieval error showing optimum laser frequency offset and PRF for a direct detection TC-DIAL system subjected to detector noise and laser frequency uncertainty (of 1.9 MHz) with a laser power emission ratio of 4.7:1 integrated over 1 second

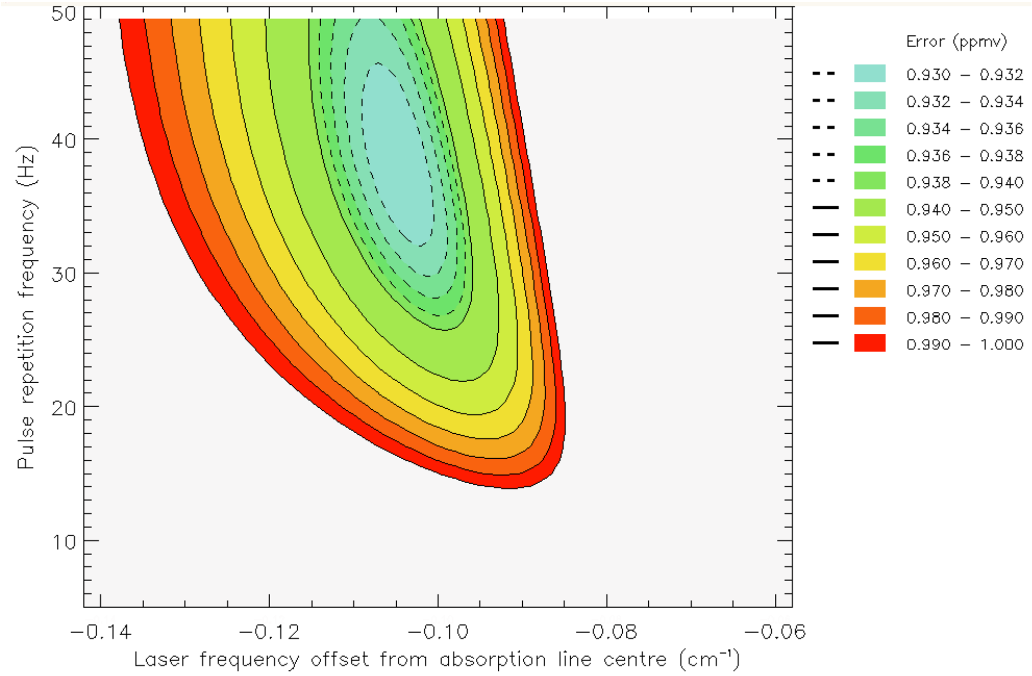

Figure 5.2.1-3 CO_2 retrieval error showing optimum laser frequency offset and PRF for a direct detection TC-DIAL system subjected to detector noise, laser frequency uncertainty and ancillary data errors with an online to offline laser power emission ratio of 5:1 and integrated over 1 second

Error source	Error (ppm) contribution	Total Error (ppm)	PRF (Hz)	Frequency offset (cm^{-1})	Power ratio (ON:OFF)
Detector noise	0.438	0.438	22	-0.105	5.0:1
+ Frequency Unc	0.077	0.445	25	-0.108	4.7:1
+ Reflectance Var	0.338	0.559	48	-0.120	4.0:1
+ Ancillary Err	0.741	0.928	37	-0.103	5.0:1

Table 5.2.1-1 Space-borne TC-DIAL retrieval errors at various levels of error contribution showing the configuration of the systems free parameters for 1 second integration time.

As demonstrated in Table 5.2.1-1 the laser frequency stability error has a relatively minor effect on the overall retrieval error and the systems optimum configuration. The lack of influence is largely due to the quadratic addition of the laser frequency stability error to the much larger error associated with detector noise which dominates throughout the entire spectral domain. The magnitudes of the random errors when added to the overall retrieval error are partly mitigated by adjustments in the systems configuration in response to the added sources of uncertainty. The reaction of the systems configuration to the initial two changes in system error is a general increase in the instruments PRF and a shift in the emission frequency away from the centre of the absorption line where the system is most sensitive to frequency uncertainties. Upon introduction of the systematic ancillary data however the systems reaction is the opposite, and the laser frequency is pulled toward the centre of the spectral line and the PRF is reduced. The PRF changes are specific responses to the availability of more or less energy per sounding as a result of the DOD changing.

The greatest influence on the instrument configuration for a direct detection TC-DIAL system is shown in Table 5.2.1-1 to be the uncertainties in the ancillary data used in the retrieval. The error contribution by the ancillary data is highly influential to the system configuration owing to it being a systematic source of error over the integration interval and therefore not reducible by equation 152.

The addition of the ancillary data errors to the retrieval causes the optimisation algorithm to significantly shift the free parameters in the system configuration as shown in both Table 5.2.1-1 and in Figure 5.2.1-1 to Figure 5.2.1-3. The system configuration is moved towards a higher DOD as both the temperature and pressure error profiles encourage a laser emission frequency closer to the spectral line centre (see Figure 5.1.4-1 and Figure 5.1.4-2). The increase in the DOD caused by the laser emission frequency being pulled towards the line centre results in the PRF being reduced and the online to offline emission ratio being increased to compensate.

Table 5.2.1-2 presents a series of system configurations and retrieval errors for various integration distances along the Earth's surface to demonstrate the influence the integration distance has on the configuration of the free parameters. The results presented in Table 5.2.1-2 are produced from simulations containing all key error sources.

Integration time (seconds)	Integration distance (km)	PRF (Hz)	Frequency offset (cm^{-1})	Power ratio on:off	Total Error (ppm)
1	7	37	-0.103	5.0:1	0.927
2	14	27	-0.092	7.6:1	0.817
3	21	22	-0.086	9.5:1	0.766
4	28	18	-0.082	11.5:1	0.735
5	35	14	-0.079	13.0:1	0.713
6	42	13	-0.077	14.7:1	0.696
7	49	13	-0.076	15.5:1	0.682

Table 5.2.1-2 Retrieval errors and optimum system configurations for various integration distances for a space-borne direct detection TC-DIAL instrument

Table 5.2.1-2 demonstrates that increasing a TC-DIAL systems integration distance causes a significant change in the optimum laser emission frequency. The frequency shift is driven by the inability of the temperature and pressure errors to be statistically reduced along with the detector noise, laser frequency stability and surface reflectance variability errors by equation 152. The statistical reduction of the random errors by the integration of multiple soundings causes the ancillary data errors to become significantly more influential to the systems configuration. The increased sensitivity of the retrievals to the ancillary data errors as the integration distance increases causes the laser frequency to move towards the centre of the absorption line which greatly increases the magnitude of the DOD. The systems response to this change is to drastically increase the power ratio and to reduce the PRF to provide more energy for the online emission to overcome detector noise.

Emitting laser pulses consecutively with different energies is a technological challenge which is likely to be more difficult the greater the energy gap. The optimisation process employed in the TCDS does not account for a technological limit in this respect and as such the power ratio has been allowed to get as high as 15.5:1. To demonstrate the importance of ensuring the online and offline emissions have different powers Table 5.2.1-3 has been produced by running the optimisation algorithm with a fixed 1:1 power emission ratio in the presence of all error sources.

Integration time (seconds)	Integration time (seconds)	PRF (Hz)	Frequency offset (cm^{-1})	Power ratio	Total Error (ppm)	Δ error (ppm)
1	7	33	-0.116	1:1	1.01	0.083
2	14	25	-0.104	1:1	0.892	0.075
3	21	20	-0.097	1:1	0.828	0.062
4	28	16	-0.092	1:1	0.794	0.059
5	35	14	-0.088	1:1	0.769	0.056
6	42	13	-0.086	1:1	0.751	0.055
7	49	11	-0.084	1:1	0.736	0.054

Table 5.2.1-3 Retrieval errors and optimum system configurations for various integration distances for a space-borne direct detection TC-DIAL instrument with fixed power ratios

The final column of Table 5.2.1-3 displays the difference in retrieval errors for optimised TC-DIAL systems with and without the capacity to emit the online and offline wavelengths with different powers. The delta error values progressively decrease in line with the overall retrieval error as the integration distance increases. Comparing the delta errors with the total retrieval errors shows that the contribution is always below 10% for a system with a fixed emission power ratio. The additional source of error incurred by the system being unable to adjust the laser emission power ratio is therefore a relatively small contribution in comparison to the errors associated with the ancillary data, and as such is not at present a driver for the system design.

The effect on the retrieval of the ancillary data errors having to be treated as systematic is investigated by the production of Table 5.2.1-4 which shows the optimum TC-DIAL system in the presence of random ancillary data errors which have been reduced by equation 148.

The difference between the errors presented in Table 5.2.1-2 and Table 5.2.1-4 demonstrate that treating the ancillary data errors as random as opposed to systematic makes a significant difference to their contribution to the overall retrieval error. They also show that the system configuration adjustments that occur in Table 5.2.1-2 as a function of integration distance do so almost entirely as a result of the ancillary data errors being unchangeable with integration distance. The system configuration remaining static in Table 5.2.1-2 as opposed to highly variable as in Table 5.2.1-4 is caused by all of the error sources decreasing together, implying the system remains equally sensitive to all of the errors spectral dependencies.

Integration time (seconds)	distance (km) (seconds)	PRF (Hz)	Frequency offset (cm^{-1})	Power ratio	Total Error (ppm)
1	7	48	-0.119	4.0:1	0.569
2	14	48	-0.119	4.0:1	0.403
3	21	48	-0.119	4.0:1	0.329
4	28	48	-0.119	4.0:1	0.285
5	35	48	-0.119	4.0:1	0.255
6	42	48	-0.119	4.0:1	0.232
7	49	48	-0.119	4.0:1	0.215

Table 5.2.1-4 Retrieval errors and optimum system configurations for various integration distances for a space-borne direct detection TC-DIAL instrument with ancillary data errors considered as a random source of error.

To demonstrate the improvement achieved by assuming the ancillary data errors can be treated as random, a series of optimisation simulations have been performed in the absence of ancillary data errors and the results presented in Table 5.2.1-5.

By comparing the results of Table 5.2.1-4 and Table 5.2.1-5 it can be seen that ancillary data errors have very little influence on the system configuration and retrieval error if they can be considered random and therefore statistically reduced. The retrieval error contribution by random ancillary data errors is only approximately 1 to 2 % of the overall retrieval error, with the majority being caused by detector noise and to a slightly lesser extent surface reflectance variability.

Integration time (seconds)	Integration distance (km)	PRF (Hz)	Frequency offset (cm^{-1})	Power ratio	Total Error (ppm)
1	7	48	-0.12	4.0:1	0.559
2	14	48	-0.12	4.0:1	0.395
3	21	48	-0.12	4.0:1	0.323
4	28	48	-0.12	4.0:1	0.279
5	35	48	-0.12	4.0:1	0.250
6	42	48	-0.12	4.0:1	0.228
7	49	48	-0.12	4.0:1	0.211

Table 5.2.1-5 Retrieval errors and optimum system configurations for various integration distances for a space-borne direct detection TC-DIAL instrument without ancillary data errors

In conclusion, the results from the optimisation studies for direct detection have shown that the spectral dependencies of all four primary retrieval uncertainties have an influence on the optimal system configuration for a space-borne TC-DIAL system. They also show that the systematic nature of the NWP derived ancillary data errors results in the most significant modification to the retrieval errors. If the ancillary data errors were to be made random over the integration interval with a similar accuracy as the current capabilities of NWP models then the CO_2 retrieval error would improve from approximately 0.68 ppm to 0.21 ppm. It is therefore clear that if the ancillary data could be measured from the satellite and their errors considered random then the retrieval accuracy would significantly improve even if the measured errors were much larger.

In addition to the influence on the retrieval error it has also been shown that the systematic nature of the ancillary data error is the primary driver for the systems optimum configuration. Table 5.2.1-6 has been produced to summarise the effect of ancillary data error as a random source by comparing the optimum system configuration for the random error scenario with the error configuration from Table 5.2.2-4 for a 50 km integration interval.

Error source	Total Error (ppm)		PRF (Hz)		Frequency offset (cm^{-1})		Power ratio (ON:OFF)	
Detector noise	0.166	0.166	22	22	-0.105	-0.105	5.0:1	5.0:1
+ Frequency Err	0.168	0.168	25	25	-0.108	-0.108	4.7:1	4.7:1
+ Reflectance Var	0.211	0.211	48	48	-0.120	-0.120	4.0:1	4.0:1
+ Ancillary Err	**0.682**	**0.215**	**13**	**48**	**-0.076**	**-0.119**	**15.5:1**	**4.0:1**

Table 5.2.1-6 Retrieval errors and optimum system configurations for a space-borne direct detection TC-DIAL system using NWP derived ancillary data with systematic errors (red) and random errors (green) for a 50 km integration distance

The results presented in Table 5.2.1-6 show that a direct detection TC-DIAL system based on current technology can achieve CO_2 retrievals with a net error of approximately 0.68 ppm over vegetation scenes when integrated over 50 km's based on the error sources considered in this study. As described in Chapter 1 a CO_2 retrieval accuracy of approximately 1 ppm for a TC-DIAL system is suitable for complementing and in many cases improving the existing CO_2 measurement systems on regional scales (thousands of km), especially when measuring with such precision at all latitudes both day and night (Heaps, 2007). The instrument configuration presented in this study is able to achieve this error over only a 50 km series of integrated soundings (based on the errors considered) over vegetation and ocean scenes. However, as shown by the ancillary data component of the error study performed in this chapter the systematic error associated with the measurements is a very high component (approximately 0.5 ppm) and greatly exceeds the required 0.15 ppm threshold (Ingmann et al., 2008). The primary cause of the systematic errors in the TC-DIAL retrievals is the ancillary data errors being limited by the spatial resolution of NWP models. It is likely that when using such data over regional scales the systematic nature of the NWP derived ancillary data errors will reduce and become more random, and therefore once assimilated into carbon flux models will present a much lower bias in the results.

The results presented in this chapter originate from a study covering many of the sources of uncertainty associated with TC-DIAL retrievals, however there are important errors that have not been included including the uncertainty in the spectroscopy which defines the absorption cross sections and which is likely to be significant, and uncertainties in the laser pulse path length as a result of the instruments temporal sampling. What has been shown in this study in particular is the relative importance of many of the key error sources and their effects on the optimum system configuration.

The greatest merit of a TC-DIAL instrument lies in its ability to measure the CO_2 concentration over areas of particular interest such as the tropics where clouds are frequent. The cloudy sky scenario investigated in this chapter assumes that TC-DIAL measurements will be required to be made in cloudy conditions and as such the system will be optimised for integration distances of much less than 50 km. The possibility of optimising for shorter integration distances has already been partly investigated in Table 5.2.1-2 in which the optimum system for direct detection at various integration distances is displayed.

To compare the advantage gained by optimising the system for a cloudy environment, TC-DIAL simulations have been carried out using configurations that are deliberately not optimised for the integration distances simulated. Table 5.2.1-7 shows the results from the simulations which include (in the final column) the additional errors introduced by the TC-DIAL system operating with an integration distance it is not optimised for.

Integration time used (seconds)	**Errors if optimised for 1 second (ppm)**	**Errors if optimised for 7 seconds (ppm)**	**Error difference (ppm)**
1	0.927	1.079	0.152
7	0.748	0.682	0.066

Table 5.2.1-7 Retrieval errors for 1 and 7 second integration distances showing error differences associated with the system using a non-optimum integration distance

Table 5.2.1-7 shows that a system optimised for a 7 second integration time will suffer a penalty of approximately 0.152 ppm if it is reduced to 1 second to see between clouds. Conversely if the system is optimised for 1 second and clear sky conditions permit an integration time of 7 seconds then the penalty for this change in system configuration is approximately 0.066 ppm. The results in Table 5.2.1-7 therefore indicate that there is a much greater error penalty incurred by optimsing the system for clear sky conditions and operating in cloudy sky conditions than vice versa for direct detection.

5.2.2 Optimum system for heterodyne detection

For heterodyne detection the dependant parameters investigated in the optimisation process are the laser emission frequency and the online and offline emission power ratio. Optimum system configurations are derived for systems operating at both 5 kHz and 15 KHz PRF's which present the least possibility of cross signal contamination in the Earth's atmosphere (see Chapter 4). The sources of uncertainty included in the optimisation simulations for heterodyne detection are the ancillary data errors (pressure, temperature and humidity), the laser frequency stability error, the surface reflectance variability error and the detector noise.

Figure 5.2.2-1 and Figure 5.2.2-2 show the relationships and optimum values for the laser emission frequency and the online to offline emission power ratio for 5 and 15 kHz PRF's with all primary errors included.

For a heterodyne detection system with a very high PRF (> 5 kHz) the retrieval error is dominated by the detector noise and is only very weakly affected by the systematic errors of the ancillary data. For these reasons the relationships between the emission power ratio and the laser emission frequency are presented diagrammatically for all error contributions only and not separated into their individual components as done in section 5.2.1.

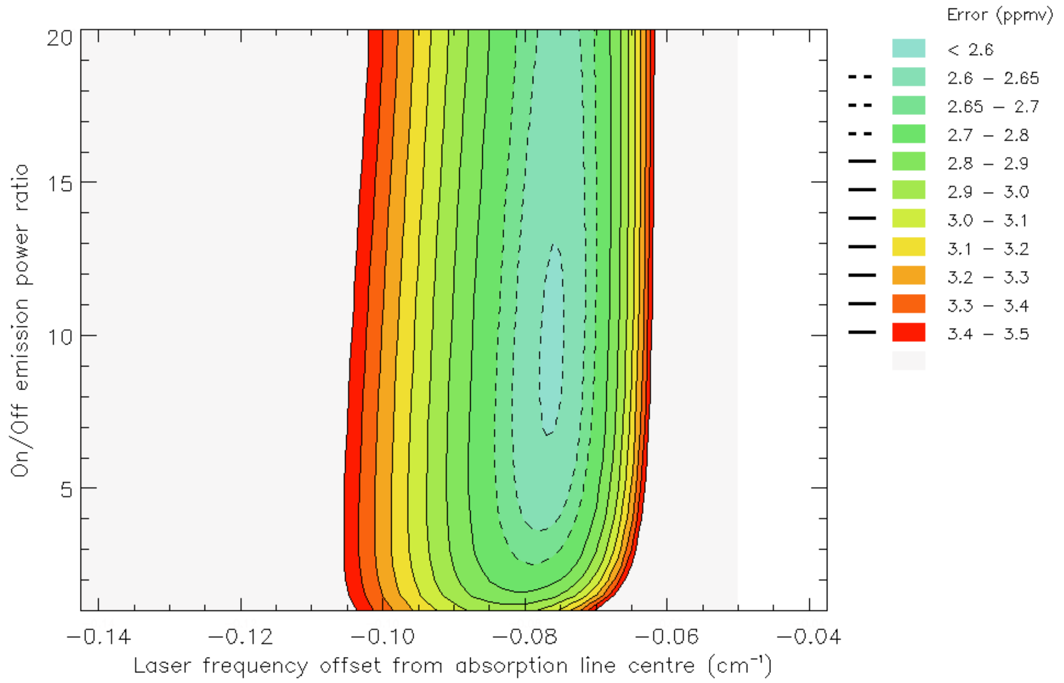

Figure 5.2.2-1 CO_2 retrieval error showing optimum laser frequency offset and power emission ratio for a heterodyne detection TC-DIAL system subjected to all primary error sources with a PRF of 5 kHz

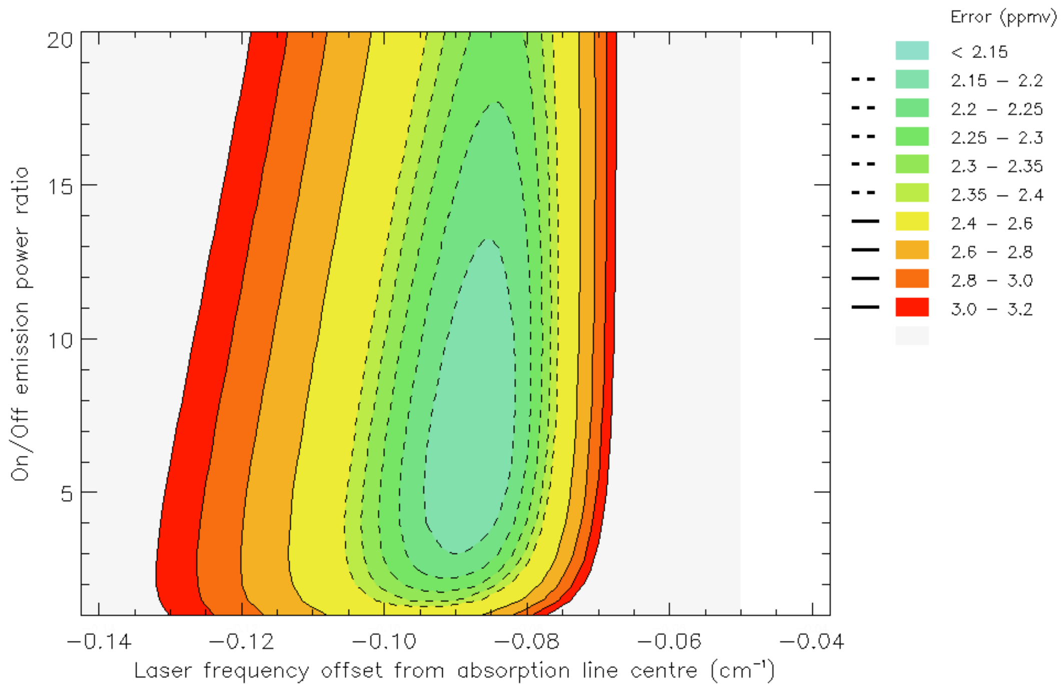

Figure 5.2.2-2 CO_2 retrieval error showing optimum laser frequency offset and power emission ratio for a heterodyne detection TC-DIAL system subjected to all primary error sources with a PRF of 15 kHz

The results of the heterodyne optimisation process are presented in tabular form for 5 and 15 kHz PRF's in Table 5.2.2-1 and Table 5.2.2-2 respectively.

Error included	**Error Contribution**	**Total Error**	**PRF (kHz)**	**Frequency Offset**	**Power ratio**
Detector noise	2.525	2.525	5	-0.076	8:1
+ Frequency Unc	0.0	2.525	5	-0.076	8:1
+ Reflectance Var	0.029	2.525	5	-0.076	8:1
+ Ancillary Err	0.590	2.593	5	-0.076	8:1

Table 5.2.2-1 Space-borne TC-DIAL retrieval errors at various levels of error contribution showing the configuration of the systems free parameters for 1 second integration time for 5 kHz PRF

Error included	**Error Contribution**	**Total Error**	**PRF (kHz)**	**Frequency Offset**	**Power ratio**
Detector noise	2.052	2.052	15	-0.088	5:1
+ Frequency Unc	0.0	2.052	15	-0.088	5:1
+ Reflectance Var	0.017	2.052	15	-0.088	5:1
+ Ancillary Err	0.655	2.154	15	-0.088	5:1

Table 5.2.2-2 Space-borne TC-DIAL retrieval errors at various levels of error contribution showing the configuration of the systems free parameters for 1 second integration time for 15 kHz PRF

As demonstrated in Table 5.2.2-1 and Table 5.2.2-2 the systematic ancillary data error increases the overall retrieval error for a heterodyne detection system over a 1 second integration distance by approximately 5 % for 15 kHz PRF and 3 % for 5 kHz PRF. The magnitude of the ancillary data error for a heterodyne detection system is almost as large as it is for a direct detection system (see section 5.2.1), however relative to the very high heterodyne detector noise the ancillary data errors are rendered almost negligible to the overall retrieval error over a 1 second integration interval.

The retrieval errors presented in Table 5.2.2-1 and Table 5.2.2-2 are particularly high owing to the systems having only been integrated over 1 second which is insufficient for a heterodyne system. Table 5.2.2-3 and Table 5.2.2-4 present the optimum heterodyne TC-DIAL system configurations and retrieval errors for a series of integration distance in the presence of all primary error sources for 5 and 15 kHz PRF's.

As shown in Table 5.2.2-3 and Table 5.2.2-4 the retrieval errors for heterodyne detection systems quickly improve as the integration distance increases, reaching approximately 1.12 ppm and 1.01 ppm for 5 kHz and 15 kHz PRF systems integrated over 50 km.

Integration time (seconds)	Integration distance (km)	PRF (kHz)	Frequency offset (cm^{-1})	Power ratio on:off	Error (ppm)
1	7	5	-0.076	8:1	2.593
2	14	5	-0.076	8:1	1.881
3	21	5	-0.076	8:1	1.573
4	28	5	-0.075	9:1	1.393
5	35	5	-0.075	9:1	1.273
6	42	5	-0.075	9:1	1.187
7	49	5	-0.075	9:1	1.121

Table 5.2.2-3 Retrieval errors and optimum system configurations for various integration distances for a space-borne heterodyne detection TC-DIAL instrument with all primary error sources applied for 5 kHz PRF

Integration time (seconds)	Integration distance (km)	PRF (kHz)	Frequency offset (cm^{-1})	Power ratio on:off	Error (ppm)
1	7	15	-0.088	5:1	2.154
2	14	15	-0.088	6:1	1.590
3	21	15	-0.087	6:1	1.351
4	28	15	-0.086	6:1	1.213
5	35	15	-0.085	6:1	1.122
6	42	15	-0.085	6:1	1.057
7	49	15	-0.085	6:1	1.008

Table 5.2.2-4 Retrieval errors and optimum system configurations for various integration distances for a space-borne heterodyne detection TC-DIAL instrument with all primary error sources applied for 15 kHz PRF

Although the retrieval errors are significantly improved by longer integration distances the system configurations in Table 5.2.2-3 and Table 5.2.2-4 change very little owing to the detector noise remaining significantly dominant over all other errors, including most importantly the systematic ancillary data error.

To demonstrate the contribution of the systematic ancillary data error to the overall retrieval error for heterodyne detection, Table 5.2.2-5 and Table 5.2.2-6 have been produced to show the optimum system configurations and retrieval errors for a system which assumes the ancillary data errors can be treated as random for 5 kHz and 15 kHz PRF systems.

The errors presented in Table 5.2.2-5 and Table 5.2.2-6 are identical to three decimal places to results from simulations that were performed which did not include any ancillary data errors at all (not presented). The very close similarities between the results of the two scenarios are caused by the heterodyne systems high PRF statistically reducing most of the random errors to non-influential levels (< 0.05 ppm). The only random error remaining influential after the statistical reduction is the detector noise itself which is initially very high owing to the effects of speckle in the heterodyne mixing process.

Integration time (seconds)	Integration distance (km)	PRF (kHz)	Frequency offset (cm^{-1})	Power ratio on:off	Error (ppm)
1	7	5	-0.076	8:1	2.525
2	14	5	-0.076	8:1	1.785
3	21	5	-0.076	8:1	1.458
4	28	5	-0.076	8:1	1.263
5	35	5	-0.076	8:1	1.129
6	42	5	-0.076	8:1	1.031
7	49	5	-0.076	8:1	0.954

Table 5.2.2-5 Retrieval errors and optimum system configurations for various integration distances for a space-borne heterodyne detection TC-DIAL instrument in the presence of random ancillary data errors for 5 kHz PRF

Integration time (seconds)	Integration distance (km)	PRF (kHz)	Frequency offset (cm^{-1})	Power ratio on:off	Error (ppm)
1	7	15	-0.088	5:1	2.052
2	14	15	-0.088	5:1	1.451
3	21	15	-0.088	5:1	1.185
4	28	15	-0.088	5:1	1.026
5	35	15	-0.088	5:1	0.918
6	42	15	-0.088	5:1	0.838
7	49	15	-0.088	5:1	0.776

Table 5.2.2-6 Retrieval errors and optimum system configurations for various integration distances for a space-borne heterodyne detection TC-DIAL instrument in the presence of random ancillary data errors for 15 kHz PRF

As demonstrated in Table 5.2.2-6 heterodyne detection retrievals are improved by approximately 17 % for 5 kHz and 30 % for 15 KHz if the ancillary data errors were to be considered random over a 50 km integration distance. From these findings it is clear that it is highly beneficial for heterodyne detection if the ancillary data were to be obtained in such a way that the associated errors could be considered random (for example by onboard measurement).

The results from Table 5.2.2-5 and Table 5.2.2-6 show that the optimisation process increases the online to offline emission power ratio in order to provide additional power to the online signal to compensate for atmospheric absorption. To demonstrate the importance of allowing the power ratio to vary Table 5.2.2-7 and Table 5.2.2-8 have been produced which show the optimum configurations for heterodyne detection TC-DIAL systems which have fixed emission power ratios of 1:1.

Integration time (seconds)	Integration distance (km)	PRF (kHz)	Frequency offset (cm^{-1})	Power ratio	Total Error (ppm)	Δ error (ppm)
1	7	5	-0.084	1:1	2.953	0.799
2	14	5	-0.083	1:1	2.135	0.545
3	21	5	-0.083	1:1	1.780	0.429
4	28	5	-0.083	1:1	1.573	0.360
5	35	5	-0.083	1:1	1.434	0.305
6	42	5	-0.083	1:1	1.333	0.302
7	49	5	-0.082	1:1	1.257	0.303

Table 5.2.2-7 Retrieval errors and optimum system configurations for various integration distances for a space-borne heterodyne detection TC-DIAL instrument with a fixed power ratio and a PRF of 5 kHz

As shown in Table 5.2.2-7 and Table 5.2.2-8 fixing the power ratio provides slightly greater flexibility in the laser frequency offset as the integration time increases, however even with this enhanced variability the shift in laser frequency between 1 and 7 seconds integration time remains almost negligible.

Integration time (seconds)	Integration distance (km)	PRF (kHz)	Frequency offset (cm^{-1})	Power ratio	Total Error (ppm)	Δ error (ppm)
1	7	15	-0.097	1:1	2.473	0.319
2	14	15	-0.095	1:1	1.815	0.225
3	21	15	-0.095	1:1	1.533	0.182
4	28	15	-0.094	1:1	1.371	0.158
5	35	15	-0.094	1:1	1.263	0.141
6	42	15	-0.093	1:1	1.186	0.129
7	49	15	-0.093	1:1	1.127	0.119

Table 5.2.2-8 Retrieval errors and optimum system configurations for various integration distances for a space-borne heterodyne detection TC-DIAL instrument with a fixed power ratio and a PRF of 15 kHz

The final columns of Table 5.2.2-7 and Table 5.2.2-8 present the additional retrieval errors incurred by restricting the instruments emission power ratio to 1:1. The additional errors are relatively high on their own, but in comparison to the already large errors associated with heterodyne detection the additional errors form only approximately 10 % for 15 kHz and 5% for 5 kHz of the total retrieval error.

In conclusion it has been demonstrated that detector noise is the primary driver for heterodyne detection retrieval errors (of the errors considered) and is almost entirely responsible for the optimal system configuration. The results have shown that the systematic nature of the NWP derived ancillary data errors results in only a minor source of additional uncertainty to the overall retrieval errors owing to the large magnitude of the detector noise. If the ancillary data errors were to be made random over the integration interval with a similar accuracy as the current capabilities of NWP models then the CO_2 retrieval error has been shown to improve from approximately 1.01 ppm to 0.78 ppm for 15 kHz and 1.12 ppm to 0.95 ppm for 5 kHz. As a result it may be concluded that if the ancillary data could be measured from the satellite and their errors considered random then the retrieval accuracy would significantly improve for heterodyne detection even if the measured errors were much larger.

To summarise the optimum system configurations and retrieval errors for heterodyne detection Table 5.2.2-9 and Table 5.2.2-10 have been produced (based on a series of TC-DIAL error sources) showing scenarios for both random and systematic ancillary data errors for a 50 km integration intervals for 5 and 15 kHz PRF's.

Error source	**Total Error (ppm)**		**Frequency offset (cm^{-1})**		**Power ratio (ON:OFF)**	
Detector noise	0.954	0.954	-0.076	-0.076	8:1	8:1
+ Frequency Err	0.954	0.954	-0.076	-0.076	8:1	8:1
+ Reflectance Var	0.954	0.954	-0.076	-0.076	8:1	8:1
+ Ancillary Err	**1.121**	**0.954**	**-0.075**	**-0.076**	**9:1**	**8:1**

Table 5.2.2-9 Retrieval errors and optimum system configurations for a space-borne heterodyne detection TC-DIAL system using NWP derived ancillary data with systematic errors (red) and random errors (green) for a 50 km integration distance and 5 kHz PRF.

Error source	**Total Error (ppm)**		**Frequency offset (cm^{-1})**		**Power ratio (ON:OFF)**	
Detector noise	0.776	**0.776**	-0.088	-0.088	5:1	5:1
+ Frequency Err	0.776	**0.776**	-0.088	-0.088	5:1	5:1
+ Reflectance Var	0.776	**0.776**	-0.088	-0.088	5:1	5:1
+ Ancillary Err	**1.008**	**0.776**	**-0.085**	**-0.088**	**6:1**	**5:1**

Table 5.2.2-10 Retrieval errors and optimum system configurations for a space-borne heterodyne detection TC-DIAL system using NWP derived ancillary data with systematic errors (red) and random errors (green) for a 50 km integration distance and 15 kHz PRF.

The results presented in Table 5.2.2-10 show that a 15 kHz PRF heterodyne detection TC-DIAL system based on current technology can achieve CO_2 retrievals with an error of approximately 1 ppm over vegetation when its measurements are integrated over 50 km's based on the errors included in the study. A CO_2 measurement precision of approximately 1 ppm has been theoretically determined to be suitable for complementing and in many cases improving the existing CO_2 measurement systems for measuring surface fluxes of CO_2 (Heaps, 2007). The instrument configuration presented in this study is able to achieve this error over only a 50 km series of integrated soundings (based on the errors considered) over vegetation and ocean scenes with a 15 kHz PRF. However, as shown by the ancillary data component of the error study performed in this chapter the systematic error associated with the measurements is a significant component and exceeds the required 0.15 ppm threshold (Ingmann et al., 2008). The primary cause of the systematic errors in the TC-DIAL retrievals is the ancillary data errors being limited by the spatial resolution of NWP models. It is likely that when using such data over regional scales the systematic nature of the NWP derived ancillary data errors will reduce and become more random, and therefore once assimilated into carbon flux models will present a much lower bias in the results.

The results presented in this chapter originate from a study covering many of the sources of uncertainty associated with TC-DIAL retrievals, however there are important errors that have not been included including the uncertainty in the spectroscopy which defines the absorption cross sections and which is likely to be significant, and uncertainties in the laser pulse path length as a result of the instruments temporal sampling. What has been shown in this study in particular is the relative importance of many of the key error sources and their effects on the optimum system configuration. As with direct detection the greatest merit of a heterodyne detection TC-DIAL instrument lies in its ability to measure the CO_2 concentration over areas of particular interest such as the tropics where cloud is frequent. Optimising the heterodyne detection TC-DIAL system for cloudy conditions is a feasible methodology for improving retrievals over cloudy regions of interest at the expense of retrieval accuracy under clear sky conditions. To compare the advantage gained by optimising the system for a cloudy environment, TC-DIAL simulations have been carried out using configurations that are deliberately not optimised for the integration distances simulated. Table 5.2.2-11 and Table 5.2.2-12 show the results from the simulations for 5 kHz and 15 kHz which include (in the final column) the additional errors introduced by the TC-DIAL system operating with an integration distance it is not optimised for.

The results from Table 5.2.2-11 and Table 5.2.2-12 show that for a heterodyne detection TC-DIAL system very little additional error is incurred by operating outside of the optimum integration distance. Despite the error consistency between clear and cloudy sky scenarios however, the errors associated with 1 second integration is so high (> 2 ppm) it is unlikely that heterodyne detection measurements made between clouds would be of great value.

Integration time used (seconds)	Errors if optimised for 1 second (ppm)	Errors if optimised for 7 seconds (ppm)	Error difference (ppm)
1	2.593	2.593	< 0.001
7	1.125	1.121	0.004

Table 5.2.2-11 Retrieval errors for 1 and 7 second integration distances showing error differences associated with the system using a non-optimum integration distance for a 5 kHz PRF TC-DIAL system

Integration time used (seconds)	Errors if optimised for 1 second (ppm)	Errors if optimised for 7 seconds (ppm)	Error difference (ppm)
1	2.154	2.160	0.006
7	1.014	1.008	0.006

Table 5.2.2-12 Retrieval errors for 1 and 7 second integration distances showing error differences associated with the system using a non-optimum integration distance for a 15 kHz PRF TC-DIAL system

5.2 Summary

Throughout this chapter the TC-DIAL system configuration and retrieval error capabilities have been explored and defined for a number of different scenarios. The clear sky scenario which is generally used in the scientific literature for defining system configurations assumes a fixed integration path length of approximately 50 km. In this chapter it has been demonstrated however that the instruments integration path length is a free parameter in the determination of the systems optimum configuration and as such can be used to optimise the system for different observation scenarios. It has been shown through simulation that optimising the system for 'cloudy sky' conditions (shorter integration distances with no measurements through the clouds) yields measurements with lower errors over areas of particular scientific interest (such as the tropics) which are generally quite cloudy. The results from these simulations indicate the presence of error penalties associated with a direct detection TC-DIAL instrument operating with an integration path length it is not optimised for. The error penalty incurred is much larger if the instrument is optimised for 50 km and operated at 7 km (0.152 ppm) than vice versa (0.066 ppm), and as such it has been concluded that it would be most beneficial to optimise the system for a shorter integration distance if the primary mission objective is to observe CO_2 in cloudy regions. For heterodyne detection there is very little difference between the errors associated with systems optimised for long and short integration distances, however the retrieval error associated with measurements integrated over 7 km is very poor and unlikely to be of great value (> 2 ppm).

In addition to the scenarios influencing the integration path length this chapter has also investigated the effects of a series of systematic and random ancillary data uncertainties on the overall retrieval error for heterodyne and direct detection. The results from the simulations for the various scenarios are summarised in Table 5.2-1.

The results in Table 5.2-1 demonstrate the importance of ancillary data as a source of systematic error for both heterodyne and direct detection by comparison of the *normal* scenario (systematic error) with the random error scenario. As demonstrated the systematic uncertainty of the ancillary data has been proven to be the most significant source of error for direct detection retrievals as a consequence of its systematic nature. For heterodyne detection the systematic ancillary data error contributes a relatively significant addition to the overall retrieval error but is not the primary driver. The effect of the systematic ancillary data error on heterodyne detection is most noticeable at very long integration distances, as the detector noise error becomes statistically reduced as the integration distance increases allowing the systematic ancillary data error to become more influential.

To obtain ancillary data of atmospheric properties with a random source of error the satellite platform on which the TC-DIAL system is based could in principle include an instrument which could measure some of the atmospheric properties directly beneath the satellite. This methodology would likely involve a significant increase in the satellite instruments complexity but the benefit gained in retrieval error could be significant.

Retrieval type	Direct error (ppm)	Heterodyne error (ppm)
Clear sky normal	0.682	1.008
Cloudy sky normal	0.927	2.473
Clear sky random ancillary	0.215	0.776

Table 5.2-1 Optimised direct and heterodyne TC-DIAL retrieval errors for various measurement scenarios. The normal scenario refers to the use of systematic ancillary data errors, the clear sky scenario refers to 50 km integration distance and the cloudy sky scenario refers to a 7 km integration distance

As mentioned throughout this chapter the systematic errors associated with both direct and heterodyne detection systems exceed the requirements for measuring CO_2 from space on a regional scale (Ingmann et al., 2008). However the errors and biases defined in this chapter often refer to a 50 km integrated series of measurements which imply the NWP derived ancillary data errors are required to be treated as systematic. On a regional scale (thousands of km) the systematic nature of the ancillary data errors are likely to be treatable as more random than systematic and are therefore likely to be greatly reduced for regional scale carbon flux modeling.

Table 5.2-2 presents the system configurations for a current technology TC-DIAL system using the clear sky scenario and systematic ancillary data error scenarios for heterodyne and direct detection based on a series of important sources of uncertainty. The red values shown in Table 5.2-2 are the optimum values derived in this thesis. The black values are obtained from a literature review on TC-DIAL technology (see Chapter 2).

In addition to the system optimisation studies the technology development priorities for a TC-DIAL system has also been investigated through the expansion of the detector noise parameter space. It has been shown by comparison of the noise dependant parameters that the most desirable improvement for a system based on current technology is to attain a more powerful signal on the instruments detector to allow the use of a higher PRF and a larger DOD. To achieve a greater signal at the detector a laser is required to produce a more powerful emission whilst retaining desirable emission properties (such as good laser frequency stability). Laser development has been one of the major challenges for space-borne TC-DIAL concepts and as such it cannot be assumed that such improved laser powers will be readily available in the near future.

Parameter	Direct detection	Heterodyne detection
Satellite altitude	450 km	450 km
Satellite velocity	7 km s^{-1}	7 km s^{-1}
Integration distance	50 km (variable)	50 km (fixed)
Receiver telescope diameter	1 m	1 m
Emission power	5 W	5 W
Emission efficiency	0.9	0.9
Receiver efficiency	0.9	0.9
Heterodyne efficiency	N.A	0.2
Surface footprint	180 m	180 m
Pulse repetition frequency	**13 Hz**	**15 kHz**
Detector efficiency	0.7	0.7
Detector NEP	5×10^{-14}	5×10^{-14}
Noise factor	1	1
Frequency offset from 4875.7489 cm^{-1}	**-0.076**	**-0.085**
Emission power ratio	**15.5:1**	**6:1**

Table 5.2-2 Direct and heterodyne detection TC-DIAL system configurations based on current technology parameters. Red terms are optimised values for a 50 km integration path length (clear sky scenario) and ancillary data as a systematic source of error

It has been demonstrated in this chapter that the emission power ratio is an influential free parameter in the instruments configuration and overall retrieval error. Simulations performed have demonstrated that if the TC-DIAL system does not have the ability to alter the emission power ratio then it incurs a retrieval error of < 10% for both heterodyne and direct detection systems. As a result the facility within the instrument to adjust the emission power ratio is not a development priority at present but a desirable ability.

For both heterodyne and direct detection systems the optimum configurations have been derived for measurements made specifically over vegetation and ocean biomes for a series of some of the most important sources of error. It has been shown that the high variability of the Earth's surface reflectance implies a TC-DIAL system is required to be optimised for one particular surface reflectance value. Vegetation and ocean scenes present similar surface reflectance's, and this fact combined with their importance to the global carbon cycle implies a TC-DIAL system measuring atmospheric CO_2 fluxes would likely be optimised for vegetation and ocean scenes.

Some of the primary sources of random error for TC-DIAL retrievals have been investigated including the surface reflectance variability, detector noise and the laser frequency stability errors. It has been found that based on these errors the frequency stability error provides relatively minor additional uncertainty to the overall retrieval error with an addition of approximately 0.4 ppm per sounding (depending on laser frequency). The surface reflectance variability has been shown to be the second weakest additional retrieval error contributing approximately 2.1 ppm per sounding. The relative contribution of the instruments detector noise depends heavily on the detection technique employed. For heterodyne detection detector noise is the primary source of random error contributing approximately 180 ppm per sounding, but for direct detection it is of equal magnitude to the surface reflectance variability error with a contribution of approximately 2.1 ppm per sounding. The addition of surface reflectance variability and laser frequency stability errors is almost completely negligible for heterodyne detection owing to its very high PRF and detector noise. For direct detection however the surface reflectance variability contributes a significant source of additional uncertainty. Minimising the footprint overlap is desirable in order to reduce the source of uncertainty associated with surface reflectance variability, particularly as it is likely to introduce regional biases which are detrimental to a global study on carbon fluxes. To improve the surface footprint collocation the satellite is required to be built to minimise internal vibrations and if possible operate two lasers with slightly different viewing angles so that the temporal delay between the online and offline emissions results in footprints that completely overlap on the surface.

Despite the significant contributions from both detector noise and surface reflectance variability the primary error for direct detection TC-DIAL is associated with the systematic nature of the ancillary data uncertainties, and being able to treat this source of error as random would lead to the most significant retrieval error improvement.

From the research presented in this chapter it may be concluded that of the two detection techniques direct detection TC-DIAL is likely to be the preferable method for measuring atmospheric CO_2 owing to its lower retrieval error for both long and short integration distances. In addition direct detection is a technologically simpler technique and therefore more appropriate for space-borne applications.

6. A methodology for determining the errors introduced to TC-DIAL retrievals of atmospheric CO_2 by surface reflectance variability

TC-DIAL measurements made from a moving platform such as an aircraft or a low Earth orbiting satellite are performed under constantly changing surface reflectance conditions. The resulting variability introduced to the attenuation of the transmitted laser signals within the measurement environment has consequences on the accuracy of TC-DIAL retrievals on two different spatial scales. On the scale of kilometers the variability of the Earth's surface reflectance introduces unavoidable changes in the magnitude of the signal intensities received on the instruments detector for each measurement pair (online and offline). The changing signal intensities combined with the presence of detector noise leads to fluctuations in the measurements signal to noise ratio (SNR) as a function of orbital position. The potential for high magnitude signal fluctuations renders the Earth's surface reflectance and its variability around the globe one of the key drivers for the optimum system configuration (see Chapter 5).

The variability of the Earth's surface reflectance on much smaller spatial scales (< 10 m) is also of importance to the accuracy of TC-DIAL retrievals and is the main focus of this chapter. The small scale surface reflectance variability within a single laser footprint introduces uncertainties to the TC-DIAL retrieval owing to the online and offline footprints being incompletely collocated on the surface. The footprint collocation ambiguity produces undefined modifications in the ratio of the online and offline signal intensities returned to the detector for each measurement pair (Figure 6.1-2). The S_{on} and S_{off} values (see Chapter 3) derived from the online and offline soundings are the only source information available to the TC-DIAL retrieval regarding the probed volume of atmosphere, and any modulation in the ratio of their intensities which does not arise from atmospheric CO_2 absorption leads to errors in the measured differential optical depth. The footprint collocation ambiguity present in each TC-DIAL measurement is created by two independent factors. First the presence of vibrations within the satellite can create laser pointing jitter which generates random offsets in the relative positions of the online and offline surface footprints. Second, a time delay between the online and offline transmissions designed to avoid cross signal contamination in the lower atmosphere (> 15 km) results in a fixed and predictable surface footprint separation of over 1 meter owing to the satellites high orbital velocity (7 km s^{-1}). The combination of the two main footprint collocation ambiguities can lead to footprint deviations of up to 10 meters (Amediek et al., 2009; Loth et al., 2005).

The following chapter investigates the retrieval error introduced by small scale surface reflectance variability over agricultural surfaces using passive satellite remote sensing data with the aim of deriving an approximate magnitude for the retrieval error for a low Earth orbiting TC-DIAL system.

6.1 Modeling surface reflectance variability

To investigate the error introduced to TC-DIAL retrievals by small scale surface reflectance variability the Earth's surface must be modeled with a suitable resolution to capture the variability on a spatial scale of approximately 10 meters (maximum laser footprint overlap). The Earth's surface reflectance is defined in the TCDS computer model using a 500 m resolution bi-directional reflectance distribution function (BRDF) parameterised with MODIS MCD43A1.5 BRDF data (see Chapter 3). The BRDF model provides TCDS simulations with surface reflectance values for the entire Earth at 2 µm from the perspective of a space-borne TC-DIAL instrument. Unfortunately, the TCDS BRDF model's resolution of 500 m 0imposes limitations on the realism of its surface reflectance variability on the scale required. To compensate scaling factors are derived from higher resolution 2 µm Landsat 7 radiance data.

Landsat 7 is a sun synchronous orbiting satellite at 705 km altitude carrying an enhanced thematic imager which measures at 2 µm in the nadir direction with a spatial resolution of approximately 30 m (GSFC, 2011). The Landsat 7 orbit has an equatorial overpass time of between 10 and 11 am local time which implies the solar zenith angle (SZA) of the surface radiance measurements is generally quite high. In the summer time when the SZA is at its minimum for 11 am local time (approximately 30 degrees in the UK) significant shadowing is present in the Landsat 7 data from tall objects on the surface. To avoid incorrectly deriving surface reflectance variability from the Landsat 7 data owing to surface shadowing, the scenes are required to be flat and empty of all tall objects such as tall buildings, forests and cliffs. Rural agriculture on flat land is a surface type which is sufficiently shadow free for the purposes of this study as typical obstructions such as small trees and hedgerows are sufficiently short and sparse to be of significance (Figure 6.1-1). To ensure only rural agriculture is used as regions of interest for this study careful vetting of Landsat 7 imagery is carried out by eye to mask settlements, forestry and cloud obscurations from the scenes.

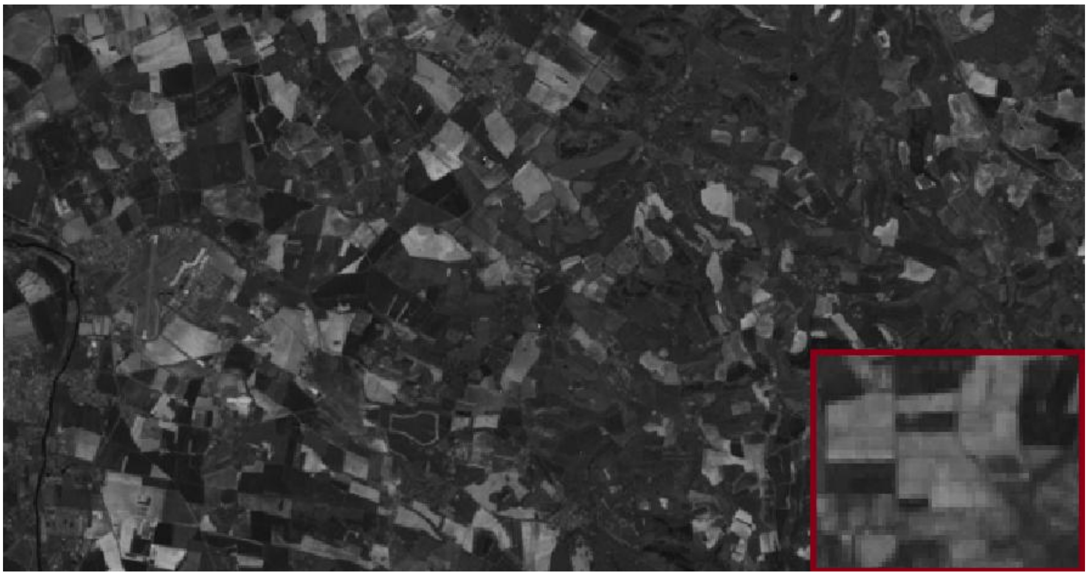

Figure 6.1-1 An example of 2 µm Landsat 7 radiance data over a region of agriculture in the UK used in the derivation of resolution scaling factors, inset is a zoomed in portion of the scene to show 30 m resolution pixilation relative to the size of typical fields.

The 2 µm Landsat 7 radiance data are obtained in 120 km^2 scenes for various regions of Europe and the United States in units of W sr^{-1} m^{-2}. The data are converted into unitless surface reflectance values using the TC-DIAL viewing geometry and instrument configuration presented in Table 5.2-2.

The conversion process from radiance to reflectance is performed for error checking purposes only, as the unit difference between reflectance and radiance has no effect on the results owing to the data being used to derive relative variability scaling factors which are independent on absolute magnitudes. Equation 153 is presented to demonstrate the conversion calculation showing that the terms within the function are constant for all measurements taken by the same instrument.

$$S = \frac{2\pi RA(1 - \cos\theta)}{P} \qquad 153$$

where S is the surface reflectance, R is the surface radiance from the Landsat data, A is the laser's surface footprint area in m^2, θ is the angle between the centre of the laser footprint and the edge of the satellite's receiver mirror in units of radians and P is the power of the incident electromagnetic radiation in W.

The TC-DIAL viewing geometry for a measurement pair (online and offline soundings) consists of two closely overlapping circular footprints on the Earth's surface (Figure 6.1-2). The energy across each footprint is distributed as symmetrical 2 dimensional Gaussian distributions with intensity maxima at the centre of each footprint. The non-linearity in the spatial energy density within the laser pulse allows variations in surface reflectance anywhere within the surface footprints to cause CO_2 retrieval ambiguities. In general a surface with greater reflectance variability within the area of the laser footprints will cause greater retrieval error for a given offset in footprint collocation.

Each of the 120 km^2 Landsat 7 agricultural scenes is divided up into 57,600 individual 500 x 500 m MODIS pixel sized areas known here as MPA's. Within each MPA there are 256 complete 30 m Landsat 7 pixels which are averaged over to simulate the surface reflectance observed by a complete MODIS pixel. The surface reflectance variability at 500 m resolution is then simulated by calculating the relative difference between two spatially adjacent MPA's.

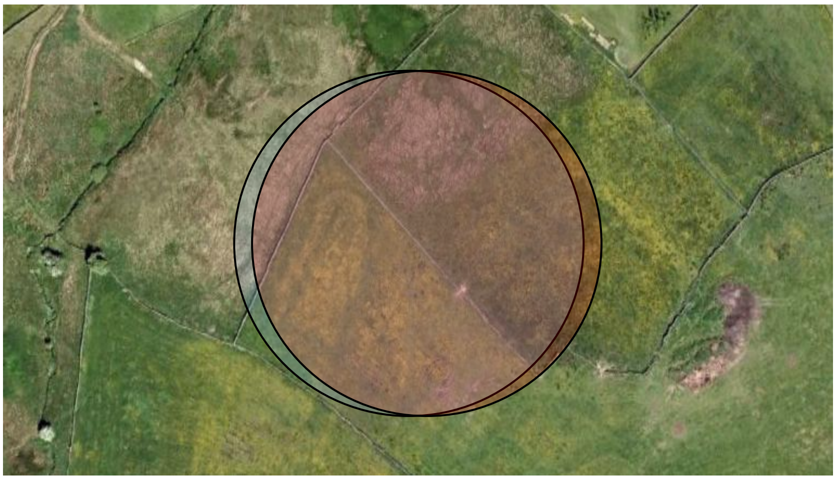

Figure 6.1-2 Overlapping 150 m wide online and offline laser footprints (to scale) 10 m apart demonstrating the level of variability over a typical area of agriculture within the footprints, background image produced by Google Earth from a scene over the UK.

An arrangement of Landsat 7 samples within each MPA pair is selected by a Landsat arrangement template known as LAT's. The template is laid out to best match the footprint areas of the TC-DIAL viewing geometry with a diameter of 150 m (Figure 3-2). Two LAT's of equal dimensions are defined to simulate the online and offline surface footprints with one positioned a single Landsat 7 pixel along from the other to simulate a 30 m footprint separation distance. The intensity of each LAT is multiplied by a 2 dimensional Gaussian weighting function to account for the power distribution across the footprints scaled such that 95% of the total power exists within the footprint area (2 standard deviations of the normal distribution).

The Gaussian weighted LAT pairs are moved around within each MPA pair to all 324 possible positions. At each position the reflectance within the LAT's is averaged to provide simulated measurements at 30 m resolution. The relative difference between the LAT's is recorded at each location within the MPA and the differences between the reflectance variabilitys measured by the LATS and the MPA pair is used to generate a distribution of scaling factors. The distribution is averaged to provide a single scaling factor for that MPA pair and the process is carried out for all 28,800 MPA pairs within each of the Landsat 7 scenes.

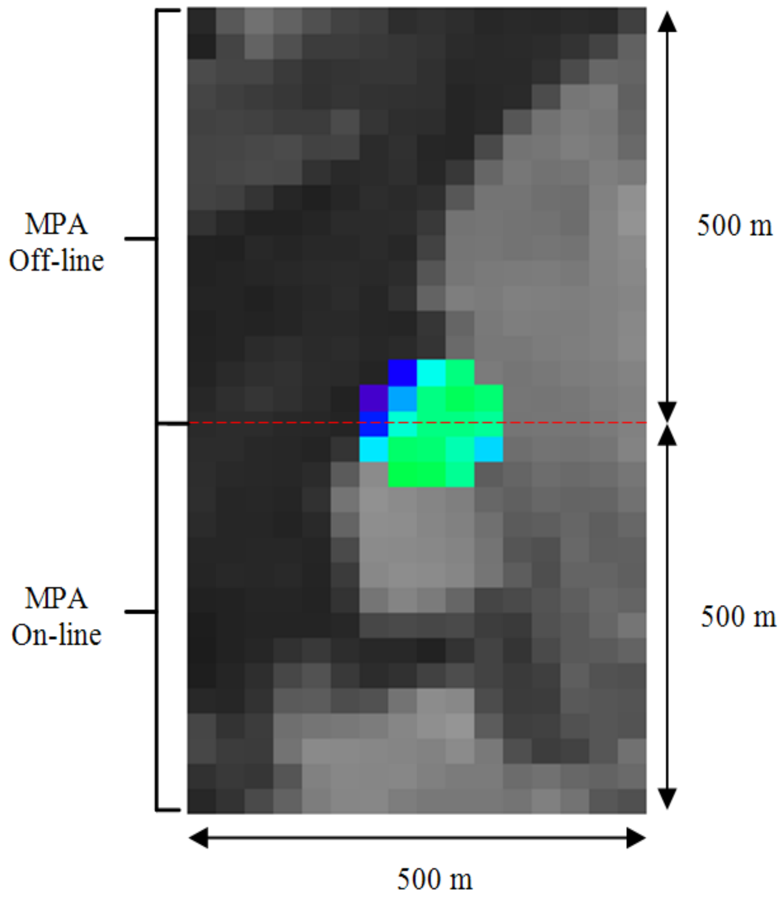

Figure 6.1-3 Landsat 7 reflectance data (grey scale) for two spatially adjacent MPA's with a single TC-DIAL viewing geometry LAT highlighted in colour in the centre.

The resulting distribution of scaling factors derived for each region is relatively well constrained with standard deviations of between 0.14 and 0.46. The scaling factor distributions are presented as number density plots for all MPA's for regions in the UK, US, Czech Republic and France in Figure 6.1-4.

The width of the distributions presented in Figure 6.1-4 demonstrate the influence that location has on the difference observed in the surface reflectance variability between 500 and 30 m resolutions. In Europe the average size of a field is significantly smaller than in the United States, and this is particularly true for the Czech Republic where field sizes are exceptionally small. The difference between average field sizes influences the distributions presented in Figure 6.1-4 by the derived scaling factors being more constrained about the mean for the United States than Europe. The larger fields in the United States allow 500 m resolution data to more closely represent the reflectance variability observed at 30 m resolution owing to their fields generally exceeding an area of 500 m^2. The statistics of the distributions are presented in Table 3.1.9-1.

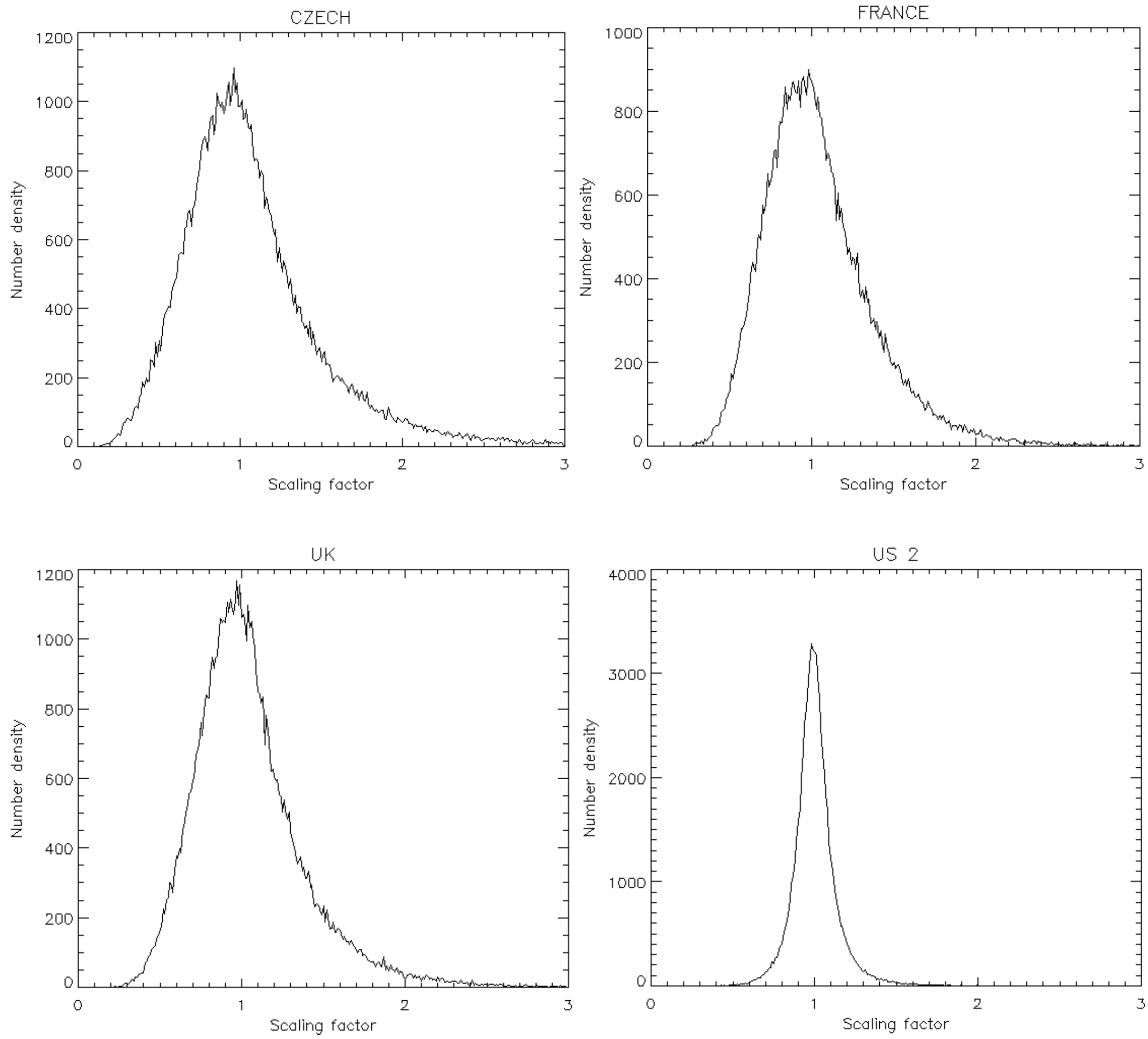

Figure 6.1-4 Number density of scaling factors derived for various regions of agriculture from a comparison of 500 m MODIS data with 30 m Landsat data

The MODIS BRDF model in the TCDS is used in the present study to provide the absolute magnitude of the surface reflectance for each simulated TC-DIAL sounding from the perspective of an orbiting satellite instrument. The BRDF model provides a realistic magnitude for the received signal intensities onto which the signal variability can be added (see Chapter 3). The surface reflectance variability is applied to the measurement by adjusting the offline (trailing) signal intensity by a relative variability determined from two vertically adjacent MODIS pixels modified by the nearest available scaling factor (equation 154).

Region of interest	Longitude minimum	Longitude maximum	Latitude minimum	Latitude maximum	Mean (F)	Standard deviation
UK	-2.901	0.614	50.712	52.708	1.049	0.34
US	-90.741	-87.801	37.864	39.861	1.025	0.25
US 2	-90.196	-87.304	39.299	41.295	1.01	0.14
France	-2.457	0.830	47.899	49.863	1.046	0.34
Czech R.	13.041	16.363	47.835	49.865	1.084	0.46

Table 6.1-1 Statistics for scaling factor distributions for resolution conversions between MODIS 500 m and Landsat 30 m resolution data sets over various regions

The application of the resolution scaling factors achieves an approximation for the retrieval error associated with two TC-DIAL footprints with a collocation ambiguity of 30 m. It is expected however that the separation distance between the footprints from a TC-DIAL instrument in low Earth orbit will be no larger than approximately 10 m. Further modifications to the scaling factors are therefore required to determine the approximate error magnitude associated with a < 10 m resolution overlap. A recent study by Amediek et al. 2009 investigated the effect of surface footprint separation distance on TC-DIAL retrieval accuracy for the 1.6 µm region (Amediek et al., 2009). Their research involved an airborne LiDAR system flown over a variety of surface types to determine the retrieval error associated with surface reflectance variability. Owing to their laser system having a much smaller surface footprint than a TC-DIAL system in low Earth orbit the authors were required to upscale their surface footprint size which involved investigating the effect of footprint separation on the measured reflectance variability. The results from their study indicated a relative reflectance variability difference of approximately 3 between a 30 and a 10 m overlap and 5 between a 30 and 5 m overlap for the 1.6 µm wavelength. Assuming this value is similar to the relative difference in surface reflectance variability for the 2 µm wavelength the magnitude of the scaling factors (from unity) are divided by this corrective factor to achieve an approximation for the retrieval error associated with a 10 and 5 m footprint overlap over agricultural regions (equation 154).

$$S_{off} = S_{on} + \frac{VFS_{on}}{A} \qquad 154$$

where S_{off} is the received offline signal intensity, S_{on} is the received online signal intensity derived from the TCDS BRDF model, V is the 500 m resolution relative variability, F is the 500 to 30 m resolution scaling factor from Landsat data for the appropriate MODIS pixel, and A is a resolution scaling factor derived from airborne measurements of surface reflectance variability to attain an approximation for the error associated with < 10 m footprint overlap.

6.2 Results from surface reflectance variability study

The results of the surface reflectance variability study for each region investigated are presented in Table 6.2-1 for 30, 10 and 5 m footprint overlaps. The retrieval errors from the studies are calculated for instruments with 50 km integration distances and 50 Hz PRF to provide continuity with results from the study carried out by Amediek et al. 2009. The statistical reduction of the retrieval errors is achieved using Gaussian error statistics using the function presented in Section 5.1.5.1.

The results presented demonstrate a significant difference in retrieval errors at various footprint offsets and highlights the need to ensure that TC-DIAL surface footprints are as closely overlapping as possible. The results also show a significant difference in retrieval error over various regions of agricultural surface types demonstrating the systems sensitivity to the spatial scale of the surface reflectance variability.

Region of interest	30 m retrieval error (ppm)	10 m retrieval error (ppm)	5 m retrieval error (ppm)
UK	0.626	0.283	0.159
France	0.312	0.167	0.112
Czech R.	0.696	0.318	0.187
US	0.275	0.116	0.062
US 2	0.202	0.083	0.044
Average	**0.422**	**0.193**	**0.113**

Table 6.2-1 Approximations for TC-DIAL retrieval errors owing to surface reflectance variability for 30, 10 and 5 m footprint overlap distances over various regions using 50 km integration distances and 50 Hz PRF (for comparative purpose to Amediek et al. 2009)

An example of the retrieval error distribution from a number of simulated TC-DIAL satellite orbits over UK agriculture is presented in Figure 6.2-1.

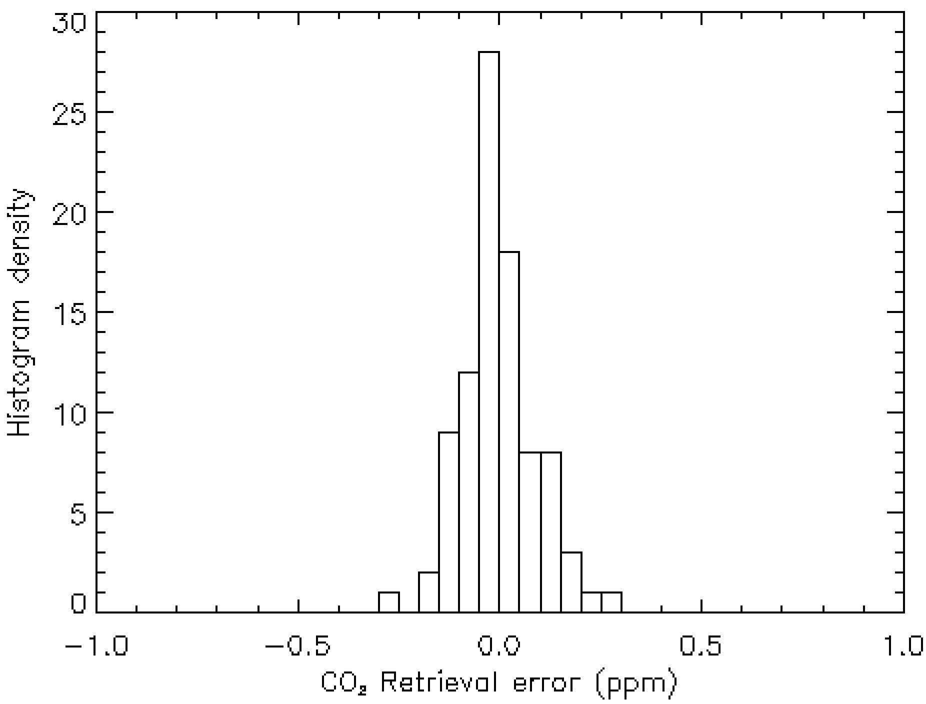

Figure 6.2-1 Number density of retrieval errors for a number of simulated TC-DIAL satellite overpasses over UK agriculture for 50 km integration distance and 50 Hz PRF

6.3 Summary

The use of satellite remote sensing data to determine an approximation for the TC-DIAL retrieval error associated with small scale surface reflectance variability has been demonstrated. The results produced are in general agreement with a study carried out by Amediek et al. 2009 with the determination of retrieval errors of approximately 0.2 ppm for a 10 m footprint collocation ambiguity. The retrieval errors have been derived for a range of different surface footprint overlaps including an approximation for the retrieval error associated with a 5 m overlap for the TC-DIAL optimisation study in Chapter 5. It has been demonstrated that a 5 m footprint collocation ambiguity will result in a TC-DIAL retrieval error of approximately 0.1 ppm for a 50 km integrated series of soundings with a PRF of 50 Hz. This value equates to an average of approximately 2.1 ppm per sounding.

Through comparison of results obtained from different regions it has been shown that the surface reflectance variability over agriculture is highly dependent on the size of the fields over which the measurements are made. For the US data set the scaling factors between 500 and 30 m resolutions are more tightly constrained around the mean than in Europe, particularly in the Czech Republic where field sizes are exceptionally small. The difference between the variability in the scaling factors is an indicator for the magnitude of the small scale surface reflectance variability, and this is reflected in the retrieval errors generated which are greater in Europe than in the US.

The greatest limitation in the presented study is the resolution of the available satellite imagery at the appropriate wavelength which has resulted in the frequent use of scaling factors. The study could be improved if higher resolution satellite imagery at 2 μm were available. The second greatest limitation to this study is the shadowing present in the data owing to the high solar zenith angle associated with Landsat 7 imagery rendering the study suitable only to regions of flat land where there are no tall objects. A greater range of surface types could be investigated if data were available with a lower solar zenith angle.

7. Investigating the retrieval error associated with detector integration time for a space-borne TC-DIAL instrument

The following chapter investigates the influence of detector integration time on the accuracy of space-borne direct detection TC-DIAL retrievals. In the context of TC-DIAL the detector integration time may be defined as the length of time over which the detector is exposed to returning electromagnetic radiation for each individual laser sounding. In general the detector integration time is required to be roughly the same magnitude as the temporal width of the returning waveform in order to capture as much signal as possible whilst minimising the influence of detector noise. The precise relationship between the detector integration time and the shape and size of the returning waveform is required to be suitably defined in order to achieve an optimised system.

This chapter investigates a parameter tradeoff that exists between the duration of exposure to detector noise and the signal strength captured from a returning laser pulse when the detector integration time is altered. The error contribution is relatively minor in comparison to those described in Chapter 5, however understanding the nature of its influence on the retrieval error may allow it to be reduced to a negligible level without comprise to other error sources.

7.1 The detector noise and received signal intensity tradeoff

A space-borne TC-DIAL system emits laser pulses through the Earth's atmosphere with a finite size in both the spatial and temporal domains. When the pulses reach the surface they are scattered in many different directions with part of their energy returning to the satellite with temporal waveforms which carry information about the surface terrain. At the point of emission and throughout the downward journey through the atmosphere the laser pulses have a temporal shape which can be approximated as a skewed Gaussian distribution as demonstrated on the left of Figure 3.1.14-1 (see Chapter 3 for the formulation). The temporal integration over the returning waveform is a system parameter which is required to be carefully defined in order to avoid unnecessary noise. The detectors integration time drives a tradeoff between the total signal strength received on the detector and the detector noise associated with the measurement. Increasing the magnitude of the temporal integration allows for greater received signal intensity by extending the time over which the signal is collected, however it also allows for greater exposure to detector noise (see Chapter 3).

The highly variable nature of the Earth's surface introduces variability to the shape of the temporal waveform scattered from the surface, rendering a global optimum integration time impossible to achieve. An example of the potential differences between returning waveforms can be seen by comparing the images presented in Figure 7.1-1. The left image of Figure 7.1-1 shows the waveform of a simulated pulse returning from a smooth surface, whereas the right image shows a simulated waveform scattered from a tree canopy.

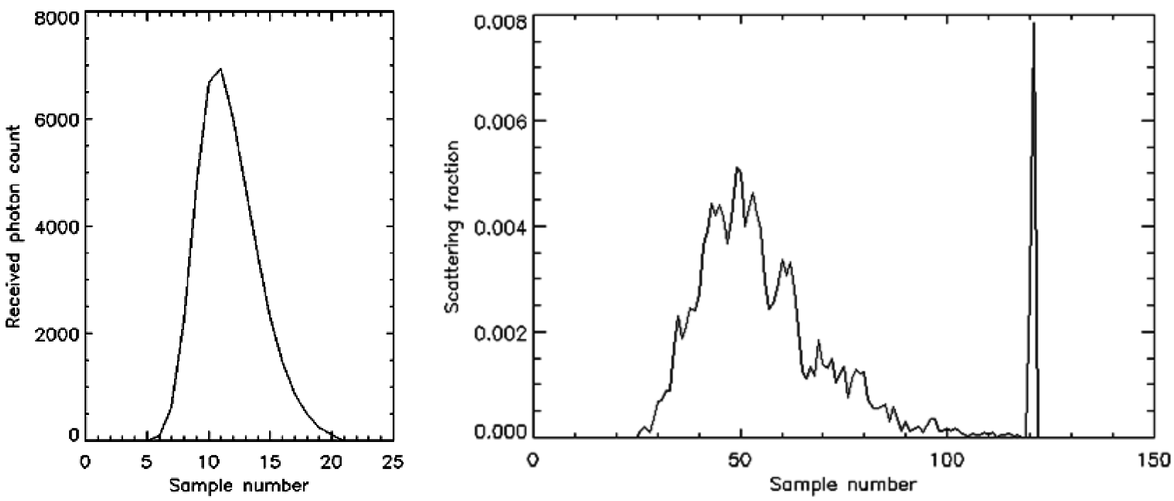

Figure 7.1-1 Laser pulse waveforms defined as a function of detector sample number in the temporal domain for a simulated space-borne TC-DIAL instrument for smooth (left) and forest canopy (right) signal returns

This chapter investigates the case of a waveform scattering off a smooth surface and therefore largely retaining its original shape. Surfaces which could produce this effect include smooth oceans, snow, ice or desert. The study is only performed for a direct detection TC-DIAL system owing to heterodyne detections high PRF rendering small error fluctuations negligible.

To demonstrate the relative contribution of the dependant parameters in modifying the retrieval error Figure 7.1-2 has been produced showing the effects of changing integration time on detector noise owing to both an increase in signal intensity and an increase in detector noise due to a greater exposure time. The system configuration for the simulations performed is given in Table 5.2-2 for a direct detection system. The results are produced by simulating direct detection TC-DIAL retrievals over a series of integration times for different *artificial* scenarios. The scenarios are referred to as artificial as the effects of altering the integration time on the retrieval are removed for one of the two dependant parameters in the simulations. The first scenario has a fixed integration time over the returning pulse in order to demonstrate the error gained solely by increasing the integration time for the detector noise, the second scenario has a fixed integration time for the detector noise to demonstrate the effect of changing the integration time over the pulse waveform (to gain more signal on the detector).

Figure 7.1-2 demonstrates the relative importance of the dependant parameters that directly influence the retrieval error associated with the detector integration time. For the fixed pulse integration time scenario the increase in the single shot retrieval error is a direct result of an increase in exposure to detector noise. For the fixed detector noise integration time scenario the retrieval error curve is defined by the amount of signal received on the detector as the integration window extends over the returning waveform. The retrieval error initially decreases as more of the returning signal is received on the instruments detector, however a saturation point is eventually reached as the integration extends over the wings of the received pulse. By comparing the two error curves it is clear that an optimum integration time exists for a given pulse width and shape.

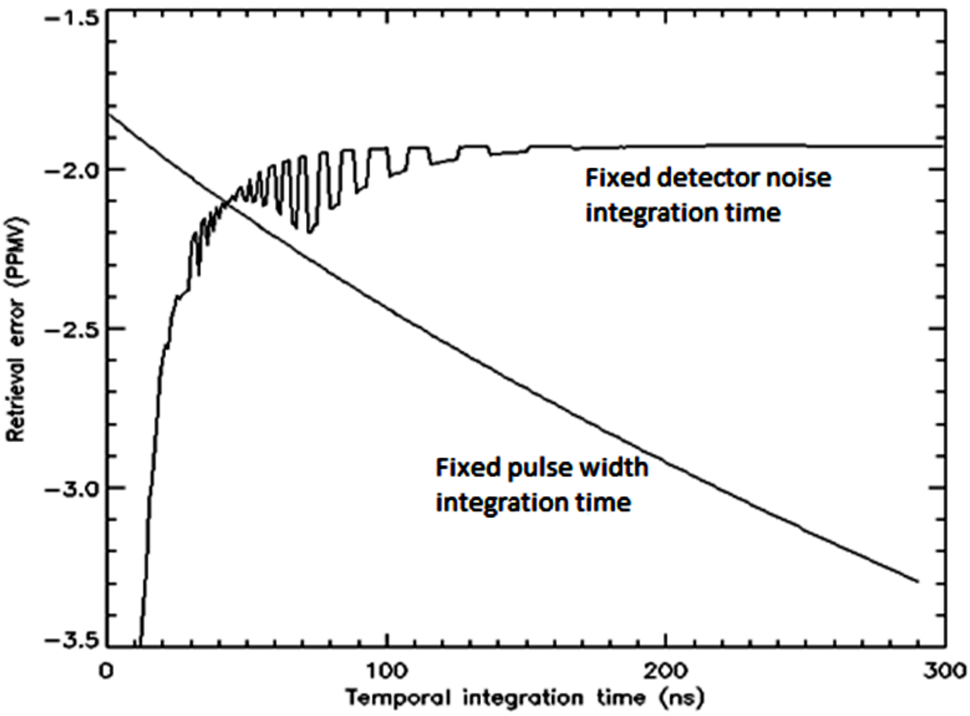

Figure 7.1-2 Single shot direct detection TC-DIAL retrieval error as a function of detector integration time for two scenarios to show their relative effects, scenario 1 is for a fixed pulse width integration time (detector noise varies), scenario 2 is for a fixed detector noise integration time (signal intensity from pulse integration varies)

The negative y axis of Figure 7.1-2 demonstrates the influence on the retrieval by positive signal intensity noise contributions which were used in the simulation. The jagged nature of the fixed detector noise integration time is caused by a sampling error introduced by differences in the exact positioning of the temporal integration window relative to the centre of the returning pulse. These fluctuations may be considered artifacts of the simulation given its objective to provide the theoretical tradeoffs between the two dependant parameters, however the TCDS model is design to accommodate uncertainty in the exact position of the centre of the returning pulse, and therefore each sample is likely to be slightly offset from the very middle of the pulse resulting in the error fluctuations observed in Figure 7.1-2.

To determine the optimum detector integration time for the perfect surface reflection scenario the TCDS is run iteratively using its batch mode of operation with a pulse width of 100 ns and a Gaussian skew factor of 3 to define the returning pulse waveform (see Chapter

3). The intensity of the received signal is split across multiple samples of the returning pulse for very small integration times. The TCDS uses a simple maximum intensity filter to isolate the highest intensity sample for use in each retrieval.

Figure 7.1-3 shows the results from the simulation over a range of 5 to 150 ns.

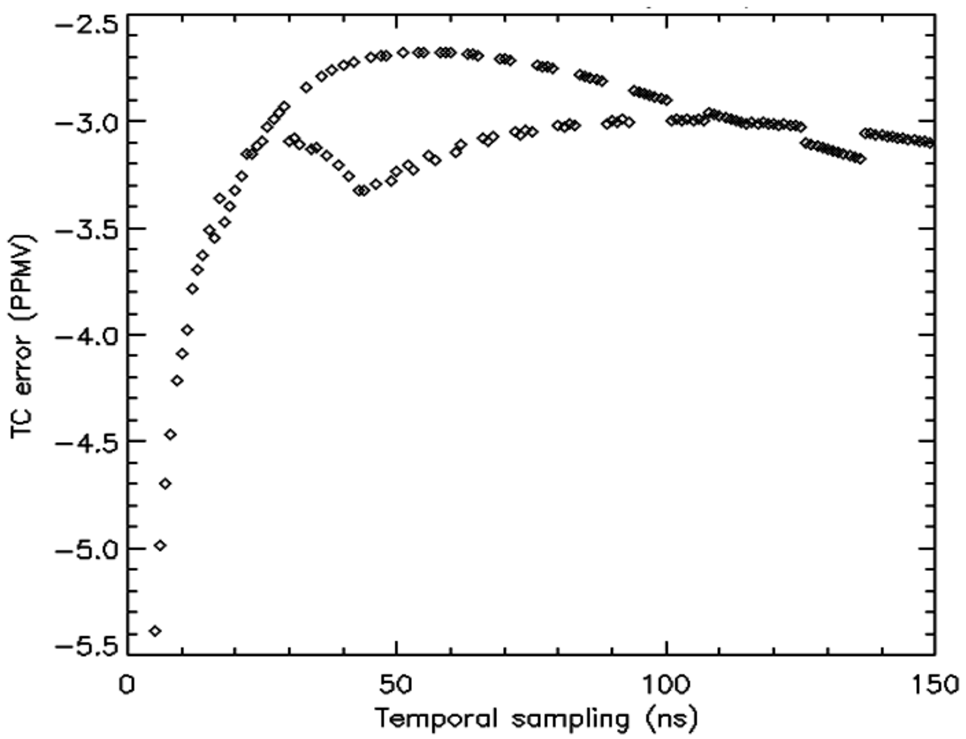

Figure 7.1-3 Direct detection TC-DIAL single shot retrieval errors for various detector integration times (temporal sampling) for a pulse full width half maximum of 100 ns and a skew factor of 3

Figure 7.1-3 presents the retrieval errors for various integration times (temporal sampling) showing the combination of the error sources presented in Figure 7.1-2. At very small integration times the absolute magnitude of the retrieval error is significantly higher than elsewhere owing to there being fewer photons available for detection. As the integration time increases greater signal intensity is available and the retrieval error begins to decrease, however at very long integration times the detector noise begins to dominate and the absolute magnitude of the overall error begins to increase again.

Two separate retrieval error modes are present in Figure 7.1-3 as a result of the aforementioned pulse sampling position which creates (in this case) two different peak amplitudes. Accommodating the entire distribution of possible error modes is essential owing to the exact position of the pulse centre being unknown largely due to the variability of the Earth's surface topography. Two examples of high resolution pulse sampling are presented in Figure 7.1-4 with the left image showing sampling in the very middle of the pulse which captures the peak, and the right image showing sampling which is slightly offset from the middle which misses the peak.

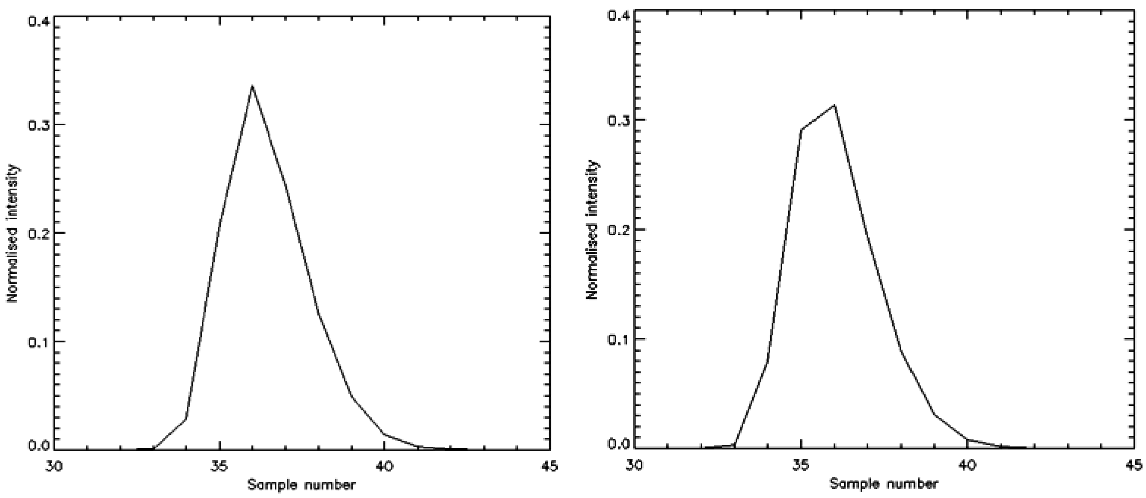

Figure 7.1-4 Two example of pulse sampling at different positions, left image shows ideal sampling where the very peak is captured at the middle of the sample, the right image shows a situation where the sampling does not properly capture the peak

To investigate the optimum detector integration time for the perfect surface reflectance scenario all possible error modes are required to be incorporated in the study and this is carried in section 7.2.

7.2 Determining the optimum detector integration time for a skewed Gaussian laser waveform

To ensure a sufficiently large range of possible sampling positions are explored a sample shift algorithm is applied in the TCDS which allows the sampling of the returning pulse to differ by a given amount. With this feature enabled the TCDS is iteratively run using its batch mode of operation to generate hundreds of different sampling positions for 50, 100, 200 and 300 ns pulse widths (full width half maximum) with a skew factor of 3 in order to derive optimum detector integration times. The results are presented in Figure 7.2-1. The green lines in Figure 7.2-1 show the running mean of the distributions and the red lines show the middle point between the maximum and the minimum of the distributions.

The minimum retrieval error for each of the results presented in Figure 7.2-1 is determined based on the minimum error point of the retrieval errors running means (green line). The optimum integration times for each of the pulse widths are presented in Table 3.1.9-1 along with the ratio of the two quantities.

As presented in Table 3.1.9-1 the ratio of the optimum integration times for a given pulse width is very stable at approximately 0.46 implying a direct relationship between the optimum integration time and the width of the pulse for a perfectly reflected laser signal. The magnitude of the pulse FWHM to optimum integration time ratio is likely to be driven by the shape of the waveform, and therefore for a perfectly reflected signal this refers to the skew factor for the Gaussian distribution. A similar study for waveforms returning from various surfaces would be required to produce a greater distribution of possible optimum integration times. A more complete data set representing the main surface types of the Earth could be used to optimise the system for a given biome or to create a general optimum TC-DIAL system for all surface type.

The magnitude of the error differences associated with the detectors temporal integration for a perfectly reflected signal are relatively minor, particularly as the error incurred by a deviation from the optimum would be reduced by the integration of multiple soundings. As shown in Figure 7.2-1 the optimum point for each pulse width sits on a relatively flat peak, and therefore even a system operating as much as 50 ns outside of the optimum would result in generally less than 0.3 ppm additional retrieval error per sounding, corresponding to approximately 0.08 ppm for each 50 km integrated series of measurements (13 Hz PRF).

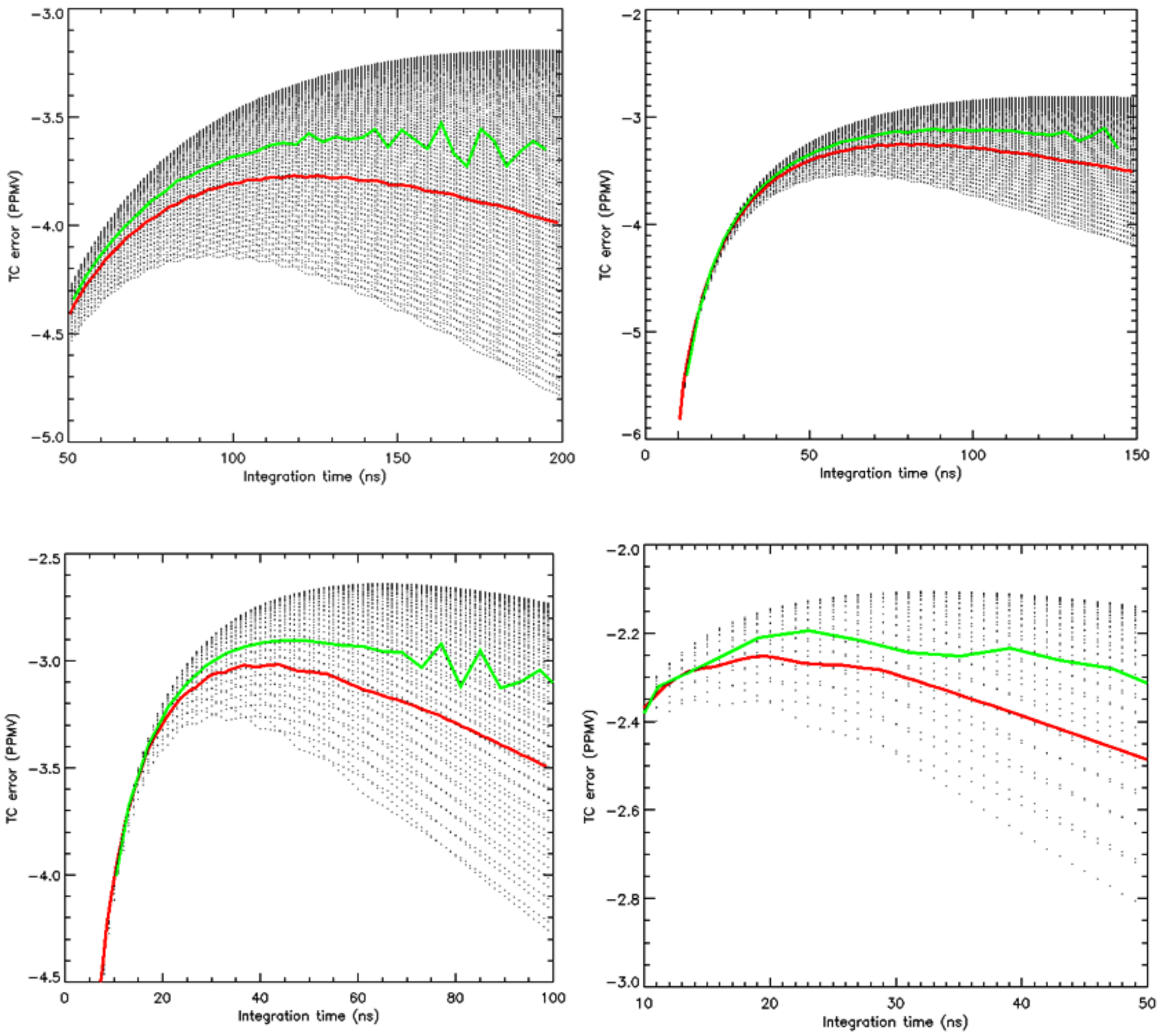

Figure 7.2-1 Direct detection TC-DIAL retrieval errors for 300 (top left), 200 (top right), 100 (bottom left) and 50 ns (bottom right) pulse widths (full width half maximums) for a range of pulse sampling positions as a function integration time, red lines show middle values (between max and min), and green lines show the running means

Pulse FWHM (ns) (A)	Optimum integration time (ns) (B)	B/A Ratio
50	23	0.46
100	47	0.47
200	90	0.45
300	140	0.46

Table 7.2-1 Optimum integration times for various pulse full width half maximums (FWHM) with the ratio of the optimum integration time against the pulse FWHM for Gaussian distributions with a skew factor of 3.

By comparing the plots in Figure 7.2-1 it can be seen that the magnitude of the error penalty associated with a deviation from the optimum detector integration time changes depending on the pulse width. A narrower pulse is more effected by a given offset than a wider pulse, however as shown by Figure 7.2-1 the error magnitude is relatively minor in all cases, particularly in comparison to the retrieval errors described in Chapter 5. It can also be seen by considering the gradient of the green and red lines presented in Figure 7.2-1 that a much larger error penalty would be in incurred if the detector integration time were shorter than an optimum than if it were greater. It is therefore clear that in all cases a small over estimation of the optimum would be desirable as opposed to a small under estimation.

In theory it is possible that a TC-DIAL system with a very short integration time could average more than one sample of the received pulse to form a more accurate retrieval, however multiple low intensity samples will result in a greater overall retrieval error than a single high intensity sample owing to the non-linear relationship between signal intensity and detector noise. To properly determine the merit of potentially oversampling the returning laser pulse a separate study investigating this effect would be required and this would be recommended for further research.

7.3 Summary

The parameter tradeoffs associated with the alteration of the detector integration time have been explored in the context of their influence on direct detection TC-DIAL retrieval errors. For the specific case of a perfect reflection scenario as investigated in this chapter, a direct relationship has been demonstrated between the received pulse FWHM and the detector integration time. For a skewed Gaussian waveform with a skew factor of 3, the optimum detector integration time has been shown to be approximately 0.46 times the FWHM of the pulse. Through extrapolation of the results from the ideal reflection scenario it may be inferred that for any given pulse shape and width there will be an optimum detector integration time. To accommodate the variety of waveform shapes that would return from surfaces around the Earth a more comprehensive study would be required with simulations of waveforms representing a large range of the Earth's surface types. Determination of the optimum integration time for the most important surface types for CO_2 TC-DIAL (such as forestry) would allow the selection of a detector integration time which would minimise the detector noise whilst maximising the signal intensity received over the most important regions.

By considering the retrieval errors associated with a variety of pulse widths it has been shown that narrower pulses are slightly more sensitive than wider pulses to deviations in the detector integration time from the optimum value. However, it has also been demonstrated that the additional retrieval error for a very large (positive) deviation from the optimum of 50 ns results in < 0.1 ppm additional retrieval error over a 50 km integrated series of measurements. The effect of being away from the optimum value is therefore relatively low in comparison to other sources of error which combine to > 0.6 ppm, however it remains desirable for a TC-DIAL system to be configured to minimise this error for the most important surface types to CO_2 research.

Finally it has been shown that the retrieval error associated with a non optimum detector integration time is far more sensitive to an underestimation than overestimation; therefore it would be recommended to ensure a generous detector integration time is selected in the region surrounding the optimum value.

8. Conclusions and future work

Anthropogenic emissions of greenhouse gases are leading to a warming of Earth's surface and atmosphere via the greenhouse effect with unknown consequences on the Earth's future climate. Atmospheric CO_2 has been shown to be the most important of the anthropogenic contributors to the enhanced greenhouse effect owing to its relatively high atmospheric concentration and positive trend. The current atmospheric CO_2 measurement systems are unable to provide sufficient spatial and temporal coverage of the Earth's atmosphere to suitably constrain the main CO_2 sources and sinks and as a result additional measurement systems are needed to provide a more comprehensive understanding of the Earth's carbon cycle.

This thesis has investigated the technological readiness of a new approach for measuring global atmospheric CO_2 concentrations known as space-borne TC-DIAL, and has highlighted recent improvements in detector technology at 2 μm. The advancements in 2 μm detector technology have led to a new interest in 2 μm TC-DIAL and for this reason the 2 μm wavelength has been focused on in this thesis.

Previous studies have investigated much of the parameter space for space-borne TC-DIAL retrievals and have arrived at optimum system configurations and capabilities, however many of these studies have been based on out of date spectroscopy (HITRAN 2004) and detector technology, and have omitted a number of important parameters in the determination of the optimum system. To advance on the previous studies a similar approach has been adopted in this thesis by the development of a computer simulation using up to date spectroscopy and technology specifications to determine the capabilities and optimum configuration of a space-borne TC-DIAL system.

A TC-DIAL computer simulation known as the TCDS has been developed to provide a tool with which to investigate the parameter space surrounding the accuracy of TC-DIAL retrievals. The model was written using well established physical principles for its spectroscopy, atmospheric scattering and surface interaction (BRDF) procedures.

In addition to the TCDS a multiple scattering Monte Carlo model has been written and used to generate correction factors to compensate for errors incurred by the limitations of the single scattering model incorporated in the TCDS. It has been found that at cloud optical depths > 0.5 errors begin to appear in the single scattering geometry regime of the TCDS, and therefore for simulations with cloud optical depths in excess of 0.5 the Monte Carlo correction factors are applied to the simulations.

Using Monte Carlo corrected TCDS simulations in combination with height resolved cloud statistics it has been shown that heterodyne detection is required to operate a PRF of either 5 or 15 kHz in order to minimise the possibility of cross signal contamination occurring in the presence of cloud. Cross signal contamination has been demonstrated to have the potential to result in very high retrieval errors which can be avoided by careful selection of the instruments PRF. For heterodyne detection which theoretically has no optimum PRF the restriction to the 5 and 15 kHz regions has provided an important constraint in the determination of the optimum heterodyne system configuration.

For both direct and heterodyne TC-DIAL systems the optimum configurations for clear sky and cloudy sky conditions (shorter integration times) have been derived based on a number of important error parameters. It has been shown that optimising a direct detection system for cloudy conditions will aid in reducing retrieval errors over regions of patchy cloud with very little effect on the accuracy of clear sky retrievals. This finding is particularly important for direct detection as it has been shown that direct detection systems are very sensitive to a reduction in signal intensity through cloud scattering and therefore avoidance of cloudy scenes is of great importance. For heterodyne detection cloudy scenes are of less importance owing to its ability to see through relatively thin cloud, however despite this advantage under clear sky conditions heterodyne detection retrieval errors are approximately 0.35 ppm higher over a 50 km integrated series of measurements than direct detection. As a result of this general retrieval error difference and because direct detection can see between patchy clouds with an accuracy comparable to heterodyne detection seeing through the clouds, it is concluded that for space-borne TC-DIAL a direct detection approach is most desirable based on the error parameters considered.

Many of the primary retrieval errors (but not all) for both direct detection and heterodyne detection have been investigated, including surface reflectance variability, ancillary data errors, detector noise (dark current) and laser frequency stability. Based on the sources of error considered the uncertainties in the ancillary data have been found to be the most influential owing to them being systematic and therefore not reducible by integration over multiple soundings on a 50 km scale. It has been postulated that a satellite carrying the TC-DIAL system could include some form of additional instrument to measure the ancillary data as opposed to relying on NWP models which may reduce the systematic error in the retrieval process. In addition it has also been mentioned that the systematic nature of the NWP derived ancillary data is likely to only be systematic on the scale of individual integrated measurements (< 100 km), however on a regional scale (> 1000 km) the systematic error is likely to become more random and therefore reduced when combined in a carbon flux model.

A more comprehensive investigation into the optimum system configurations for heterodyne and direct detection could be achieved with a more realistic spectroscopy model than the simplistic Voigt convolution process applied in the TCDS and by considering addition retrieval error sources. This thesis provides approximate magnitudes for many of the main retrieval errors and technology development priorities and demonstrates methodologies for determining the importance of some of the components which make up the TC-DIAL retrieval parameter space. For precise quantification and definition of the optimum system however a more realistic simulation would be required with improvements in the realism of the spectroscopy being the top priority alongside incorporating other important sources of retrieval uncertainty such as errors in the spectral line strengths and shapes which will greatly influence the retrieval accuracy, additional noise associated with the analogue to digital conversion process within the detector and path length uncertainties associated with instrument temporal sampling.

In addition to improving the accuracy of the simulations by improving the realism of various model components and including more error components in the optimisation process, it is also recommended that the following two investigations are carried out. First a more comprehensive cloud study would lead to a better understanding of the improvement TC-DIAL viewing geometry will gain over the current passive remote sensing instruments in the presence of patchy cloud, and second a more thorough study on the variety of returning laser waveforms would allow the derivation of a more precise optimum detector integration time for a TC-DIAL system.

Bibliography

Abedin, M. N, Refaat, T. F, Ismail, S., Koch, G., and Singh, U. N: Progress of 2-micron detectors for application to lidar remote sensing, Proc. Earth Science Technology Conference ESTC 2008, 2004,

Abshire, J., Krainak, M., Sun, X., and Andrews, A.: Laser sounder approach for measuring atmospheric CO_2 from orbit, 24th international laser radar conference, Boulder, Colorado, 637-640, 2008.

Amediek, A., Fix, A., Ehret, G., Caron, J., and Durand, Y.: Airborne lidar reflectance measurements at 1.57 µm in support of the A-SCOPE mission for atmospheric CO_2, Atmospheric Measurement Techniques, 2, 755-772, 2009.

Anderson, B. E , Gregory, G. L, Collins Jr, J. E, Sachse, G. W , Conway, J., and Whiting, G. P: Airborne observations of spatial and temporal variability of tropospheric carbon dioxide, Journal of Geophysical Research, 101, 1985-1997, 1996.

Azzalini, A.: A class of distributions which includes the normal ones, Scandinavian Journal of Statistics 12, 171–178, 1985.

Bakwin, P. S, Tans, P. P, Hurst, D. F, and Zhao, C.: Measurements of carbon dioxide on very tall towers: Results of the noaa/cmdl program, Tellus, 5-B, 14, 1998.

Barkley, M. P., Monks, P. S., Freiβ, U., Mittermeier, R. L., Fast, H., Korner, S., and Heimann, M.: Comparisons between sciamachy atmospheric co_2 retrieved using (FSI) WFM-DOAS to ground based FTIR data and the TM3 chemistry transport model., Atmos. Chem. Phys, 6, 4483-4498, 2006.

Barnola, J., -M: Status of the atmospheric co_2 reconstruction from ice cores analyses, Tellus, 51B, 151-155, 1998.

Berger, A.: Global warming, fact or fiction: From weather forcasing to exploring the solar system., 2000.

Berner, R., A: The phanerozoic carbon cycle CO_2 and O_2, Oxford University Press, 2004.

Bovensmann, H., Burrows, J. P., Buchwitz, M., Frerick, J., Noel, S., Rozanov, V. V., Chance, K. V., and Goede, A. P. H.: Sciamachy: Mission objectives and measurement modes, American Meteorol. Soc. Journal of the Atmospheric Sciences, 56, 127-150, 1999.

Bruneau, D., Gibert, F., Flamant, P., and Pelon, J.: Complementary study of differential absorption lidar optimization in direct and heterodyne detections, Applied Optics, 45, 4898-4908, 2006.

Buchwitz, M., de Beek, R., Noel, S., Burrows, J. P, Bovensmann, H., Schneising, O., Khlystova, I., Bruns, M., Bremer, H., Bergamaschi, P., Korner, S., and Heimann, M.: Atmospheric carbon gases retrieved from sciamachy by wfm-doas: Version 0.5 CO and CH_4 and impact of calibration improvements on CO_2 retireval, Atmospheric Chemistry, 6, 24, 2006.

Chevallier, F., Engelen, R., and Peylin, P.: The contribution of airs data to the estimation of co_2 sources and sinks, Geophysical Research Letters, 32, 2005.

Chevallier, F., Feng, L., Boesch, H., Palmer, P., Rayner, P.: On the impact of transport model errors for the estimation of CO_2 surface fluxes from GOSAT observations, Geophysical Research Letters, 37, 2010.

Ciais, P., Denning, A. S, Tans, P. P, Berry, J. A, Randall, D. A, Collatz, G. J, Sellers, P. J, White, J. W, Troiler, M., Meijer, H., Francey, R. J, Monfray, P., and Heimann, M.: A three-dimensional synthesis study of $\delta^{18}O$ in atmospheric CO_2, Geophysical Research Letters, 102, 5857-5872, 1997.

Cornette, W. M., Shanks, J. G: Physically reasonable analytic expression for the single-scattering phase function, Applied Optics, 31, 3152 - 3160, 1992.

Disney, M. I., Kalogirou, V., Lewis, P., Prieto-Blanco, Hancock, S., and Pfiefer, M.: Simulating the impact of discrete-return lidar system and survey characteristics over young conifer and broadleaf forests, Remote Sensing of Environment, 114, 1546-1560, 2010.

Douglas, B.: Sea level change in the era of the recording tide gauges, Sea level rise: History and consequence, 2001.

Dufour, E., and Breon, F.: Spaceborne estimates of atmospheric CO_2 column by use of the differential absorption method: Error analysis, Appl. Opt, 42, 3595-3609, 2003.

Ehleringer, J., Cerling, T., and Dearing, M.: A history of atmospheric co_2 and its effects on plants animals and ecosystems, Springer, 2005.

Ehret, G., and Kiemle, C.: Requirements definition for future dial instruments, Institut fur Physik der Atmosphare (API), DLR, 2005.

Ehret, G., Kiemle, C., Wirth, M., Amediek, A., Fix, A., and Houweling, S.: Space-borne remote sensing of CO_2, CH_4 and N_2O by integrated path differential absorption lidar: A sensitivity analysis, Appl. Phys. B, 90, 593-608, 2008.

El-Sherif, A., and King, A.: Analysis and optimization of Q-switched operation of a Tm^{3+} -doped silica fiber laser operating at 2 µm, IEEE Transactions on Geoscience and Remote Sensing, 39, 759-765, 2003.

Feely, R. A, Sabine, C. L, Takahashi, T., and Wanninkhof, R.: Uptake and storage of carbon dioxide in the ocean: The global CO_2 survey, Journal of Oceanography, 14, 14, 2001.

Fiocco, G., and Smullin, L. D.: Detection of scattering layers in the upper atmosphere (60 - 140 km) by optical radar, Nature, 199, 1275-1276, 1963.

Gibert, F., Flamant, P. H, Bruneau, D., and Loth, C.: Two-micrometer heterodyne differential absorption lidar measurements of the atmospheric co_2 mixing ratio in the boundary layer, Applied Optics, 45, 4448-4458, 2006.

Gloor, M., Gruber, N., Sarmiento, J., Sabine, C. L, and Feely, R. A: A first estimate of present and preindustrial air-sea co_2 flux patterns based on ocean interior carbon measurements and models., Geophysical Research Letters, 30, 2002.

GSFC: Landsat 7 science data users handbook, Landsat 7 Project Office, National Aeronautics and Space Administration, Goddard Space Flight Center Maryland, 2011.

Hamazaki, T., Kaneko, A., Kuze, A., and Kondo, K.: Fourier transform spectrometer for greenhouse gases observing satellite (GOSAT), Enabling sensor and platform technologies for spaceborne remote sensing, 5659, 73-80, 2005.

Hanson, J., Sato, M., Kharecha, P., Russell, G., Lea, D. W., and Siddall, M.: Climate change and trace gases, Philosophical transactions of the royal society A, 365, 1925 - 1954, 2007.

Hays, J. D, Imbrie, J., and Chackleton, N. J: Variations in the Earth's orbit: Pacemaker for the ice ages, 1976.

Hayward, R. A., Clarkson, W. A., Turner, P. W., and Nilsson, J., Grudinin, A. B. and Hanna, D. C. : Cladding-pumped Tm-doped silica fibre laser with high power single-mode output at 2µm, Electron. Lett., 36, 711-712, 2000.

Heaps, W.: Measurement of carbon dioxide via space borne laser absorption, LiDAR technologies, techniques, and measurements for Atmospheric Remote Sensing III, SPIE 6750, 2007.

Hönninger, G.: Halogen oxide studies in the boundary layer by multi axis differential optical absorption spectroscopy and active longpath-doas, PhD. Thesis, Institut für Umweltphysik, Universität Heidelberg, 2002.

Houghton, J.: Global warming, Rep. Prog. Phys, 68, 2005.

Houweling, S., Breon, F.-M., Aben, I., Rodenbeck, C., Gloor, M., Heimann, M., and Ciais, P.: Inverse modeling of CO_2 sources and sinks using satellite data: A synthetic inter-comparison of measurement techniques and their performance as a function of space and time, Atmos. Chem. Phys., 4, 523–538, 2004.

Hu, Y. X., and Stamnes, K.: An accurate parameterization of the radiative properties of water clouds suitable for use in climate models, Journal of Climate, 6, 728-739, 1992.

Hungershoefer, K., Breon, -M. F., Peylin, P., Chevallier, F., Rayner, P., Klonecki, A., Houweling, S. and Marshall, J.: Evaluation of various observing systems for the global monitoring of CO_2 surface fluxes, Atmos. Chem. Phys., 10, 10503-10520, 2010.

Hurwitz, M. D, and Ricciuto, D. M: Transport of carbon dioxide in the presence of storm systems over a northern wisconsin forest, American Meteorological Society, 61, 2003.

Ingmann, P., Bensi, P., Duran, Y., Griva, A., and Clissold, P.: Candidate earth explorer core mission: A-scope - advanced space carbon and climate observation of planet Earth, 2008.

IPCC: Climate change 2007 the physical science basis, Cambridge, 996 pp., 2007.

Ismail, S., Koch, G. J., Barnes, B. W., Abedin, N., Refaat, T. F., Yu, J., Vay, S. A., Kooi, S., Browell, E., and Singh, U. N.: Technology developments for tropospheric profiling of co_2 and ground-based measurements, 22nd Internation Laser Radar Conference (ILRC 2004), Proceedings of the Conference held 12-16 July, 2004 in Matera, Italy. Edited by Gelsomina Pappalardo and Aldo Amodeo. ESA SP-561. Paris: European Space Agency., 65, 2004.

Jackson, S. D., and King, T.: High-power diode-cladding-pumped tm-doped silica fiber laser, Optics Letters, 23, 1462-1464, 1998.

Keeling, C., D: Aspects of climate variability in the pacific and the western americas, 1989.

Keeling, C. D., Whorf, T. P., Wahlen, M., and Van der Plicht, J.: Interannual extremes in the rate of rise of atmoshperic carbon dioxide since 1980, Nature, 375, 666-670, 1995.

Koch, G. J., Beyon, J. Y., Gibert, F., Barnes, B., and Ismail, S.: Side-line tunable laser transmitter for differential absorption lidar measurements of co_2: Design and application to atmospheric measurements, Applied Optics, 47, 944-956 2008.

Kulawik, S. S., Jones, A. D. B., Nassar, R., Irion, F. W., Worden, J. R., Bowman, K. W., Machida, T., Matsueda, H., Sawa, Y., Biraud, S. C., Fischer, M. L., Jacobson, A. R.: Characterization of Tropospheric Emission Spectrometer (TES) CO_2 for carbon cycle science, Atmos. Chem. Phys., 10, 5601,5623, 2010.

Lacaze, R.: Polder-2 algorithm description & product validation, 2005.

Loth, C., Flamant, P. H., Breon, F., Bruneau, D., Desmet, P., Pain, T., Dabas, A., Prunet, P., and Cariou, J.: The future of atmospheric carbon dioxide testing from space. Esa study 17852/04/nl/cb, IPSL, 2005.

Lutgens, F., K, and Tarbuck, E., J: The atmosphere: An introduction to meteorology (8th edition), 8th ed., Prentice Hall, 2000.

Maignan, F., Breon, F. M., and Lacaze, R.: Bidirectional reflectance of earth targets: Evaluation of analytical models using a large set of spaceborne measurements with emphasis on the hot spot, Remote Sensing of Environment, 90, 2003.

McCartney, E. J.: Optics of the atmosphere, John Wiley & Sons Inc, 1976.

Mitchell, A. G. G.: Resonance radiation and excited atoms, Cambridge University Press, 1971.

Muller, D., Vincent, W., and Jefferies, M.: Break-up of the largest arctic ice shelf and associated loss of an epishelf lake, Geophysical Research Letters, 30, 2003.

Nakazawa, T. K. Miyashita, S. Aoki, and M. Tanaka: Temporal and spatial variations of upper tropospheric and lower stratospheric carbon dioxide, Tellus, 106-117, 1991.

Olsen, S. C, and Randerson, J. T.: Differences between surface and column atmospheric and implications for carbon cycle research, Journal of Geophysical Research, 109, 2004.

Pan, Y., Birdsey, R. A., Fang, J., Houghton, R., Kauppi, P. E., Kurz, W. A., Phillips, O. L., Shvidenko, A., Lewis, S. L., Canadell, J. G., Ciais, P., Jackson, R. B., Pacala, S. W., McGuire, A. D., Piao, S., Rautiainen, A., Sitch, S., Hayes, D.: A Large and Persistent Carbon Sink in the World's Forests, Science, 333, 988, 2011.

Peltier, R.: Global glacial isostatic adjustment and modern instrumental records of relative sea level history, Sea level rise: History and consequences, Academic Press, 2001.

Phillips, O., L, Aragao, L., Lewis, S., Fisher, J., Lloyd, J., Lopez-Gonzalez, G., Malhi, Y., Monteagudo, A., Peacock, J., Quesada, C., van der Heijden, G., Almeida, S., Amaral, L., Arroyo, L., Aymard, G, Baker, T., Banki, O., Blanc, L., Bonal, D., Brando, P., Chave, J., Oliveira, A., Cardozo, N., C, C., Feldpausch, T., Freitas, M., Gloor, E., Higuchi, N., Jimenez, E., Lloyd, G., Meir, P., Mendoza, C., Morel, A., Neill, D., and Nepstad, D.: Drought sensitivity of the amazon rainforest, Sience, 323, 2009.

Platt, U., and Stutz, J.: Differential optical absorption spectroscopy principles and application, Springer, 2008.

Prentice, I., C, and Lenton, T.: The carbon cycle and atmospheric carbon dioixde., In Climate Change 2001:The Scientific Basis, 2001.

Rayner, P. J., and O'Brien, D. M.: The utility of remotely sensed co_2 concentration data in surface source inversions, Geophysical research letters, 28, 175-178, 2001.

Refaat, T. F, Abedin, M. N, Sulima, O., Ismail, S., and Singh, U. N: AlGaAsSb/InGaAsSb phototransistors for 2-µm remote sensing applications, Optical Engineering, 43, 1647-1650, 2004.

Remedios, J. J., Leigh, R. J., Waterfall, A. M., Moore, D. P., Sembhi, H., Parkes, I., Greenhough, J., Chipperfield, M. P., and Hauglustaine, D.: Mipas reference atmospheres and comparisons to v4.61/v4.62 mipas level 2 geophysical data sets, Atmos. Chem. Phys Discuss, 2007.

Rothman, L., Lafferty, W., Mandin, J.-Y., Massie, S. T., Mikhailenko, S. N., Miller, C. E., Moazzen-Ahmadi, N., Naumenko, O. V., Nikitin, A. V., Orphal, J., Perevalov, V. I., Perrin, A., Predoi-Cross, A., Rinsland, C. P., Rotger, M., Simeckova, M., Smith, M. A. H., Sung, K., Tashkun, S. A., Tennyson, J., Toth, R. A., Vandaele, A. C., and Vander Auwera, J.: The hitran 2008 molecular spectropscopic database, Journal of Quantitative Spectroscopy & Radiative Transfer, 110, 533-572, 2009.

Rozanov, A., Rozanov, V., Buchwitz, M., Kokhanovsky, A., and Burrows, J. P.: Sciatran 2.0 - a new radiative transfer model for geophysical applications in the 175-2400 nm spectral region, Advances in Space Research, 36, 1015-1019, 2005.

Salomon, J. G., Schaaf, C. B., Strahler, A. H., Gao, F. and Jin, Y.: Validation of the modis bidirectional reflectance distribution function and albedo retrievals using combined observations from the aqua and terra platforms, IEEE Transactions on Geoscience and Remote Sensing, 44, 1555-1565, 2006.

Sarmiento, J. L., and Gruber, N.: Sinks for anthropogenic carbon, Physics Today, 30-36, 2002.

Sarmiento, J. L., Gloor, M., Gruber, N., Beaulieu, C., Jacobson, A. R., Mikaloff Fletcher, S. E., Pacala, S. and Rodgers, K.: Trends and regional distributions of land and ocean carbon sinks, Biogeosciences, 7, 2351 - 2367, 2010.

Scambos, T., Hulbe, M., Fahnestock, M., and Bohlander, J.: The link between climate warming and breakup of ice shelves in the Antarctic peninsula, Journal of Glaciology, 46, 516-530, 2000.

Siegenthaler, U., Stocker, T. F., Monnin, E., Luthi, D., Scheander, J., Stauffer, B., Ratynaud, D., Barnola, J., Fischer, H., Masson-Delmotte, V., and Jouzel, J.: Stable carbon cycle-climate relationship during the later pleistocene, Science, 310, 131-137, 2005.

Siegman, A., E: Lasers, University Science Books, 1986.

Sneep, M. U., Ubachs, W.: Direct measurement of the Rayleigh scattering cross section in various gases, Journal of Quantitative Spectroscopy & Radiative Transfer, 92, 293-310, 2004.

Strahler, A. H., Muchoney, D., Borak, J., Friedl, M., Gopal, S., Lambin, E., and Moody, A.: Modis land cover product algorithm theoretical basis document (atbd), version 5.0, 1999a.

Strahler, A. H., Muller, J.-P., and Members, M. S. T.: Modis brdf/albedo product, algorithm theoretical basis document, 1999b.

Takahashi, T., Stewert, C., Sweeney, C., Poisson, A., Metzl, N., Tilbrook, B., Bates, N., Wanninkhof, R., Feely, R., A, Sabine, C., L, Olafsson, J., and Nojiri, Y.: Global sea-air co_2 flux based on climatological surface ocean pco_2, and seasonal biological and temperature effects, Deep Sea Research Part II, 49, 1601-1622, 2002.

Toth, R. A., Miller, C. E., Brown, L. R., Malathy Devi, V., and Benner, C.: Line positions and strengths of $^{16}O^{12}C^{18}O$, $^{18}O^{12}C^{18}O$ and $^{17}O^{12}C^{18}O$

between 2200 and 7000 cm^{-1}, Journal of Molecular Spectrscopy, 243, 43-61, 2007.

United Nations: Kyoto protocol to the united nations framework convention on climate change, in, edited by: Nations, U., 1998.

Wanner, W., Li, X., and Strahler, A. H.: On the derivation of kernels for kernel-driven models of bidirectional reflectance, Geophysical Research Letters, 100, 21077-21089, 1995.

Weitkamp, C.: Lidar range-resolved optical remote sensing of the atmosphere, Springer, 2005.

WMO: WMO WDCGG data summary, no.34 volume iv, greenhouse gases and other atmospheric gases, 2010.

Wylie, D., Eloranta, E., Spinhirne, J. D., Palm, S. P.: A comparison of cloud cover statistics from the GLAS lidar with HIRS, Journal of Climate, 20, 4968-4871, 2007.